MEERKAT POLARIMETRIC OBSERVATIONS OF PICTOR A

Lexy A. L. Andati

Supervisors:

Prof Oleg M. Smirnov
Dr Lerato M. L. Sebokolodi Baidoo

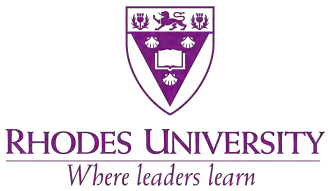

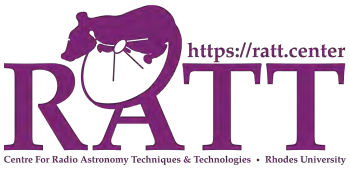

A thesis submitted in fulfilment of the requirements for the degree of

Doctor of Philosophy

At the

Centre for Radio Astronomy Techniques and Technologies
Department of Physics and Electronics
Rhodes University

The financial assistance of the National Research Foundation (NRF) towards this research is hereby acknowledged.
Opinions expressed and conclusions arrived at, are those of the author and are not necessarily to be attributed to the NRF.

July 2024

ABSTRACT

Pictor A is one of the brightest and closest radio galaxies in the Southern Hemisphere, offering a unique opportunity for in-depth studies of the astrophysics of radio galaxies and their interactions with their environments. Many multi-wavelength studies of this source have been done. However, the most comprehensive radio frequency study of Pictor A's morphological components was conducted by Perley et al. (1997) using the Very Large Array (VLA) located in the Northern Hemisphere. To date, that work remains the most detailed study of Pictor A.

In this thesis, we conducted a spectropolarimetric study of Pictor A using new L-band data obtained in 2019 from the high-sensitivity MeerKAT telescope, which provides the deepest and most sensitive data of this source at a continuous and finely sampled frequency coverage in the L-band. Thus, due to Pictor A's proximity, high luminosity, and the MeerKAT's high sensitivity, the data delivers a unique dataset for our study of the magnetic field structure of Pictor A and allows for a detailed study of the source's morphological structures.

We presented the steps taken during our calibration and data reduction, leading to polarimetry-ready images. During the first phase of calibration, excision of data corrupted by instrumental effects and radio frequency interference (RFI) resulted in only 50% useable data. Pictor A's exceptionally bright western hotspot introduced significant artefacts in our images, mitigated in the second calibration phase through direction-dependent calibration. The calibrated data resulted in a multi-frequency synthesis (MFS) Stokes I image of Pictor A at $7.5''$ in resolution with an off-source RMS noise of $\sim$22 μJy/beam. The off-source noise in the Stokes Q and U sub-band images ranged between 95 – 278 μJy/beam and 41 – 233 μJy/beam, respectively. Additionally, we briefly highlighted the effects of RFI in the L-band on polarimetry, particularly the considerable loss of λ^2 coverage of $\sim$50%. All the calibration recipes used for this work were made available in this thesis.

Using Pictor A's data as a testbed, we introduced a `Python`-based tool, `Smops`, developed during the calibration stages of our work. `Smops` was designed for an intermediate post-processing step. It interpolates input sub-band model FITS images (such as those produced by `WSClean`) into finely channelized sub-band model FITS images, thereby generating model images at a higher frequency resolution. `Smops` reduces the need to generate model images with numerous sub-bands, which is computationally intensive and time-consuming. A higher resolution in frequency of the models facilitates more efficient model subtraction during self-calibration.

We then presented the total intensity features of Pictor A, which the calibrated data reveals. We confirmed the presence of Pictor A's radio jet extending from its core to the western hotspot. Notably, this feature, faint and barely visible in previous radio images, is now distinctly observed. The counterjet remains undetectable. Furthermore, we demonstrated the coexistence of radio emission, which is expected to align with previously observed X-ray diffuse emission. This observation confirmed the inverse Compton origin of Pictor A's lobe emission.

Employing the RM-synthesis technique for the spectropolarimetric study of Pictor A, we identified a relatively consistent rotation measure (RM) across its lobes, with an average RM of 48.06 ± 10.19 rad m^{-2} for the entire source. However, the eastern lobe displayed a wider RM dispersion than the western lobe. Moreover, our study affirmed the depolarisation asymmetry previously observed between the western and eastern lobes of Pictor A, where the eastern lobe exhibited significantly more depolarisation than its western counterpart. Most lines-of-sight across Pictor A displayed single-peaked Faraday spectra, indicating a single Faraday rotating screen. However, we also noted that several lines-of-sight ($\sim$23%) showed more than one Faraday peak. An investigation into the

possible causes of the multiple observed peaks using *QU*-fitting suggested that there is a possibility of a Faraday thick structure or multiple Faraday components along these paths. Furthermore, we estimated a Galactic RM contribution towards Pictor A of 23.57 ± 10.87 rad m^{-2}. We concluded that while our Galaxy may contribute to the mean RM for this source, it cannot explain small-scale fluctuations, which suggests that some fraction of the observed rotation measures could result from some inter-galactic medium, X-ray gas near the shock boundary region (the sheath), or other unknown intervening material.

We introduced `Scrappy`, a `Python`-based tool tailored for processing lines-of-sight data. `Scrappy` yields RM-synthesis diagnostic data products such as the data associated with each line-of-sight, and their corresponding plots in ϕ-space (e.g. cleaned and dirty Faraday spectra and RMTF), and λ^2-space (e.g. the fractional polarisation, and Stokes Q and U). `Scrappy` further avails a `Bash`-based pipeline, `showrunner.sh`, that processes input sub-band Stokes images, automatically selects usable sub-bands, stacks images into Stokes cubes, generates lines-of-sight, processes their corresponding data, and produces diagnostic plots. Additionally, it creates per-pixel maps of fractional polarisation, RM, polarisation angle, peak FDF, and linear polarised intensity. The pipeline ensures reproducibility.

To visualise the diagnostic plots from `Scrappy`, we developed `PolarVis`, a simple web-based tool that enables the visualisation of diagnostic plots associated with each available line-of-sight, thus facilitating the quick exploration of interesting lines-of-sight in regions across this source. This tool facilitates the visualisation of polarisation behaviour for specific lines-of-sight, enabling quick identification of interesting regions of the source. Furthermore, its interactivity promotes the exploration of line-of-sight data. Availing data to the public with this tool permits validation or comparison of results from varying techniques, hence fostering a sense of transparency. As a result, the 2389 lines-of-sight of Pictor A are presented using `PolarVis` and are available at `https://pica.ratt.center`.

DECLARATION

I, **Lexy A. L. Andati**, declare that this thesis titled, "**MeerKAT Polarimetric Observations of Pictor A**" and the work presented in it are my own. I confirm that:

- This work was done wholly or mainly while in candidature for a research degree at this University.
- Where any part of this thesis has previously been submitted for a degree or any other qualification at this University or any other institution, this has been clearly stated.
- Where I have consulted the published work of others, this is always clearly attributed.
- Where I have quoted from the work of others, the source is always given. With the exception of such quotations, this thesis is entirely my own work.
- I have acknowledged all main sources of help.
- Where the thesis is based on work done by myself jointly with others, I have made clear exactly what was done by others and what I have contributed myself.

Makhanda, July 2024

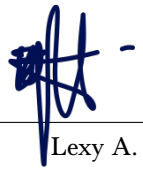

Lexy A. L. Andati

Asifuye Mvua, Imemnyea!

—Wahenga

ACKNOWLEDGMENTS

What a journey!

It has taken a lot of determination and inward fight to get here. However, of greater significance is the support of my supervisors, who have made this thesis possible and shaped my current opinions on research and personal development. Prof. Smirnov: Thank you for your leadership. I have had the privilege of "creative freedom" in this degree, which has been my biggest reward. Thank you for your constant patience, encouragement, presence and calmness, even when things seemed to fall apart. I owe this degree to you. Dr. Makhathini: Thank you for always gassing me up about my abilities when I least expected it. I got the courage to apply to this PhD and other things because of a spark you ignited. Dr. Sebokolodi Baidoo: Thank you for being the mentor I never knew I needed, keeping me in check, and always realising when things were not going okay. This degree was completed in a reasonable time because of your efforts. Javas: Thank you for setting the pace throughout my postgraduate, and keeping the ball rolling in the face of (ad)varsity (LoL), especially in the initial stages of this data reduction.

I'd also like to thank Prof. Rick Perley for stepping in and pushing me towards making my first observation proposal. "*In this radio astronomy business, you have to make a splash!*" he said. Dr. Landman Bester, who was basically the math support in this project, Ben Hugo for polarimetric calibration support, and all those who held the door open for me to get to this point, directly or indirectly. A special thanks to the CaraCal development team for the unforgettable experiences during busy weeks! A special thanks to Dr. Sinhenhlanhla Sikhosana for providing valuable reviews and corrections to parts of this thesis, and Prof Martin Hardcastle for being open to consultation when the need arose.
In the same breath, I also thank my examiners for providing clear, detailed, and useful suggestions on the improvement of this work, as well as their discerning corrections.

My past and present colleagues in the physics department: Alex, Damilola, Cyndie, Kingsley, Eric, Ulrich, Joel, Victoria, Vasco, Findje, and Elizabeth, for providing much-needed companionship during this liberation struggle :D. Special thanks to Ulrich, Damilola, Joel and Cyndie for making it look possible and being constant sources of encouragement and perspective. My sincere gratitude goes to the admins: Verushca, Zizipo and Ncebakazi for organising my stuff even on short notice and being always ready to help.

Lastly, I thank those of my family and friends who took time and effort to check up and motivate me. My dad who sacrificed a lot to ensure I got the best education, and instilled moral values in my being. "*Always be firm but polite*," he used to say. I am honoured to put a 'BIG' title on your name :); This is my ode to you.

More importantly, I acknowledge that it is God's hand, and grace that have sustained me up to now through Psalms 124: 2-8: " *If the Lord had not been on our side when people attacked us, they would have swallowed us alive when their anger flared against us; the flood would have engulfed us, the torrent would have swept over us, the raging waters would have swept us away. Praise be to the Lord, who has not let us be torn by their teeth. We have escaped like a bird from the fowler's snare; the snare has been broken, and we have escaped. Our help is in the name of the Lord, the Maker of heaven and earth.* "

Onwards and Upwards!

PUBLICATIONS

Paper

Andati, Lexy A L et al. (Feb. 2024). 'A Spectropolarimetric Study of Pictor A Radio Galaxy with MeerKAT'. In: *Monthly Notices of the Royal Astronomical Society*, pp. 1626–1641. ISSN: 0035-8711. DOI: 10.1093/mnras/stae598.

Software

Andati, L. A. L. et al. (Dec. 2023a). *PolarVis: Towards Web-based Polarimetric Analysis*. DOI: 10.48550/arXiv.2312.07645. arXiv: 2312.07645 [astro-ph]. URL: https://github.com/Mulan-94/polarvis.

Andati, Lexy A. L. and Lerato M. L. Baidoo (Dec. 2023). *Scrappy: A set of tools geared towards radio-polarimetric analysis*. URL: https://mulan-94.github.io/scrappy/.

Andati, Lexy A. L., Oleg M. Smirnov and Landman H. Bester (Dec. 2023b). *Smops: A Sub-Band Model FITS Image Interpolator*. URL: https://github.com/mulan-94/smops.

CONTENTS

i Some Kind of Manual

1 Introduction 2
- 1.1 Radio Galaxy Morphology . . . 2
- 1.2 Magnetic Fields In And Around Radio Galaxies . . . 6
- 1.3 The Role of Visualisation . . . 8
- 1.4 This Thesis . . . 9

2 Previously on Pictor A 10
- 2.1 Radio Observations . . . 10
  - 2.1.1 Total Intensity . . . 10
  - 2.1.2 Polarisation . . . 13
- 2.2 Optical and X-ray Observations . . . 15
  - 2.2.1 AGN core . . . 15
  - 2.2.2 Jets . . . 16
  - 2.2.3 Hotspots . . . 17
  - 2.2.4 Lobes . . . 19
- 2.3 The General Significance of Pictor A . . . 20
- 2.4 Pictor A And The MeerKAT? . . . 20
- 2.5 Summary . . . 23

3 Techniques and Tools 24
- 3.1 Synchrotron Radiation . . . 24
- 3.2 Polarisation and Faraday Rotation . . . 26
  - 3.2.1 The Polarisation of an Electromagnetic Wave . . . 28
  - 3.2.2 Determining the Rotation Measure . . . 29
  - 3.2.3 Depolarisation . . . 36
- 3.3 Visibilities and Radio Interferometers . . . 37
  - 3.3.1 The Two-element Interferometer . . . 37
  - 3.3.2 Aperture Synthesis . . . 38
  - 3.3.3 Sensitivity . . . 40
  - 3.3.4 SKA and The MeerKAT telescope . . . 41
- 3.4 Summary . . . 41

ii Body of Work

4 Data, Calibration and Imaging 44
- 4.1 Calibration 101 . . . 44
- 4.2 Observation Details . . . 47
- 4.3 Data Reduction . . . 49
  - 4.3.1 Flagging . . . 50
  - 4.3.2 First Generation Calibration . . . 52
  - 4.3.3 Second Generation Calibration . . . 60
  - 4.3.4 Third Generation Calibration (3GC) . . . 64
- 4.4 Smops . . . 69
  - 4.4.1 Architecture . . . 69
  - 4.4.2 Operation . . . 69
  - 4.4.3 Validity Test . . . 70
- 4.5 Towards Polarimetry . . . 71
  - 4.5.1 Polarimetric Imaging . . . 71
  - 4.5.2 What Do Bad Channels Look Like? . . . 74

4.6 Summary . . . 76
5 Keeping Up With Pictor A: A Spectropolarimetric Study 77
5.1 Extracting Spectropolarimetric Information . . . 77
5.2 Total Intensity . . . 78
5.2.1 Hotspots . . . 78
5.2.2 Lobes . . . 80
5.3 Polarimetry . . . 85
5.3.1 Linear Polarised Intensity and Fractional Polarisation . . . 85
5.3.2 Line-of-Sight Fractional Polarisation . . . 85
5.3.3 Depolarisation . . . 88
5.3.4 Faraday Rotation Measures . . . 89
5.3.5 Magnetic Fields . . . 91
5.3.6 RM Gradients and Multiple-Peaked Faraday Spectra . . . 92
5.3.7 Do the Missing Frequencies Affect RM Measurements? . . . 95
5.4 Summary and Conclusions . . . 95
5.5 Chapter Appendix . . . 97
5.5.1 Data Simulations and QU-fitting Specifics . . . 97
5.5.2 Estimating Magnetic Fields of the Radio Plumes . . . 99
5.5.3 Estimating the Jet-Counterjet Ratio . . . 100
6 Seeing is Believing 101
6.1 PolarVis . . . 102
6.1.1 Architecture . . . 102
6.1.2 Operation . . . 104
6.1.3 Application: Visualising Pictor A's Lines-of-Sight . . . 110
6.1.4 Application: Visualising Cygnus A's Lines-of-Sight . . . 112
6.1.5 Known Issues . . . 116
6.1.6 Metrics . . . 117
6.2 Scrappy . . . 118
6.2.1 `sc-beam-plot` . . . 118
6.2.2 `sc-los` . . . 119
6.2.3 `sc-losrm` . . . 120
6.2.4 `sc-rmmap` . . . 121
6.2.5 Tying It All Together: `showrunner.sh` . . . 121
6.3 Future Work . . . 122
6.4 Summary . . . 123
7 Summary, Conclusions, and Future Work 125

iii Appendix
a Region Definitions Used For This Thesis 128
a.1 Pictor A's noise estimate region . . . 128
a.2 Lobes . . . 128
a.3 Novel Jet-like Feature . . . 129
a.4 Jet Position angle . . . 129
a.5 Missing IC/CMB radio emission . . . 129
a.6 Spectral index regions . . . 130
a.7 Profile bins . . . 131
b Data Reduction Recipes 132
b.1 Caracal: lGC . . . 132
b.2 SelfCal . . . 139
b.2.1 Selfcal Steps . . . 139
b.2.2 `CubiCal` config file . . . 141
b.2.3 Generating a custom MFS image . . . 146
c Setting Up PolarVis on a Web Server 148
c.1 Setting up Apache . . . 148

c.2 Website Setup 149
d Calibration and Imaging Gotchas/Tips/Tricks 153
d.1 In General 153
d.2 Some CubiCal 153
d.3 Image Presentation 154

Bibliography 155

LIST OF FIGURES

Figure 1.1 An illustration of the AGN unification scheme from Beckmann and Shrader (2013). . . . 3
Figure 1.2 Illustrating the difference between FR-I and FR-II sources. . . . 4
Figure 1.3 Illustration of jet propagation leading to the formation of hotspots and radio lobes. Image adapted from Carilli and Barthel (1996). . . . 4
Figure 1.4 A composite image of Pictor A in radio and X-ray. . . . 5
Figure 1.5 The extent of Galactic synchrotron radiation. . . . 7
Figure 1.6 Rotation measures from the NVSS catalogue of 37,543 sources from Taylor et al. (2009). . . . 7
Figure 1.7 Rotation measures from sources in the Northern and Southern Hemispheres from Schnitzeler et al. (2019). . . . 8
Figure 2.1 Older arcminute resolution contour images of Pictor A. . . . 10
Figure 2.2 Pictor A at 5 and 1.4 GHz from VLA data. . . . 11
Figure 2.3 The total intensity map of Pictor A at 7.5″ resolution obtained from the observations of Perley et al. (1997) using the VLA. . . . 12
Figure 2.4 A long baseline VLBI image of Pictor A's parsec-scale jet. . . . 12
Figure 2.5 High resolution contour images of Pictor A's WHS. . . . 13
Figure 2.6 A comparison of older polarisation profiles of Pictor A. . . . 14
Figure 2.7 Polarisation angle orientation and depolarisation ratio across Pictor A from VLA data. . . . 15
Figure 2.8 Pictor A at 2.2″ from the ATCA telescope. . . . 21
Figure 2.9 Pictor A in X-ray superimposed with radio contours. . . . 22
Figure 3.1 An illustration of a synchrotron emitting electron. . . . 25
Figure 3.2 Illustrating the amount of energy required from emission at different field strengths. . . . 27
Figure 3.3 A linearly polarised wave passing through a magneto-ionised medium. . . . 28
Figure 3.4 Illustrating the effect of derotating the RMTF to a common λ_0^2. . . . 32
Figure 3.5 A simple illustration of nested sampling. . . . 35
Figure 3.6 The two-element interferometer. . . . 38
Figure 3.7 The layout of the MeerKAT antenna dishes. . . . 42
Figure 3.8 Parts of a MeerKAT dish. . . . 42
Figure 4.1 A comparison of the uv coverage from VLA to that of MeerKAT for Pictor A. . . . 48
Figure 4.2 The typical structure of a Measurement Set. . . . 50
Figure 4.3 The different RFI affecting the MeerKAT L-band. . . . 51
Figure 4.4 Typical MeerKAT fraction of flagged data. . . . 51
Figure 4.5 Calibrator data flag summaries before 1GC. . . . 52
Figure 4.6 K-Jones solutions from our data. . . . 53
Figure 4.7 G-jones solutions from our data. . . . 54
Figure 4.8 B-Jones solutions from our data. . . . 55
Figure 4.9 Calibrator data flag summaries after first generation calibration (1GC). . . . 56
Figure 4.10 The leakage and position angle calibrator visibilities after 1GC. . . . 57
Figure 4.11 Complex gain calibrator visibilities after 1GC: XX and XY. . . . 58
Figure 4.12 Complex gain calibrator visibilities after 1GC: YY and YX. . . . 59
Figure 4.13 Target data flag summaries after 1GC. . . . 60
Figure 4.14 An illustration of the Cotton-Schwab deconvolution algorithm. . . . 61
Figure 4.15 A comparison of the dirty and deconvolved image of Pictor A before selfcal. 65

Figure 4.16 A comparison of the deconvolved images before and after one round of delay selfcal. . . . 66
Figure 4.17 A comparison of deconvolved images of before and after complex gain phase-amplitude selfcal. . . . 67
Figure 4.18 Pictor A in log scale. . . . 68
Figure 4.19 Channel selection based on channel weights. . . . 73
Figure 4.20 Illustrating the correspondence between the heavily flagged channels and bad images. . . . 75
Figure 4.21 An example of how a bad image looks. . . . 76
Figure 5.1 The RMTF of our data. . . . 78
Figure 5.2 An annotated image of Pictor A showing its various features. . . . 79
Figure 5.3 An illustration of both low and high emission structures in Pictor A. . . . 80
Figure 5.4 Pictor A in X-ray (greyscale) with radio contours image showing the missing X-ray emission. . . . 81
Figure 5.5 A novel collimated feature close to Pictor A's radio core reminiscent of a radio jet. . . . 82
Figure 5.6 The spectral index map of Pictor A. . . . 84
Figure 5.7 Pictor A's linear polarised intensity map. . . . 86
Figure 5.8 The spectra of example LoSs across Pictor A's lobes. . . . 87
Figure 5.9 An illustration of where the various categories of Faraday spectra are found across Pictor A. . . . 88
Figure 5.10 The depolarisation ratio map of Pictor A. . . . 89
Figure 5.11 Binning regions used for RM and depolarisation profiles. . . . 90
Figure 5.12 Binned depolarisation profiles from Pictor A's core towards the hotspots . . . 90
Figure 5.13 RM map and the magnetic field orientation of Pictor A. . . . 92
Figure 5.14 Binned rotation measure profiles with increasing distance from the radio core of Pictor A. . . . 93
Figure 5.15 Model selection using the Bayes Factor selection criterion for modelling done on real data. . . . 94
Figure 5.16 Example plots from the experimental QU-fitting using simulated Q and U. 96
Figure 5.17 The exact rotation measure (RM) and ϕ values used for our simulated experiment. . . . 98
Figure 5.18 The exact fractional values used for our simulated experiment. . . . 99
Figure 6.1 Illustrating the client-server model. . . . 103
Figure 6.2 `PolarVis`' FITS image viewer using `JS9`. . . . 105
Figure 6.3 Plot layout in `PolarVis`' GUI. . . . 106
Figure 6.4 The full GUI of `PolarVis`. . . . 107
Figure 6.5 Parts of an interactive plot. . . . 108
Figure 6.6 Demonstrating `PolarVis`' plot selection capabilities. . . . 109
Figure 6.7 Tab switching on `PolarVis`' plots. . . . 109
Figure 6.8 The current setup of `PolarVis`. . . . 110
Figure 6.9 Cygnus A and its $\sim$ 2000 LoS represented by the green circles. . . . 113
Figure 6.10 Different categories of spectra for Cygnus A on the western lobe. . . . 114
Figure 6.11 Demonstrating tab selection. . . . 115
Figure 6.12 Illustrating interactive legends of `PolarVis`' plots. . . . 116
Figure 6.13 Metrics for the Cygnus A website measured by Lighthouse. . . . 117
Figure 6.14 Example `sc-los` plots showing locations of the autogenerated regions. . . . 121

LIST OF TABLES

Table 4.1 Observational setup information for Pictor A. 47
Table 4.2 Comparison of residual statistics from 4, 16 and 80 channel models. 71
Table 5.1 Mean spectral indices for selected regions within Pictor A. 83
Table 6.1 Software required for the automation script. 123

LISTINGS

4.1 Snippet showing the installation and basic functionality of `Smops`. 70
4.2 A simple workflow involving `Smops`. 70
4.3 The `WSClean` command used in generating our polarimetric images. 72
6.1 Setting up a daemon service for `JS9Helper`. 111
6.2 Setting up `Scrappy`. 118
6.3 Initialising `showrunner.sh` 122
B.1 The `CARACal` pipeline configuration file used for 1 GC 139
B.2 Our specific selfcal steps 141
B.3 `CubiCal` parset file used for 2GC 146
B.4 A simple script to generate a new MFS image by excluding the problematic ones. . 147
C.1 Virtual host file to setup an example website for `PolarVis`. 149
C.2 Dockerfile to build container with `PolarVis`. 152
C.3 Running a Docker container for `PolarVis` 152

ACRONYMS

1GC	first generation calibration
2GC	second generation calibration
3GC	third generation calibration
AGN	Active Galactic Nucleus
API	Application Programmers Interface
ATCA	Australia Telescope Compact Array
`CARACal`	Containerized Automated Radio Astronomy Calibration
CABB	Compact Array Broadband Backend
`CARTA`	Cube Analysis and Rendering Tool for Astronomy
CLI	command-line Interface
CMB	cosmic microwave background
CPU	central processing unit
DDE	direction dependent effects

DIE	direction independent effects
DR	dynamic range
EHS	eastern hotspot
EM	electromagnetic
FDF	Faraday dispersion function
FITS	flexible image transport System
FWHM	full width at half maximum
GB	gigabytes
GUI	graphical user interface
H.E.S.S.	High Energy Stereoscopic System
HST	Hubble Space Telescope
IC	inverse Compton
IC/CMB	inverse Compton cosmic microwave background
JS	JavaScript
LAT	Large Area Telescope
LoS	line-of-sight
MB	megabytes
MS	Measurement Set
MWA	Murchinson Widefield Array
PSF	point spread function
RAM	random access memory
RIME	Radio Interferometer Measurement Equation
RFI	radio frequency interference
RM	rotation measure
RMTF	rotation measure transfer function
selfcal	self-calibration
SED	Spectral Energy Diagram
SKA	Square Kilometre Array
SMBH	supermassive black hole
SSC	synchrotron self-Compton
TB	terabytes
VLA	Very Large Array
VLBI	Very Long Baseline Interferometry
WHS	western hotspot

Part I

SOME KIND OF MANUAL

Atafutaye hachoki, akichoka keshapata.

1

INTRODUCTION

Radio galaxies are some of the most powerful astrophysical sources in the Universe. Pioneering studies of these sources sparked after a Galactic radio signal was accidentally discovered by Karl Jansky (Jansky, 1933a; Jansky, 1933b). Soon after, Cygnus A was discovered in 1939 by Grote Reber due to its strong radio emission (Reber, 1940; Reber, 1949). It was the first identified radio galaxy and remains one of the brightest radio galaxy ever observed (Hey et al., 1948; Bolton, 1948; Bolton and Stanley, 1948). Due to the advancements in observing instruments, and calibration and imaging techniques, thousands of radio galaxies are now known, amongst the most famous being Centaurus A, Virgo A, Hydra A and Pictor A.

Galaxies within the Universe are classified as either normal or active. The active galaxies, often referred to as Active Galactic Nuclei (AGNs), feature a supermassive black hole (SMBH) situated at the galaxy's centre, with masses ranging from 10^6 – 10^{10} times that of the Sun (Xie et al., 1998; Fan et al., 1999; Barth et al., 2003). The SMBH accretes surrounding matter, emitting a substantial amount of power with extreme bolometric radio luminosities of $< 10^{42}$ erg s^{-1} for low-luminosity AGNs, ranges of between 10^{42} – 10^{45} erg s^{-1} for moderate luminosity AGNs, and $> 10^{45}$ erg s^{-1} for high luminosity AGNs such as quasars. This emission exhibits significant variability on time scales of less than a day, suggesting its origin from a compact region at the galactic centre. Furthermore, AGN emissions are generally broad-spectrum, covering the entire electromagnetic spectrum.

According to the Unified model, AGNs can be classified based on radio loudness – radio-quiet (unjetted) or radio-loud (jetted) – and optical emission lines (broad or narrow permitted emission lines). The idea behind the unification scheme is that the type of AGN observed depends on the viewing angle. Fig. 1.1 best illustrates this point. In addition to the black hole, other main components of an AGN are the broad and narrow line regions, the accretion disc, a dusty torus (also known as a dusty absorber) and the jet – we refer the reader to Beckmann and Shrader (2013) and references therein for details regarding the unification model. In short, the difference between the radio-quiet and radio-loud galaxies is that the radio-loud tend to have a prominent jet emission. Low-power and high-power radio galaxies, and blazars are examples of radio-loud AGNs.

1.1 Radio Galaxy Morphology

The development of radio interferometers by Ryle's group (using what is commonly known as the Michelson interferometer that was first described in Ryle and Vonberg, 1946), and later Earth rotation aperture synthesis (Ryle, 1962) improved the angular resolution attainable by radio telescopes and propelled subsequent radio surveys that led to the mapping of radio sources across the sky. Interferometric observations resulted in various catalogues such as the popular 3C catalogue (Edge et al., 1959).[1] A revision of the 3C catalogue by Bennett and Smith (1962) was done, excluding sources below the confusion limit and providing a more reliable list of sources. With new data based on the sources in 3CR and a resolution of $23''$, Mackay (1971) measured the brightness distribution of sources, revealing their morphological structure. This formed the basis of the galaxy classification scheme by Fanaroff and Riley (1974).[2]

1 We introduce the concepts of radio interferometry and telescope resolution in Sec. 3.3.

2 For a brief history of radio interferometry, aperture synthesis and the Cambridge catalogues, see Goss et al. (2023) and https://www.astro.phy.cam.ac.uk/about/history

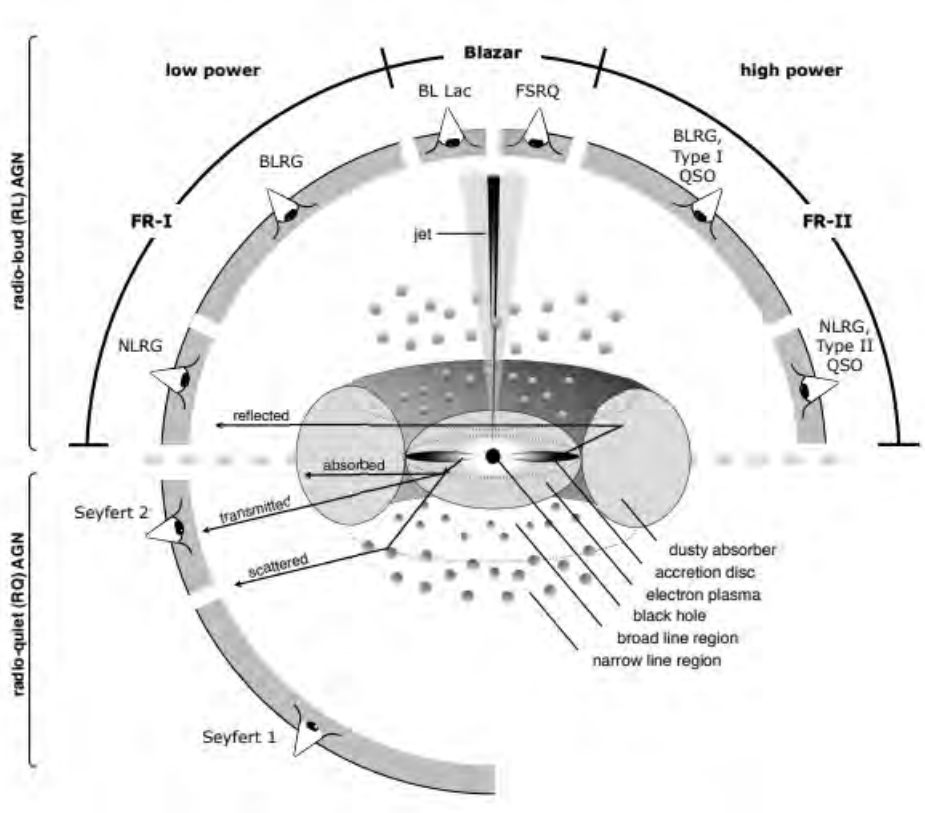

Figure 1.1: An illustration of the AGN unification scheme from Beckmann and Shrader (2013). AGNs can be classified into different categories depending on the viewing angle.

In the Fanaroff and Riley (1974) classification scheme, sources were categorised based on the ratio of the distance between their high brightness regions (called hotspots) on opposite sides relative to their centres (the galaxy core) and the total source extent, which was determined by its lowest brightness value contour. Where the ratio was greater than 0.5, a source was classified as class II (now commonly known as FR-II), meaning the hotspots were further away from the core. As a result, such sources are also known as edge-brightened. On the other hand, those with a ratio of < 0.5 were classified as class I (FR-I). Fanaroff and Riley also noted that in their samples, sources where luminosity $L_{178\,\mathrm{MHz}} < 2 \times 10^{23}$ W Hz^{-1}sr^{-1} were FR-I, indicating a direct relationship between galactic evolution due to its energy transport mechanism and observed morphology. However, Ledlow and Owen (1996), using strongly flux-limited samples from Very Large Array (VLA) data, discovered that the FR-I/FR-II luminosity break depends on the host galaxy's magnitude, with FR-Is exhibiting higher radio luminosities in brighter host galaxies. On the other hand, Mingo et al. (2019) using data from the LOFAR Two-metre Sky Survey (LoTSS) showed that radio luminosity is not a reliable predictor of the FR-I/FR-II dichotomy, as they found an overlap in the luminosities of their FR-I and FR-II radio galaxy populations – with FR-II of low luminosities and FR-I above the previously defined FR-I/FR-II luminosity break.

The typical morphology of radio galaxies consists of a central engine (the core), which hosts a SMBH, jets, radio lobes/plumes, and possibly hotspots. Although many theories exist attempting to explain the formation and evolution of these components, the current best and well-accepted model is the *jet-model*, which was first conceived and developed by Longair et al. (1973) and Hargrave and Ryle (1974). In this model, the SMBH in the core releases massive amounts of energy as a result of material accreting onto it. Some energy is then dissipated away from the core through powerful, highly collimated, supersonic, bright and relativistic[3] outflows of plasma and magnetic fields called jets (see also Rees, 1971; Scheuer, 1974; Blandford and Rees, 1974). FR-I galaxies generally have two recognisable jets. On the other hand, FR-II galaxies tend to have a single detectable jet and

3 Moving close to the speed of light.

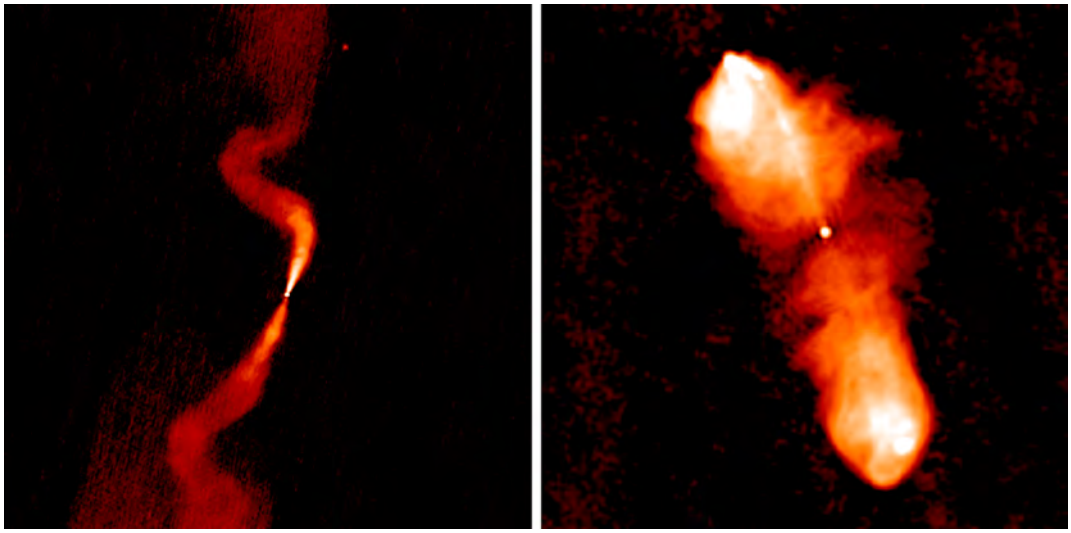

Figure 1.2: Illustrating of the difference between FR-I and FR-II sources. Left panel: An FR-I source (3C 31) exhibiting a bright core and dimmer edges. Right Panel: FR-II source, 3C 98, showing bright edges (hotspots). Image adapted from Hardcastle and Croston (2020).

a weak or undetectable counterjet. Examples of FR-I and FR-II sources are shown in Fig. 1.2. The jets of FR-I sources are disrupted close to the nucleus, resulting in more diffuse structure at its extremes. On the other hand in FR-II sources, these jets largely travel unhindered until they eventually encounter some external medium surrounding the galaxy, which in some cases causes their sudden termination.

When jet termination occurs suddenly – as is the case with FR-II radio galaxies – fluid at the shock areas where they terminate emits large quantities of synchrotron emission, leading to the extremely bright regions known as hotspots. Due to the sudden impact with the ambient medium, most of the jets' kinetic energy is converted to relativistic particles through first order Fermi acceleration, and magnetic fields through complex dynamo processes or shock compression (Carilli and Barthel, 1996). The remaining jet material convects into the cavity and inflates it, forming the radio lobes (Begelman and Cioffi, 1989; Carilli and Barthel, 1996). This process is illustrated in Fig. 1.3.

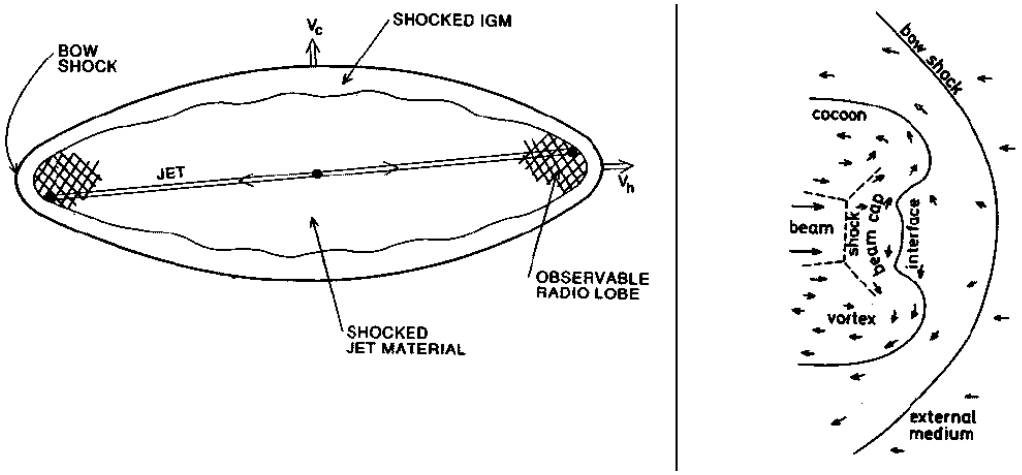

Figure 1.3: Illustration of jet propagation leading to the formation of hotspots and radio lobes. Image adapted from Carilli and Barthel (1996).

AGNs play a crucial role in the transportation of material within radio galaxies (e.g. McNamara and Nulsen, 2012). The energy released from an AGN impacts its surrounding medium, leading to what is known as feedback. This has one of two effects: preventing gas cooling or gas expulsion from the galaxy, or promoting star formation (Morganti, 2017). One way in which AGN feedback

manifests is in jet-mode (e.g. Rawlings and Jarvis, 2004), where the primary energetic output takes the form of the bulk kinetic energy transported in jets (see Heckman and Best, 2014, for a review on feedback modes). Jetted AGN expend most of their energy at radio frequencies through non-thermal processes such as synchrotron emission[4] and inverse Compton cosmic microwave background (IC/CMB) scattering.[5]

The study of powerful radio galaxies plays a pivotal role in understanding the astrophysics of these sources through careful examination of their morphologies and surrounding environments. One such example is the prominent and proximal radio galaxy Cygnus A at redshift 0.05 in the Northern Hemisphere, whose studies have further advanced our knowledge of galaxies (e.g. Perley et al., 1984; Katz-Stone et al., 1993; Carilli and Barthel, 1996). Additionally, the study of this source has also contributed to the advancement of interferometric imaging techniques (see e.g. Offringa and Smirnov, 2017). More recently, a wideband study of Cygnus A characterised its depolarisation behaviour spatially and by resolution (Sebokolodi et al., 2020).

A similar and closer source, Pictor A, exists in the Southern Hemisphere. It is a powerful radio galaxy within redshift 0.04, as such, companion studies like those performed on Cygnus A could also be feasible for this source. Pictor A consists of the following typical components of an edge-brightened galaxy as depicted in Fig. 1.4:

- A compact core hosting a SMBH, that is extremely luminous and spectrally flat.
- Highly collimated radio jets emanating from this radio core.
- Bright hotspots at the source edges at which these jets terminate.
- Double radio lobes, which are cavernous regions filled with diffuse low surface brightness radio emission.

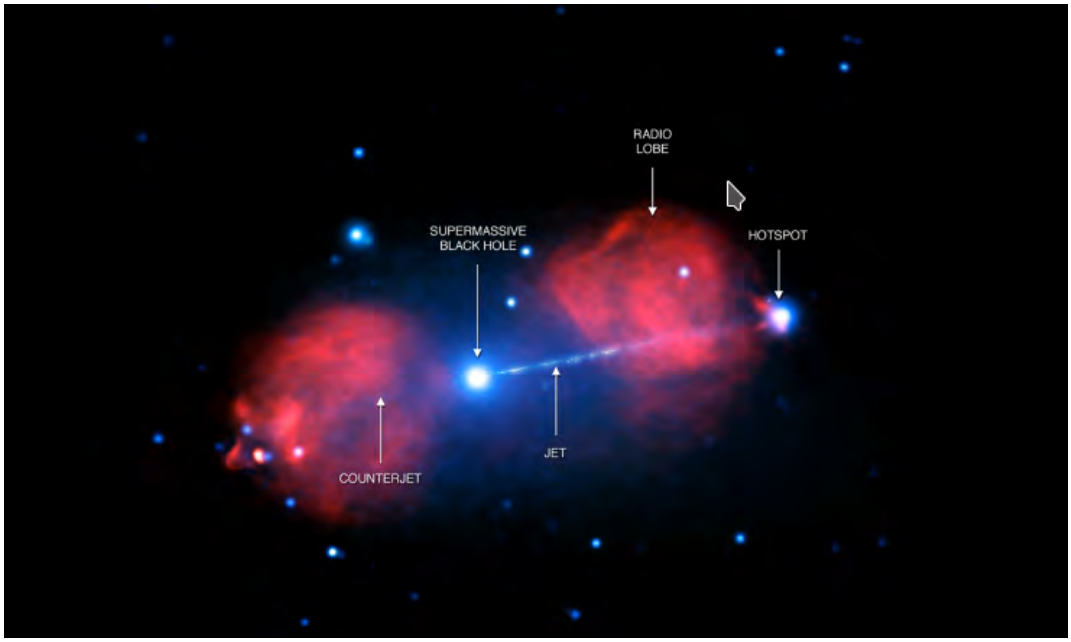

Figure 1.4: A composite image of Pictor A derived from Chandra X-ray data in blue, and ATCA radio data in red. It shows the four basic components of a radio galaxy of type FR-II. Image source: Blast From A Black Hole in a Galaxy Far, Far Away.

4 We formally introduce synchrotron emission in Sec. 3.1 of this thesis.

5 Inverse Compton emission is radiated when a photon gains the energy that a relativistic electron loses due to its collision with the photon. This process is called inverse Compton scattering (see Sec 9.3 of Longair, 2010). When photons from the cosmic microwave background (CMB) are involved, it is referred to as IC/CMB scattering.

1.2 Magnetic Fields In And Around Radio Galaxies

Magnetic fields can be found in objects such as stars, galaxies and galaxy clusters.[6] The field strengths, measured in Gauss (1 G = 10^{-4} Tesla), vary significantly across astrophysical sources and structures. They tend to be stronger in more compact sources or structures, e.g. pulsars (up to 10^{15}G) and weaker in larger and less dense sources such as 'normal' stars (up to 10 G). For example, the Earth's magnetic field is 0.3 G, while the field at the Sun's poles is 10 G. Even though the details of their origin, evolution and effects on astrophysical structures are still not yet well understood, magnetic fields are believed to play a key role in the evolution of galaxies and their clusters as they regulate AGN feedback, star formation and heat distribution in those sources. They also influence the jet's structure and progression, and affect the spatial mixing of gases (Eilek and Owen, 2002).

There are multiple ways of probing magnetic fields. One direct way is using the Zeeman effect (see a review in Crutcher and Kemball, 2019), whereby a magnetic field along a line of sight splits a spectral line into two opposite-handed circularly polarised components. This technique requires precise measurements of the left and right circular components with careful instrumental polarisation correction besides well-defined and conspicuous line intensities. Another approach to studying magnetic fields is the use of optical polarised emission, as it occurs due to the alignment of dust gains along a magnetic field, which scatters optical radiation (Klein and Fletcher, 2014, provide a good summary of these techniques).

Alternatively, there are two main indirect methods: synchrotron radiation and Faraday rotation. Early work showed that the radio emission observed by Karl Jansky was non-thermal (Reber, 1940; Reber, 1949).[7] Subsequent works (e.g. Schwinger, 1949; Kiepenheuer, 1950; Alfvén and Herlofson, 1950) then postulated that the emission originated from cosmic ray electrons under the influence of a magnetic field, also known as *synchrotron radiation*, whose theory was proposed initially by Schott (1912). Synchrotron radiation is caused by the acceleration of ultra-relativistic electrons by a magnetic field, and is widely recognised as the characteristic radio emission from most Galactic and extragalactic radio sources, thereby asserting the existence of magnetic fields in those sources. Synchrotron radiation is associated with the radio objects themselves. However, an exception is with radio halos and relics, whose radiation and, hence, magnetic fields are also associated with the external cluster gas. The ubiquity of synchrotron emission was portrayed by the 2-D map from Haslam et al. (1982) at 408 MHz, which Fig. 1.5 displays.[8] This map implicitly highlighted the pervasiveness of magnetic fields in our Galaxy.

Faraday rotation occurs when a magneto-ionised gas rotates the plane of polarisation of an incident linearly polarised wave. This effect provides an indirect way to measure magnetic fields in and around radio objects (or radio galaxies). Faraday rotation results in a change in polarisation angle as a function of wavelength-squared. Quantifying the amount of rotation experienced by a polarised wave, i.e. the rotation measure (RM), gives information about intervening magnetised material between the radio-emitting source and an observer along a line-of-sight (LoS).[9] This is done by inspecting variations of the polarisation angle in wavelength. Already, a great deal of work has been done using this approach (e.g. Cooper et al., 1965; Heald et al., 2009; O'Sullivan et al., 2012; Schnitzeler et al., 2015; Anderson et al., 2018; Loi et al., 2022). A well-known example of the use of this approach was the study by Taylor et al. (2009), which used the NRAO VLA Sky Survey (NVSS, Condon et al. 1998) and produced the largest catalogue to date of the RMs of 37,543 extragalactic sources above a declination (Dec) of -40°, using two frequencies. This work resulted in the map in Fig. 1.6.

6 A galaxy cluster is a collections of galaxies; they are the largest gravitationally bound structures in the universe, spanning up to mega-parsec scales.

7 Initially, this emission was thought to be thermal Bremsstrahlung (free-free). However, the required temperatures did not match up (see Reber, 1940).

8 This map was generated using `healpy`: `https://github.com/healpy/healpy` because the original map was in the HEALPix scheme.

9 We shall formally introduce Faraday rotation, the RM, and concepts related to it in Chap. 3 of this thesis.

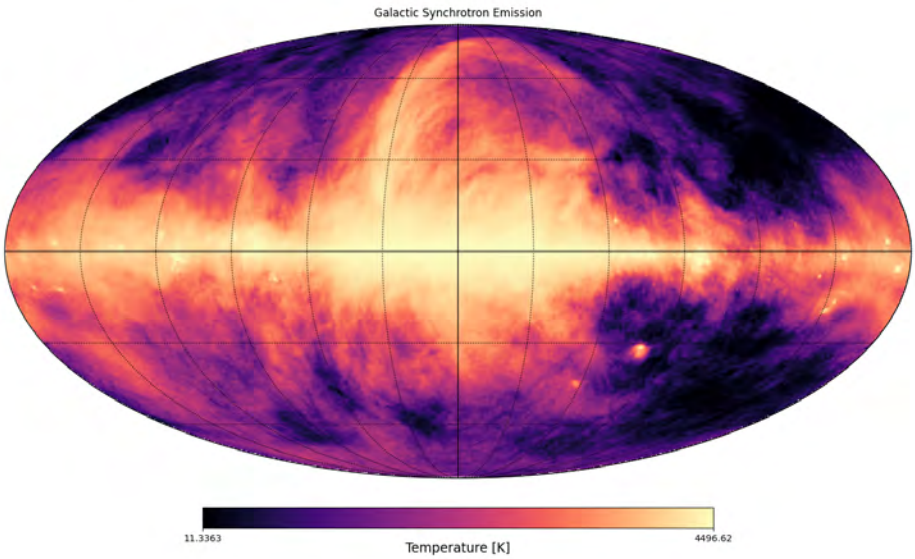

Figure 1.5: The extent of Galactic synchrotron radiation reported by Haslam et al. (1982) and later revised by Remazeilles et al. (2015). The ubiquity of this radiation points to the prominent presence of magnetic fields around us. The map is in the Molleweide projection.

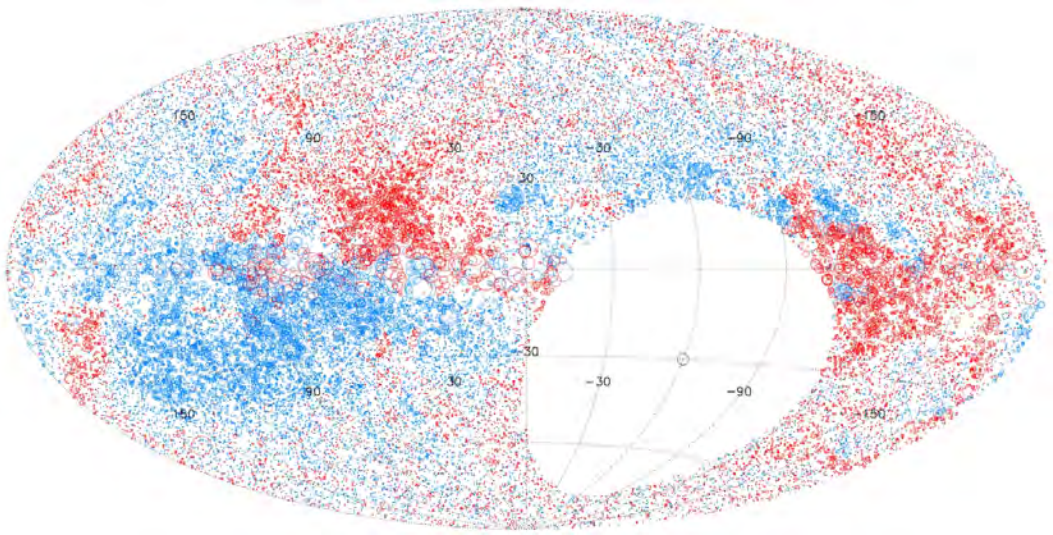

Figure 1.6: RMs from the NVSS catalogue of 37,543 sources from Taylor et al. (2009). The circle size indicates the RM magnitudes; red circles are positive RMs, and the blue are negative.

Although the map excludes a large part of the Southern Hemisphere, it was integral to exhibiting the large scale RM structure towards the Galactic plane (earlier studies already associated this large scale Faraday structure to the Galactic plane e.g. Gardner and Whiteoak, 1966a). One observed trend was that RM magnitudes increase towards the Galactic plane. By contrast, lower RM values were seen towards the poles. Supplementary work by Schnitzeler et al. (2019) covering the Southern Hemisphere using the S-band Polarisation All-Sky Survey (S-PASS/ATCA, Carretti et al. 2019, with 3,811 sources) showed that in the Southern Hemisphere, RMs were generally negative above the Galactic plane and positive below it, as shown by the top panel of Fig. 1.7. Combining SPASS and the NVSS catalogue data (the bottom panel of the same figure) made more areas of opposite signs of RM above and below the Galactic plane apparent. Schnitzeler et al. (2019) termed this as a 'butterfly pattern' and attributed it to the large-scale magnetic field of the Milky Way.

Other continuing surveys, such as the Very Large Array Sky Survey (VLASS, Lacy et al. 2020) with the VLA telescope aim to provide high angular resolution $\sim 2.5''$, high-sensitivity and wideband

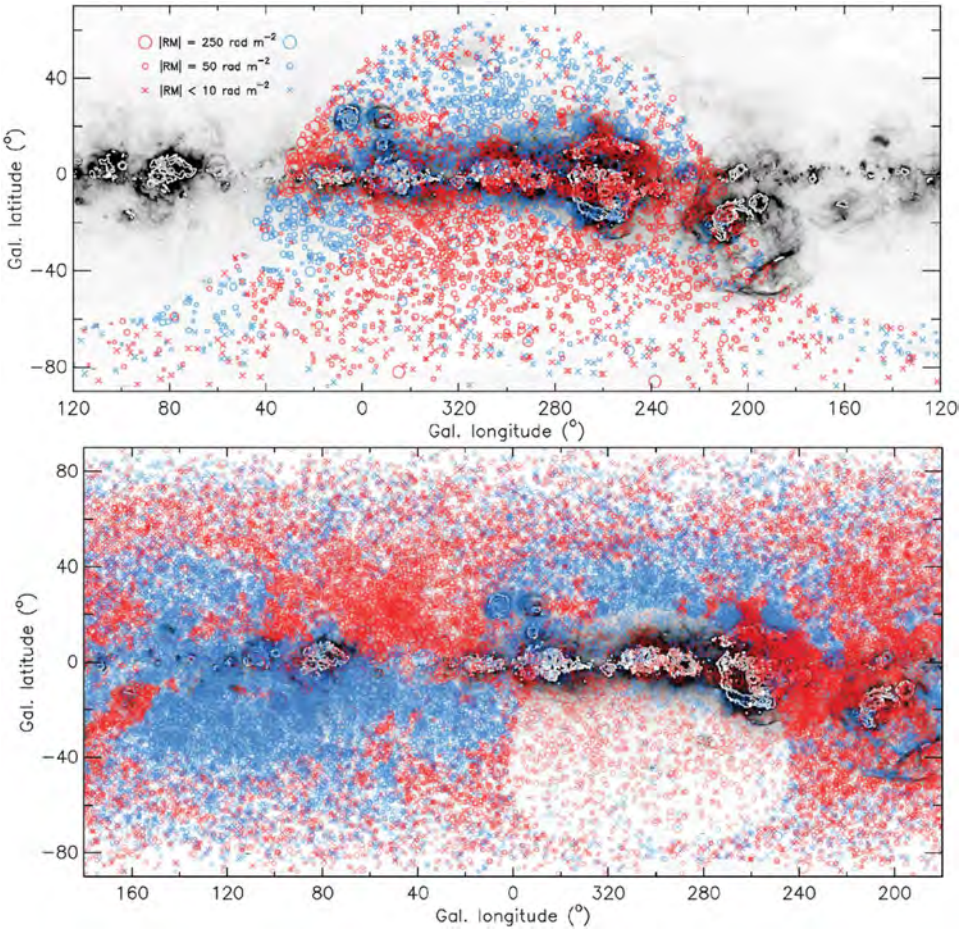

Figure 1.7: Rotation measures from sources in the Northern and Southern hemispheres from Schnitzeler et al. (2019). The greyscale background image is the Hα intensity map on the Galactic plane. Negative RMs are shown in blue and positive in red. The crosses represent small RM values that would otherwise be invisible. Top panel: RMs from S-PASS/ATCA including data on the area of the Southern hemisphere not covered by Taylor et al. (2009). Bottom panel: Combined S-PASS+NVSS RM catalogues. Visualising RMs from the individual LoSs shows generalised trends above along the Galactic plane. This image is from Schnitzeler et al. (2019).

(2 – 4 GHz) observations of the sky above Dec -40°, increasing the density of observed polarised sources with reliable Faraday rotation in comparison to those from Taylor et al. (2009).

1.3 The Role of Visualisation

Throughout the preceding section, the importance of visualisation in polarisation studies has been an implicitly overarching theme. Its most direct and significant role is facilitating quick trend, pattern, and potential anomaly identification in polarisation-related structure across the sky. Two discernible modes of visualisation have emerged so far: pixel-by-pixel maps, which are more geared towards diffuse emission such as that shown in Fig. 1.5, and individual source-based representations, e.g. Fig. 1.6 for cases where multiple disparate astrophysical sources are involved.

Nevertheless, another composite alternative is also plausible; this involves the combination of the previous two, allowing the simultaneous display of diffuse emission and independent LoSs as is exemplified in Fig. 1.7. One benefit of such a representation is clear from this example: it fosters the ability to associate spatial structure to the RM at a specific LoS. Scaling this down to a single diffuse radio-galaxy like Pictor A, polarisation structure along LoSs on its different components

(e.g. the lobes and hotspots) is depictable in this way. This is especially useful considering that polarisation properties could be coupled to source structure (Van Eck et al., 2023).

Thanks to the advancements in modern technology, visualisation is no longer limited to static representations. Interactivity afforded by current visualisation tools enables the addition of extra 'layers of detail' associated with a LoS. For example, in the polarisation context, ancillary information such as the polarisation angle and depolarisation behaviour across wavelength, amongst other data of benefit to the larger astronomical community – that would previously not be part of a publication – could be released as easily accessible data products, thus encouraging exploratory data analysis (these are known as enhanced data products, EDPs, as described in Lacy et al. 2020). Furthermore, making such rich visualisations available to the public fosters a sense of transparency in the sense that comparison or validation of results from newer, or varying, or similar techniques can be done directly.

1.4 This Thesis

This thesis showcases the end-to-end life cycle of radio data. We present a spectropolarimetric study of the Pictor A radio galaxy using new L-band data from the MeerKAT telescope. The author's contributions began with the data reduction of the observed data, which resulted in the Stokes cubes used for spectropolarimetry. The analysis and interpretation of our findings from the data followed this. Using the resulting data products, the author developed software tools to visualise the obtained LoS data of Pictor A.

A summary of the structure of the rest of this thesis is as follows:

- Chapter 2 provides a brief multi-wavelength history of Pictor A based on its morphological features, which are also described.
- Chapter 3 gives a basic introduction to concepts related to the significance of polarimetry and polarimetric analysis and some of the associated diagnostic tools. This chapter also introduces radio interferometers and how they are used to obtain visibilities – the staple of radio astronomy.
- Chapter 4 highlights the data reduction, calibration, and imaging steps undertaken to result in the science-ready images used for polarimetric analysis. We introduce data used in this work and the basic concepts of calibration using the Radio Interferometer Measurement Equation (RIME).
- Chapter 5 presents the spectropolarimetric analysis of Pictor A based on the reduced MeerKAT data, applying the diagnostic tools presented in Chap. 3. We also present our new observations of Pictor A and the new features they reveal.
- Chapter 6 addresses the need for reproducibility and transparency in the scientific process. As such, this chapter introduces new software tools developed as part of this project to aid in producing, reproducing and sharing data products from our spectropolarimetric pipelines.
- Chapter 7 summarises this research and suggests practicable future directions of the work described here.

We assume a ΛCDM cosmological model, with $H_0 = 70$ km s^{-1}Mpc^{-1}, $\Omega_m = 0.3$ and $\Omega_\Lambda = 0.7$. Further, any discussions of the radio spectral index are given in the sense that $S_\nu \propto \nu^\alpha$.

2

PREVIOUSLY ON PICTOR A

Pictor A was first discovered and named in 1949 by Stanley and Slee (1950). Designated the letter 'A', it was the first significant identified source in the Pictor Constellation located in the Southern Hemisphere at a Right Ascension (RA, J2000) of $5^h18^m23^s$, Declination (Dec) -45° 49′ 41″ and a redshift, z, of 0.035. Pictor A is considered a very bright radio source in the sky at low frequencies (Simkin et al., 1999), and is classified as a broad-line radio galaxy based on the AGN unification model. Furthermore, it is an FR-II galaxy according to the Fanaroff-Riley classification scheme, with a maximum extent of 8′ along the East-West (along the source-axis) and 4′ along the North-South (perpendicular to the source-axis, Hardcastle et al., 2016). This galaxy is located in a poor cluster environment.[1] Its bright inverse Compton (IC) X-ray emission makes its lobes one of the brightest yet in X-ray (Hardcastle et al., 2016).

2.1 Radio Observations

2.1.1 *Total Intensity*

Pioneering radio observations of Pictor A at 4′ resolution initially revealed its two bright components, the hotspots, elongated along a line which joined their peaks (e.g. Morimoto and Lockhart, 1968; Gardner and Whiteoak, 1971, at 80 MHz and 5 GHz respectively). As shown in the left panel Fig. 2.1, similar structure was also exhibited at 1.9′ resolution and 160 MHz (Slee and Sheridan, 1975). The brightness ratios between the eastern and western components exhibited values around ∼1.2 at lower frequencies (Schwarz et al., 1974; Morimoto and Lockhart, 1968, 80 – 160 MHz), which was interpreted as an indication of a steeper spectrum.[2] In contrast, Morimoto and Lockhart (1968) noted a brightness ratio of 0.9 at 5 GHz.

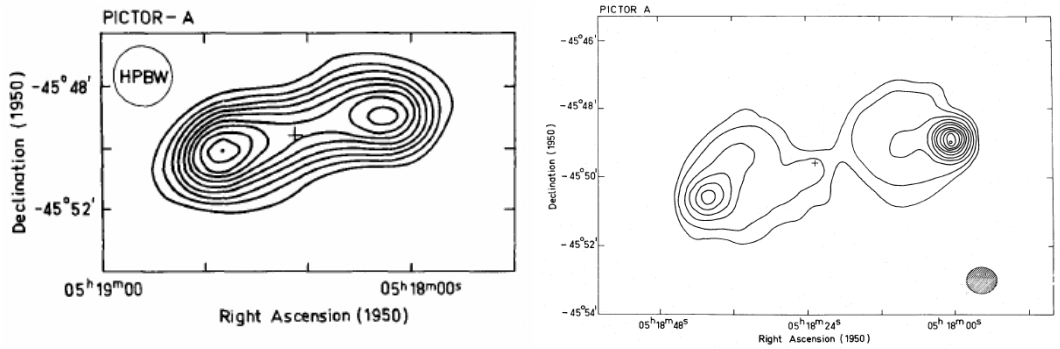

Figure 2.1: Low resolution contour images of Pictor A. The left panel is the 1.9′ resolution image at 160 MHz from Slee and Sheridan (1975). The right panel shows the ∼50″ resolution image at 1.4 GHz from Christiansen et al. (1977).

1 The richness of a galaxy cluster is defined by the density of galaxies within a certain radius from the galaxy cluster's centre (e.g. the Abell radius). A poor cluster has few galaxies, approximately in the tens.

2 Spectrum here refers to the variation of a source's flux density with frequency. The gradient of this curve gives the spectral index, α; thus, a steep spectrum is a large gradient that indicates a rapid decline in flux density with increasing frequency. More on the spectral index of Pictor A is discussed in Sec. 5.2.2.2 of this thesis.

However, observations by Schwarz et al. (1974) at a higher resolution of 1.3′ and 140 MHz showed that Pictor A had four components: two strong outer peaks and two weaker inner peaks, noting that the inner peaks appeared fainter than the outer ones. These confirmed predictions by Ekers (1969), whose modelling with data at 468 and 1403 MHz were best fitted by four-component models whereby the outer peaks were separated by ∼6.9′, while the inner peaks were separated by ∼4.1′. At this high resolution, the first semblance of Pictor A's radio core appeared in the image by Schwarz et al. (1974), shown in the left panel of Fig. 2.6, though no measurements of flux density or size were given. Christiansen et al. (1977) then confirmed the compact radio core of this source, with a stated flux of 0.6 ± 0.2 Jy[3] using observations from the Fleurs Synthesis Telescope at 1.4 GHz and ∼50″ resolution. The corresponding contour image is highlighted by the right panel of Fig. 2.1. Subsequent contour maps shown by Prestage (1985) from the VLA at 5 and 1.4 GHz distinctly displayed the components of Pictor A known at that point and are shown in Fig. 2.2. The radio core's stated flux was 0.92 Jy.

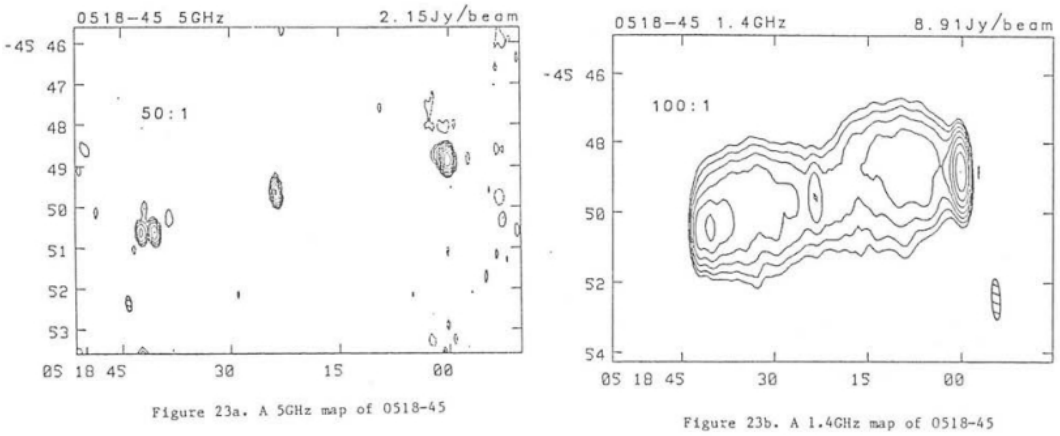

Figure 2.2: Pictor A at 5 and 1.4 GHz in the left and right panels, respectively, showing its distinct features. The radio core is evident at this point. These figures are from Prestage (1985).

Later, Perley et al. (1997) performed a study of Pictor A using VLA observations at radio bands 4, P, L, C, X, and U, which correspond to wavelengths of 400, 90, 20, 6, 3.6, and 2 cm respectively. The observations at 1.4 GHz (20 cm wavelength) and 7.5″ resolution revealed dim, relaxed, and circular lobes with an ellipticity of >0.9, an extraordinarily bright western hotspot (WHS) and double hotspots in the eastern lobe. Fig. 2.3 shows a total intensity map from this VLA observation. The eastern lobe was found to be smaller than the western lobe, whereby the lobe length ratio of the western to eastern lobe was stated as 1.2, and the western lobe was reported to be 5% wider. Both lobes showed thick filamentary structure – a common feature in radio galaxies (e.g. Cygnus A and Fornax A Perley et al., 1984; Fomalont et al., 1989). However, it was noted that these filaments were more prominent in the western lobe.

From these observations, a faint radio jet was also visible for the first time, but there was no visible counterjet. Nonetheless, Perley et al. (1997) estimated a jet-counterjet ratio of > 3. At 5 GHz (6cm) and 1.3″ resolution, these observations showed that the eastern hotspot (EHS) was completely resolved to a linear resolution of 1 kpc (see Fig. 15 of Perley et al., 1997), while the WHS remained compact up to ∼40 pc at the same resolution and 8 GHz frequency. Furthermore, the spectral index of the eastern lobe was found to be steeper, thus confirming speculations made in the previous studies by Morimoto and Lockhart (1968) and Slee and Sheridan (1975).

Very Long Baseline Interferometry (VLBI) observations at 8.39 GHz and 2.1 by 0.6 mas resolution later revealed the parsec scale structure of Pictor A's jet, at 9.8 pc westwards from the core for

3 1 Jansky (Jy) = 10^{-26} $Wm^{-2}Hz^{-1}$

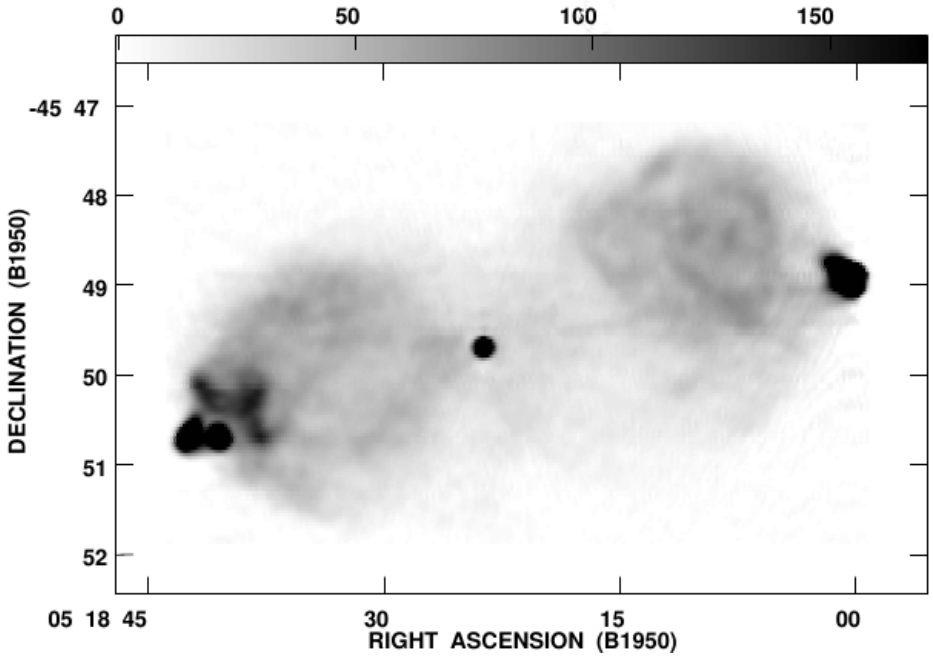

Figure 2.3: The total intensity map of Pictor A at 7.5″ resolution obtained from the observations of Perley et al. (1997) using the VLA at 1.4 GHz (20 cm). The colour map shown ranges from 0 to 179 mJy/beam.

the first 3.5 pc[4], and bending 40° north from there on (Tingay et al., 2000).[5] This is illustrated in Fig. 2.4. Two suggestions were made for the explanation of the bending pc-scale jet; the first

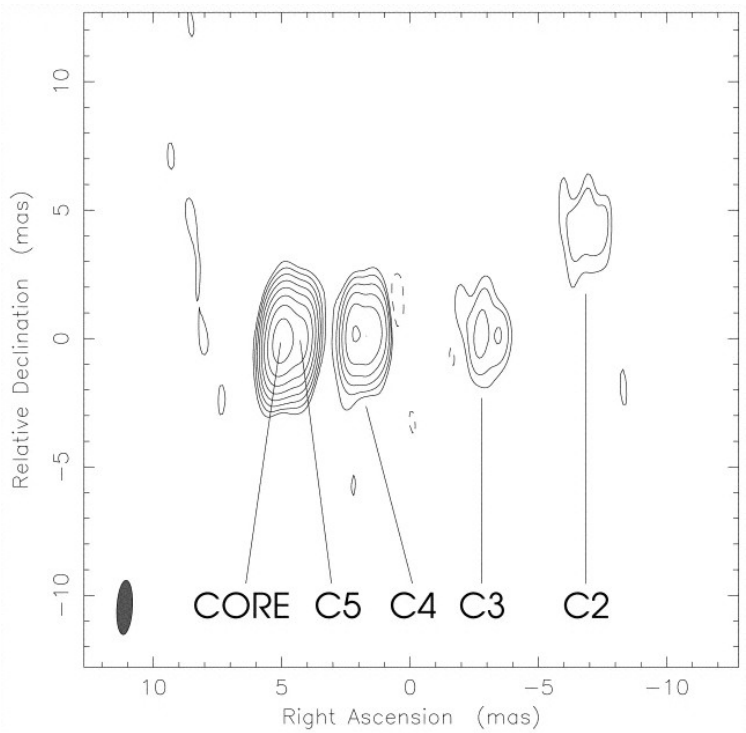

Figure 2.4: A long baseline VLBI image of Pictor A's parsec-scale jet at 8.39 GHz with 2.1 by 0.6 mas resolution showing labelled components bending from the original position. This is Fig. 4 from Tingay et al. (2000).

4 Tingay et al. (2000) originally stated these values as $\frac{14}{h}$ and $\frac{5}{h}$, respectively, using $H_0 = 100$ km (s Mpc)$^{-1}$ and $h = 1$. These have been converted for consistency with the rest of this thesis.

5 Miliarcseconds (mas) is the standard resolution designation for VLBI observations.

was that the jet precessed over time, but this requires the formation of a more complex lobe and hotspot structure (e.g. multiple hotspots for the WHS) than observed. Thus, these authors preferred the other proposed model whereby deflections by single oblique shocks caused intrinsic bending of the jet. However, in this case, the initial intrinsic bend required to cause the observed 40° bend would be 30° and this would mean that the jet no longer points towards the WHS unless there were additional deflections downstream from the jet. Nevertheless, these authors considered that either of the models was still plausible despite the negating factors.

Due to its extraordinary brightness, the WHS drew more interest from the community in understanding its astrophysical properties. More VLBI observations exploring the WHS at 23 mas revealed the presence of pc-scale regions within it, as shown in Fig. 2.5, which pointed towards regions with strong shocks in the fluid flow (Tingay et al., 2008). It was suggested that these components represented recently accelerated regions of electrons with higher break frequencies compared to the rest of the hotspot, alluding to synchrotron emission as the dominant emission mechanism in the X-ray. While the visible jet (with the width near the WHS estimated to range from 70–700 pc) led directly to the WHS, an extrapolation of the same jet to the EHS was not possible, as they were misaligned by almost 20°. These authors attributed the complex structure of the EHS to this misalignment. Even though the EHS was not visible from these observations, jet precession for this counterjet was deemed unlikely because there was no evidence for precession on the western lobe's jet. Since there was no apparent visible component in the X-ray to cause the bending of the counterjet, the cause for this jet misalignment remains unknown.

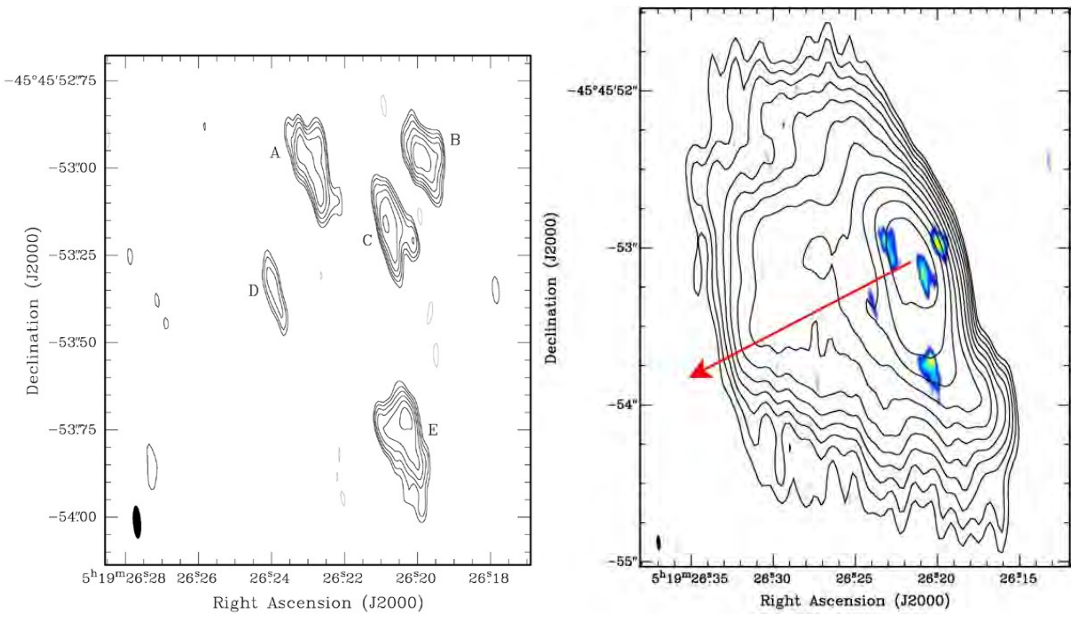

Figure 2.5: High resolution contour images of the WHS. The left panel shows the 94 by 23 mas resolution VLBI image at a wavelength of 1.6 GHz (18 cm). The right panel illustrates the same components highlighted by the left panel using the colour, overlaid with contours from 0.45″ by 0.09″ resolution VLA images from Perley et al. at 2 cm. The red arrow indicates the direction towards the radio core. The labelled components were speculated to represent regions of recently accelerated electrons compared to the rest of the hotspot. These figures were obtained and adapted from Tingay et al. (2008).

2.1.2 *Polarisation*

Early low-resolution surveys placed the polarisation of Pictor A as a whole at a maximum of ∼3%, using wavelengths ranging from 11 to 74 cm (e.g. Gardner and Davies, 1966; Gardner et al., 1969;

Haves, 1975).[6] The general trend showed that the percentage reduced towards lower frequencies – e.g., they showed ∼3% at 11 cm and ∼0.7% at 74 cm. Improved sensitivity of observing telescope at 6 cm revealed a polarisation of ∼8.7% for the WHS and ∼4.3% for the EHS (Gardner et al., 1975). At a better resolution of 1.3′, Schwarz et al. (1974) showed a strongly and uniformly polarised western component – of up to 17% polarisation. In contrast, the eastern component only showed ∼4% polarisation, with most of the polarisation being concentrated on the outer edge of the EHS, as highlighted on the left panel of Fig. 2.6. The low degree of polarisation associated with the EHS was attributed to beam depolarisation due to small-scale variations of the polarisation angle.[7]

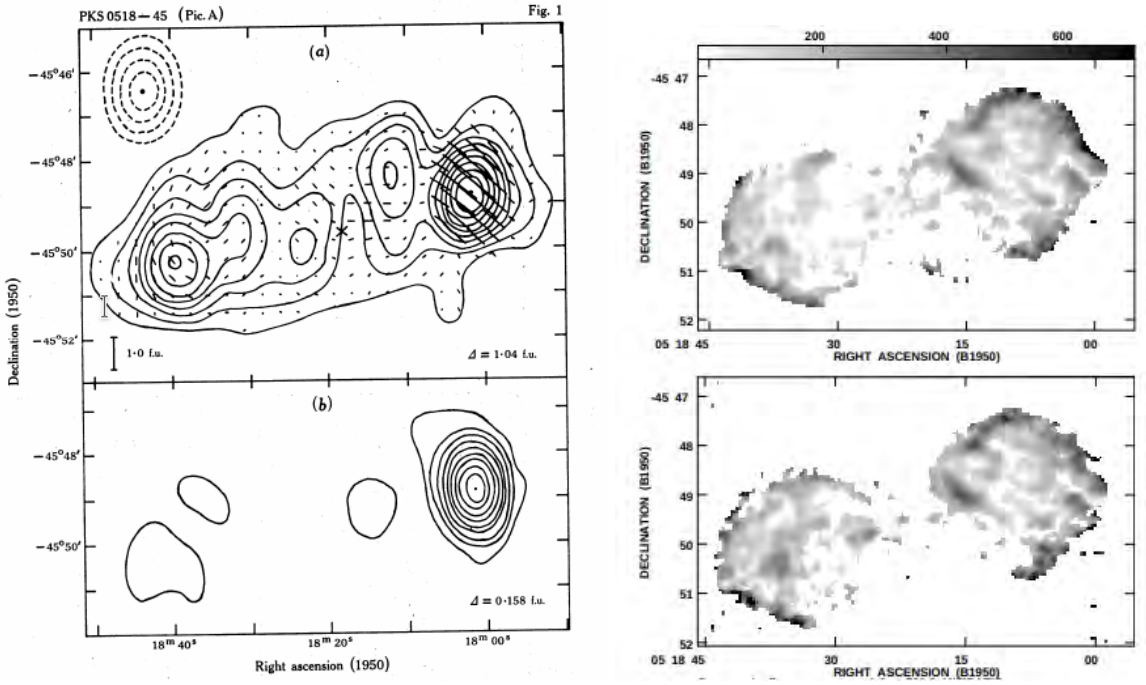

Figure 2.6: A comparison of older polarisation profiles of Pictor A. *Left Panel*: Figures from Schwarz et al. (1974) at 1.3′ resolution. The top plot illustrates the total intensity contours. The four components, two strong outer peaks and two weak inner peaks are visible. Furthermore, the radio core's position is visible but indistinctly. Polarisation vectors are superimposed on this image. The bottom plot shows the distribution of polarised intensity. *Right panel*: From Perley et al. at 10″ resolution; the top image shows the degree of polarisation from the VLA data at 20 cm while the bottom plot shows the same at 6 cm. Both plots' colour maps show a fractional polarisation range between 0 and 70%.

Perley et al. (1997) later showed a considerably higher degree of polarisation for Pictor A, with regions around the lobe edges showing fractional polarisation as high as 60%, illustrated by the right panel of Fig. 2.6, while regions within the lobes exhibited 20% or lower degrees of polarisation. That work also showed that the projected magnetic field directions of Pictor A were well-aligned with its outer edges, a common occurrence in radio galaxies due to shearing and compression along the edges. Furthermore, the eastern lobe showed significant depolarisation compared to the western lobe between 20 and 6 cm wavelengths while being completely depolarised at the longer wavelength of 90 cm. Low polarisation estimates in older observations of this source were attributed to beam depolarisation resulting from poor angular resolution of the observing telescopes. A mean RM of 43.5 ± 1.4 was reported for the entire source, with 49 ± 4.9 and 46 ± 10.2 rad m^2 reported for the western and eastern lobes, respectively. Perley et al. (1997) attributed the higher dispersion

6 Most of the observations by Gardner and collaborators were done with the Parkes 64 m telescope.
7 Concepts of polarisation, including the degree of polarisation, polarisation angles and depolarisation are introduced in Sec. 3.2.

of the eastern lobe to a more complex RM-screen and speculated that the higher depolarisation observed on the eastern lobe at 90 and 20 cm was due to unresolved RM gradients.

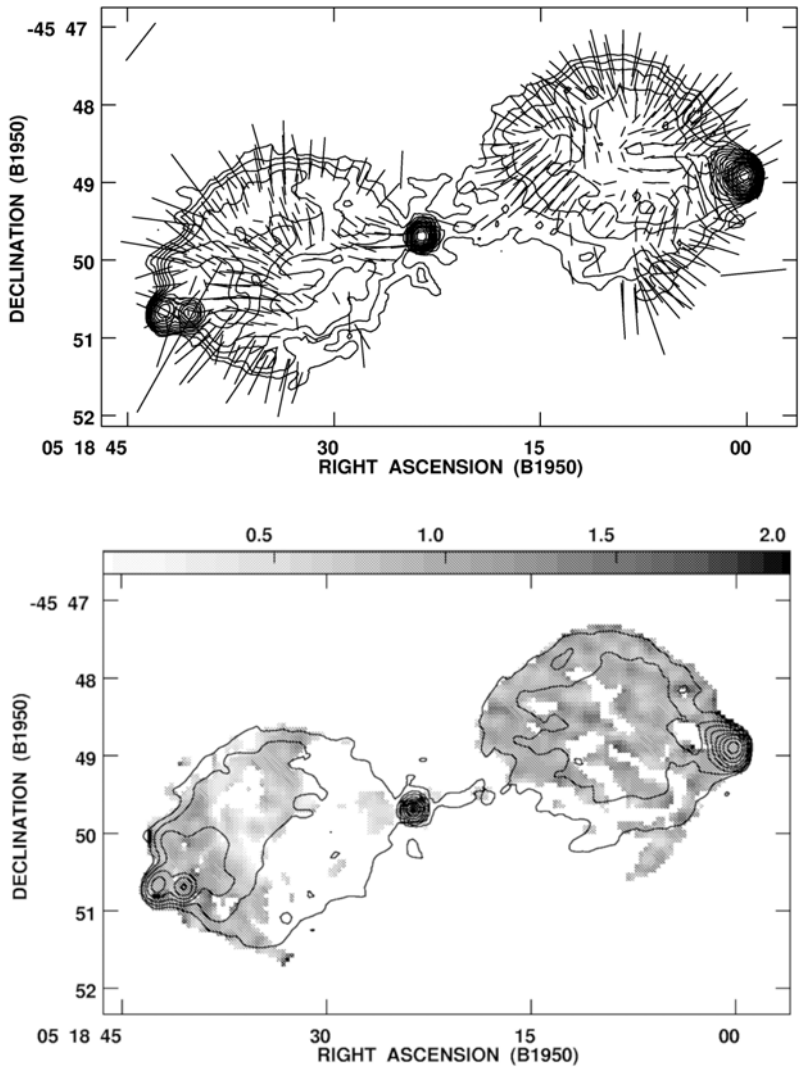

Figure 2.7: The polarisation angle orientation and depolarisation ratio across Pictor A from VLA data. *Top panel*: At 6 cm wavelength and 10″ resolution, this figure shows the orientation of the polarisation angle vectors overlaid on total intensity contours. The length of the vector indicates the degree of polarisation, also showing the increased degree of polarisation at the lobe edges. They are also well aligned with the lobe edges. *Bottom panel*: Depolarisation ratios across Pictor A between 20 and 6 cm wavelengths, at 10″ resolution. Values below 1 indicate depolarisation, while those above 1 indicate re-polarisation. Both images are from Perley et al., 1997.

2.2 Optical and X-ray Observations

2.2.1 *AGN core*

A study of emission line strengths across wavelengths between 3700 and 7000 Å by Danziger et al. (1977) using observations of Pictor A's core from the Anglo-Australian telescope revealed strong emission lines of various ions, symmetric Balmer lines, and broad emission lines, resembling those of broad-line radio galaxies. Thus, Pictor A's core was suggested to have a high ionisation within the core. Balmer lines are spectral line emissions from the hydrogen atom and occur when electrons

in excited states transition back to energy level two. Practical applications of the study of these lines are the determination of radial velocities due to Doppler shifting, which could be used to detect compact objects such as black holes and determine redshifts of extragalactic sources. On the other hand, broader emission lines point to a high kinetic energy – probably caused by high-velocity shocks within the nucleus – which causes heating and electron excitation. This resulted in the classification of Pictor A as a Broad Line Radio Galaxy (BLRG, Simkin et al., 1999).

Initial reports of strong X-ray emission from Pictor A's core were made by Marshall et al. (1979) and Kriss (1985). Singh et al. (1990) also reported strong X-ray emission from this core, and their data was adequately modelled by Power-law models. They speculated this emission to be caused by a non-spherical cloud of matter around this nucleus that is edge-on and along our line-of-sight. Those authors also suggested that they did not detect additional soft X-ray possibly due to the speculated edge-on orientation of Pictor A. Since soft X-rays likely originate near an accretion disk, an edge-on matter distribution would block the soft X-rays along the LoS. However, the picture of an edge-on disk painted by Singh et al. (1990) is inconsistent with the modern unified scheme view of BLRGs (summarised in Fig. 1.1). In particular, the presence of a one-sided radio jet, and depolarisation asymmetry in Pictor A implies that the accretion disk and jet are angled with respect to the plane of the sky. Assuming the validity of unified models, the observation of a broad-line region implies that the axis of Pictor A 's accretion disk – presumed coaxial with the jets – is at $<\sim 45^\circ$ to the line of sight, which is important to an understanding of the depolarisation and Faraday rotation differences between the approaching and receding lobes.

Work by Halpern and Eracleous (1994) showed new separated, twin-peaked Balmer lines in Pictor A's spectrum that were not seen in earlier spectra. Multiple suggestions of the origin of double-peaked emission lines have since been placed forward, including relativistic rotating accretion disks, binary broad and narrow line regions around binary SMBHs, disk winds and outflows (Chen and Halpern, 1989; Chen et al., 1989; Gaskell, 1983; Zheng et al., 1990; Eracleous and Halpern, 2003). This remains a question under investigation.

2.2.2 *Jets*

Before 1999, no optical jet of Pictor A had been observed. However, the spatial relationship between previously observed radio and optical features on different scales was found to appear aligned, thus suggesting that the radio jet pushed the ambient interstellar gas within the source northward to make way for the jet (Simkin et al., 1999). Simkin et al. (1999), using the Hubble Space Telescope (HST) data, also reported the first hint of the optical continuum jet as "a continuum feature in the direction of the large-scale radio jet." They found this to be in good alignment with extended structure in the East-West direction from VLBI data[8] and the faint radio jet highlighted by (Perley et al., 1997) because all ranged in a position angle between 280 – 288 degrees.

It was Wilson et al. (2001) who reported and showed the first image of Pictor A's X-ray jet, spanning $1.9'$ towards the WHS and having a width of $2''$. Hardcastle and Croston (2005) then showed that a steep, well-constrained X-ray photon index (Γ) model favoured the dominant X-ray jet emission mechanism to be synchrotron.[9] They argued against the suggestion by Wilson et al. (2001) that this emission was due to IC because this would result in a derived magnetic field strength of $\sim$2 μG within the jet, which requires that the jet have a much steeper low-energy electron index (and hence, a steeper radio spectral index) than the lobe, which is implausible.

In terms of physical size, this X-ray jet had a projected length of $\sim$150 kpc and width of $\sim$1 kpc (Marshall et al., 2010). The X-ray observations by Marshall et al. further revealed some surprising flux variability within a region of Pictor A's jet – located at about $48''$ from the core – within two years (the year 2000 and 2002). The authors estimated the variability to occur on a timescale of

8 Obtained from the SHEVE VLBI array.

9 The photon index describes how the photon flux $N(E)$ (number of photons per unit area per unit time) varies with photon energy, E. They are related as: $N(E) \propto E^{-\Gamma}$. A higher value of Γ indicates soft X-ray (low energy) emission.

a year, which happens to be far smaller than the expected synchrotron loss time of about 1200 years, assuming minimum energy conditions in the jet flow.[10] Therefore, as a result of the observed variability, the X-ray emission was proposed to originate from a sub-region of the jet, possessing a significantly higher magnetic field strength than the jet as a whole. Marshall et al. (2010) also stated that the energy loss timescale of individual relativistic electrons was unlikely to influence the flare. Rather, the energy they release likely caused an expansion of the emitting region, leading to a decrease of brightness through adiabatic losses.

Newer data from the HST led to the first detection of a continuous optical jet by Gentry et al. (2015), including multiple knots with a length of $\sim 4''$ leading towards the WHS. Using a 5 GHz radio flux density to derive an equipartition magnetic field strength[11] of 15 μG, Gentry et al. (2015) determined that the estimated synchrotron electron cooling time to be 1200 years. This was much longer than the observed jet flare timescale of one year. Therefore, they concluded that this flaring resulted from a knot as small as $0.002''$ within the jet. While the exact emission mechanisms of Pictor A's optical jet are not well known, Gentry et al. (2015) determined that the radio and X-ray jets result from synchrotron emission, whereby they are produced by low-energy and high-energy electrons respectively. Due to the high polarisation levels observed in this source, IC/CMB scattering due to bulk jet relativistic motions was ruled out.

A faint X-ray counterjet in the EHS of Pictor A was reported by Hardcastle and Croston (2005) and confirmed by Hardcastle et al. (2016).

2.2.3 *Hotspots*

The bright optical component of the WHS of Pictor A was identified by Roeser and Meisenheimer (1987) using the ESO telescope (La Silla), with a flux of 130 μJy at 400 THz and 68 μJy at 700 THz. The continuum spectrum shape of the radio and optical emission suggested that optical emission from this hotspot is of synchrotron origin, with a spectral index of -1.2$\pm$1, which was in good accord with the radio to optical index of -0.89.[12] At this point, IC/CMB scattering was rejected as it would require that the radio optical emission originates from a source of < 1 mpc or a magnetic field strength far below the equipartition value of 530 nT. On the other hand, a high particle density within the core would be required to generate a temperature of 10^8 K within the core plasma, ruling out the possibility of a thermal Bremsstrahlung origin. High resolution X-ray observations of the hotspot were presented by Wilson et al. (2001).

Various models have been proposed for particle acceleration within hotspots of radio galaxies. The *diffusive shock particle acceleration* model is the most widely accepted one, suggesting that the shocks (and hence, hotspots) generated by a mildly relativistic advancing jet accelerate particles through first-order Fermi acceleration (Bell, 1978; Blandford and Ostriker, 1978; Begelman et al., 1984; Meisenheimer et al., 1989). This is done efficiently and produces a non-thermal electron population.[13] Another model put forward is the *stochastic acceleration* model (second-order Fermi acceleration), which occurs due to the random scattering of particles caused by turbulent magnetised plasma. This model is usually often ignored due to its inefficiency (see Petrosian and Bykov, 2008, for a summary). *Magnetic reconnection* is an alternative particle acceleration mechanism. In this scenario, magnetic field lines of opposite polarity are pushed towards each other due to external plasma forces breaking from their respective field lines and reconnecting to form new magnetic field lines. Large magnetic field energies are released at the reconnection sites, which could result in particle acceleration (see e.g. Lazarian, 2005; De Gouveia Dal Pino, 2012).

10 Minimum energy conditions occur when the energy contributions from relativistic particles and the magnetic field are **approximately equal**. This is sometimes known as the *equipartition energy*. See Sec. 16.5 of Longair (2010).

11 This is the magnetic field strength at minimum energy. Equipartition and minimum energy conditions *are* similar. Govoni and Feretti (2004) gives a concise summary of these concepts.

12 The radio-to-optical index, α_{RO}, is given by $\frac{\log_{10}(S_{\mathrm{radio}}/S_{\mathrm{optical}})}{\log_{10}(\nu_{\mathrm{radio}}/\nu_{\mathrm{optical}})}$ (Ledden and O'Dell, 1985).

13 Efficiency here refers to the effective transfer of energy to particles resulting in a substantial increase in their kinetic energy; acceleration.

Meisenheimer et al. (1989) found that Pictor A's WHS exhibited a straight power-law spectrum from the radio to the optical frequencies (10^{10} – 10^{15} Hz). However, they were not sure whether this would extend into X-ray frequencies. Nonetheless, they concluded that this spectrum supported the diffusive shock model. However, Fan et al. (2008) later argued that this model could not account for the broadband X-ray observed from the Chandra X-ray telescope data, as the lifetime of X-ray emitting electrons was too short (less than 100 years) for the shock to produce the high observed flux for this hotspot. Instead, they advocated for stochastic acceleration to explain their observed X-ray spectral hardening of this hotspot.

Zhang et al. (2009) also supported that synchrotron emission from the hotspots could generate high energy gamma-ray photons through IC scattering. Multi-zone models (i.e. models whereby X-ray and radio emissions originate from different regions) combining both synchrotron and synchrotron self-Compton (SSC)[14] models provided better fits to the Spectral Energy Diagram (SED) of Pictor A with data from the radio to X-ray band[15], implying that X-ray emissions in the WHS originate from sub-compact regions within that hotspot. Furthermore, their models predicted GeV and TeV band emissions in cases where the magnetic field was smaller than the equipartition for this hotspot. The projected high energy emissivities were placed well below the sensitivities of the Fermi telescope and High Energy Stereoscopic System (H.E.S.S.).

However, in 2012, the first Gamma-ray emission from Pictor A was reported by Brown and Adams (2012) using observations from the Fermi Large Area Telescope (LAT). These emissions were reported to have an energy $\langle E \rangle = 0.2$ GeV, described by a power-law spectrum of $\Gamma = 2.93 \pm 0.03$, with variability on a timescale of one year or less. Brown and Adams (2012) argued that these emissions originate from the jet or core.

The WHS has also been shown to be a near- and far-infrared emission emitter (Isobe et al., 2017; Isobe et al., 2020) originating from sub-structures (of up to 10 pc) in the hotspot where the magnetic field is stronger than that of the minimum-energy condition. The mid-infrared component contributed significantly towards the far-infrared emission, with an estimated magnetic field strength of $\sim$ 1 – 4 μG, a factor of 3 – 10 larger than the minimum-energy magnetic field of those sub-structures. This confirmed the speculations of Hardcastle et al. (2016) that the magnetic field is stronger in these regions. These magnetic fields are amplified through local boosting by turbulence due to plasma inhomogeneities or instabilities, or both (Isobe et al., 2020). So far, stochastic acceleration and magnetic reconnection have been put forward as the dominant acceleration mechanisms in the sub-structures (Hardcastle et al., 2016; Isobe et al., 2020).

More recently, a discovery of high energy (above 10 keV) X-ray emission from the WHS of Pictor A was made, making it the first of its kind from AGN hotspots (Sunada et al., 2022). The emission has been considered to originate from the thin shock front at the jet termination point, similarly suggested by Thimmappa et al. (2020). Radio peaks of this WHS have been seen to be offset from the X-ray peak. The offset is speculated to result from an increasing volume of the emitting plasma at the point where shocked jet material diverges (Thimmappa et al., 2020). The presence of variability in this hotspot has been observed, suggesting that if it is an inherent characteristic of the source, it can be attributed to fluctuations in flux emanating from the brightest region of the hotspot. Moreover, X-ray observations reveal a region ($\sim 4''$ long) of unresolved emission perpendicular to the WHS, which is thought to be the shock front where efficient particle acceleration takes place (Thimmappa et al., 2020).
Despite many speculations on the particle acceleration mechanism in the WHS of Pictor A, it remains unclear.

On the eastern hotspot, Hardcastle and Croston (2005) suggested that extended X-ray emission around it was synchrotron due to the acceleration of high energy particles within this region. IC/CMB would require a much lower equipartition magnetic field strength (which they estimated to be at most two below equipartition value).

14 Synchrotron self-Compton occurs when the same electrons that emit synchrotron radiation also scatter the produced photons (see Sec 9.6 of Longair, 2010).
15 See Figs. 1 and 2 of (Zhang et al., 2009).

2.2.4 *Lobes*

IC lobes provide a means for directly measuring electron density. This gives information about the particle content and magnetic field within the lobe and affords constraints for source dynamics since it enables comparison between external and internal pressures of X-ray emitting hot gas. Such constraints are impossible with synchrotron emission because the magnetic field strength and electron density cannot be decoupled. Variations of the magnetic field and particle densities with positions provide a probe into dynamical plasma evolution (e.g. see Hardcastle and Croston, 2005).

After XMM-Newton observations of the diffuse X-ray emission from Pictor A's eastern lobe (Grandi et al., 2003), it was suggested that the emission resulted from IC/CMB scattering by relativistic electrons within the lobe as a power-law model with an X-ray spectral index of $\alpha_X = -0.6 \pm 0.2$ showed good agreement with the radio spectral index. Seed photons were speculated to originate from synchrotron photons produced within the lobe, AGN in the core or cosmic microwave background (CMB) photons. The adoption of this model, however, required that the magnetic field strength be a factor of 2 lower than the equipartition value. Thermal emission mechanisms resulting from the shock of the radio lobe towards the surrounding gas were not ruled out based on the possibility that this could have resulted in the observed eastern lobe depolarisation by Perley et al. (1997) at 90 cm. While Perley et al. (1997) reported and average RM of 43 rad m^{-2} for this lobe, Grandi et al. (2003) stated that it was inconsistent with the idea of the coexistence of thermal and synchrotron plasma, as the thermal plasma would cause Faraday rotation.

A later study by Croston et al. (2005) on the lobes of FR-II sources confirmed that their primary emission mechanism is IC/CMB because CMB photons are more dominant than synchrotron photons within the lobes. Such lobes were also proposed to be devoid of energetically dominant proton populations, which require that the magnetic field energy density equals electron energy density, so the contribution from relativistic protons is small.[16] Hardcastle and Croston (2005) suggested this for Pictor A, implying that the external pressure of the surrounding medium is comparable to the internal lobe pressure for reasonable assumptions of external temperature and density. Perley et al. (1997) proposed that this could be the reason for the nearly circular and relaxed lobes of this source.

Contrary to the expected scenario of a constant ratio between X-ray and radio emissions in the presence of an assumed constant magnetic field strength within the lobe, Hardcastle and Croston (2005) interestingly found that the X-ray to radio ratio exhibits variability. It was proposed that this variation resulted from a combination of the variation of both the actual magnetic field strength as a function of position, and the electron energy spectrum implied by the changing spectral index across the source's lobes. The magnetic field strength was derived to be a factor of 1.6 – 2 below the equipartition value, implying an internal pressure of the order of 2×10^{-13} Pa. This implied that Pictor A is in a poor external thermal environment; thus, extended thermal emission has no significant contribution to the X-rays. Migliori et al. (2007) determined that IC scattering occurred at either between $\gamma = 10^3$ electrons and CMB photons, or $\gamma = 100 \sim 300$ electrons and nuclear photons (γ is the Lorentz factor).[17] Photon indices of the western and eastern lobe were found to be 1.7 ± 0.2 and 1.8 ± 0.2, respectively. Each lobe's magnetic fields were estimated to be a factor of 2.7 below the equipartition value.

The total intensity radio filaments in the lobes of Pictor A have been shown to lack correlation with the observed polarised emission filaments. In the eastern lobe, a reported X-ray filament similarly did not show any correlation with the polarised emission. However, regions around this filament exhibited reduced rotation measures. Possible explanations for this have been magnetic field reversals caused by thermal matter distributed within the shells. Thermal matter would introduce a dispersion of RM within this filament. Alternatively, it could be caused by locally altered magnetic

16 A system's total energy, U_{tot}, is given as $U_{tot} = U_B + U_p + U_e$, which are the contributions of the magnetic field energy and relativistic particles (protons and electrons), respectively.

17 This would mostly apply for smaller <100 kpc galaxies.

fields and electron heating or acceleration conditions since lobes are a potential acceleration site for ultra high energy cosmic rays (Thimmappa et al., 2021).

2.3 The General Significance of Pictor A

Pictor A's proximity makes it an excellent laboratory for investigating astrophysical phenomena occurring in extragalactic sources. By studying this nearby source, we can gain valuable insights into distinguishing characteristics between radio-loud and radio-quiet AGNs, as well as examine radio jets in the form of concentrated radio plasma directed towards hotspots (Simkin et al., 1999). These investigations are crucial in unravelling the intricate interactions between the jets and the surrounding interstellar medium (ISM). At its distance, it is possible to resolve small and faint features whose studies could enhance our comprehension of the underlying physical processes within radio jets.

Additionally, Pictor A's brightness facilitates good estimations of lobe magnetic field strengths. It enables detailed analyses of spectral variations in X-ray surface brightness with respect to radio brightness due to the abundance of X-ray detection counts (Hardcastle and Croston, 2005). Though sources such as Centaurus A and Cygnus A are much larger physically or more powerful – respectively – than Pictor A in radio, their emissions are dominated by thermal Bremsstrahlung from their environments, contrary to Pictor A, which seems to have little thermal emission.

Pictor A is also used as a flux scale calibrator for frequencies between 100 – 200 MHz for the 21 cm Epoch of Reionisation (EoR) experiments in the Southern hemisphere using Precision Array from Probing Epoch of Reionisation (PAPER). Complications from the primary beam arise from the fact that because sources fall at different positions within the primary beam, it is impossible to accurately relate source fluxes at different positions without an accurate beam. Because calibration of the primary beam at these frequencies is difficult, Southern sources such as Pictor A reduce their reliance of the experiments on accurate beam calibration (Jacobs et al., 2013).

2.4 Pictor A And The MeerKAT?

To date, the most detailed and extensive study within the radio regime was the one by Perley et al. (1997), using various configurations and wideband data (∼70 MHz to 15 GHz; G, P, L, C, X, and U bands) from the VLA telescope. This study accorded an in-depth treatment towards this source's morphology and spectral and polarimetric characteristics as seen in the total intensity image in Fig. 2.3. However, the adverse differences in positions between the telescope in the Northern Hemisphere and the source in the Southern Hemisphere presented some challenges to those authors. To begin with, the elevation limit (7.5°) of the VLA and the low maximum elevation (10°) of the source enforced a maximum value of two and a half hours on target. The effect was restricted uv-coverage and a reduced sensitivity due to the reduction in the shorter baselines. Furthermore, these data were more prone to atmospheric corruption at the low elevation because of the Earth's ionospheric refraction of lower frequency waves (Condon and Ransom, 2016). A combination of these effects led to a limited image fidelity and dynamic range.

A subsequent radio observation of Pictor A was done in 2009 using the Australia Telescope Compact Array (ATCA) by Wilson et al. (2011). The source was observed for 12 hours, with a 2 GHz bandwidth, 2 × 2048 MHz channels, at 6 cm (5.5 GHz) and in the 6A configuration. ATCA's new Compact Array Broadband Backend (CABB) correlator facilitated this wideband observation, removing the need to observe the source at multiple and varied telescope configurations. As a result of this wideband observation, the uv-space was well sampled (see Fig. 15 of Wilson et al., 2011). This reduced the required observation times, improved the telescope's sensitivity, and enabled simultaneous Stokes I, Q, U, V (full Stokes) observations.[18] It also meant an expected improvement

18 In practice, it is assumed Stokes $V = 0$ for reasons explained in Sec. 3.2.1.

in the resulting image's dynamic range (DR). Through standard calibration using the ATCA-centric data reduction package, MIRIAD (Sault et al., 1995), an image with a DR of 38,000:1 at 2.2″ resolution was produced. It is displayed in Fig. 2.8.

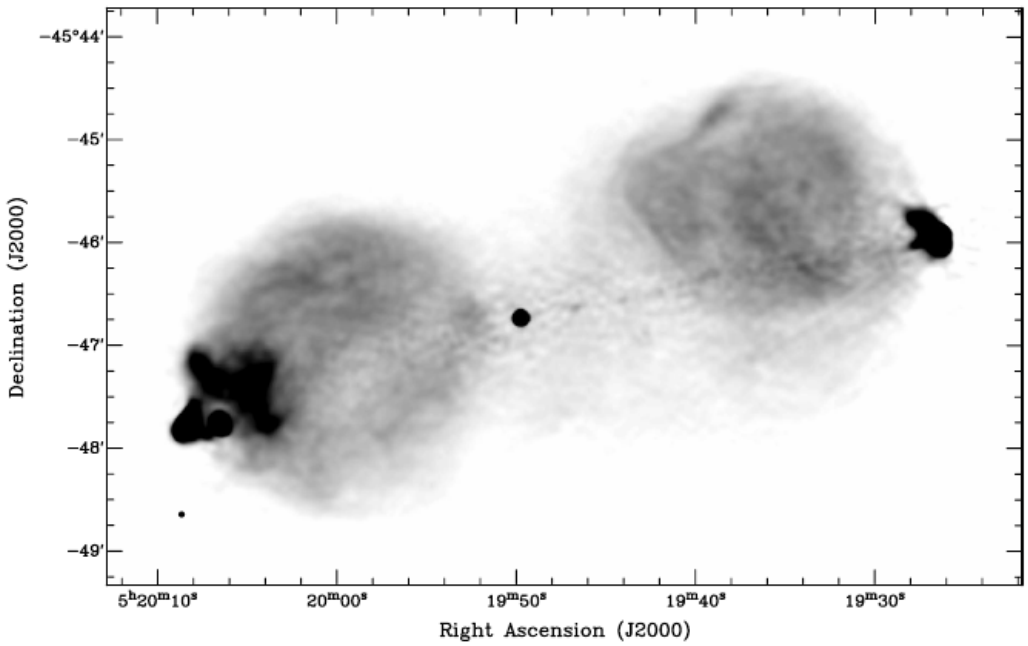

Figure 2.8: A 2.2″ resolution image resulting from the observations of Wilson et al. (2011) using the ATCA telescope with 2 GHz bandwidth, configuration 6A, at 6 cm (5.5 GHz).

The challenge with these observations was that the calibration and deconvolution algorithms at that time could not accurately converge towards a solution representative of the source, especially around the brightest hotspot. The data from Wilson et al. (2011) were later reprocessed by Hardcastle et al. (2016) in tandem with performing an X-ray study of Pictor A. However, the limited capability of MIRIAD drove Hardcastle et al. (2016) towards alternative approaches to achieve their goal. They used DIFMAP (Shepherd, 1997), which permitted isolation of spectral effects and visibility modelling of the different source components. Each component was modelled individually, and after an improvement in the recovered flux, phase self-calibration followed. The final step to their self calibration recipe was the calibration of amplitude. The peeling technique (discussed in Sec. 4.3.4) was used on the extremely bright WHS for better imaging, resulting in an image with a DR of 46000:1 (in Fig. 2.9 we show their resulting radio contours in red overlaid on an X-ray image). So far, this has been the highest DR achieved for Pictor A.

The MeerKAT Motivation

The various observational and, consequently, calibration challenges faced while observing Pictor A with the VLA and ATCA motivated the observations of Pictor A using the MeerKAT telescope.

In contrast with the VLA, MeerKAT is in the Southern Hemisphere, allowing for extended observation time of the source. A longer source tracking time corresponds to a better uv-coverage. The dense core (more antennas towards the centre) leads to more samples on the shorter baselines, which directly improves MeerKAT's sensitivity to large-scale and extended structures than the VLA. Therefore, issues with source elevation aggravating atmospheric corruptions are expected to be less. On the other hand, the MeerKAT telescope has significantly more unique baselines – 2016 with 64 antennas – compared to those of the ATCA – 15 with six antennas. Therefore, the difficulty in convergence of calibration and deconvolution challenges encountered with the ATCA observations should be significantly reduced.

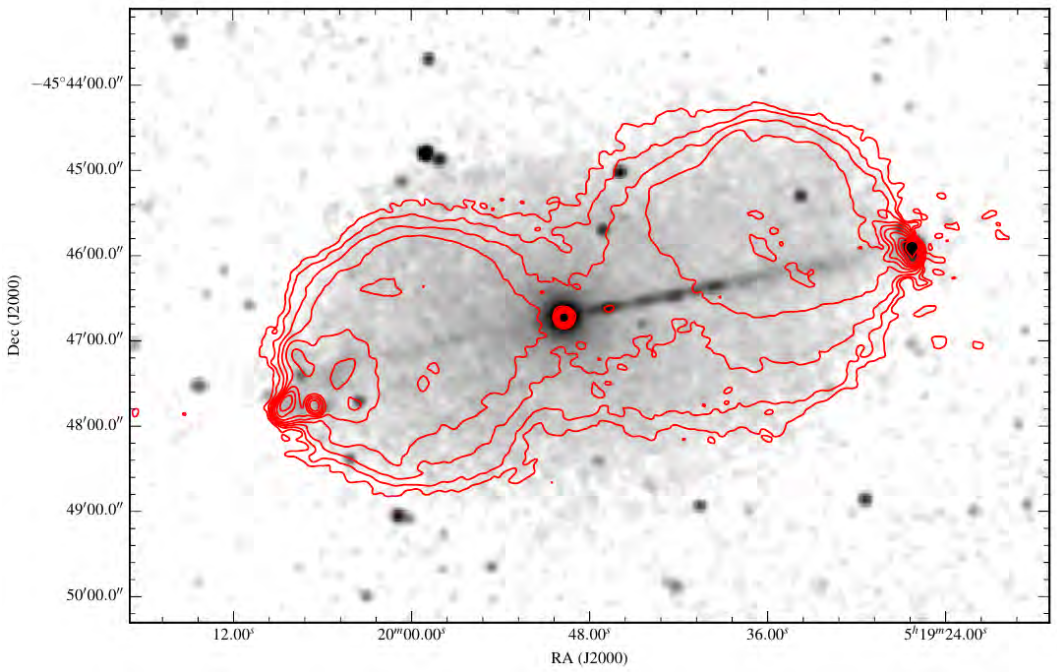

Figure 2.9: An X-ray image of Pictor A by Hardcastle et al. (2016) overlaid with red contours showing radio observations from ATCA at a resolution of 5″.

MeerKAT's high sensitivity to extended structure facilitates the detection of low-level emission in Pictor A. For example, regions exhibiting IC emission are expected also to feature low-frequency radio synchrotron emission. However, work by Hardcastle et al. (2016) using ATCA radio observations at a sensitivity of 40 μJy/beam compared against X-ray emission failed to detect the radio emission at the waist of Pictor A. It was proposed that the X-ray emission is predominantly thermal or the radio emission is very faint if present. In addition, Fig. 2.9 illustrates that Pictor A has a prominent jet and a faint counterjet in the X-ray regime. On the contrary, the radio jet is barely visible, while its counterjet is undetected, as shown by the previous radio images of Pictor A in Figs. 2.3 and 2.8. Hence, MeerKAT becomes a suitable instrument to confirm the presence of this missing radio emission and to facilitate the detection of the kpc-scale jet, which was previously only faintly observed.

In terms of the sheer imaging capability, the MeerKAT telescope lends itself as a perfectly suitable instrument for observing Pictor A because of its location and its high sensitivity. Furthermore, it is capable of full polarised (I, Q, U, V) observations, which is paramount for use within polarimetric studies. Its observations additionally provide continuous coverage in frequency, allowing us to see small deviations in the polarisation behaviour of the source. Similar studies, such as those of Cygnus A (Sebokolodi et al., 2020) and Hydra A (Baidoo et al., 2023), have revealed the importance of closely sampled frequencies over a continuous band – where non-linearities and interesting depolarisation structures are observed, thus, revealing very interesting underlying magnetic fields structures. Therefore, these observations could aid in understanding the possible location of the Faraday rotation medium towards Pictor A. While the spectropolarimetric study by Perley et al. (1997) was comprehensive, the reduced coverage and large amounts of flagged data significantly impacted their analysis.

This work uses high-sensitivity interferometric data to perform a spectropolarimetric study of Pictor A using the RM-Synthesis technique.

2.5 Summary

In this chapter, we have briefly highlighted the multi-wavelength studies of Pictor A over the years, and the challenges previous radio observations faced during data reduction and imaging of this source. Reasons for the observations of Pictor A using the MeerKAT telescope have also been provided. The next chapter formally introduces the basics of spectropolarimetry and related diagnostic tools. Furthermore, we introduce the basics of radio interferometers, thus establishing the link between Stokes parameters (I, Q, U, V) and radio telescopes' data. The MeerKAT telescope is formally introduced in that chapter.

3

TECHNIQUES AND TOOLS

While still an open question, the origins of magnetic fields are suggested to either be primordial or injected. A more accepted theory is that magnetic fields are introduced through small seed fields deposited into space at a point in time, e.g. during the formation of the Universe, or during structure formation/evolution. The small seed fields are then amplified to the observed magnetic field strengths by dynamo processes such as cluster mergers. Various models have been proposed to establish the origin of these seed fields, such as transportation of magnetic fields as a result of galactic AGN feedback or cosmological factors[1] (see Sec. 4 of Subramanian, 2016, for a detailed review of the origin of primordial magnetic fields). Additionally, processes like magnetic field compression and turbulence-induced dynamo effect (Larmor, 1919) have been suggested as amplification mechanisms (Donnert et al., 2018; Beck, 2015, give a concise summary of this).

Multiple approaches are available for probing the magnetic fields of astrophysical objects. In radio frequencies, the most commonly used approaches are synchrotron emission and the Faraday rotation effect. Since the electric and magnetic fields of an electromagnetic (EM) wave are known to be orthogonal to each other, the orientation of the electric field, i.e. its polarisation, can be used to infer its magnetic field.

Radio interferometers can intercept faint radio emissions from astrophysical objects near and far away from us enabled by their high resolution and sensitivity capabilities, thus facilitating polarisation studies. In this thesis, we use observed synchrotron emission and Faraday rotation to explore the polarimetric structure of Pictor A. The first part of this chapter formally introduces synchrotron emission, Faraday rotation, and diagnostic tools used for spectropolarimetric analysis. The second part introduces radio interferometers and the basic concepts of radio interferometry.

3.1 Synchrotron Radiation

Synchrotron emission[2] is produced by the transverse[3] acceleration of relativistic electrons due to a magnetic field. Lorentz forces[4] acting on these electrons causes their helical acceleration paths; hence, these electrons are said to gyrate around the magnetic field (see Sec. 6.1 of Rybicki and Lightman, 1991). If we consider the case of a single relativistic electron, its velocity vector as the particle precesses around a magnetic field results in a *velocity cone*. We illustrate the path and radiation of a single electron in Fig. 3.1.

Effects such as relativistic aberration (stretching of the radiation pattern in the electron's direction of motion) and beaming cause this electron's radiation pattern to stretch forward along its velocity trajectory, which confines the radiation within some pencil-shaped beam, as highlighted in the top left panel of Fig. 3.1. Therefore, synchrotron emission is only observable in a line of sight within

1 E.g. baryogenesis, electroweak phase transitions (EWPT) or quantum chromodynamics (QCD) phase transitions, quantum fluctuations during inflation and expansion of the Universe.

2 Its name originates from the synchrotron particle accelerator from General Electric where linear polarised light was first observed.

3 This means acceleration that is perpendicular to the velocity and a magnetic field.

4 $F = m\gamma a = \frac{q}{c}\mathbf{v} \times \mathbf{B}$; γ is the Lorentz factor and ν is the velocity of the electron.

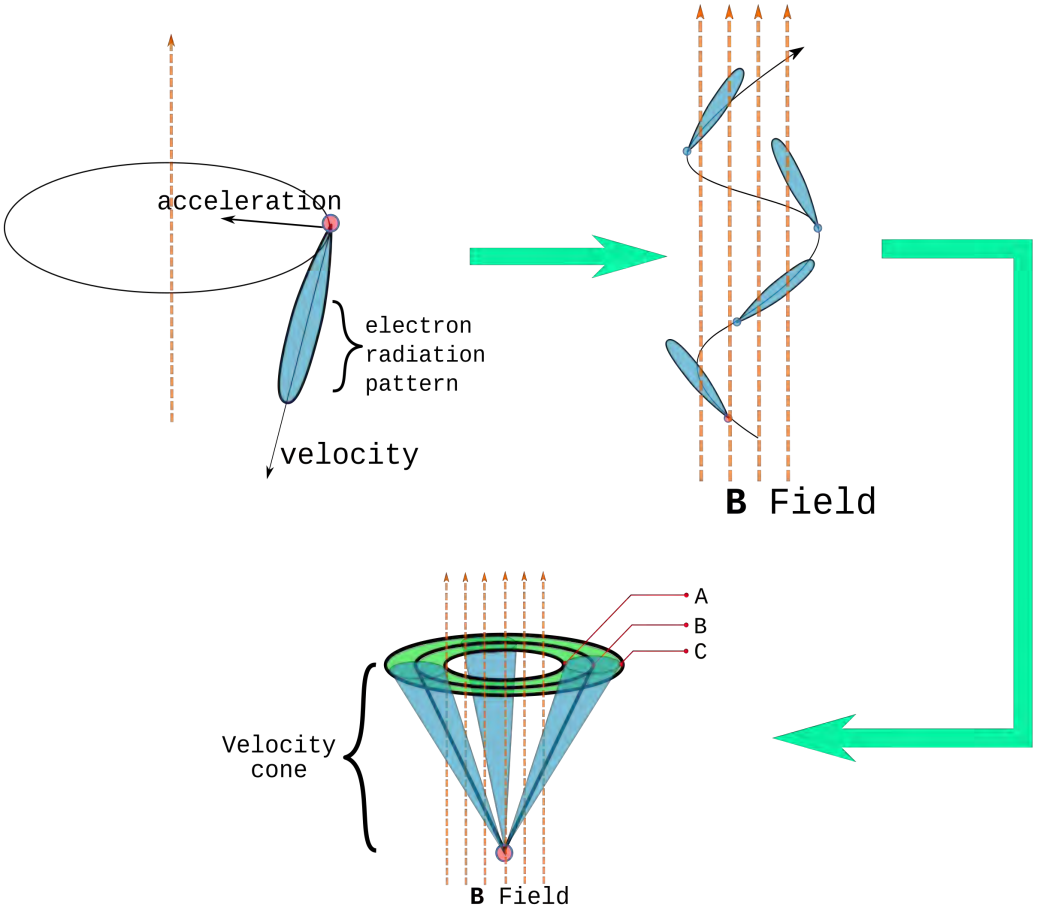

Figure 3.1: *Top left*: A single relativistic electron is accelerated due to a magnetic field (in orange). It beams radiation in an elongated radiating pattern (in blue) pointing the direction of its instantaneous velocity vector, which is perpendicular to its acceleration vector. *Top right*: As the electron accelerates, it gyrates around the magnetic field spiralling in a helical path. Meanwhile, its velocity vector as it moves traces out a velocity cone as shown in the bottom panel. *Bottom*: The velocity cone combined with the beamed synchrotron radiation. Radiation from this electron is confined within the green shaded area on the velocity cone. These images are adapted from Fig 6.5 of Rybicki and Lightman (1991) and Synchrotron emission lecture notes by Francesca Perrotta.

this pattern whose full width at half maximum (FWHM) is estimated using the Lorentz factor, γ, as:

$$\theta \sim \frac{1}{\gamma}, \text{ where}$$
$$\gamma = \frac{1}{\sqrt{1 - \frac{\nu^2}{c^2}}},$$

where ν is the electron's velocity, and c is the speed of light in a vacuum. If the observer's line-of-sight is at position B, the observed emission will appear linearly polarised. On the other hand, if one observes at positions A or C, the emission will appear left- or right-handed circularly polarised. Under normal circumstances, many electrons undergo this same process simultaneously. Thus, given a smooth distribution of the pitch angle of these electrons (e.g. a power-law distribution: $N(\epsilon)d\epsilon = N_0\epsilon^{-\delta}d\epsilon$, where ϵ is the energy of an electron given by $\epsilon = \gamma m_e c^2$.), their ellipticities cancel out, leading to the commonly observed linear polarisation of synchrotron emis-

sion (Gardner and Whiteoak, 1966b; Rybicki and Lightman, 1991; Lang, 2013). Since the electrons' high kinetic energy resulting from their speed translates to a temperature much higher than is probable for thermal emission[5] and their energy distribution does not show a Maxwellian distribution, synchrotron emission is considered non-thermal.

Thus, an observer sees continuum radiation with a spectrum peaked around the critical frequency,

$$\nu_c = c_1 (B \sin\theta) \epsilon^2, \text{ where,}$$
$$c_1 = \frac{3e}{4\pi m_e^3 c^5}.$$

Therefore, synchrotron power emitted by an electron is:

$$-\frac{d\epsilon}{dt} = c_2 (B \sin\theta)^2 \epsilon^2, \text{ where}$$
$$c_2 = \frac{2e^4}{3m_e^4 c^7},$$

where θ is the pitch angle between electron velocity and magnetic field lines, m_e is the electron mass, c the speed of light in a vacuum, B is the magnetic field in Gauss (G), and e is the electric charge. Practically, these are given as:

$$\nu_c \approx 4.2 (B \sin\theta) \gamma^2,$$
$$-\frac{d\epsilon}{dt} = 1.6 \times 10^{-15} (B \sin\theta)^2 \gamma^2$$

Using the above equations, we can infer that the energy of emitting electrons at a given frequency depends on the magnetic field strengths, i.e. if the magnetic field strength is high, lower energy will be required to produce emission and vice versa. This is illustrated in Fig. 3.2 from Govoni and Feretti (2004).

Synchrotron radiation provides a way of probing a magnetic field, as it can provide an estimate of magnetic field strengths. Moreover, the degree of polarisation could hint at the magnetic field's uniformity and structure. In a uniform magnetic field and an optically thin case, the degree of polarisation from a power-law distribution of isotropic and homogeneous relativistic electrons is related to the spectral index, α, and is given by :

$$p_{\text{int}} = \frac{3\alpha - 3}{3\alpha - 5}, \tag{3.1}$$

with typical spectral index values of radio sources of between 0.6 and 1 resulting in a theoretical maximum intrinsic polarisation degree of 75%. However, in reality, this theoretical value is not observed, possibly due to depolarisation (the various causes of depolarisation are discussed briefly in Sec. 3.2.3) or a complex magnetic field along the line-of-sight (Govoni and Feretti, 2004).

As an EM wave propagates through space, it could encounter a magneto-ionised medium that potentially slows it down because of the differences in refractive index caused by variations in the electron density within the medium, causing a variation in the propagation speeds of the left and right circularly polarised components in the magnetised plasma. As a result, some amount of scattering and refraction could occur. Because these two waves have opposite handedness of circular polarisation with respect to each other, the net result is a rotation of the electric field, causing *Faraday rotation.*

3.2 Polarisation and Faraday Rotation

Astronomical sources emit EM radiation at various frequencies; of concern to us in this thesis is the radio frequency. As the EM waves propagate, they may encounter various "obstacles" before they

5 By equating thermal energy to kinetic energy using the formula $\frac{m_e \nu^2}{2} = \frac{2\kappa T_e}{2}$.

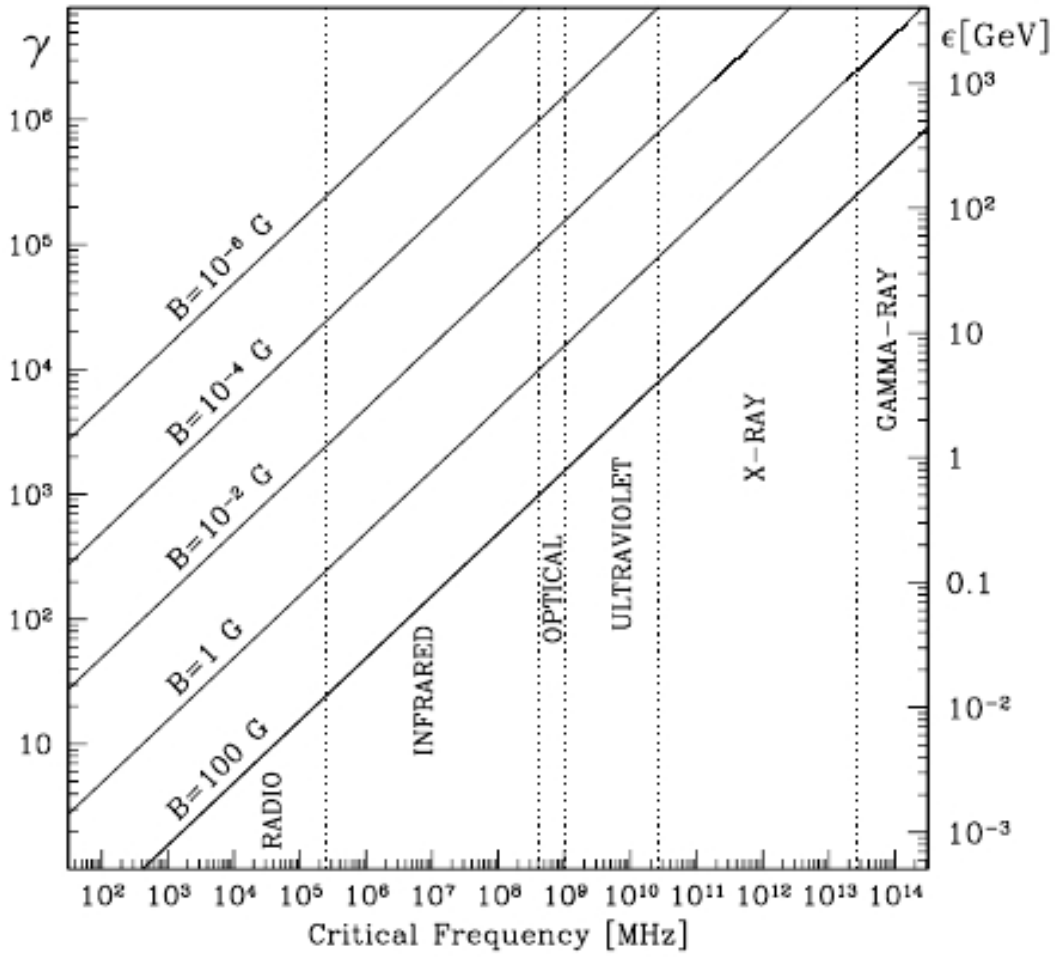

Figure 3.2: Illustrating the amount of energy required to produce emission at different magnetic field strengths. This is Fig.1 from Govoni and Feretti (2004).

reach an observer's eye. The path a signal takes from the emission source to the observer is called the *line-of-sight* (LoS). In the context of astronomy, instances of the obstacles could be magnetised or ionised media. As a result of the interaction with magnetic fields and thermal electrons found in these environments, the plane of polarisation, henceforth known as the *polarisation angle*, ψ (measured from North), is rotated by the *rotation measure* (RM) as $\mathrm{RM}\lambda^2$. This is called the Faraday rotation effect, an effect of a change in velocity (due to refractive index) of the incident wave on the intervening medium. Fig. 3.3 illustrates the Faraday rotation of a single idealised and linearly polarised EM wave from a single electron. However, the realistic situation is different because the observed polarised emission is from the net average of multiple waves with varying polarisation angles.

RMs encode valuable information for studying the magnetic environment around or within a source. Since EM waves comprise an electric and magnetic field, a direct probe of the electric field provides an indirect measure of the interacting magnetic fields involved. Additionally, Faraday rotation caused by the various intervening media (both environmental and instrumental) as polarised emission propagates towards the observer along a LoS could cause incoherent addition of ψ of its constituent emissions, resulting in a net reduction of the observed fractional polarisation. This is called *depolarisation*.

At this point, we introduce the basic foundations used in radio astronomy for polarimetric studies, following the works of Burn (1966) and Sokoloff et al. (1998). We will define the basic equations and briefly describe depolarisation, its mechanisms, and various techniques and tools useful for spectropolarimetric diagnosis.

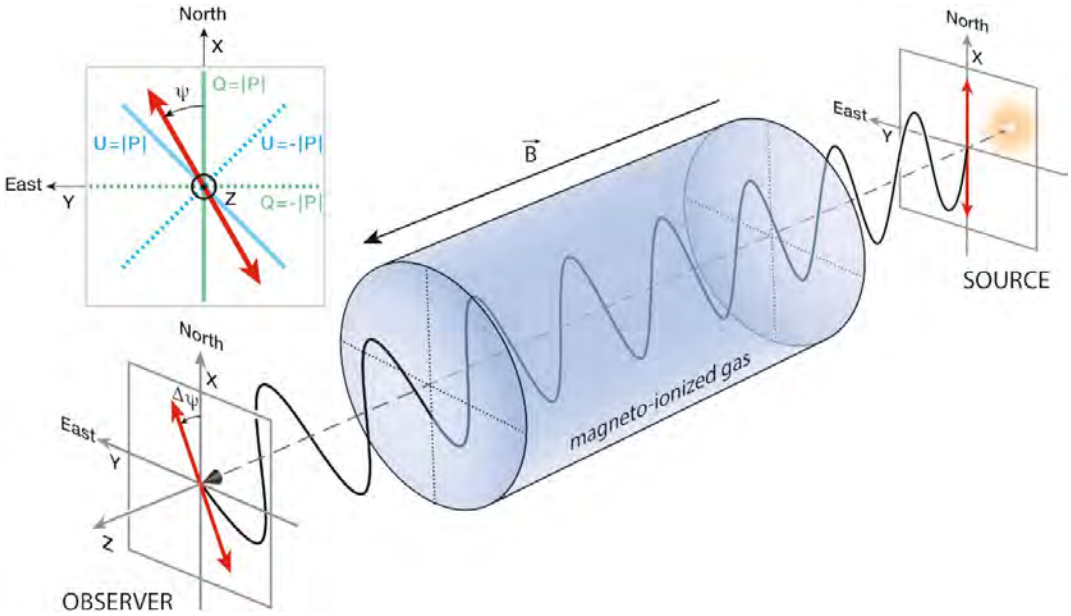

Figure 3.3: An illustration of Faraday rotation as a linearly polarised wave passes through a magneto-ionised medium. Image from Ferrière et al. (2021).

3.2.1 *The Polarisation of an Electromagnetic Wave*

The polarisation state of a wave is determined by the shape traced out as it propagates (for example, the red arrows shown in Fig. 3.3). This is the resultant vector from the contributions of the x and y components of the electric vector. Let us consider that our signal in Fig. 3.3 has electric field vectors e_x and e_y. Ideally, the signal is received by an antenna with two orthogonal feeds, each distinctly sensitive to the separate components. Therefore, considering the reality that an antenna receives a group of waves that are variable over time, non-monochromatic and measured as complex signals, the observed signals can be described using the Stokes parameters I, Q, U and V as:

$$
\begin{aligned}
I &= \langle e_x e_x^* \rangle + \langle e_y e_y^* \rangle \\
Q &= \langle e_x e_x^* \rangle - \langle e_y e_y^* \rangle \\
U &= \Re(\langle e_x e_y^* \rangle + \langle e_y e_x^* \rangle) \\
V &= \Im(\langle e_x e_y^* \rangle - \langle e_y e_x^* \rangle)
\end{aligned}
$$

where $\langle\rangle$ represents averaging, $(*)$ represents the complex conjugate, and $\Re, \Im$ represent real and imaginary components, respectively. From this mathematical description, Stokes I represents the total contributions from both x and y components, i.e. the total intensity (total power) of the EM wave. On the other hand, Q, U, and V represent the linear parallel and diagonal states, and the circular states of polarisation, respectively.[6] Polarimetric analysis begins with imaging of the observable quantities, the Stokes parameters. This technically means that $I^2 \geq Q^2 + U^2 + V^2$, meaning the polarised quantities cannot exceed Stokes I. Because most radio galaxies exhibit linear polarisation (Carilli and Barthel, 1996), we limit ourselves to linear polarisation in this thesis.

A wave is described as linearly polarised if it oscillates in a direction parallel to its plane of polarization and, thus, traces out an upward or downward motion if an observer were looking at it face-on. Its intensity (amplitude), the linear polarised intensity, is often defined as

$$
|P| = \sqrt{Q^2 + U^2}, \tag{3.2}
$$

with contributions from the Q and U components. It is realistically improbable to obtain perfectly polarised emission. Hence, only a fraction of the observed emission is polarised. Since there is

6 More on the Stokes parameters and their relation to visibilities in Sec. 4.1.

little to no circular polarised emission, the Stokes V term is often assumed to be 0. Therefore, the fraction of linear polarised emission, otherwise known as *fractional polarisation* or *degree of polarisation*, is given by[7]:

$$p = \frac{|P|}{I} = \frac{\sqrt{Q^2 + U^2}}{I} \tag{3.3}$$

Consider a source only producing linearly polarised emission situated behind a purely Faraday rotating foreground screen with no additional polarised emission; the observed polarisation angle will be:

$$\psi_{\text{obs}} = \psi_0 + \text{RM}\lambda^2, \tag{3.4}$$

where ψ_0 is the intrinsic polarisation angle, RM is the rotation measure, and λ^2 is the squared wavelength of observational frequency bands. The RM could be described as the rate of change of the polarisation angle with λ^2. On the other hand, the polarisation angle is defined as:

$$\psi = \frac{1}{2} \arctan \frac{U}{Q} \text{ [rad]}. \tag{3.5}$$

3.2.2 *Determining the Rotation Measure*

3.2.2.1 *Linear Fitting*

The fundamental method of quantifying the RM was fitting a least squares regression line on the plot of ψ measured over multiple wavelengths, against λ^2. I.e. it was given as the slope of the line of Eqn. 3.4, which is directly observed by measuring ψ at various intervals of λ^2. While direct, this method suffered from a significant issue resulting from phase wrapping, where discontinuities are caused by jumps in the angle at 180°. This means multiple solutions exist for a polarisation angle in the scenario with insufficient spectral data, leading to inaccuracies in the derived RMs. This is called the nπ ambiguity problem. Unreliable results from the least squares fitting drove the development of newer, more reliable methods that attempt to avoid or mitigate ambiguity problems, such as Pacerman (Dolag et al., 2005) and the Rotation Measure Synthesis (RM-Synthesis, Brentjens and de Bruyn, 2005). Furthermore, it was not possible to distinguish contributions from various components along a LoS.

3.2.2.2 *Rotation Measure Synthesis and RM-CLEAN*

RM-Synthesis was developed by Brentjens and de Bruyn (2005) based on the work of Burn (1966). Its power lies in its ability to (1) Predict the nπ ambiguities and overcome them (2) produce reliable results even in a low signal-to-noise ratio, (3) It tries to predict the individual RM contributions along a LoS. Below, we briefly summarise concepts related to RM-Synthesis.

Consider our previous scenario whereby a single linearly polarised wave passes through a magneto-ionised medium. In more physical terms, we could define RM (from Eqn. 3.4) in terms of the magnetic field strength and orientation along a LoS as:

$$\text{RM} = 0.81 \int_{\text{source}}^{\text{observer}} n_e \mathbf{B}_{||} \cdot dr, \tag{3.6}$$

whereby a positive value of RM indicates a magnetic field pointing towards us by convention. Here, n_e is the electron number density in cm^{-3}, $B_{||}$ is magnetic field strength in micro-Gauss (μG) along a LoS, and dr is the infinitesimal path length along a LoS from the source to the observer in parsecs (pc). This measure links the observed quantities to the magneto-ionic properties of the intervening medium.

In reality, we do not observe a single wave originating from a unique LoS. Instead, our telescopes perceive a combination of waves from an angular area of the source, with each wave possibly

7 Note that this holds regardless of the value of V as long as P and p are specified as linear polarisation.

traversing through a uniquely varying and significantly different magneto-ionic structure along its LoS. Thus, our telescopes actually observe an averaged observed polarised flux density along various LoSs. To account for the various intervening magneto-ionic media and possibly the co-existence of Faraday rotating and synchrotron emitting media, Burn (1966) introduced the notion of *Faraday depth*, ϕ, which incorporates their unique contributions along a LoS. This is a physical term that can be defined anywhere within a magneto-ionised medium as:

$$\phi(L) = 0.81 \int_{L}^{\text{observer}} n_e \mathbf{B}_{||} \cdot dr \text{ [rad m } ^{-2}]. \tag{3.7}$$

This equation is similar to Eqn. 3.6, except that the integration limit in this case is from a specific point L along a LoS to the observer, and not the entire path length from the source. Faraday depth gives information about the strength of Faraday rotation that polarised emission experiences at some distance from the observer (Van Eck, 2018). Information about the order (or lack thereof), direction and strength of magnetic fields parallel to the LoS can be deduced with this formalism. In the case of a single Faraday rotating screen, the RM of the foreground screen will be exactly equal to its Faraday depth.

We now introduce the concept of complex linear polarisation, $P(\lambda^2)$, which is the observed polarisation of a source's integrated emission defined as:

$$P(\lambda^2) = Q(\lambda^2) + iU(\lambda^2). \tag{3.8}$$

Stokes Q and U parameters are the real and imaginary components in this equation, respectively. However, spectral variations in the total intensity, I, could introduce variations in the observed complex polarisation. These are decoupled by normalising Q and U with respect to Stokes I. These fractional values separate effects due to the spectral index from those caused by depolarisation, in addition to minimising RM estimate errors for RM-Synthesis in the analysis of polarisation dependence on wavelength (O'Sullivan et al., 2012). Hence, the complex polarisation can be written in phasor notation by first considering $q = Q/I$ and $u = U/I$ so that $P/I = q + iu$. Eqns. 3.3 and 3.5 give the amplitude and phase of this formulation, respectively. Thus, in phasor notation we rewrite Eqn. 3.8 as:

$$\begin{aligned} &\frac{P}{I} = pe^{2i\psi}, \text{ and making } P \text{ the subject of the formula} \\ &P = pIe^{2i\psi}. \end{aligned} \tag{3.9}$$

We can now define the relationship between the observed polarised quantities in λ^2 space and true physical quantities in ϕ space. Considering our earlier statement that emission may pass through multiple magneto-ionised environments, the observed complex polarised emission is a total of contributions from all possible Faraday depths along a given LoS. Burn (1966) described this relationship through a Fourier relationship:

$$P(\lambda^2) = \int_{-\infty}^{\infty} F(\phi) e^{2i\phi\lambda^2} d\phi, \tag{3.10}$$

where $F(\phi)$ is known as the Faraday dispersion function (FDF), a complex-valued function indicating the polarised emission at a specific Faraday depth. Thus, the integral in this equation is the sum of contributions from all Faraday depths. Since values of $\lambda < 0$ are not physically observable, various assumptions about the source and the observations must be made to allow the inversion of Eqn. 3.10. Furthermore, telescopes append the additional constraint that λ space can only be sampled at discrete intervals, i.e. the sampling is incomplete. To cater for this, Brentjens and de Bruyn introduced a weighting function (sampling function) with a value of one only where measurements of λ^2 are available, and zero elsewhere, resulting in the *observed complex polarised emission* $P_{\text{obs}}(\lambda^2)$ as:

$$P_{\text{obs}}(\lambda^2) = W(\lambda^2) P(\lambda^2). \tag{3.11}$$

Substituting this into Eqn. 3.10 gives:

$$P_{\text{obs}}(\lambda^2) = W(\lambda^2) \int_{-\infty}^{\infty} F(\phi) e^{2i\phi\lambda^2} d\phi. \tag{3.12}$$

The inverse Fourier transform of the sampling function normalised to unity at $\phi = 0$ then introduces the rotation measure transfer function (RMTF), R(ϕ), as:

$$\begin{aligned} R(\phi) &= \left(\int_{-\infty}^{\infty} W(\lambda^2) d\lambda^2 \right)^{-1} \int_{-\infty}^{\infty} W(\lambda^2) e^{-2i\phi\lambda^2} d\lambda^2 \\ &= K \int_{-\infty}^{\infty} W(\lambda^2) e^{-2i\phi\lambda^2} d\lambda^2, \end{aligned} \tag{3.13}$$

which is the response to a single polarised component in Faraday space for a given wavelength along a LoS. It is a complex, unitless and normalised function. When inverted, this becomes

$$W(\lambda^2) = \left(\int_{-\infty}^{\infty} W(\lambda^2) d\lambda^2 \right) \int_{\infty}^{\infty} R(\phi) e^{2i\phi\lambda^2}. \tag{3.14}$$

Therefore, substituting Eqn. 3.14 into 3.12, followed by application of its Fourier transform and using the convolution property of Fourier transforms[8], we find that:

$$\begin{aligned} F_{\text{obs}} &= F(\phi) * R(\phi) \\ &= K \int_{-\infty}^{\infty} P_{\text{obs}}(\lambda^2) e^{-2i\phi\lambda^2} d\lambda^2. \end{aligned} \tag{3.15}$$

Brentjens and de Bruyn (2005) showed that derotating λ^2 to a reference wavelength, λ_0^2, mitigates the difficulties in estimating the correct polarisation angle at the peak of $|F(\phi)|$ due to the rapid rotation of the real and imaginary components of the RMTF by maintaining its imaginary component as close to zero as possible (e.g. as illustrated in Fig. 3.4). They showed that a good choice of λ_0^2 is the weighted average of the observed λ^2. However, Rudnick and Cotton (2023) have also demonstrated that setting $\lambda_0^2 = 0$ and using a restoring beam with the size of the FWHM of the resulting RMTF's real component, Θ_{full} (in that paper, the FWHM of the reference wavelength $< \lambda^2 >$ is termed as Θ_{nominal}), does not change the accuracy and phase stability of the restoring component but results in a higher RMTF resolution. This ameliorates the accuracy in discrimination of Faraday components in Faraday complex cases where Faraday components are separated by $\geq \Theta_{\text{full}}$, and causes a reduction of spurious features in the recovered Faraday spectra. Derotating the polarisation vector to a common $\lambda_0^2 \neq 0$ generalises Eqns. 3.15 and 3.13 which become:

$$F_{\text{obs}} = K \int_{-\infty}^{\infty} P_{\text{obs}}(\lambda^2) e^{-2i\phi(\lambda^2 - \lambda_0^2)} d\lambda^2, \tag{3.16}$$

and

$$R(\phi) = K \int_{-\infty}^{\infty} W(\lambda^2) e^{-2i\phi(\lambda^2 - \lambda_0^2)} d\lambda^2. \tag{3.17}$$

Derotation does not affect the amplitude of the RMTF because it is just a Fourier shift; we also highlight this in Fig. 3.4.

RM-Synthesis operates within two realms: ϕ-space and λ^2-space, which are Fourier transform pairs of each other. Consequently, Eqns. 3.12 and 3.15 form the Fourier pair that maps λ^2 to ϕ space and back. The FDF is the polarised intensity distribution as a function of Faraday depth, so a Faraday spectrum exhibiting a single peak indicates a source with a single RM. Side lobes within the FDF occur because of insufficient coverage in λ^2. Therefore, a higher sampling mode in λ^2 space results in reduced side lobes in the RMTF, thus, a more reliable derived RM. This effect was illustrated in Fig. 7 of Brentjens and de Bruyn (2005), who showed that using more wavelength samples significantly lowered the side lobes. However, using RM-CLEAN (Heald, 2009) reduces the side lobes further, leading to a more stabilised RM value.

RM-CLEAN (Heald, 2009) was introduced to reduce sidelobes in the RMTF introduced by the incomplete sampling of the λ^2 space to avoid confusion of these lobes with actual components in the case of multiple RM components. It is somewhat similar to the traditional deconvolution CLEAN (discussed in Sec. 4.3.3), except it occurs in Faraday depth space and involves complex quantities of the FDF. We summarise the algorithm as follows:

8 A multiplication in Fourier domain becomes a convolution in the inverse domain.

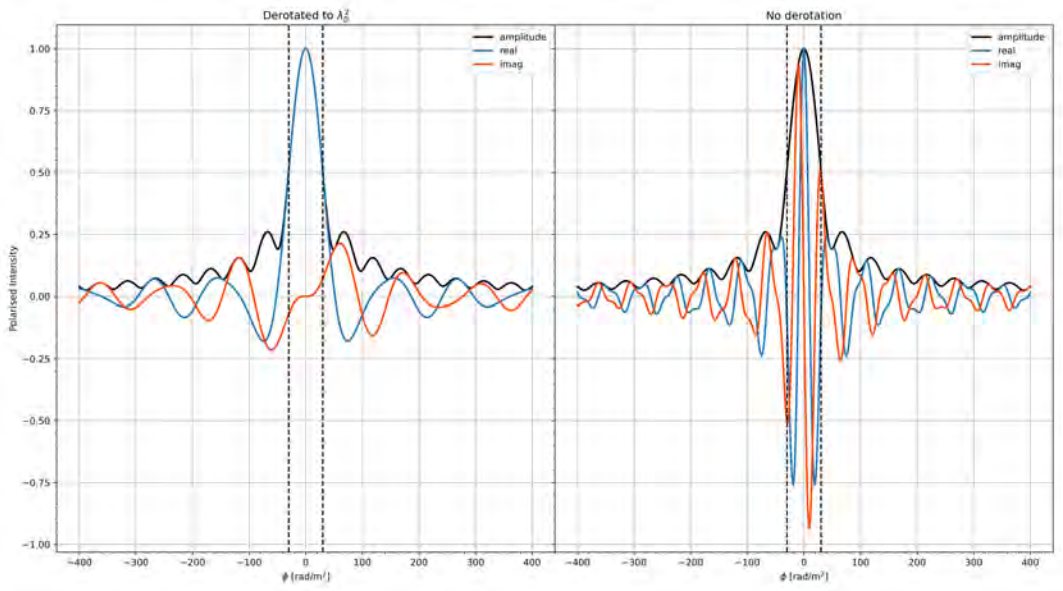

Figure 3.4: Illustrating the effect of derotating the RMTF to a common λ_0^2. Derotation stabilises the phase between the complex components by reducing the rate of oscillations between them and keeping the imaginary component close to zero, thereby enabling the acquisition of more accurate polarisation angle values. The amplitude is maintained in both cases. The black dashed lines show its FWHM, which is 0.5.

1. Find the peak of the FDF i.e. the peak amplitude from $\|F(\phi)\|$.
2. Scale the real and complex values of RMTF at this peak by some fraction of the peak (the loop gain) and store it as a CLEAN component.
3. Shift the RMTF to this peak's location, then scale its amplitude at this peak's depth location by the loop gain and finally, subtract this result from the RMTF.
4. Repeat steps 1–3 with the residual FDF until the maximum number of iterations or threshold is met.
5. Convolve the CLEAN components with the restoring function (i.e. a real-valued Gaussian with a width same as the RMTF's main lobe FWHM).

Pitfalls

The combination of the RM-Synthesis and RM-CLEAN is not without its challenges. It can sometimes be unreliable, as it may fail to accurately represent the RM locations (peaks) in ϕ-space from reconstructed FDFs, especially when multiple RM components are present along a LoS. This depends on some combination of the separation between these components in depth space, and the relative phase of their intrinsic polarization angles. For example in the case of relative phase difference, two RM components of equal amplitude separated by depths greater than the resolution of the RMTF and a phase difference of 90° between their intrinsic polarisation angles have been shown to cause RM-CLEAN to place two peaks at the wrong Faraday depths, and also introduce a spurious extra peak, thus causing its inability to correctly recover their original locations (e.g see Fig. 22 of Farnsworth et al., 2011, for an illustration). On the other hand, a smaller separation between RM components causes RM-Synthesis to place peaks at the wrong Faraday depths, understandably so because of the lower RMTF resolution. However, the depths do not evenly mix; instead, they interfere, resulting in complicated $Q(\lambda^2)$ and $U(\lambda^2)$ structures, which is why RM-Synthesis fails.

These RM-Synthesis shortcomings inevitably prevent RM-CLEAN from accurate recovery of the original FDF structure. The various problems plaguing RM-Synthesis + RM-CLEAN have been sep-

arately and exhaustively investigated by Frick et al. (2010), Farnsworth et al. (2011) and Kumazaki et al. (2014). Furthermore, RM-Synthesis assumes that the spectral index fit to total intensity, I, is similar to that of the spectral index fit to linear polarised intensity. Therefore, using the ratios between Q/I and U/I for RM-Synthesis to remove spectral effects has become commonplace. However, the dissimilarity between these spectral index profiles could lead to misleading results, especially with extragalactic sources emitting at a single RM – i.e. with a single peak in the FDF (Schnitzeler et al., 2019).

3.2.2.3 *QU-fitting*

Farnsworth et al. (2011) realised that most polarimetric studies were more focused on the behaviour of $\psi(\lambda^2)$ in traditional least squares fitting, and $F(\phi)$ from RM-Synthesis, and largely ignored the behaviour of $p(\lambda^2)$. Others performed RM fitting only in regions of λ^2 where p was constant or decreasing monotonically, and excluded where p showed signs of increasing at short wavelengths. This came at the detriment of excluding underlying Faraday structure that could indicate the existence of multiple Faraday components along a LoS. Moreover, it was noted that while least square fitting produced RMs, the resulting chi-square value (χ^2) did not offer any information about the suitability of the fit, other than the fit has failed if its value is too high.[9] Additionally, least squares fitting did not take depolarisation into account. Farnsworth et al. (2011), O'Sullivan et al. (2012) and Sun et al. (2015) demonstrated that *QU*-fitting was the better-suited method in scenarios whereby multiple Faraday thin[10] RM components exist in a line-of-sight. Because of this and the apparent confusion of RM-Synthesis in the presence of multiple components along a single LoS, great emphasis was placed on the importance of fitting models on the observed $Q(\lambda^2)$ and $U(\lambda^2)$.

QU-fitting involves performing a direct parameter space search for a combination of components that best fit the observed data, hence the least χ^2 value. This way, models consisting of depolarisation and even multiple RM components could be tested, and the $p(\lambda^2)$ behaviour better monitored and understood. The immediate implication of *QU*-fitting is that models could directly be mapped to physical phenomena and accorded appropriate interpretations. Furthermore, complicated models could be explored to suit the observed data better. This modelling is also unaffected by $n\pi$ ambiguities (see Sec. 3.2.2.1) since it is done in the $Q(\lambda^2)$ and $U(\lambda^2)$ space. Below, we outline the general steps in *QU*-fitting:

1. Define the model to be tested. For example, the simplest model is one with a purely external Faraday rotating screen given by substituting Eqn. 3.4 into Eqn. 3.9.
2. Define the parameter space to be searched (e.g. the range of RMs, ψ) and its probability distribution.
3. Fit the model to the data and inspect their suitability to $Q(\lambda^2)$, $U(\lambda^2)$ and $p(\lambda^2)$. For example, our simple model should exhibit simple sine and cosine waves in Q and U.
4. Using the selected parameters, model and inspect the behaviour of $p(\lambda^2)$.
5. Repeat with other models until the best fit is found.

9 In basic terms, the χ^2 statistic informs how much the model, M, deviates from the real observed data D. It's given as $\chi^2 = \sum_i \frac{(D_i - M_i)^2}{M_i}$, where i is a data point.

10 A Faraday thin source is one whereby $\lambda^2 \Delta\phi \ll 1$, where $\Delta\phi$ is the span of the source in Faraday depth. A Faraday thin source can be modelled by a delta function.

One method used for data modelling and parameter estimation is Bayesian inferencing, a statistical approach that amends the probability of a model being correct as more information is made available.[11] It is based on Bayes' theorem[12]:

$$\underbrace{\mathcal{P}(B|A)}_{\text{Posterior}} = \frac{\overbrace{\mathcal{P}(A|B)}^{\text{Likelihood}}\overbrace{\mathcal{P}(B)}^{\text{Prior}}}{\underbrace{\mathcal{P}(A)}_{\text{Evidence}}}, \tag{3.18}$$

where B is the model being tested and A is a pre-specified condition. Then the ***prior*** probability is the probability of the model being correct before anything is observed, that is, any information we have before looking at the data. The ***likelihood*** is the probability of observing the specified condition given a specific model, and the ***evidence*** is the sum of the model's probabilities at each tested condition – that is, the marginal probability across B. It is used to normalise the ***posterior*** probability, which is the probability of a correct model after considering the observed data, in other words, the probability of the model being correct given the prior information. In terms of observed data D, and parameters θ, we can rewrite Bayes' rule as:

$$\mathcal{P}(\theta|D, M) = \frac{\mathcal{P}(D|\theta, M)\mathcal{P}(\theta)}{\mathcal{P}(D)}, \text{where} \tag{3.19}$$

$$\mathcal{P}(D) = \int_{\theta} \mathcal{P}(D|\theta)\mathcal{P}(\theta)d\theta = Z, \tag{3.20}$$

where we renamed the evidence/marginal likelihood, $\mathcal{P}(D)$, as Z for simplicity. Some assumptions must be made about the prior probability distribution to account for prior information about our data within our model. Including prior information makes Bayesian inferencing a powerful tool; therefore, choosing the prior distribution forms its most crucial part. Sometimes, no prior information is available; thus, the prior is unconstrained and is aptly called a non-informative prior. In this case, all that can be said is that $\mathcal{P}(\theta)$ lies between 0 and 1, with all values of θ are equally probable, giving a tophat shape. However, if the parameters are known within certain margins of error, perhaps from previous experiments, then the prior distribution can be $\mathcal{P}(\theta) \sim \text{Gaussian}(\mu, \sigma)$. The prior distribution could also be informed based on previous distributions of the data parameters in question. Whatever the choice of distribution is, the important thing is that the parameters with the largest likelihood should be included.

We could then infer what parameters best model our data by finding the parameter's value that maximises the posterior probability $\mathcal{P}(\theta|D)$. Since Z is an average likelihood over a given parameter space, the more suitable parameters yield higher values, indicating a better model. The suitability of a model (i.e. whether it is improving or not) should become more apparent with increasing evidence. Overfitting adds needlessly high variability as it may include unnecessary complexity, while underfitting adds bias as it may exclude important features. Thus, a good statistical model should be as simple as possible without compromising its fit to the data. Hence, Z is used in model selection. Simpler models (models with fewer parameters) tend to have higher marginal likelihood values than more complex models unless the complex model is substantially better.

An inherent shortfall with parameter space search is that the search can get stuck in a localised likelihood maximum and thus fail to converge towards a global likelihood maximum (Miyashita et al., 2019). Furthermore, since computing the Bayesian evidence, Z, involves integrating over the entire parameter space, it is a resource-intensive affair. This is akin to solving a massive problem in one go. Nested sampling (Skilling, 2004; Mukherjee et al., 2006; Shaw et al., 2007; Feroz and Hobson, 2008) tries to break down the problem into a series of smaller problems that are solved repetitively until reaching some convergence. The parameter space is randomly sampled within

11 Texts by Forsyth (2018) and Kruschke (2014) provide an excellent introduction to Bayesian inferencing and form the foundation of some of our definitions.

12 Bayes' theorem shows that $\mathcal{P}(B|A) \neq \mathcal{P}(A|B)$; thus, we can adapt the words of Dr. Carl Sagan to say that the presence of evidence is not an evidence of presence.

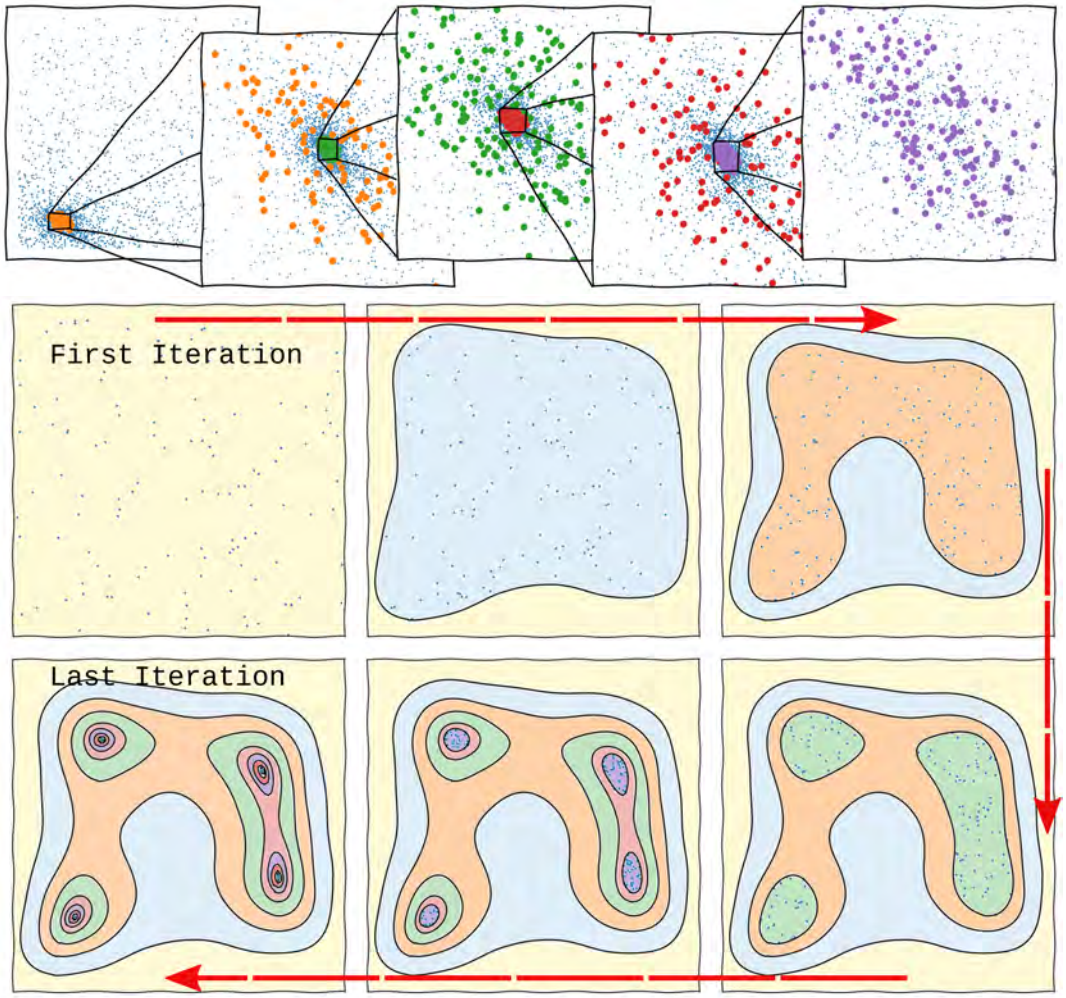

Figure 3.5: A simple illustration of nested sampling. Dead points (blue) are discarded with each iteration, while the remaining live points are sampled further within a smaller search space until some convergence is achieved. The parameter search spaces are highlighted with a coloured background. Images adapted from the talk "REACH: Nested Sampling tools" (Handley, 2023).

regions where the likelihoods are above a certain threshold. The samples below the threshold (dead points) are discarded. On the other hand, the set of samples meeting this threshold (live points) form a new sample space that is sampled again, effectively emphasising regions in the parameter space with higher likelihoods. The process is illustrated by Fig. 3.5 and is done iteratively, reducing the parameter space until the most suitable parameters are found. This algorithm's innate computation of the Z of a given model facilitates the process of model comparison and selection.

We use the `PyQufit`[13] python package in part of this work for *QU*-fitting which uses nested Bayesian sampling techniques for parameter estimation.[14] In this setup, the likelihood distribution for the free parameters, defined as priors[15] are provided by the user and the models to be tested. This tool generates the estimated parameters and chi-squares for the various models and diagnostic q on regions and u plots for the data. The application of this technique will be discussed briefly in Sec. 5.3.6 of this thesis.

13 https://github.com/Sebokolodi/PyQUfit

14 This is done through the adaptation of `pyMULTINEST` (Buchner et al., 2014) which is a Python wrapper around `MULTINEST` (Feroz et al., 2009) to *QU*-fitting.

15 I.e. the information we know beforehand.

3.2.3 *Depolarisation*

Depolarisation is an effect whereby the observed fractional polarisation from an astrophysical object is reduced from the theoretical projected value (given by Eqn. 3.1). It sometimes manifests as a reduced fractional polarisation with increasing λ^2 or changing spatial resolution. Depolarisation generally occurs due to the incoherent addition of polarised vectors, $p_0 e^{2i\psi+\phi\lambda^2}$, of the constituent synchrotron emission, leading to a reduction of the net observed degree of polarisation. Various mechanisms, both intrinsic and external to extragalactic sources, can result in depolarisation. This section briefly summarises the major causes of depolarisation, driven by the detailed works of Burn (1966) and Sokoloff et al. (1998).

Differential Faraday Rotation

Differential rotation is a wavelength-dependent effect that can occur in a region that is both synchrotron emitting and Faraday rotating within a source, or a purely Faraday rotating region along a single LoS. Its effects can be categorised into: differential Faraday rotation and internal Faraday dispersion (IFD).

Differential Faraday rotation occurs when synchrotron emitting and Faraday rotating regions coexist in a *regular* (coherent) magnetic field. Emission produced at various Faraday depths each experiences different amounts of Faraday rotations, i.e. *polarised emission from the far side experiences multiple Faraday rotations* along a LoS. Since the rotation measures at each depth differ, the resulting observed polarised emission reduces due to averaging over differing polarisation angles.

When depolarisation occurs due to Faraday rotation caused by the presence of a *turbulent* magnetic field, it is termed as dispersion. Suppose a synchrotron emitting and Faraday rotating region coexist in the presence of a turbulent magnetic field. In that case, the emission's polarisation plane may experience multiple random fluctuations as it passes through turbulent magneto-ionised cells along a LoS, resulting in a net reduction of the observed polarisation. This is known as internal Faraday dispersion (IFD).

Bandwidth Depolarisation

Modern telescopes are equipped with wideband channelised correlators – for example, the ATCA and MeerKAT telescopes (Wilson et al., 2011; Jonas and MeerKAT Team, 2016) – which allow for easier and time-effective observations in multiple wavelengths, with significantly improved uv-coverage. Moreover, such observations facilitate wideband imaging. However, the data around each channel's central frequency must be averaged to obtain data for a specific channel. Suppose data for various lines-of-sight are encompassed in the channel, and they are averaged. In that case, the effective observed polarised signal may be reduced due to the destructive interference of different existing polarisation states, otherwise known as bandwidth depolarisation. This implies the need to balance between obtaining a reasonable signal-to-noise and recovering the maximum polarisation structure while selecting the number of imaging channels (see e.g. Fine et al., 2023).

Beam Depolarisation

Beam depolarisation occurs when the highest angular resolution of a telescope is insufficient for resolving polarised structure. If the beam is not small enough to resolve RM gradients caused by the significant variations of RM within a region, these RMs average out, causing depolarisation. Therefore, the only remedy is using a telescope with better resolution, which is fortunately offered by radio interferometry.

3.3 Visibilities and Radio Interferometers

Radio interferometry stemmed from the need for improved angular resolution, θ, which is the minimum angular separation such that two close point sources are perceived as distinct. This is because, for a single dish antenna, the angular resolution is diffraction-limited[16] as θ is dependent on the dish diameter D, and is estimated using the Rayleigh criterion as $\theta = 1.22\lambda/D$ for a dish with a circular aperture.[17] Thus, to obtain a higher angular resolution, one would require a very large dish, which is possible to an extent – e.g. the Five-hundred-meter Aperture Spherical Telescope (FAST, Nan et al. 2011) – but largely impractical. Radio interferometry surmounts this challenge using the *aperture synthesis* technique, which combines signals from multiple single-dish antennas coherently to form an image of the sky. In this section, we briefly introduce the 2-element interferometer and aperture synthesis based on the work of Thompson (1999) and Clark (1999).

3.3.1 *The Two-element Interferometer*

A basic interferometer consists of two elements, the antennas, separated from each other by a distance known as the *baseline*, $\mathbf{b}$. Because multiple antennas are involved in interferometry, multiple baselines also exist. Thus, the longest baseline separation $\mathbf{b_{max}}$, between the antennas determines the interferometer's resolution, which is then given by:

$$\theta \sim \frac{\lambda}{\mathbf{b_{max}}} \text{ [rad]} . \tag{3.21}$$

With this setup, extremely high angular resolution is made possible as baselines can span towards kilometre distances.[18] Telescopes such as MeerKAT and the VLA use aperture synthesis, allowing the generation of high-resolution, high-sensitivity images of Galactic and extragalactic sources.

EM waves arriving from astrophysical sources are usually assumed to be planar when they arrive at the antennas using the far-field approximation, as illustrated in Fig. 3.6. If we consider a point source radiating emission with an electric field e towards antennas p and q from this illustration, signals will arrive at q first because the path to antenna p is longer. The additional time taken for this signal to arrive at p is the *geometric delay*, τ_g, given by:

$$\tau_g = \frac{\mathbf{b} \cdot \mathbf{s}}{c}, \tag{3.22}$$

where c is the speed of light in a vacuum, and $\mathbf{s}$ is a direction unit vector pointing towards a distant radio source. The signals, measured as voltages by the antennas, are then transmitted into the correlator, where τ_g is incorporated into the signal of p to maintain spatial signal coherence. Thus, the voltages measured by p and q become $v_p(t) = \cos(2\pi(t - \tau_g))$ and $v_q(t) = \cos(2\pi t)$.[19] The signals are then multiplied and averaged over a time, known as the *integration time*, for stability. Thus, the correlator's output is proportional to:

$$\left\langle v_p(t) v_q(t) \right\rangle , \tag{3.23}$$

where $\langle\rangle$ represents time averaging.

The spatial coherence measured by an interferometer is given in terms of *visibilities*, which are complex-valued. Spatial coherence and visibilities are related through the Van Cittert-Zenike theorem defined as:

$$V = \int_S \mathcal{A}(\mathbf{s}) I(\mathbf{s}) e^{-2\pi i \nu \frac{\mathbf{b}\mathbf{s}}{c}} d\Omega, \tag{3.24}$$

16 The theoretical maximum resolution obtainable from a radio telescope is limited by diffraction.
17 This is the collecting area of a dish.
18 Sub-arcsecond resolution is possible using Very Long Baseline Interferometry techniques. A telescope such as the Very Long Baseline Array (VLBA) can achieve 0.17 mas resolution.
19 In signals and systems, a negative shift implies a signal delay.

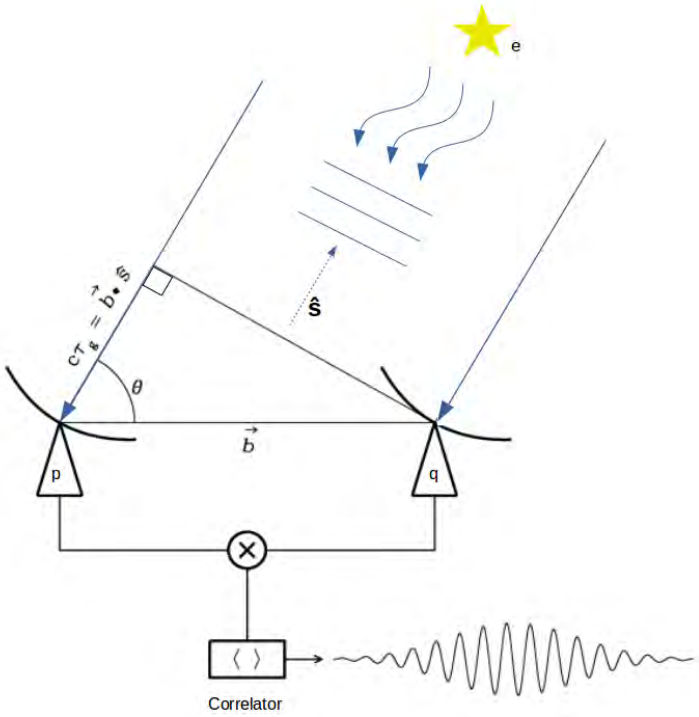

Figure 3.6: A two-element interferometer.

where $\mathcal{A}$ is the effective antenna collecting area (aperture), $I(\mathbf{s})$ is the source intensity: the amount of flux per frequency ν at $\mathcal{A}$ through a solid angle Ω measured in $\mathrm{Wm^{-2}Hz^{-1}sr^{-1}}$. However, $\mathcal{A}(s)$ is normalised to unity to simplify matters. Integrating over the entire solid angle gives the source's *flux density* measured in Jansky (Jy), where 1 Jy = 10^{-26} $\mathrm{Wm^{-2}Hz^{-1}}$.

3.3.2 *Aperture Synthesis*

To become more useful, multiple two-element interferometers spread over a large area (spatially separated) are connected to form an array whose signals are combined electronically. This mimics a larger telescope (synthesised telescope) that has a diameter equivalent to $\mathbf{b_{max}}$. This technique is known as aperture synthesis. At the start of an observation, an interferometer is usually pointed towards a position at the centre of an intended field of view used as a phase reference. This is the *phase tracking centre*, $\mathbf{s_0}$, which is updated constantly as the telescope tracks as a source as it moves across the sky. An arbitrary direction within the field of view and close to the phase centre could then be denoted as $\mathbf{s} = \mathbf{s_0} + \boldsymbol{\sigma}$. Realistically, measurements of visibilities require the introduction of a suitable coordinate system for convenience that allows the practical application of Eqn. 3.24.

In this system, the baseline vector, $\mathbf{b}$, has components (u, v, w) that are measured in wavelengths $(\frac{\nu}{c})$ at the central observing frequency. The w component points towards the phase centre, while the u, v components point towards the East and North, respectively. From the observer's standpoint, i.e. the telescope, the value of $w = 0$. Positions in the sky are defined using (l, m, n), whereby l and

m are directional cosines relative to u and v, respectively. These also represent the projection of the celestial sphere onto a tangent plane at the origin of (l, m). Thus, we define some parameters:

$$\begin{aligned}\nu\frac{\mathbf{b}\cdot\mathbf{s}}{c} &= ul + vm + wn,\\ \nu\frac{\mathbf{b}\cdot\mathbf{s_0}}{c} &= w,\\ d\Omega = \frac{dldm}{n} &= \frac{dldm}{\sqrt{1-l^2-m^2}}.\end{aligned}$$

Applied to Eqn. 3.24, we obtain an expression of visibility as a function of (u, v, w) given as:

$$V(u,v,w) = \int_{-\infty}^{\infty}\int_{-\infty}^{\infty} \mathcal{A}(\mathbf{s})I(\mathbf{s})e^{-2\pi i[ul+vm+w(\sqrt{1-l^2-m^2}-1)]}\frac{dldm}{\sqrt{1-l^2-m^2}}. \tag{3.25}$$

If we enforce the condition that all the antennas are on a flat plane, or assume that $|l|$ and $|m|$ are small such that the field being imaged is so small that w becomes insignificant, and assume $\mathcal{A}(l, m) = 1$ for simplicity, Eqn. 3.25 is reduced to a 2-D Fourier transform of the sky brightness $I(l, m)$:

$$V(u,v) = \int_{-\infty}^{\infty}\int_{-\infty}^{\infty} I(l,m)e^{-2\pi i(ul+vm)}dldm. \tag{3.26}$$

The complex-valued visibilities obtained from Eqn. 3.26 are the interferometer's output, and $I(l, m)$ is known as the ***true sky***. This data is usually stored in a standard format, the Measurement Set (MS) (van Diepen, 2015; van Diepen and Farris, 1994, and see Sec. 4.3), from which it is then processed for calibration and imaging. Therefore, it is possible to obtain an image of the sky by inverting this equation so that:

$$\begin{aligned}I(l,m) &= \mathcal{F}^{-1}\{V(u,v)\}\\ I(l,m) &= \int_{-\infty}^{\infty}\int_{-\infty}^{\infty} V(u,v)e^{2\pi i(ul+vm)}dudv.\end{aligned} \tag{3.27}$$

This is an ideal case. Realistically, the uv-space is only sampled at finite and discrete intervals. Therefore, the recovered sky image will not accurately represent the observed sky. uv sampling is dependent on the number of frequency channels, number of baselines available, and the length of the observation, and it results in the sampled uv-space known as ***uv-coverage***, examples of which are shown in Fig. 4.1. A well-sampled uv-space is vital as it ensures a better representation of the sky as the telescope observes. uv-coverage could be improved by increasing the bandwidth and number of observing channels, increasing the number of baselines[20], or increasing observation time taking advantage of the Earth's rotation.[21] The Earth's rotation gives uv-coverage its elliptical shape as one moves away from the equator.

Thus, Eqn. 3.27 must account for this discrete sampling. To do this, we can introduce a sampling function $S(u, v)$ such that:

$$S(u,v) = \begin{cases}1 & \text{where } u \text{ and } v \text{ are sampled,}\\ 0 & \text{elsewhere}\end{cases}$$

Eqn. 3.27 is therefore modified to become:

$$I^D(l,m) = \int_{-\infty}^{\infty}\int_{-\infty}^{\infty} V(u,v)S(u,v)e^{2\pi i(ul+vm)}dudv. \tag{3.28}$$

$I^D(l, m)$ is known as the dirty image because the interferometer's incomplete sampling introduces artefacts to the generated image. In lm-space, the sampling function manifests itself as the ***point***

20 Number of unique baselines $N_{\text{bl}} = \frac{N_{\text{ant}}(N_{\text{ant}}-1)}{2}$, where N_{ant} is the total number of antennas.
21 This is limited by the amount of time a target source is above the horizon i.e visible to the telescope.

spread function (PSF) or the *dirty beam* $P(l, m)$, and this is the inverse Fourier transform of the uv-coverage. The convolution theorem states that multiplication in the non-Fourier space translates to a convolution in the Fourier space. Hence, the dirty image is the true sky convolved with the PSF:

$$I^D(l, m) = I(l, m) * P(l, m) \tag{3.29}$$

This means that the PSF affects the brightest sources the most because their introduced artefacts are numerically larger. Therefore, deconvolution from the PSF is required to recover a better representation of the true sky. Introduction of the PSF gives a practical meaning to Eqn. 3.21; a longer baseline results in a wider uv-coverage. Based on this and the scaling property of the Fourier transform, the result will be a narrower and smaller PSF. Thus, the availability of longer baselines improves a synthesised image's resolution.

3.3.3 *Sensitivity*

A telescope's sensitivity refers to the faintest signal it can detect. However, a signal must exceed the noise induced by the antennas' electronics and other environmental noise to be detectable. Radio astronomers commonly measure antenna noise as fluctuations in antenna measurements in terms of temperature (Kelvins) for convenience. Thus, temperature fluctuations per antenna are given as:

$$\sigma_{\text{rms}} \approx \frac{T_{\text{sys}}}{\sqrt{\Delta\nu\Delta t}} \tag{3.30}$$

Here, $T_{\text{sys}} = T_{\text{ant}} + T_{\text{rx}}$ is the total system temperature encompassing all the noise measured by the antenna, T_{ant}, i.e. from the CMB, atmosphere etc., while T_{rx} is the thermal noise induced by antenna receiver electronics. $\Delta\nu$ and Δt are the total observation bandwidth and observation time, respectively. A simple way to conceptualise this idea is to think of an antenna as an analogue to a resistor; any power applied to that resistor increases its temperature. In the same way, power measured by the antenna also raises its temperature. Hence, when an antenna receives emission (and thus power) from an astrophysical source, its temperature increases by some value T_{src}. Based on these definitions, sensitivity requires that $T_{\text{src}} > \sigma_{\text{rms}}$, with a value of $\geq 5\sigma_{\text{rms}}$ yielding reliable detections (Wrobel and Walker, 1999; Campbell, 2002).

Measurements of the source temperature could provide insight into possible astrophysical processes occurring within the source. For example, extremely high temperatures could allude to highly energetic astrophysical processes.

Source temperature is convertible to Janskys using the Rayleigh-Jeans blackbody radiation approximation ($P = \kappa_B T \Delta\nu$) as follows:

$$T_{\text{src}} = \frac{A_e \eta}{2\kappa_B} S_\nu, \tag{3.31}$$

$$S_\nu = \frac{2\kappa_B}{A_e \eta} T_{\text{src}}, \tag{3.32}$$

where A_e is the effective antenna collecting area, η is the antenna efficiency, κ_B is the Boltzmann's constant and S_ν is the spectral flux density. Likewise, it is also possible to convert T_{sys} from units of K to Jy using the system equivalent flux density (SEFD), which is defined as:

$$\text{SEFD} = \frac{2\kappa_B}{A_e \eta} T_{\text{sys}}. \tag{3.33}$$

This is the flux density of a source that would double T_{sys}. The signal to RMS noise can now be determined as $T_{\text{src}}/\sigma_{\text{rms}}$. We divide 3.31 by 3.30 to get:

$$\frac{S_\nu}{\sigma_{\text{rms}}} = \frac{S_\nu A_e \eta \sqrt{\Delta\nu\Delta t}}{2\kappa_B T_{\text{sys}}},$$

$$\sigma_{\text{rms}} = \frac{2\kappa_B T_{\text{sys}}}{A_e \eta \sqrt{\Delta\nu\Delta t}} \tag{3.34}$$

This is the theoretical sensitivity of a single dish telescope, which is simplified using SEFD as:

$$\sigma_{\text{rms}} = \frac{\text{SEFD}}{\sqrt{\Delta\nu\Delta t}}.$$

A smaller SEFD points to a higher sensitivity. Thus, it is clear from Eq. 3.30 that T_{rms} is reducible by either lowering T_{sys} or increasing the observational bandwidth, or the integration time. T_{sys} could be reduced by decreasing T_{rx}, typically done using cryogenic coolers in the antenna receiver systems. Assuming that each antenna in an interferometric array is identical and has the same SEFD, the sensitivity of that interferometer becomes:

$$\sigma_{\text{rms},pq} = \frac{\text{SEFD}}{\sqrt{N(N-1)\Delta\nu\Delta t}}.$$

For a derivation, see Wrobel and Walker (1999).

3.3.4 *SKA and The MeerKAT telescope*

Technological advancements have spurred innovation within radio astronomy, leading to upgrades in some older radio telescopes, e.g. the VLA and the ATCA, to improve sensitivity and resolution capabilities. Newer and more ambitious observatories have been envisioned to meet these increasing needs, such as the Next Generation Very Large Array (ngVLA, McKinnon et al. 2019) which is currently in the design phase, and phase 1 of the Square Kilometre Array (SKA) whose construction is a currently ongoing project.[22] The SKA, whose goal is to have a collective aperture of one square kilometre, is also expected to span frequencies between 50 MHz and 20 GHz and will be located in two sites: the Karoo desert in South Africa and Murchinson, Western Australia; both remote and radio-quiet regions with reduced radio frequency interference (RFI) (Dewdney et al., 2009). As such, both sites host precursor telescopes to forecast and demonstrate the technical and scientific capabilities of the forthcoming SKA. These are the Murchinson Widefield Array (MWA), Tingay et al. 2013, for low radio frequencies, and the MeerKAT telescope (Jonas and MeerKAT Team, 2016) for mid radio frequencies. Since the data used in this thesis were obtained using the MeerKAT telescope, we shall focus on it.

The MeerKAT telescope operates at decimetre-wavelengths – UHF band at 580 to 1015 MHz, L-band at 900 to 1670 MHz, and S-band at 1750 to 3500 MHz divided into five smaller sub-bands – and consists of 64 antenna dishes. These dishes are organised to be more densely spaced towards the array's centre and sparsely spaced as one moves away, as shown in Fig. 3.7.

At the time of writing, MeerKAT has 2016 unique baselines (based on the 64-antenna layout); the maximum baseline is ∼7.7 km long. Each antenna dish has a nominal width of 13.5 m and a Gregorian offset design, meaning that its feeds are mounted away from the focal point of the main concave dish as depicted in Fig. 3.8. Due to this design, the main aperture's blockage is decreased, thus leading to higher efficiency, near circularly symmetric beams and reduced sidelobes, hence a well-behaved primary beam as it rotates relative to the sky. Furthermore, ground radiation scattering is also minimised, reducing the system temperature T_{sys} (Booth and Jonas, 2012; Jonas and MeerKAT Team, 2016).

3.4 Summary

This chapter has presented the basics of the diagnostic tools used for spectropolarimetric analysis and how radio data is observed and stored. We have also introduced radio interferometers, and their operational metrics with emphasis on the MeerKAT telescope. The next chapter introduces the MeerKAT L-band data used for this work and our data reduction steps leading to the new spectropolarimetric images of Pictor A.

22 More about the SKA phase are at https://www.skao.int/en/science-users/118/ska-telescope-specifications

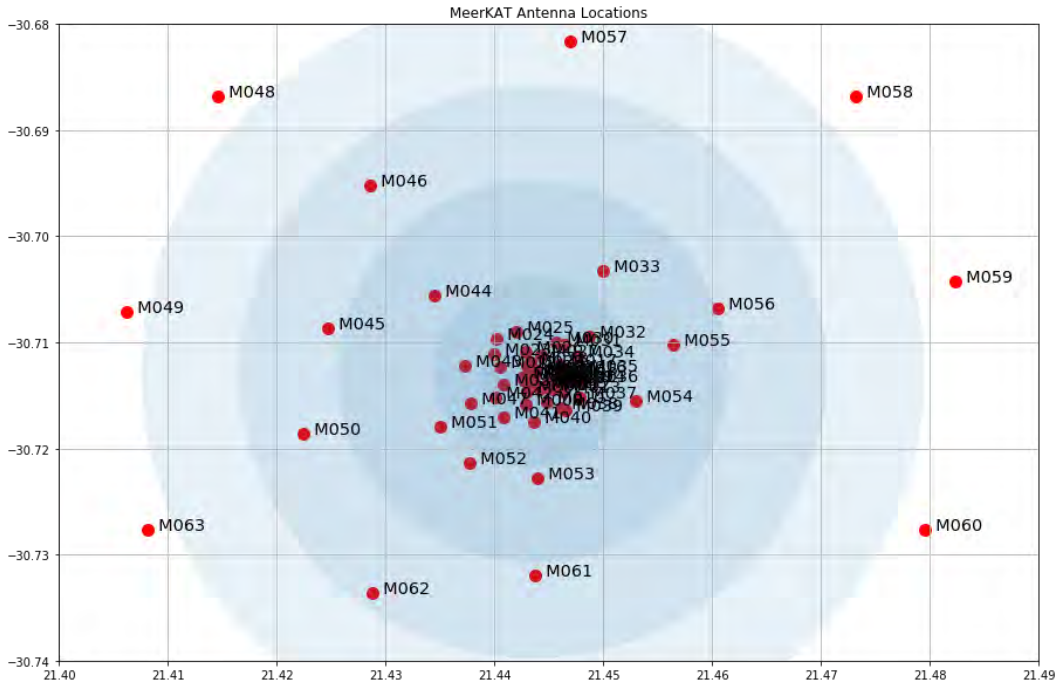

Figure 3.7: A layout diagram of the MeerKAT antenna dishes showing the dense core and sparsely spaced outer antennas. The blue rings are approximately 1, 2, 4, and 6 km in diameter. An outer ring covering all antennas would be at ∼8 km long in diameter. Image source: The MeerKAT helpdesk.

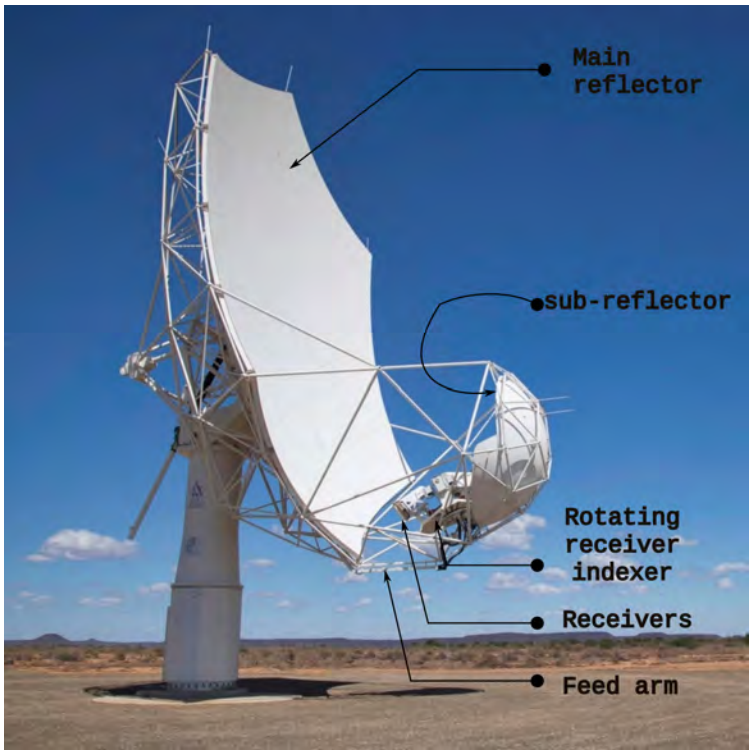

Figure 3.8: Parts of a MeerKAT dish. Image adapted from SARAO.

Part II

BODY OF WORK

Usipojichocha, nani atakuchocha?

4

DATA, CALIBRATION AND IMAGING

Pictor A's extended emission and the spectral variation in its components – i.e. the bright core, extremely bright multiple hotspots and the extended lobes – make for a challenging and complicated calibration and imaging process. Due to its size, Pictor A could introduce significant complex visibility variations in frequency and time (Wilson et al., 2011). Furthermore, Hardcastle et al. (2016) mention a significant difference between calibration solutions at the core and the hotspots. They suggested that due to the large errors associated with the brightest hotspot in Pictor A – the western hotspot – improved calibration solutions are obtainable with more modelling and peeling of this hotspot. Following these recommendations, calibration and imaging procedures employed techniques such as multi-scale and multi-frequency deconvolution (Sault and Wieringa, 1994; Rau and Cornwell, 2011), and tested some form of peeling (Noordam, 2004) through using differential gains (Smirnov, 2011a).

In this chapter, we provide a summary of our observations and an introduction to the calibration concept. This is followed by a description of the calibration procedures that we followed for our data. Finally, we will present our derived Stokes *I* images, and steps taken to create our spectro-plarimetric cubes.

4.1 Calibration 101

Incoming signals from astronomical sources encounter various unwanted environmental and instrumental effects before being recorded as visibilities. Inevitably, the corruptions become embedded into this data, leading to a somewhat altered form of the visibilities known as the *observed visibilities*. Thus, calibration involves removing these corruptions from the data to recover a proper representation of the true sky. Corruptions faced by signals are generally grouped into two: *direction independent effects* (DIE), which mostly occur closer to the observational instrumentation including effects introduced by the signal-chain and the troposphere, and *direction dependent effects* (DDE) that mostly occur closer to the target source and vary depending on the direction of the field of view, including ionospheric phase fluctuations and antenna beam errors. Consequently, the calibration process is split similarly (see Noordam and Smirnov, 2010; Smirnov, 2011c, for a description and summary).

The first part involves the observation of a well-known source, the *calibrator*, to characterise the telescope's response during observations. Suitable gain values are derived and then transferred to the target field, a process commonly referred to as *first generation calibration* (1GC).

Next is the iterative estimation of gain solutions derived from improved models of one or more bright sources in a target field, including the target itself, thus capturing local effects. This is the *second generation calibration* (2GC) is intuitively known as *self-calibration* (or selfcal) and was first developed by Cornwell and Wilkinson (1981). Selfcal is based on the premise that corruptive effects are invariant across the target field.

The final and more particular form of calibration is the *third generation calibration* (3GC), which entails estimating for DDEs towards a particular direction. At this stage, corruptive effects caused by the ionosphere are no longer assumed to be constant across an entire field of view.

Deriving and solving for gain parameters requires a mathematical framework that captures most signal propagation effects encountered. This is why the Radio Interferometer Measurement Equation (RIME) exists, developed and formulated by Hamaker et al. (Hamaker et al., 1996; Hamaker, 2000). Here, corruptions and signal transformations are defined as 2×2 matrices, the *Jones matrices* (Jones, 1941), which could often be diagonal, scalar or rotational. Based on these previous works, Smirnov (2011c) provided an intuitive approach towards the practical implementation of calibration by clearly highlighting the transition from a corrupted signal towards one where the corruptions have been mitigated. In the next section, we summarise some calibration concepts relevant to this thesis.

The Radio Interferometer Measurement Equation

If we consider that a single antenna has two feeds that are orthogonal to each other, and each feed is sensitive to different polarisations, x and y, incident from emission vector $\mathbf{e}$ from a single source as illustrated in Fig. 3.6, the feed components could be written as:

$$\mathbf{e} = \begin{pmatrix} e_x \\ e_y \end{pmatrix} \tag{4.1}$$

However, antennas record voltages; hence, signal e undergoes transformation to a voltage and becomes:

$$v = \mathbf{J} \begin{pmatrix} e_x \\ e_y \end{pmatrix},$$

where $\mathbf{J}$ is the Jones matrix representing this voltage transformation. Since each baseline consists of two antennas, p and q, the voltage in these respective antennas is denoted by:

$$v_p = \mathbf{J}_p \begin{pmatrix} e_x \\ e_y \end{pmatrix} = \begin{pmatrix} v_{px} \\ v_{py} \end{pmatrix} \text{ and,}$$
$$v_q = \mathbf{J}_q \begin{pmatrix} e_x \\ e_y \end{pmatrix} = \begin{pmatrix} v_{qx} \\ v_{qy} \end{pmatrix},$$

which, as previously mentioned in Sec. 3.3, are combined in the correlator, generating four pairwise correlations:

$$\left\langle v_{px} v_{qx}^* \right\rangle, \left\langle v_{px} v_{qy}^* \right\rangle, \left\langle v_{qx} v_{qx}^* \right\rangle, \left\langle v_{qx} v_{qy}^* \right\rangle.$$

$(\langle\rangle)$ represents time or frequency averaging over a short time, and $(*)$ represents a complex conjugate, which is taken because a reversed baseline is the complex conjugate of the original. These are conveniently written as:

$$V_{pq} = 2 \left\langle \begin{pmatrix} v_{px} \\ v_{py} \end{pmatrix} \begin{pmatrix} v_{qx}^* & v_{qy}^* \end{pmatrix} \right\rangle = 2 \left\langle v_p v_q^H \right\rangle,$$

with superscript H denoting a Hermitian transpose. Using Jones matrices, we can group the terms in the above equation and represent effects along the signal path as:

$$V_{pq} = 2 \left\langle \mathbf{J}_p \mathbf{e} \left(J_q \mathbf{e} \right)^H \right\rangle = 2 \left\langle \mathbf{J}_p \left(\mathbf{e}\mathbf{e}^H \right) \mathbf{J}_q^H \right\rangle \tag{4.2}$$

If we substitute Eqn. 4.1 into Eqn. 4.2 and expand it assuming that the $\mathbf{J}$ matrices are constant over the averaging period, we obtain:

$$V_{pq} = 2\mathbf{J}_p \begin{pmatrix} \langle e_x e_x^* \rangle & \langle e_x e_y^* \rangle \\ \langle e_y e_x^* \rangle & \langle e_y e_y^* \rangle \end{pmatrix} \mathbf{J}_q^H, \tag{4.3}$$

which were shown by Hamaker et al. (1996) to be explicitly related to the Stokes parameters and a brightness matrix $\mathcal{B}$ – the intrinsic source brightness – in the following way:

$$\mathcal{B} = 2\begin{pmatrix} \langle e_x e_x^* \rangle & \langle e_x e_y^* \rangle \\ \langle e_y e_x^* \rangle & \langle e_y e_y^* \rangle \end{pmatrix} = \begin{pmatrix} I+Q & U+iV \\ U-iV & I-Q \end{pmatrix}. \tag{4.4}$$

Therefore, Eqn. 4.3 collapses into the first form of the RIME:

$$V_{pq} = \mathbf{J}_p \, \mathcal{B} \, \mathbf{J}_q^H,$$

where $\mathbf{J}$ is composed of multiple effects on the signal propagation path represented as a single 2×2 matrix. The RIME formalism assumes linearity, so any effects occurring along a signal path must be denoted using Jones matrices in the exact order in which they occur physically, i.e. effects closer to the source are placed closer to $\mathcal{B}$. In contrast, those close to the observer – i.e. the telescope – are placed further. The basic matrix rules of non-commutative multiplication apply, except for scalar matrices. For example, an effect inherent to all interferometers is that of phase delays caused by the geometric path length difference of a signal arriving at two antennas forming a baseline, depending on the antennas' pointing direction. That is, if a source is at the phase centre, signals arriving will have zero phase difference. On the other hand if a source is offset from the phase centre, there will be a signal delay that varies with the direction of that source (making this a DDE). This effect has been shown to give a Fourier transform kernel and can be represented using the $\mathcal{K}$-Jones matrix (see Smirnov, 2011c, for its derivation where it is called the **K**-jones matrix).[1] Therefore, the most basic RIME that includes this geometric delay could be written as:

$$V_{pq} = \mathcal{K}_p \, \mathcal{B} \, \mathcal{K}_q^H = X_{pq},$$

which Smirnov (2011c) refers to as the source coherency of a single source, X_{pq}. Thus, in the realistic scheme of things where DIEs and DDEs are involved, a typical RIME would be of the form:

$$V_{pq} = G_p E_p \, \mathcal{B} \, E_q^H G_q^H,$$

whereby G represents the DIEs and E represents all the DDEs. These can be broken down into Jones matrices representing individual effects. Many effects can be described using Jones matrices of three types: diagonal, scalar and rotational (Noordam and Smirnov, 2010). Some common examples of DIEs are:

1. **G-Jones** is the complex gain corresponding to instrumental electronic receivers. It varies rapidly in time but has little to no variation in frequency. It is represented by a diagonal matrix, meaning that the different components are affected independently.
2. **B-Jones**: the electronic bandpass response with a little to no time variation but considerable frequency structure. This is also a diagonal matrix.
3. **D-Jones**: This is the on-axis polarisation leakage for associated antenna fields. This matrix has non-zero off-diagonals and unity diagonals. However, since it varies at a rate similar to B-Jones, they are sometimes combined to form a full matrix.

Example DDEs are:

1. $\mathcal{K}$**-Jones**: A scalar matrix catering to the time-dependent phase term introduced by geometric delay.
2. **Z-Jones**: Scalar ionospheric amplitude and phase induced errors.
3. **F-Jones**: Rotation matrix for the ionospheric Faraday rotation.
4. **P-Jones**: Parallactic angle correction due to the feeds' position angle projection.

1 We use $\mathcal{K}$-Jones to disambiguate this from the delay offsets solved for in 1GC, which are also called **K**-Jones in the `CASA` software, and correspond to delays introduced by extra cable lengths, the atmosphere etc.

If we assume as an example that our signal encounters all the effects mentioned earlier, a typical RIME including all these common effects daisy-chained together to form a *Jones chain* would be:

$$V_{pq} = \mathbf{G}_p\mathbf{B}_p\mathbf{D}_p\mathbf{P}_p\mathbf{F}_p\mathbf{Z}_p \; X_{pq} \; \mathbf{Z}_q^H\mathbf{F}_q^H\mathbf{P}_q^H\mathbf{D}_q^H\mathbf{B}_q^H\mathbf{G}_q^H.$$

Since each signal path could differ between two antennas on a baseline, effects along p may not be the same as those towards q. The values of these Jones terms are solved for, and are called *gain solutions*. Essentially, the RIME predicts visibilities as seen by a particular telescope, given a model of the sky and effects corrupting a signal. It is the foundation for modern calibration.

4.2 Observation Details

Using the MeerKAT telescope, observations of Pictor A were performed between the 18th and 19th of December 2019, with 62 out of the 64 MeerKAT antennas. These were in the L-band spanning between 0.8 - 1.7 GHz, resulting in a bandwidth of 856 MHz, with 4096 frequency channels, and in full-polarimetric mode.[2] The source was observed for a total duration of ∼9 hours in scans of ∼15 minutes, and an integration time of 8 seconds. The resulting measurement set was ∼3.5 terabytes (TB) in size. A summary of the observations is shown in Tab. 4.1

Table 4.1: Observational setup information for Pictor A.

Observation Details for Pictor A	
Principal Investigator	Lerato Sebokolodi
Dates (UTC)	from: 18-Dec-2019 16:46
	to: 19-Dec-2019 03:48
Antennas	62
Band	L
Frequencies	856 MHz – 1.7 GHz
Bandwidth	856 MHz
Channels	4096
Time on target	∼9 Hrs
Scan duration	∼15 min
Integration time	8 sec
Bandpass calibrator	J0408-6545
Gain calibrator	J0538-4405
Polarisation calibrator	J0521+1638

Antennas with the longest baselines available (i.e. 7700 m for MeerKAT) were included in these observations, hence enabling good achievable resolution. Furthermore, the use of multi-frequency observations (4K mode) and the fact that both the MeerKAT telescope and Pictor A are in the Southern hemisphere resulted in a reasonably good uv-coverage compared to those obtained by Perley et al. (1997). They described it as having a 'bowtie' shape due to the lack of N-S resolution especially in the v-axis, and sparse measurements along the longer baselines in the u-axis (E-W). As a result, Perley et al. (1997) tapered their long baselines and using measurements interior to a circle whose radius equals the maximum N-S spacing at $u = 0$ to achieve a more circularised coverage for imaging of large-scale low brightness regions (the region used is marked by the orange circle in the bottom panel of Fig. 4.1), while using all the data for imaging the compact regions. We compare our obtained our uv-coverage theirs in Fig. 4.1.

2 I.e. all the correlation products: XX, YY, XY and YX were made available.

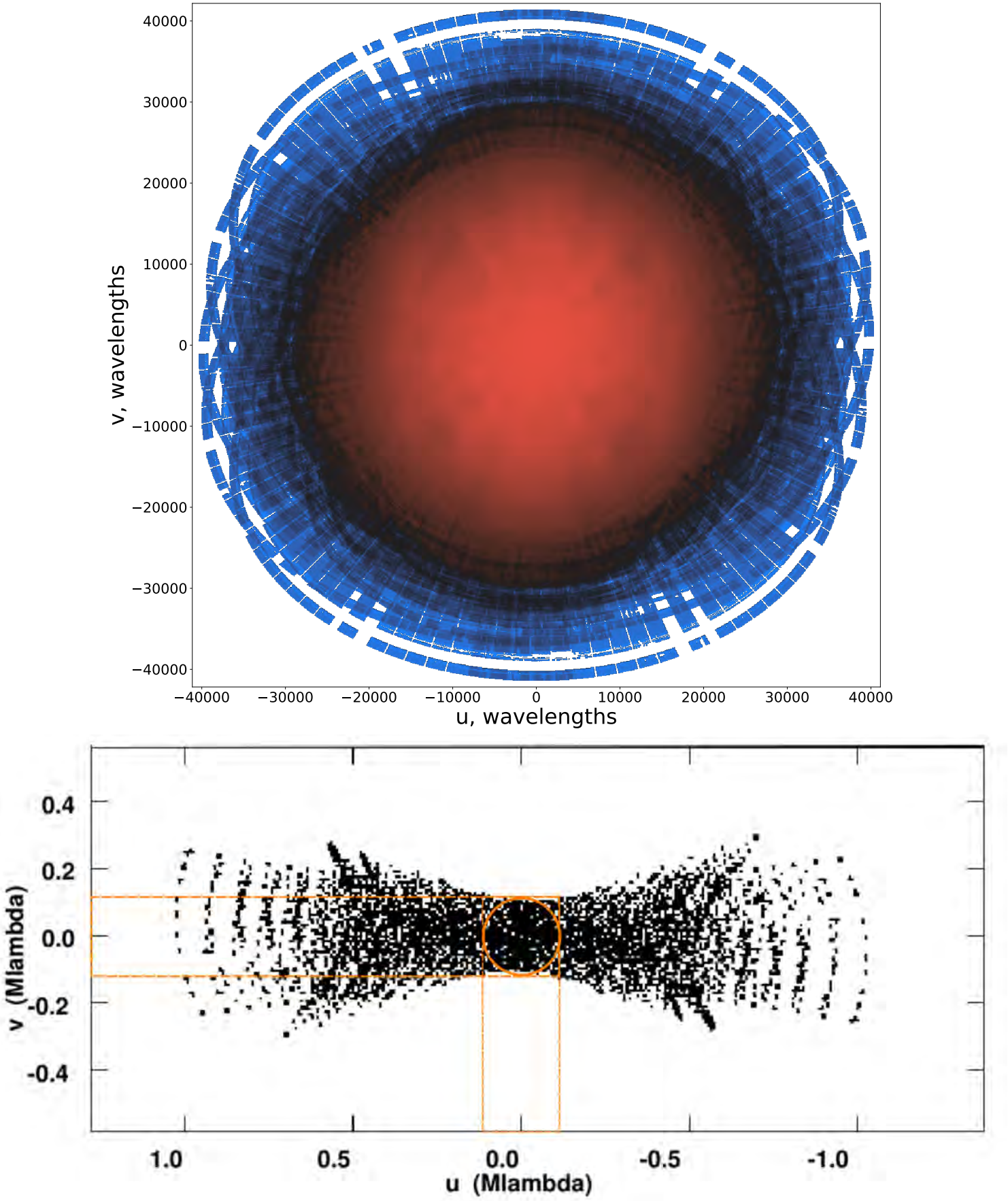

Figure 4.1: A comparison of the uv coverage from VLA to that of MeerKAT for Pictor A. The uv-coverage using MeerKAT data in the *top panel* is more "complete" in contrast to that from the VLA in the *bottom panel* taken in the A-configuration at 8.4 GHz adapted from Fig. 2 of Perley et al. (1997). We also highlight the section of VLA data that Perley et al. (1997) used to image large-scale low-brightness structure using the orange circle, while the dashed lines indicate the circle's range of covered wavelengths in the x and y axes.

4.3 Data Reduction

In the context of radio astronomy, data reduction refers to transforming "raw" data obtained from the observatory as visibilities into the ultimate end product for astronomers: the astronomical image. Several disparate steps are chained together and undertaken sequentially to achieve this, including cleaning the data by removing unwanted or irrecoverably bad data, calibrating for errors and finally imaging the best data derived from these steps. Accordingly, ***data pipelines*** exist to automate these processes. One such pipeline is the Containerized Automated Radio Astronomy Calibration (`CARACal`)[3] Józsa et al. (2020), which was our pipeline of choice. In its early stages of development, it was primarily centred around MeerKAT data, but, it is currently used with data from other telescopes.

We start with the definition of some terms used within this section. Given an initial raw MS, `CARACal` first creates a new MS containing solely the calibrators' data; we call this the ***calibrator MS***. It then works on this new MS, using it to obtain suitable solutions for 1GC through the ***crosscal step***. These solutions are then transferred to the ***target*** field, the field of interest, which in our case is Pictor A. However, to achieve this, `CARACal` creates another new MS containing only the target's data and applies the obtained solutions to that data. This way, the original MS is not tampered with, thus safeguarding it from any corruption resulting from these processes. The only downside is that, in total, three datasets will result: the original, calibrator and target MSs. This means that a large storage space will be in use if the data is extensive – a small price to pay for prized observational data, nevertheless.

We can think of the MS as a collection of tables that store data in rows and columns. Generally, two kinds of tables exist within a MS; those containing auxiliary data about the observation, such as the names of the fields observed, names of antennas used in the observations and their positions, frequency bands and channels used and where they are centred, among other things, and the main table which contains the actual visibility data. An example of this is illustrated in Fig. 4.2.

There are multiple columns in the main table, such as UVW, FIELD_ID, and DATA. Each row in the main table contains data for a single baseline taken at a specific time. Bearing this in mind, the number of rows, N_{rows}, in each data set is then dependent on the total observation time T_{obs}, the integration time t and the number of baselines N_{bl} and could be given by:

$$N_{\text{rows}} = \frac{T_{\text{obs}}}{t} \times N_{\text{bl}}$$

While a cell typically holds a single value, some cells within specific columns – such as the DATA and FLAG columns, which contain the visibility data and their associated flags – contain 2-dimensional arrays whereby the dimensions represent the number of channels and correlations. For example, in our observations, Pictor A was observed in full polarisation mode (meaning four correlations, N_{corrs}, are present) using 4096 frequency channels (N_{chans}). Thus, a single cell in the DATA column of our MS would contain an array of shape 4096 x 4. Inspecting this column would then result in a three-dimensional array with the shape: $N_{\text{rows}} \times N_{\text{chans}} \times N_{\text{corrs}}$. We can then estimate that the total number of visibility points in our MS is given by:

$$\frac{T_{\text{obs}}}{t} \times N_{\text{bl}} \times N_{\text{chans}} \times N_{\text{corrs}}$$

To put into context the size of our DATA column in the raw MS, consider that each visibility is complex and is digitally stored in a storage space of 8 bytes (64 bits).[4] The total number of unique baselines available to us because of using only 62/64 antennas was 1891, and our total observation time was ∼11 hours with an integration time of 8 seconds (see Tab. 4.1 for the observational details). This results in ∼153.36 billion visibilities totalling a size of ∼1.143 TB, consisting of all the

3 https://caracal.readthedocs.io/
4 8 bits form 1 byte.

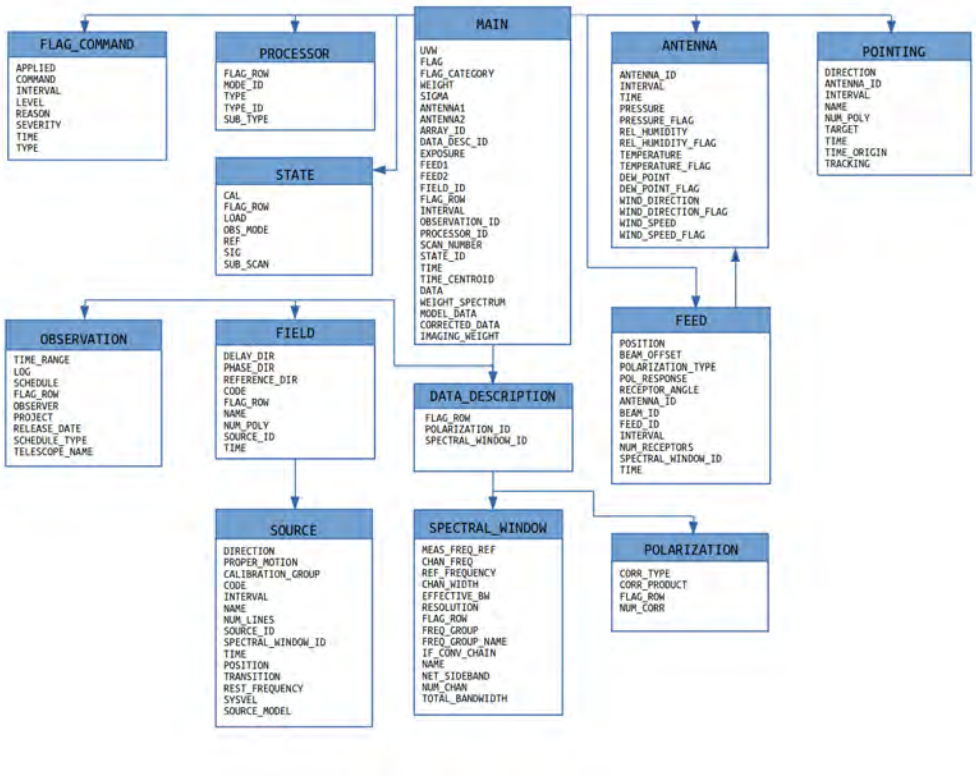

Figure 4.2: A schematic of the typical structure of an MS. The main table contains the actual visibilities, while the rest contain meta-information about a specific observation.

calibrators' and target's data. Since `CARACal` does not operate on the original raw MS, the collated size of all the associated MSs increases by more than twice.

`CARACal` takes its instructions from text files known as *recipes*, which highlight the steps to be performed, making it a straightforward tool to use. Aside from astronomical images, this pipeline generates various diagnostic data and plots that are valuable for data quality inspection. In this section, the diagnostic plots shown are sourced from the outputs of `CARACal`, which automatically performed most of the steps highlighted here. The exact recipe used for this data reduction is shown in App. B.1.

4.3.1 *Flagging*

Flagging is the excision of excessively corrupted data and is often the first step to data reduction. This mainly consists of data affected by radio frequency interference (RFI) caused by wireless telecommunication equipment such as the Global Positioning Systems (GPS), air traffic communication systems, television and radio transmissions, solar emission, among others. Because astronomical emission is extremely weak compared to RFI, spurious spikes within the amplitude of visibility data result. While RFI is the most dominant effect, it is not the only cause of bad data. Faulty and unstable antennas or components in the observation equipment could result in the same.

Unfortunately, large regions of the MeerKAT L-band are affected by RFI as highlighted in Fig. 4.3. Apriori knowledge of these frequencies allows the creation of static masks, which can be applied by default to any data observation at this band. Moreover, the period with the least RFI effect is between 2300 – 0600 SAST as shown in Fig. 4.4, which is why night time observations of Pictor A were preferred; to mitigate this effect and to reduce solar interference.

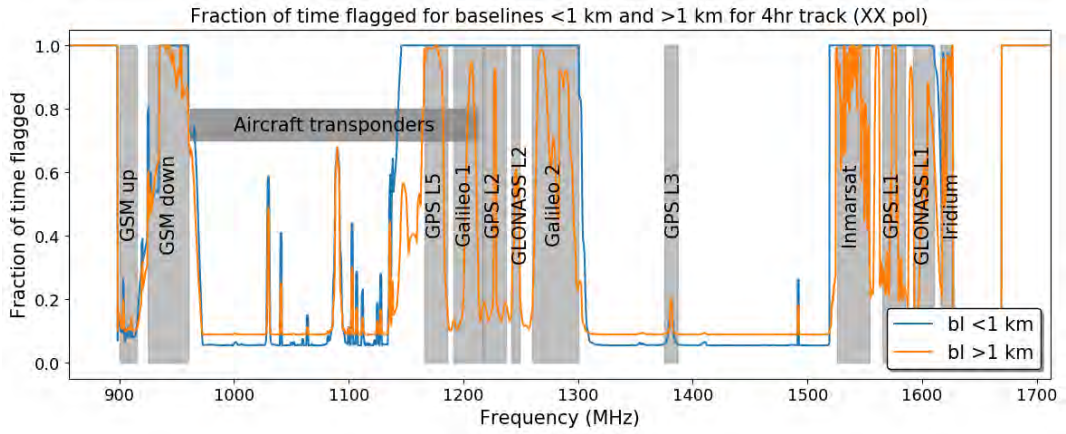

Figure 4.3: RFI from various sources that affect the MeerKAT L-band. This is the RFI frequency occupancy for an example 30 hour continuous observation for a single polarisation (XX). Image sourced from SARAO External service desk.

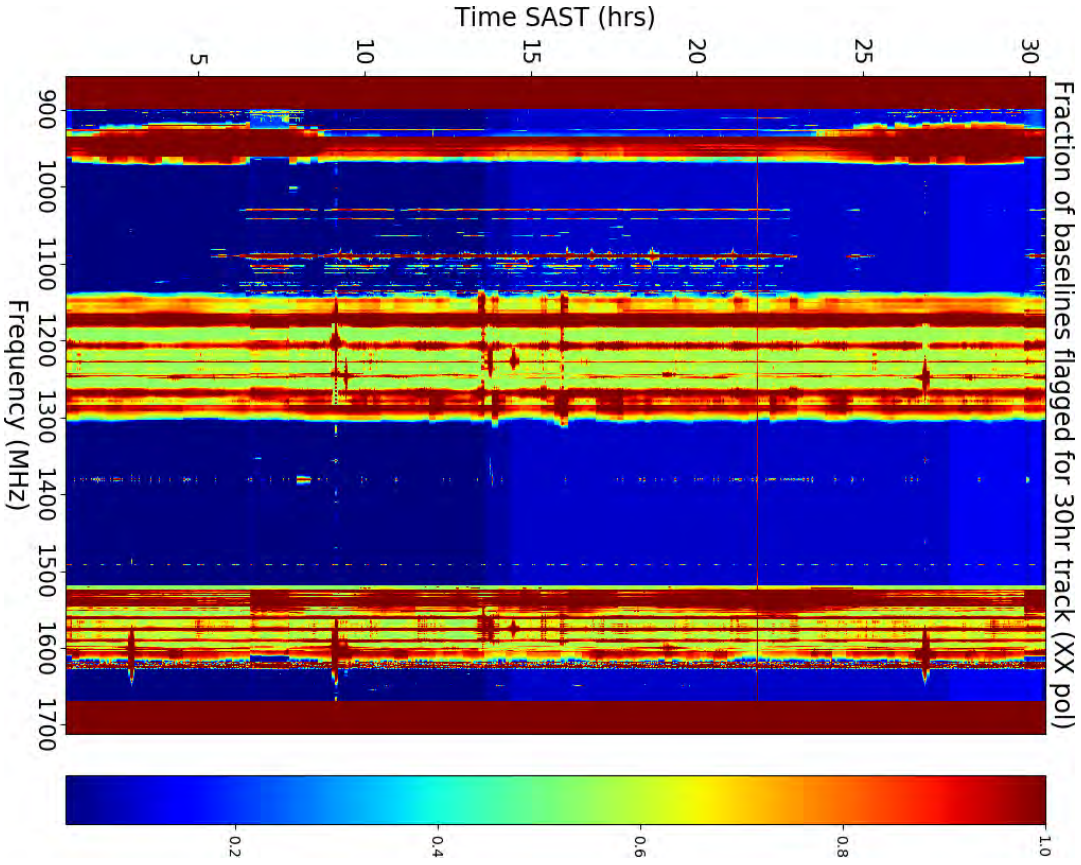

Figure 4.4: Typical fraction of flagged data as a function of time and frequency for a MeerKAT L-band observation. Image sourced from SARAO external service desk.

Since equipment issues are bound to occur during an observation, they are monitored and noted. Hence, the observatory provides initial flags – known as Control and monitoring (CAM) flags for MeerKAT – to ensure that those issues are excluded. As a preliminary step within our pipeline, we applied CAM flags and MeerKAT's static RFI masks to baselines shorter than 1000m. Frequencies between ranges 856 – 880, 1658 – 1800 and 1419.8 – 1421.3 MHz, which are close to the RFI affected regions (see Fig. 4.3) were also flagged out, after visual inspection of the visibilities. The exclusion of band edges is necessary as they are the transitional areas to the passband of the

telescope (roll-offs). Furthermore, autocorrelations (i.e. the signal from an antenna correlated with itself) were deemed useless and excluded.

The next flagging step entailed removing any remaining RFI from the calibrator data that the previous step may have left, using the `TriColour` flagging software in `CARACal`.[5] Fig. 4.5 illustrates this by showing the percentage of the calibrators' data flagged within each correlated signal at each step. We show the percentage of flagged data after the first flagging step (CAM flags applied) in blue, while orange shows the data after the second flagging step removing RFI. The data at its state at that point was ready for the initial 1GC calibration stage.

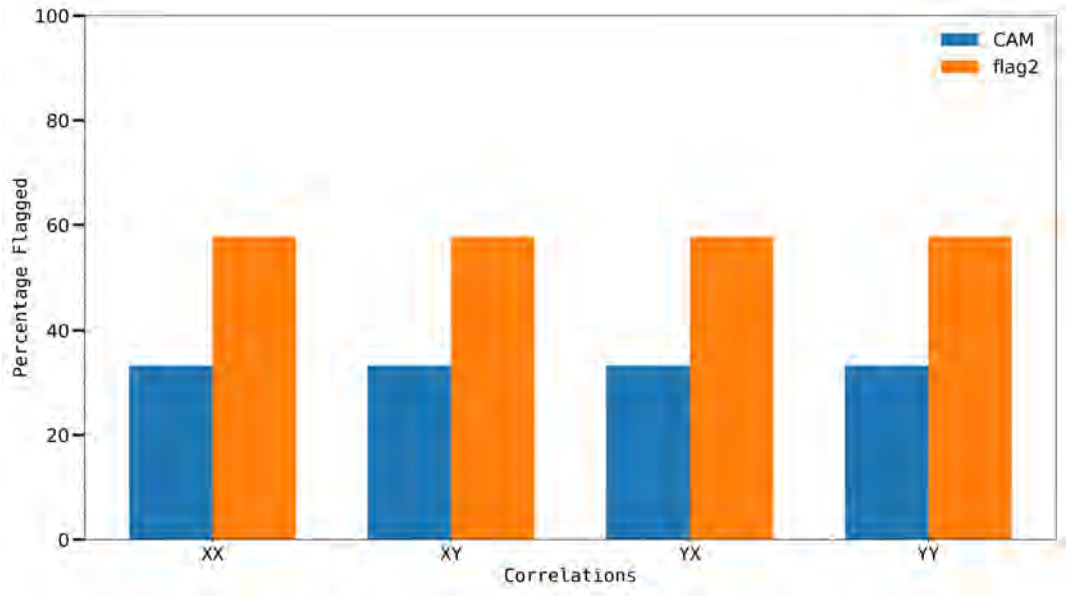

Figure 4.5: The percentage of flagged data after application of CAM flags and the MeerKAT static RFI mask, and flagging out autocorrelations. On the other hand, ∼24% more data were flagged while removing any additional remaining RFI in the correlator data.

4.3.2 *First Generation Calibration*

According to Fomalont and Perley (1999), the crux of 1GC is the derivation of relative phases with respect to a reference position. Time variable phase changes – which imitate the effect of unstable electronics – are monitored using calibrator sources to ensure the stability of the observing systems. Specific rules apply to choosing a good calibrator source; it must be compact and non-variable over short timescales, with a simple and known spectrum. Furthermore, its position should be accurately measured, and the source should be isolated from other strong sources to avoid confusion.

For these MeerKAT observations, J0408-6545 and J0538-4405 were chosen as the bandpass and gain calibrators, respectively. We chose antenna M005 as the reference antenna (hence reference position) as it was the antenna closest to the centre for the MeerKAT array with the least amount of flags. The 1GC recipe used is in App. B.1.

4.3.2.1 *Delay Calibration*

This measures small residual errors after incorporating geometric delay due to differences in the signal propagation times through various electronic components and varying atmospheric conditions. Because it is frequency dependent, the phase difference, $\Delta\Theta$, at the opposite ends of the band is given as:

$$\Delta\Theta = 2\pi\Delta\nu(\Delta\tau_g - \Delta\tau_r),$$

5 https://github.com/ratt-ru/tricolour

Δv is bandwidth, $\Delta\tau_g$ is the differential τ_g, and $\Delta\tau_r$ is the instrumental delay that remains after adding the geometric delay. This effect appears as a phase gradient across frequency. Delay calibration means removing this gradient. If not carefully done, signals will decorrelate. As mentioned in Sec. 4.1, it is represented by a diagonal scalar matrix written as:

$$K = \begin{pmatrix} e^{i\Theta} & 0 \\ 0 & e^{i\Theta} \end{pmatrix}.$$

During data reduction, delay calibration is often performed first to prevent signal decorrelation brought about by phase differences; delays exceeding tens of nanoseconds indicate problems. In Fig. 4.6, we show solutions from our delay calibration done using the bandpass calibrator source because of its stable behaviour in frequency. These solutions show delay as a function of time, and the spacing between them results from the observation cadence of this calibrator. Within the specific times, the solutions appear spread out because the selected solution interval in time resulted in multiple time bins.

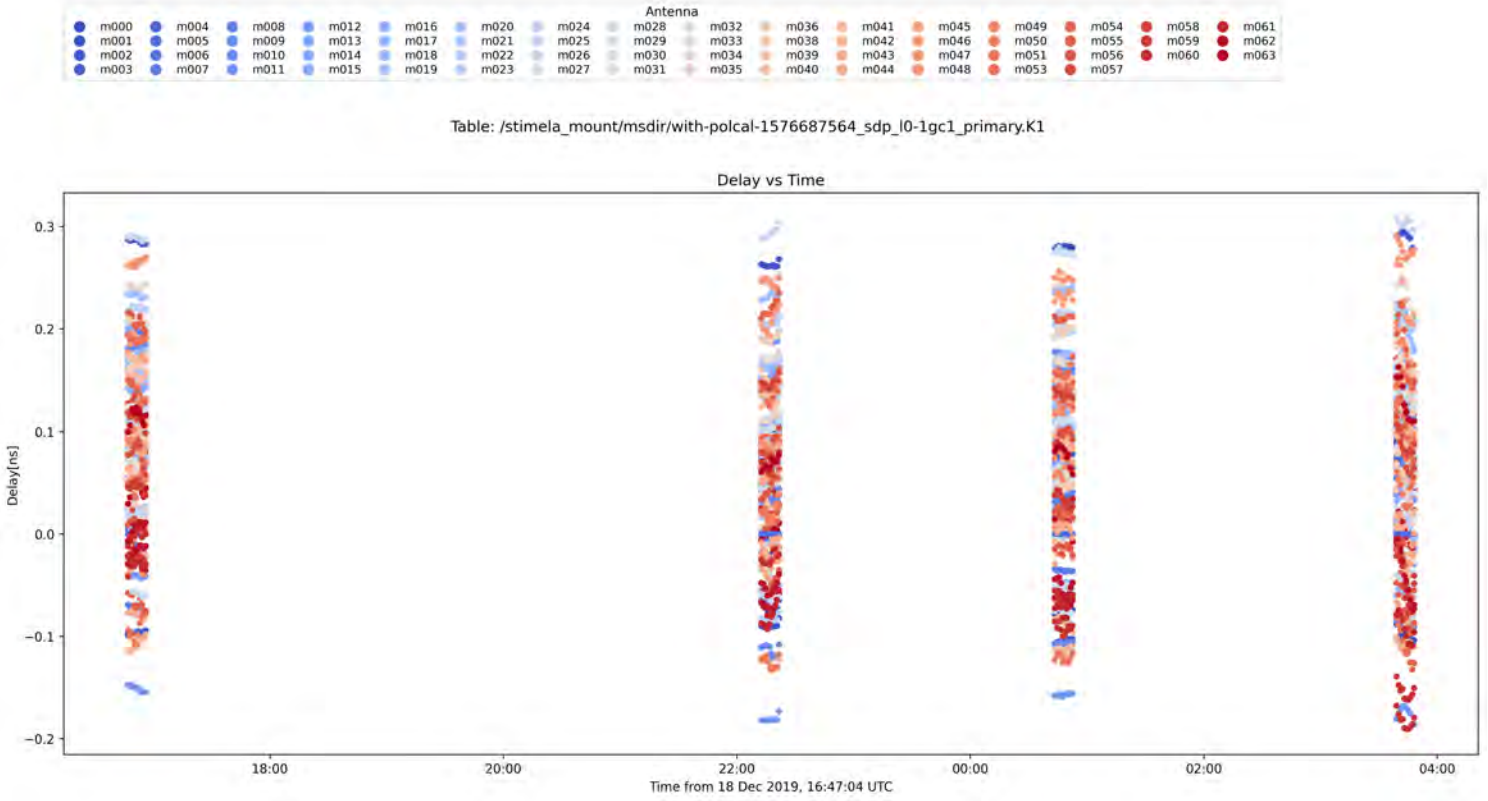

Figure 4.6: K-Jones solutions from our data plotted as delays per antenna against time.

4.3.2.2 *Complex Gain Calibration*

Gain calibration aims to remove rapid time variable gain fluctuations induced by atmospheric and instrumental effects. Normally, gain solutions are obtained from a calibrator source close to the target source to track atmospheric effects local to the target. Since the signal phase is more affected in most cases, it is usually solved first. Complex gain is given as a diagonal matrix:

$$G = \begin{pmatrix} g_p(t) & 0 \\ 0 & g_q(t) \end{pmatrix}.$$

We show some of our solutions in Fig. 4.7.

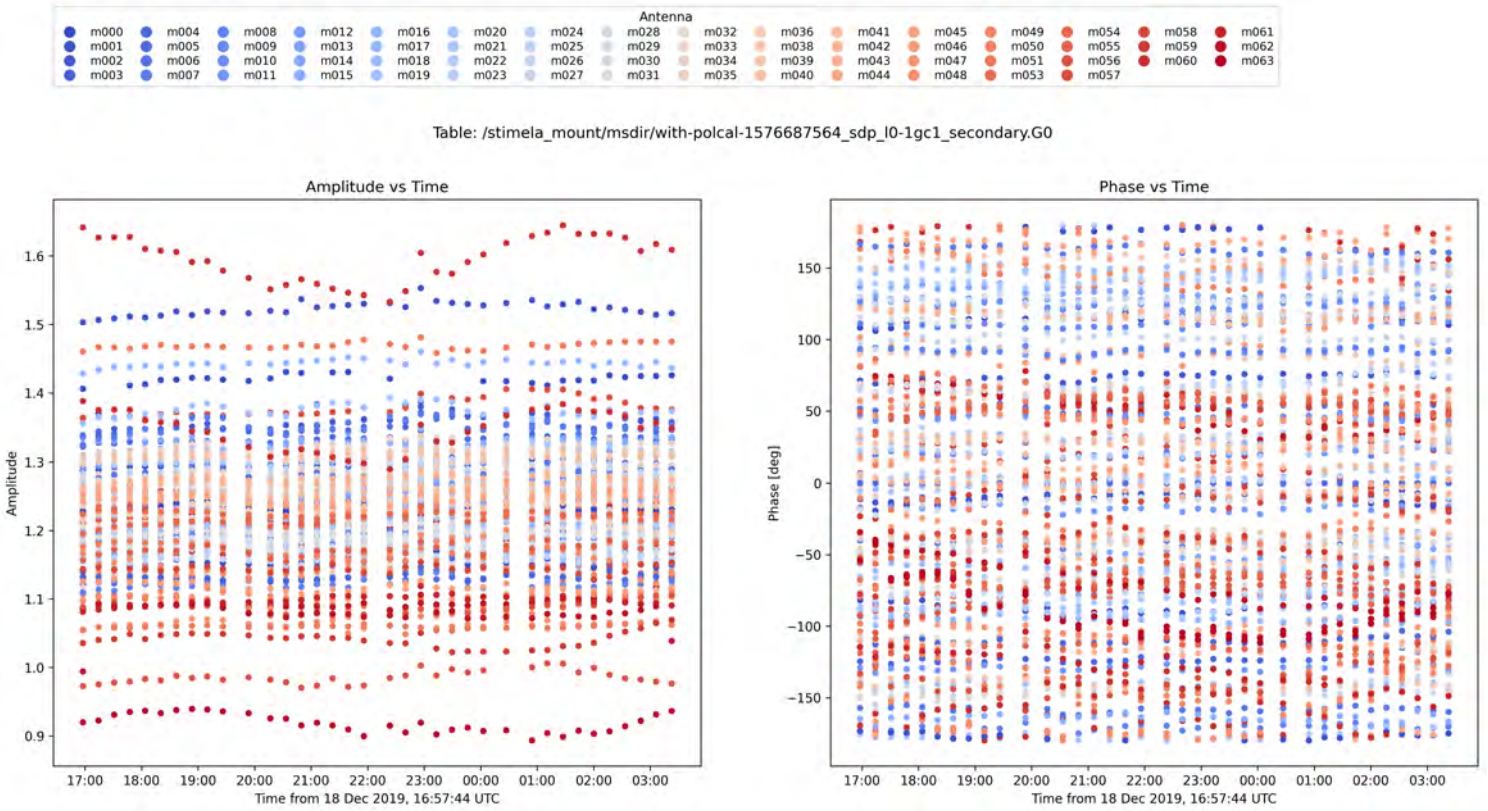

Figure 4.7: Complex gain solutions plotted as amplitude and phase against time on the left and right panels, respectively.

4.3.2.3 *Bandpass Calibration*

Because antenna gains change as a function of frequency, bandpass calibration requires observation of a bright calibrator source with a known spectrum in frequency. This step removes variations across frequency caused by instabilities in the telescope's electronics. It is written as:

$$B = \begin{pmatrix} b_p(v) & 0 \\ 0 & b_q(v) \end{pmatrix}.$$

Some of our per antenna bandpass calibration solutions are shown in Fig. 4.8. The amplitudes are seen to vary smoothly across frequency with no significant outliers. Phases are largely centred around zero, with the visible scatter caused by noise in the data. Since the solutions are generally grouped, we interpreted them as good quality.

4.3.2.4 *Polarisation Calibration*

Antennas contain two orthogonal feeds sensitive to different components of a wave's polarisation. This could be the X and Y (also sometimes labelled as H and V) components in the case of linear polarisation, and L and R for circular polarisation. Ideally, each feed should be isolated from the other and only measure a single type of polarisation. In reality, this is not always the case, as the feeds may not be perfectly orthogonal, so signals from one feed may seep into the other. This is called *leakage* and is written as:

$$D = \begin{pmatrix} 1 & D_{px} \\ -D_{py} & 1 \end{pmatrix}.$$

Notice that this is for a single antenna p for the x and y feeds. Furthermore, there may be a delay in the signal between the two antenna feeds, which causes some system-induced circular polarisation termed the *crosshand delay*. Another issue may arise because the phase in one feed is calibrated

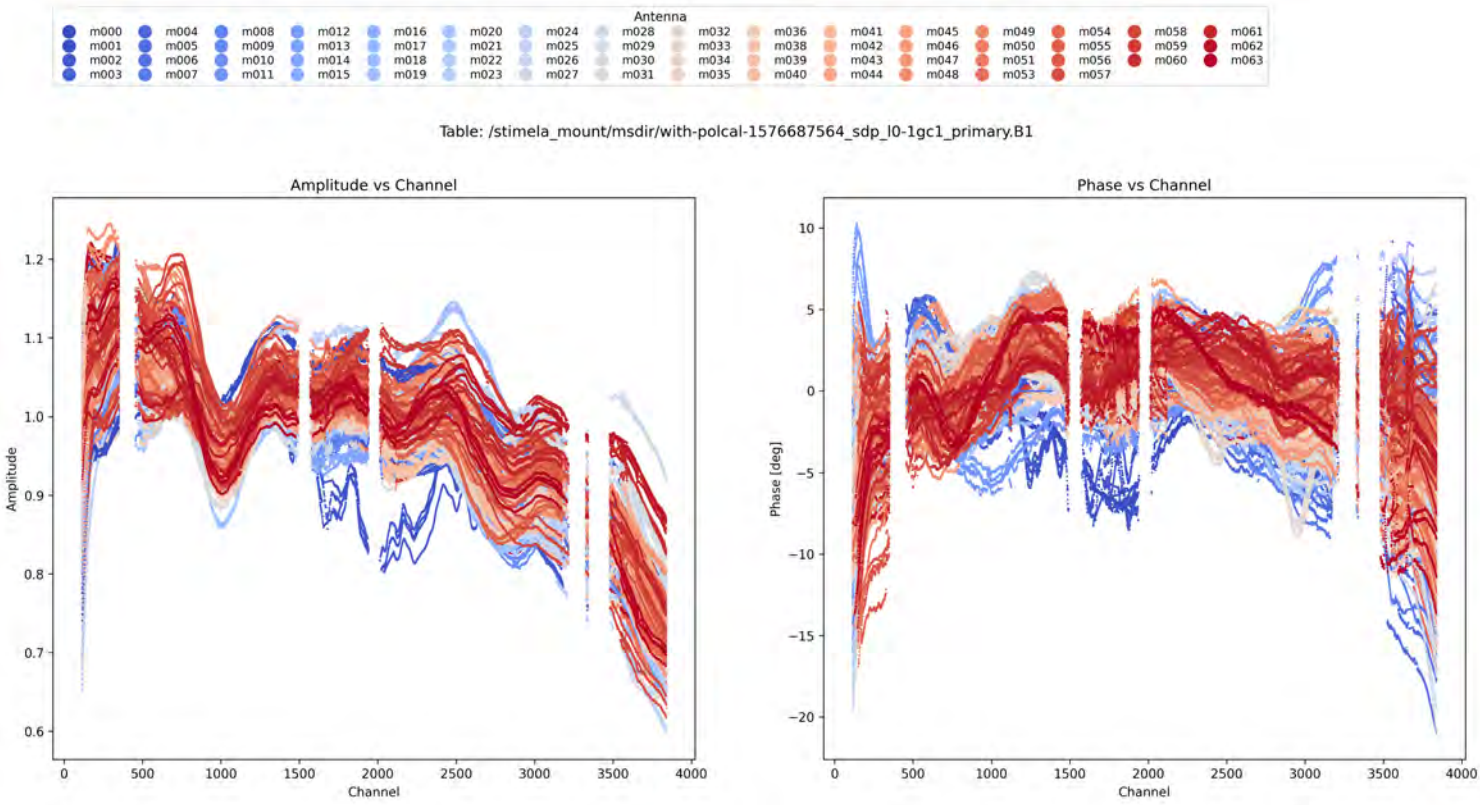

Figure 4.8: Bandpass solutions from this data are shown as amplitude, and phases plotted against frequency on the left and right panels, respectively.

with respect to the phase of the corresponding feed in the reference antenna. Realistically, some phase difference (the *crosshand phase*) remains, and must also be removed.

There are two goals to polarisation calibration: to correct for the leakages and the absolute polarisation angle by removing the mentioned effects. The former is achievable by observing a strong unpolarised calibrator source – such as the bandpass calibrator – and the latter by observing a source whose polarisation characteristics are well known. J0521+1638 (also known as 3C 138) was chosen as the position angle calibrator because it shows ∼7% degree of polarisation at 1.4 GHz, and it has a known polarisation angle of ∼-8°.[6]

We flagged all data from antenna M003 and scan 22 before cross-calibration since their data exhibited erratic behaviour during our calibration solution inspections. After ensuring that the obtained solutions were of good quality, we applied them to the calibrator data, i.e. the DATA column of the calibrated MS. This creates a new column: CORRECTED_DATA, which stores the 1GC corrected visibilities. Moreover, additional flags were added to the data, incorporating all the flags transferred from the calibration solutions. As a result, ∼5% more data was flagged after cross calibration as highlighted in Fig. 4.9.

6 According to https://skaafrica.atlassian.net/wiki/spaces/ESDKB/pages/1465548801/Polarisation+calibrators

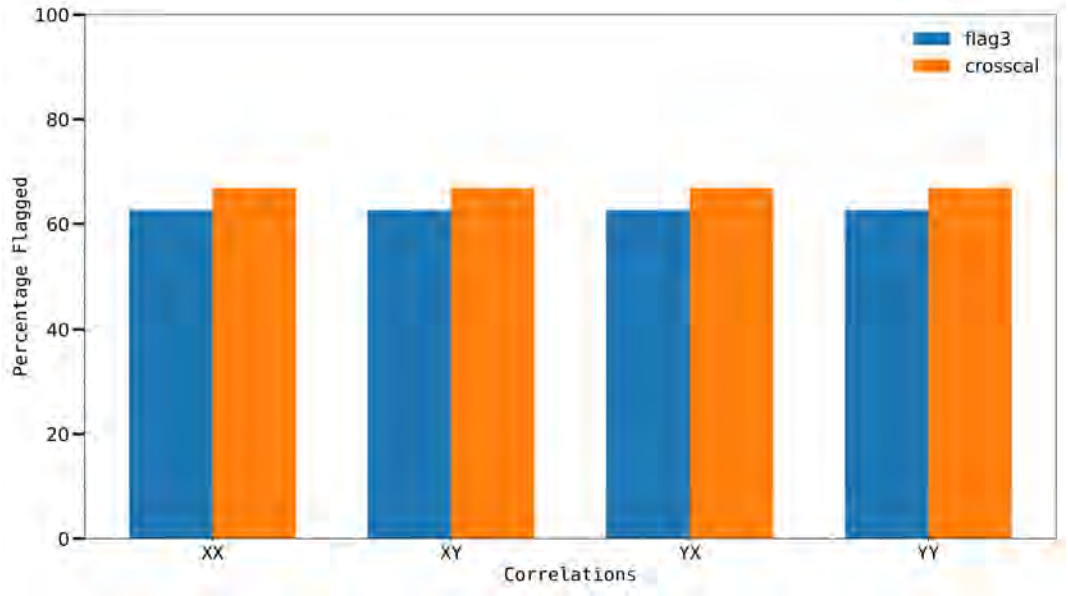

Figure 4.9: The amount of calibrator data flagged after excluding data from scan 22 and antenna M003 from our observations compared to flags after the application of cross-calibration solutions. ∼5% more flags were introduced, leaving ∼ 37% of calibrator data for use.

We then inspected plots of these new visibilities, some shown from Figs. 4.10 – 4.12 to determine if our IGC was successful. We mentioned in sec. 4.3.2.4 that leakage calibration requires using an unpolarised source, which, in our case, was chosen as the bandpass calibrator 0408-65. Therefore, we expect that if leakage calibration was successful, Stokes Q, U, V, which represent polarisation, should have zero phase and amplitude and hence centred at 0. Furthermore, since phase corrections were done, the phase of Stokes I should be centred around zero. This is what the top panel of Fig. 4.10 shows. A similar figure is shown at the bottom for the source used for position angle correction, J0521+1638.

Fig. 4.11 displays visibilities from the XX and XY correlations of the complex gain calibrator J0538-4405. Since this source is unpolarised, we do not expect to see any amplitude in the XY component, and thus, the real and imaginary components should be centred around zero. On the other hand, for the XX correlation, an amplitude is expected but no phase. This means that the real component will be centred at an offset away from zero, while the imaginary component will be centred around zero, as shown in that figure. Fig. 4.12 also shows similar information for the YY and YX correlation.

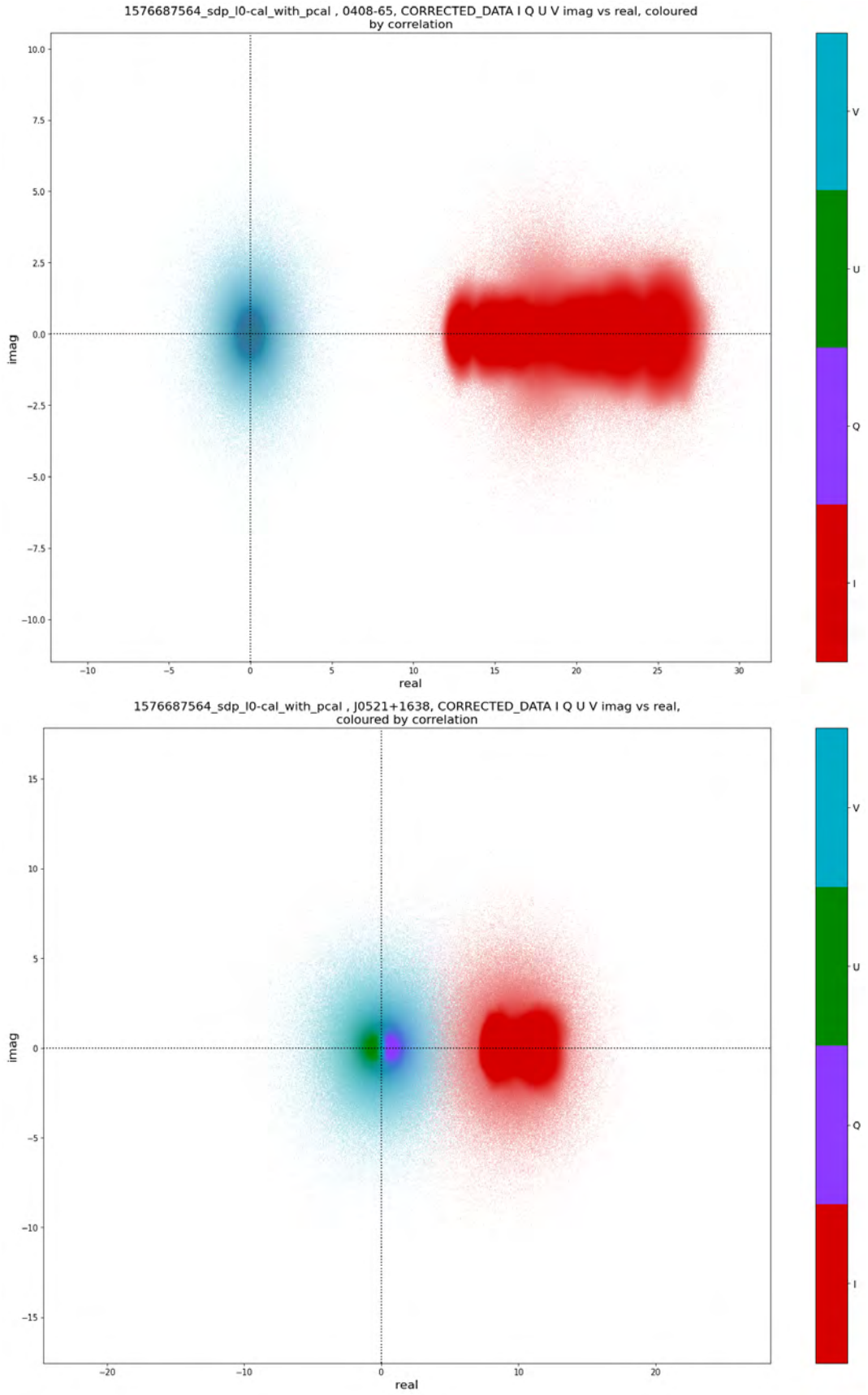

Figure 4.10: *Top panel*: The bandpass calibrator's visibilities after application of lGC solutions. *Bottom panel*: Parallactic angle calibrator after polarisation calibration. Both are plotted as the real vs imaginary components of the visibilities.

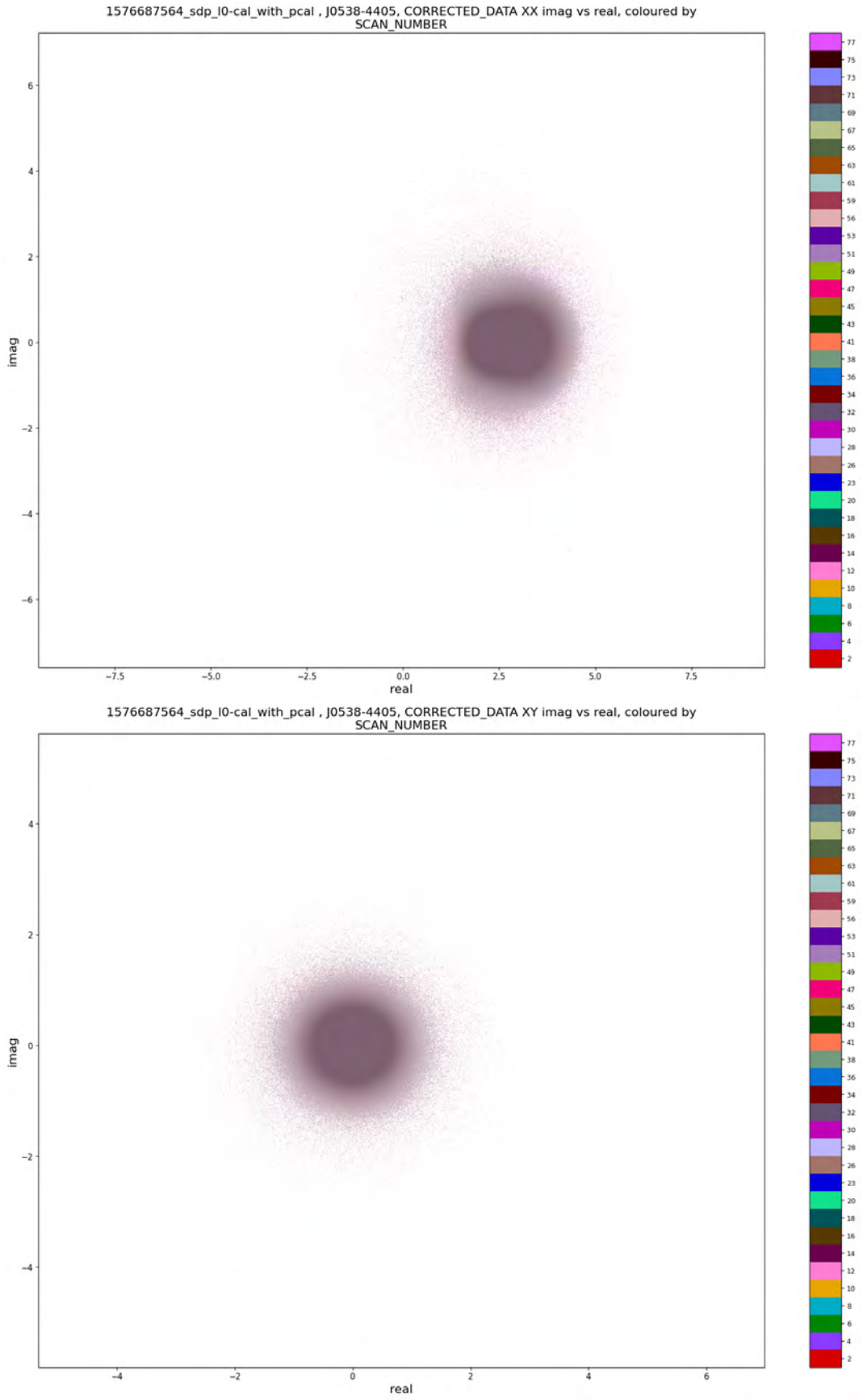

Figure 4.11: XX (*top panel*) and XY (*bottom panel*) correlations of our secondary calibrator after application of 1GC solutions plotted as the imaginary against real components of the visibilities.

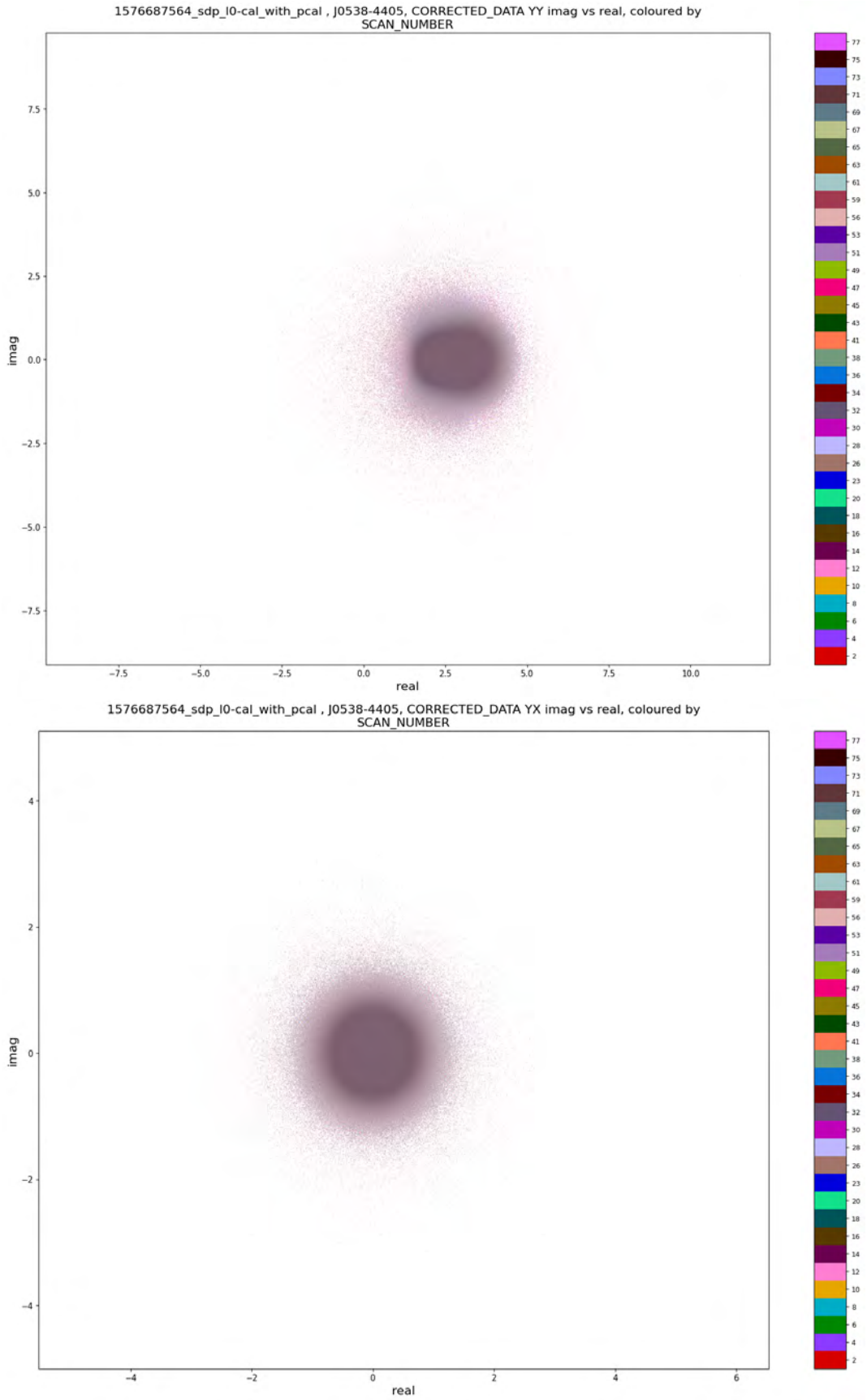

Figure 4.12: The YY (*top panel*) and YX (*bottom panel*) correlations of our secondary calibrator after application of 1GC solutions plotted as the imaginary against real components of the visibilities.

These outcomes convinced us that the derived gain solutions were suitable enough for application to the target data. Therefore, `CARACal` created a new MS containing only Pictor A's data, a subset of data from the full original MS. Note here that flags applied to the calibrator's data during 1GC were also transferred to these data. More RFI flagging was still performed on this data using a mild automated flagging strategy, Gorbachev, in `TriColour`.[7] Fig. 4.13 illustrates the status of flags in the target field. 50% of data remained after all flagging was done.

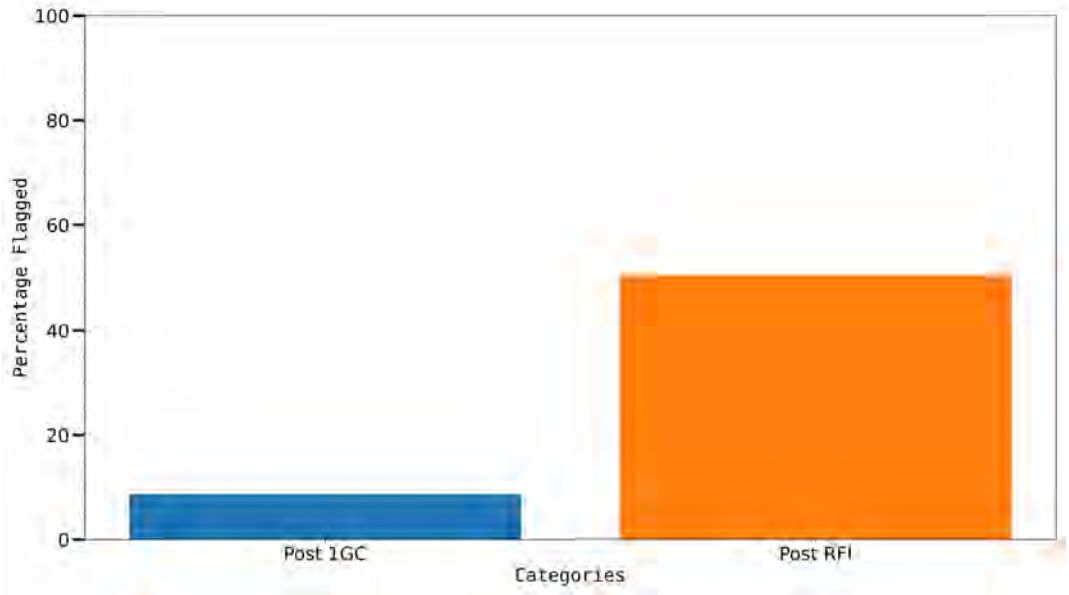

Figure 4.13: The percentage of Pictor A data flagged after 1GC in blue versus the flag status after RFI flagging in orange. ∼42% more data is flagged due to RFI leaving ∼50% data for use.

4.3.3 *Second Generation Calibration*

4.3.3.1 *Imaging*

As the name suggests, imaging entails converting visibilities into astronomical images. These are stored in flexible image transport System (FITS) files (Wells and Greisen, 1979), which are the standard format for storage, as they provide the capability of appending metadata on an observed field (such as the coordinate systems, beam information etc.) in addition to the image data. However, before an astronomical image becomes scientifically useful, the interferometer's response must be removed by deconvolution. We used the `WSClean` software (Offringa et al., 2014) for our imaging steps because it provides fast multi-scale and multi-frequency CLEAN (Rau and Cornwell, 2011; Offringa and Smirnov, 2017) deconvolution capabilities. These concepts are briefly explained in the following sections.

CLEAN

We showed in eqn. 3.29 that to obtain a better representation of the true sky, the result of imaging visibility data must be deconvolved from the interferometer's point spread function, a process aptly named *deconvolution*. Thus, the essence of deconvolution is to remove effects and artefacts introduced by the PSF, such as extended sidelobe patterns due to gaps in the uv-coverage. CLEAN (Högbom, 1974) is one algorithm that iteratively subtracts the PSF at locations with the highest peak until the stopping criterion is met. We summarise CLEAN's procedure as follows:

7 https://github.com/caracal-pipeline/caracal/blob/2d338e2afc5ed8fc723be95e74b071890d4a7bed/caracal/data/meerkat_files/gorbachev.yaml

1. Generate a dirty image, the PSF's image (also called the dirty beam), and an empty image containing only the CLEANed components, the model image.
2. Find the location of the maximum peak in the dirty image.
3. Centre the PSF at that peak's pixel location and scale the PSF's amplitude to a fraction of the peak value (this fraction is known as the loop gain and is typically less than ∼0.1).
4. Subtract the scaled and shifted PSF over the whole dirty image, leaving a residual image, and store a corresponding component in the model image.
5. Repeat steps 2 to 4 until the specified maximum number of iterations is reached or the CLEANing threshold is met.
6. Convolve the contents of the model image with the *clean beam* (i.e a Gaussian with a width of FWHM the PSF's main lobe).
7. Combine the residual image and the model image to form the CLEANed image.

All the steps of the basic Hogbom CLEAN are performed in the image domain. However, this method is computationally inefficient due to the repetitive shifting and scaling of the PSF at each iteration to achieve the desired goal. Because of this, more computationally efficient algorithms using fast fourier transforms (FFTs), such as the Cotton-Schwab algorithm (Schwab, 1984) have been devised. Cotton-Schwab CLEAN incorporates minor and major iterations, whereby the minor iteration performs the standard CLEAN steps highlighted above in the image domain. On the other hand, the major iteration performs an FFT on the CLEANed components which transforms them to what are known as the model visibilities. These are then subtracted from the original visibilities, and the process is repeated until the stopping criterion is reached (see also Cornwell and Braun, 1989; Voronkov and Wieringa, 2004, for more descriptions).[8] Fig. 4.14 illustrates this algorithm.

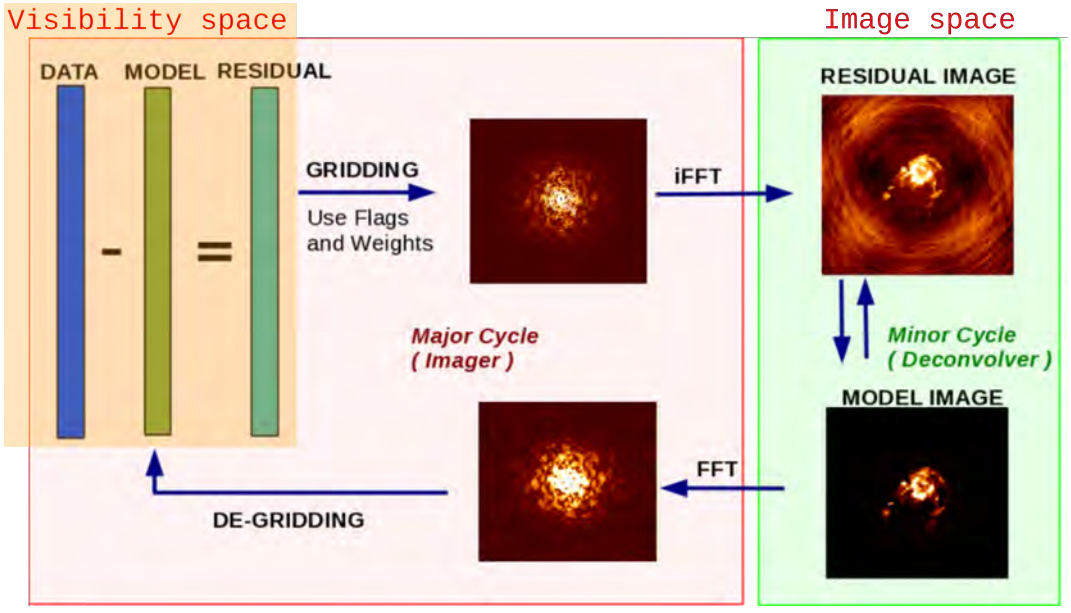

Figure 4.14: An illustration of the Cotton-Schwab deconvolution algorithm. This image has been adapted from the CASA synthesis imaging documentation.

Cotton-Schwab is is the default CLEAN algorithm used by `WSClean`. Therefore, a standard operation of CLEAN will result in five FITS images: the dirty image, PSF image, residual image (containing the remaining unsubtracted points and noise), the model image, and the CLEANed image. This algorithm works well for point sources, as they are modelled using Dirac delta func-

8 Cotton-Schwab deconvolution algorithm is a variation of Clark CLEAN algorithm (Clark, 1980).

tions.[9] By contrast, scenarios involving extended emission[10] which will be modelled as a summation of multiple point sources – such as is the case of Pictor A – may not be well deconvolved using CLEAN. One reason is that since all components are modelled as delta functions and a single peak is identified at each iteration, extended emission will require identifying a significantly larger number of pixels, leading to increased computation time. Multi-scale CLEAN was introduced to alleviate this problem.

Multi-scale CLEAN

First introduced by Cornwell (2008), this allows for the modelling of objects based on varying angular scale sizes. Unlike the conventional CLEAN, instead of measuring the strength of a pixel sequentially, multi-scale CLEAN checks the strength of multiple scales simultaneously. Here, extended components such as Gaussians are used to model a source rather than delta components; point sources are modelled at the zero scale, which is still the delta function. Since various scales are involved, this algorithm includes a small-scale bias that prevents large negative bowls around bright point sources due to subtracting inappropriate larger scales. Below is a summary of the `WSClean` multi-scale algorithm (Offringa and Smirnov, 2017):

1. Make dirty images at the chosen scales.
2. Select the scale containing the highest maximum value.
3. Convolve the PSF with the selected scale's kernel.
4. Run the standard CLEAN steps at this specific scale.
5. Find the next scale to CLEAN.
6. Stop when the threshold or the maximum number of iterations is met or when a negative component is encountered.

`WSClean` provides the option of automatic selection of appropriate scale sizes determined from the uv-coverage. The first scale is normally the zero scale, and the next is a factor of four times the FWHM of the PSF.[11] Multi-scale CLEAN allowed for better modelling of Pictor A compared to single-scale CLEAN. For our imaging runs, we first let `WSClean` automatically choose the deconvolution scales for us, and then used a modification of those automatically for our subsequent runs, excluding those we regarded as superfluous. Thus, our selected scales were 0, 19, 39, 78, 134 arcsecond scales.

Multi-frequency deconvolution

This entails sub-band imaging within a full observation bandwidth, which permits considering a source(s) spectral variation during CLEANing. Its basic operation according to Offringa and Smirnov (2017) is:

1. Divide the full band into a specified number of output channels (sub-bands).
2. Similarly to standard CLEAN, create a dirty and model image and PSF image using data from each sub-band.
3. Create an integrated image – also known as the multi-frequency synthesis (MFS) image – by combining multi-frequency weighted sub-band images and use this image for peak finding.
4. Determine the flux variation at this peak's location from all the sub-band images and optionally define the spectral shape by fitting a function to this variation.
5. Subtract the PSFs from the dirty images from each sub-band.

9 Point sources are compact and unresolved sources.
10 Sometimes called diffuse emission.
11 From the longest baseline, recall Eqn. 3.21.

The integrated image is used for peak finding to minimise the selection of sidelobes of peaks caused by noise in individual sub-band images. Furthermore, it is the use of `WSClean` in this mode that allows for the generation of multiple sub-band images for use in spectropolarimetric analysis (see Sec. 4.5). At the end of its operation in this mode, the total number of generated images will be the default five CLEAN outputs for each available sub-band, in addition to corresponding MFS images (i.e. for the dirty, residual, PSF, CLEANed and model images). For example if we set the number of output channels to four, we will get 25 (sub-band 4×5 + MFS 5) images at the end.

As we shall see in the next section, the first step towards selfcal is using an initial model of our target field. We used `WSClean` in multi-frequency and multi-scale mode to generate these model images.

4.3.3.2 *Selfcal*

1GC becomes limited because calibrator sources are usually further away from the source, so atmospheric variations in time and frequency cannot be adequately tracked close to the observation target. Hence, as briefly highlighted in the previous section, self-calibration involves using a bright source (including the target source) to estimate gains solutions in the surrounding field. It is performed after 1GC to mitigate remaining errors.

The brightness requirement ensures that there is adequate signal-to-noise to achieve suitable results. According to Noordam and Smirnov (2010), the ingress of selfcal allowed for extremely high dynamic range imaging – up to 10^6 – as shown by Smirnov (2011b) for the 3C 147 field using the Westerbork Synthesis Radio Telescope (WSRT). The steps involved as per Cornwell and Fomalont (1999) are as follows:

1. Make an initial model of the target source.
2. Solve for the direction independent gain solutions that minimise the difference between the RIME-predicted sky and the observed visibility data, over some solution interval.[12]
3. Apply these derived solutions to the observed data and image the new "corrected" data to obtain a newer and improved model.
4. Using this new model, repeat the previous steps until no further improvement occurs.

From the steps above, it is clear that a good initial model is a fundamental requirement for a successful selfcal process. We generated our first model by imaging the newly calibrated target data. Since this work focuses only on Pictor A and not its entire field, we used an image mask encompassing only the image section containing Pictor A. This is just another FITS image that defines the spatial boundaries within which imaging and deconvolution should occur. The implication is that during imaging, `WSClean` would only focus its efforts within the defined area. We highlight in Fig. 4.15 the benefits of deconvolving the PSF by comparing the dirty and CLEANed image from our 1GC data in the top and bottom panels, respectively. The "radial spokes" introduced by the PSF, known as artefacts, are reduced.

Running `WSClean` results in a model image which comprises the CLEAN components described in the previous section and is what we use as our initial model. Our selfcal proceeded in two stages. In the first stage, we performed two rounds of selfcal that involved phase-and-delay selfcal, using Stokes I models only. This is because, during our experimentation, we realised that the use of poor initial Q and U models at this stage caused corruption in the final Q, U images. These issues mostly manifested as an increase in fractional polarisation with increasing values of λ^2 (re-polarisation), contrary to the expected norm. Thus, we repeated the exact recipe as before while excluding Q, and U models (see Apps. B.2.2 and B.2 for the specific selfcal steps and `CubiCal` configuration file (parset file) used). In particular, we used the `CubiCal` (Kenyon et al., 2018) calibration software, selecting a "unislope" solver with a solution interval of 4096 channels in frequency (the full band) and a single integration in time. In effect, this solves for independent X and Y phase offsets and a

12 Here, some version of the RIME is applied to the model data to predict what the telescope sees.

common phase slope (i.e., delay term) per each solution interval. The cause of our initial problems were not clear, but we speculated that they resulted from pinning erroneous values of Q, U in this step, which affects the diagonal terms in Eqn. 4.4, and affects the resulting calibration solutions. We show in Fig. 4.16 a comparison of the image obtained immediately after 1GC and one after the first round of selfcal. The extremely bright WHS of Pictor A is severely impacted by the PSF, whose artefacts manifest as the radial spokes on that hotspot (top panel of Fig. 4.16). Artefacts on the Eastern side of this source are not as prominent, but they are also perceptible. This selfcal stage significantly reduced those artefacts on the WHS (bottom panel of Fig. 4.16). At this point, we generated Stokes I, Q and U models for use in the subsequent selfcal stage.

For the second stage, we predicted the new Stokes models resulting from the previous imaging cycle. We ran another round of selfcal, this time performing time-dependent phase-and-amplitude self-calibration (solving for **G**-Jones) using Stokes I, Q, and U models. This used `CubiCal`'s G complex 2-by-2 solver with a solution interval of 64 channels in frequency and 8 integrations in time. No Stokes V models were used. The result after imaging and deconvolution is displayed on the bottom panel of Fig. 4.17, demonstrating the comparison between it and the previously obtained image. A visible outcome is a significant reduction in artefacts at the WHS after this step, demonstrating the power of selfcal. Finally, we obtained the $7.5''$ image of Pictor A shown in Fig. 4.18, which is displayed in log scale to emphasise on the low-level emission. Lst. B.2 shows the steps taken to attain this final image. A discussion of the features observed in this image will be discussed in Sec. 5.2 of the next chapter. Figs. 4.15, 4.16, and 4.17 are set to the same linear colour scale ranging from 0 to 1 mJy.

We note that the images presented in this thesis do not include those produced with 3GC, as our initial attempts showed only marginal improvements compared to images from 2GC. Hence, we found the 2GC images sufficient to meet our scientific objectives. Consequently, the pursuit of a higher dynamic range and better image quality though 3GC was undertaken as a separate investigation, which will be detailed by Ramaila et al. (in preparation). However, for completeness sake, we briefly describe 3GC in the next section.

4.3.4 *Third Generation Calibration (3GC)*

Traditionally, corruption gain terms in observed visibilities were considered multiplicative in the uv-space, affecting the coherency function. Hence, the coherency function would be the Fourier transform of the observed sky. Because of this, DDEs were considered insignificant. However, Smirnov (2011a) explains that DDEs are a multiplication in the lm-plane, meaning they are a convolution in the uv-plane. This means the source coherency function is convolved with the DDEs, i.e. each baseline sees a unique version of the sky as different convolution kernels affect the coherency function in different ways. Smirnov (2011a) suggested a few techniques to deal with unknown DDEs, amongst which are: ***peeling*** (Noordam, 2004; Intema et al., 2009) and ***differential gains.***

In **peeling**, the most suitable gains solutions are first derived through selfcal given some model data and the observed data. These solutions are then applied to the model of the brightest source available, after which the predicted corrupted model of that source is subtracted from the observed data.[13] This process is repeated severally and has a bottleneck of a high computational cost in the presence of multiple sources.

Differential gains offer an alternative approach whereby direction-independent gain terms are solved on short solution intervals towards the bright sources while direction-independent gain terms are simultaneously solved on longer solution intervals towards the faint sources. Nonetheless, choice of solution intervals is a tricky problem (see Sob et al., 2021, for more detailed discussions on this). The idea is that the more dominant direction-dependent effects will be contained

13 Predict is the step that Fourier transforms model images in l, m-space to visibilities in u, v-space that are stored in the MS' MODEL_DATA column.

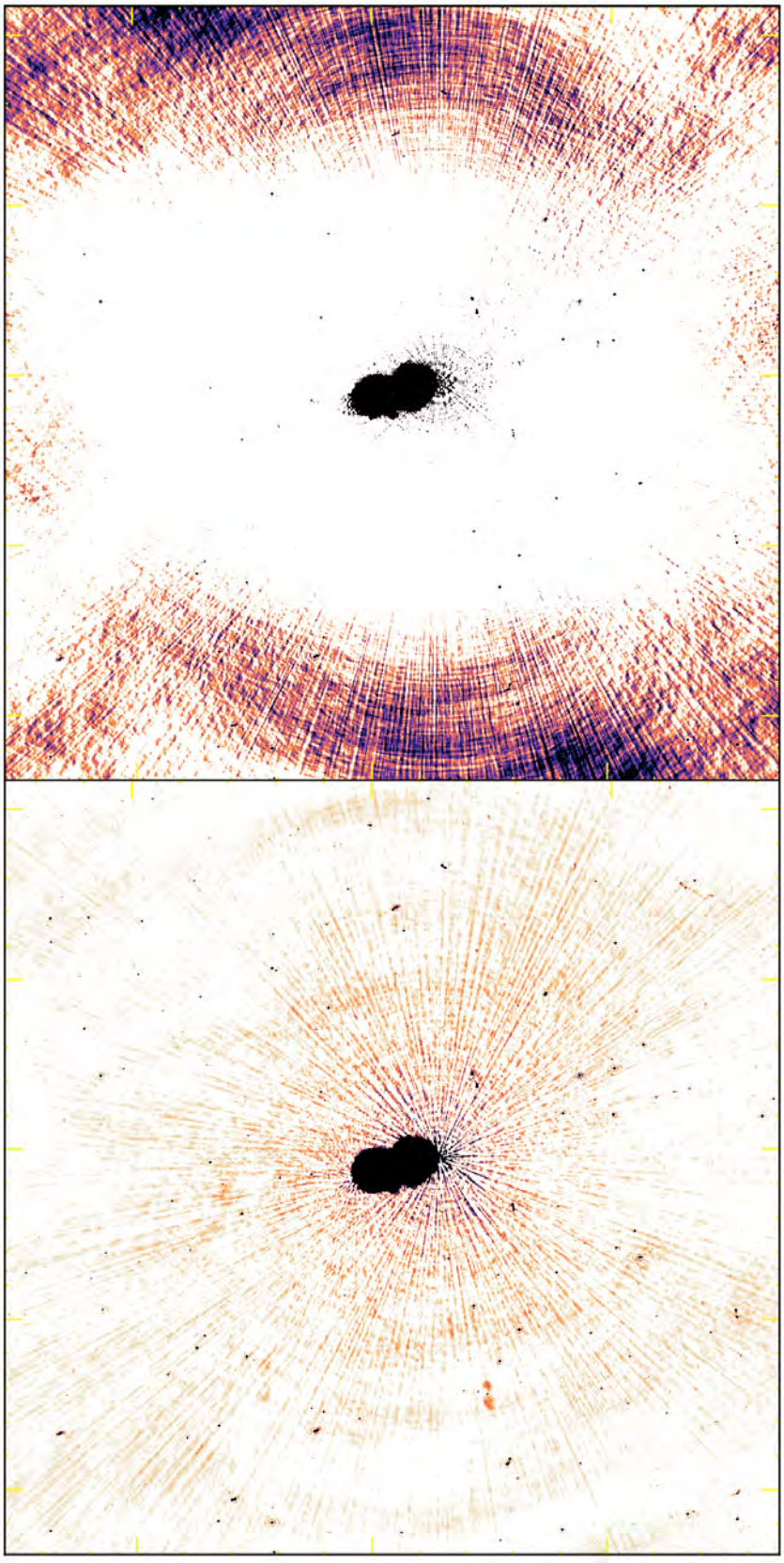

Figure 4.15: A comparison of the dirty and deconvolved MFS image of Pictor A before selfcal; the colour scale ranges from 0 to 1 mJy. *Top panel*: Dirty image of Pictor A. This is before deconvolution, and the image is still convolved with the PSF, hence the radial spokes. *Bottom panel*: The same image after deconvolution. While the PSF artefacts are significantly reduced, they are still problematic.

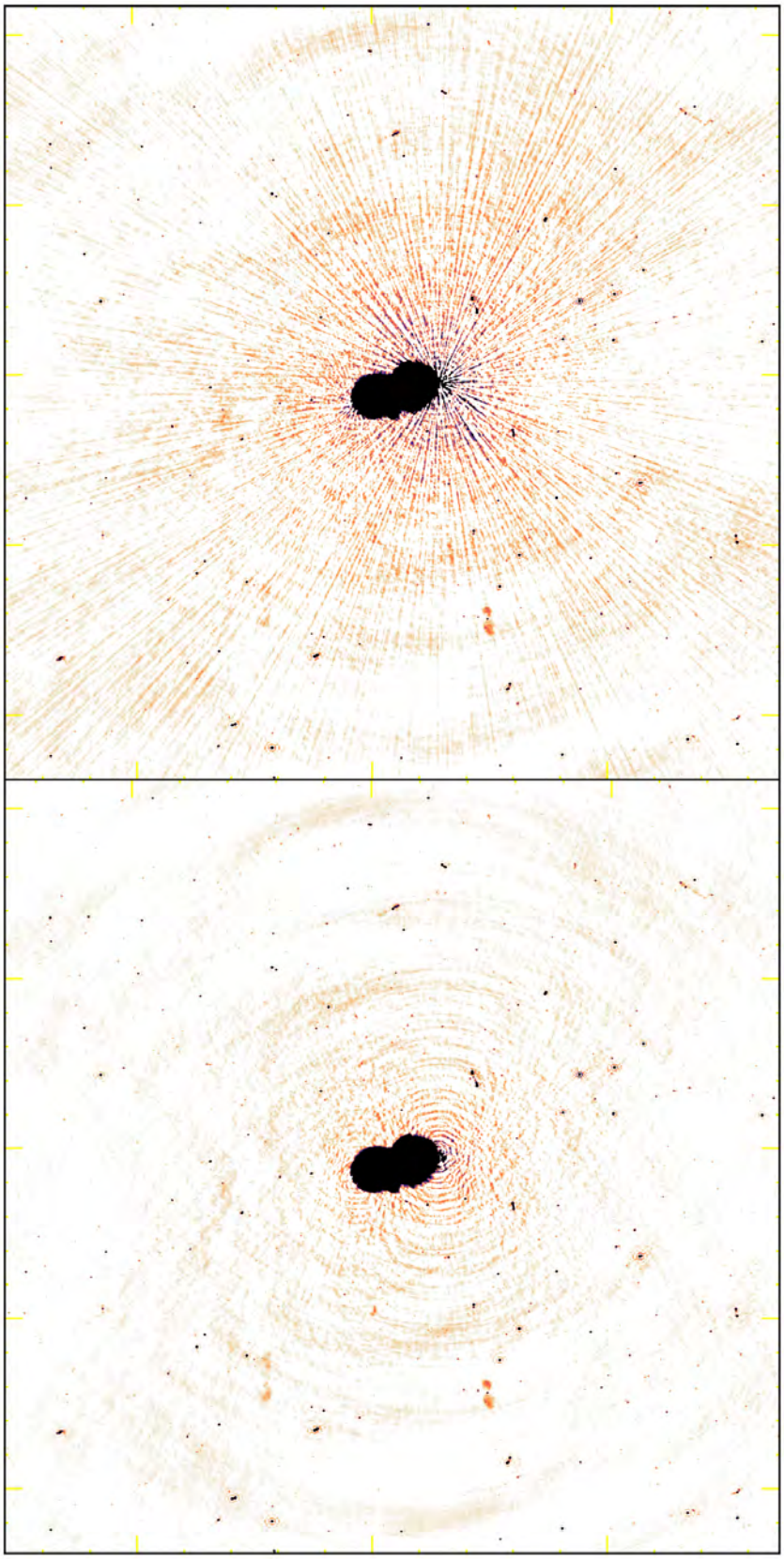

Figure 4.16: A comparison of the deconvolved MFS images before and after one round of delay selfcal. *Top*: The image immediately after 1GC. In this case, this was also the dirty image where the WHS of Pictor A is affected by the PSF, which manifests as the radial spokes on the hotspot. *Bottom*: after the first round of phase delay corrections in selfcal. The radial spokes on this hotspot are significantly reduced.

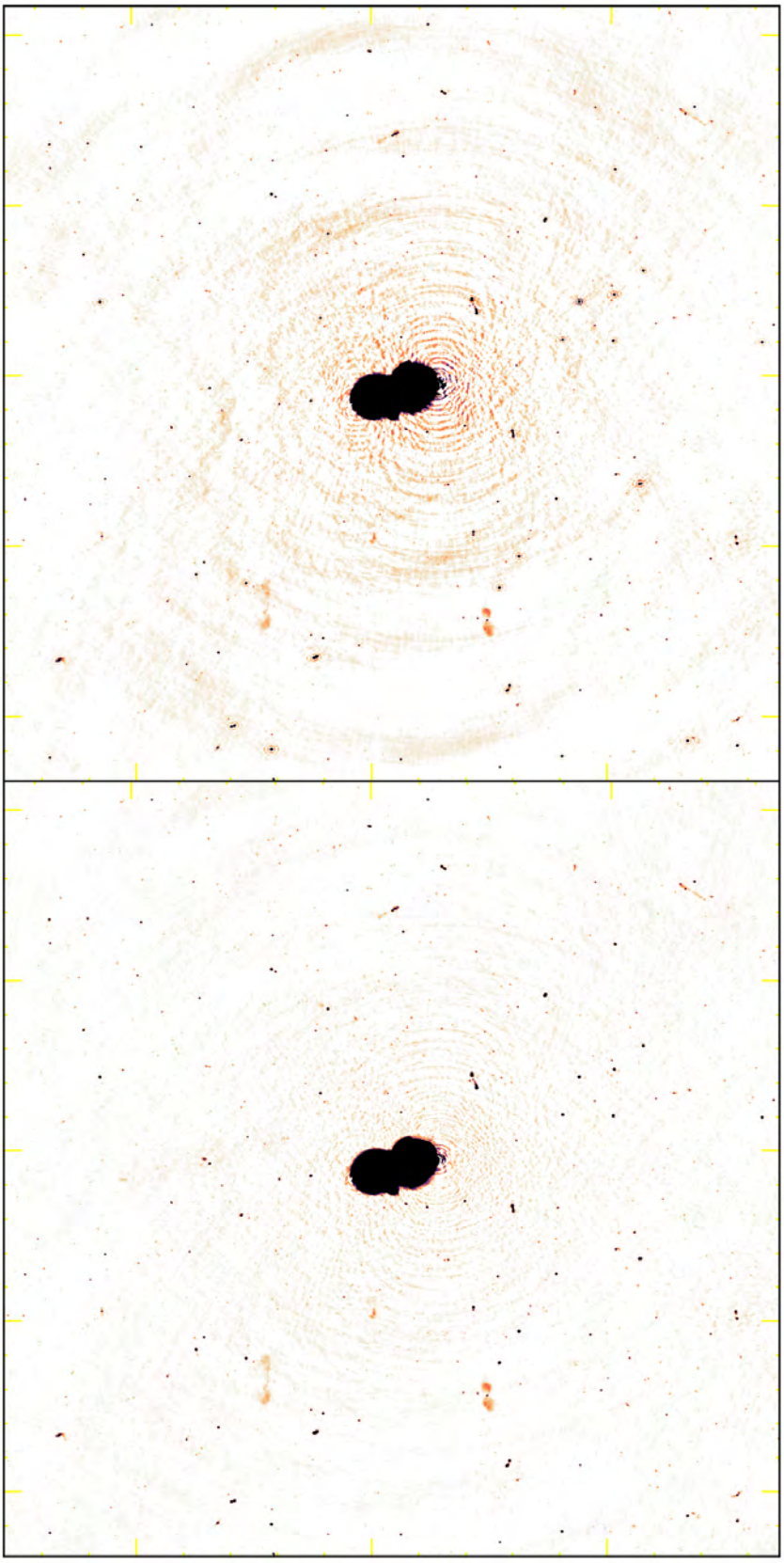

Figure 4.17: A comparison of deconvolved images of before and after complex gain phase-amplitude selfcal. This demonstrates the improvement on the WHS after complex gain phase-amplitude selfcal. *Top panel*: the resulting MFS image after the second round of delay selfcal (stage 1 selfcal). *Bottom panel*: the resulting MFS image after phase-amplitude complex gain selfcal (stage 2 selfcal).

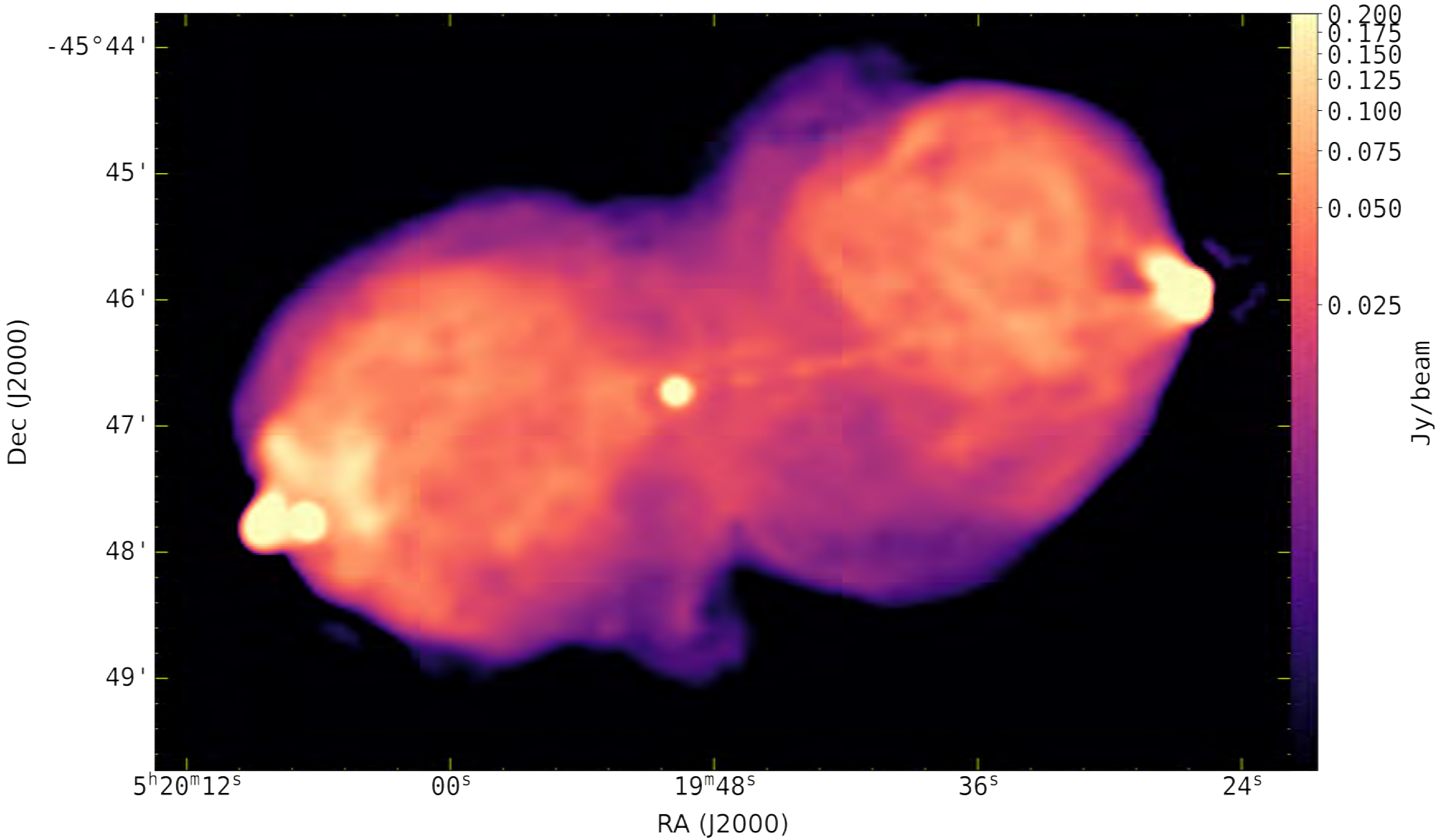

Figure 4.18: A Pictor A MFS image at 7.5″ resolution showing its various components. This is zoomed in from the bottom panel of Fig. 4.17. The log scale is used to emphasise the low-level emission.

in gain terms towards the brightest sources, leaving the residual unknown differential gains towards the faint sources. In terms of peeling, this is similar to subtracting the brightest source and solving for the remaining effects in the faint sources. Since these steps are done concurrently, the computational cost is significantly reduced.

4.4 Smops

As previously mentioned, one of the main challenges faced during our imaging and deconvolution was dealing with Pictor A's bright WHS. Mitigation of these effects necessitated the adoption of direction-dependent calibration strategies, whereby good models of the direction in question are requisite for effective subtraction and calibration. Inspired by the need of better models for this hotspot during our 3GC testing, we developed `Smops` (Andati et al., 2023b), a tool that interpolates the input sub-band model images generated by `WSClean` across frequency, and yields models at more finely-spaced frequency intervals.[14]

In typical imaging steps, `WSClean` is configured to produce a small number of sub-band images over a given bandwidth using the `-channels-out` option (for example the default value set by the `CARACal` pipeline is 4). This results in model images with a stepwise behaviour across frequency. `Smops` then fits a Taylor polynomial across frequency to the input model images, allowing for the creation of additional sub-band images within the defined bandwidth. By doing this, the model images' behaviour across frequency is made more continuous (smoothed due to smaller steps in between frequencies) and refined. The high frequency resolution allows for better model subtraction thereby facilitating improved DR.

4.4.1 *Architecture*

`Smops` is a command-line Interface (CLI) `Python`-based tool that primarily uses the `NumPy` library for its computational tasks.[15] However in cases where a large number of channel outputs is desired which demands a large random access memory (RAM) footprint, `Dask` is used for chunking an parallel processing.[16]

4.4.2 *Operation*

This tool is installable via the standard `Python` package manager `pip` as shown in Lst. 4.1. It requires the following command-line arguments for operation:

- The input MS from which the reference frequency is obtained.
- The input model images that require interpolation.
- The desired number of output channels.

The order of the polynomial to be fitted as well as other performance tuning tweaks such as the number of central processing unit (CPU) cores to use and maximum RAM are also specifiable. A typical `Smops` execution is highlighted in Lst. 4.1.

In this example execution, four sub-band Stokes I model images were input to `Smops` for interpolation from four to 10 sub-band images. This tool automatically determines the number of input images, which must be less than the desired number of output channels. At the end of its execution, 10 sub-band model images are made available. `Smops` also interpolates Stokes Q, U, V models if they are made available and specified.

14 https://pypi.org/project/smops/
15 https://numpy.org/
16 https://www.dask.org/

```
# installing smops
pip install smops

# Generate smops' help instructions
smops --help

#sample command
smops --ms onescan.ms --channels-out 10 --input-prefix inputs/image \
    --output-prefix outputs/image --stokes I \
    -order 3 --num-threads 10
```

Listing 4.1: Snippet showing the installation and basic functionality of Smops.

Since this tool only interpolates between already available model images, a typical workflow incorporating Smops is as follows:

1. Perform the first imaging and deconvolution using few output channels (e.g. 4) to generate the sub-band model images.
2. Use Smops to interpolate those images into some desired number of channels (e.g. 16).
3. Insert these new high resolution model images into the MS and proceed with calibration, ensuring the new number of channels is captured.

For example using WSClean:

```
# First imaging
wsclean -name outputs/image -channels-out 4 \
    -mem 50 -weight briggs 0.0 -size 4096 4096 -scale 1.0asec \
    -pol I -join-channels -data-column DATA -niter 200000 \
    -auto-threshold 2 -gain 0.1 -mgain 0.9 -padding 1.5 \
    -log-time -no-update-model-required onescan.ms

# use smops to interpolate the images
smops --ms onescan.ms --channels-out 16 --input-prefix outputs/image \
    --output-prefix smops-out/image --stokes I \
    -order 3 --num-threads 10


# Insert the new models into the MS
wsclean -log-time -channels-out 16 \
    -pol I -predict -name smops-out/image onescan.ms
```

Listing 4.2: A simple workflow involving Smops.

4.4.3 *Validity Test*

One way of testing the effectiveness of this tool is comparing residuals resulting from lower-frequency-resolution models, to those from the higher-frequency-resolution models. To achieve this we first imaged our CORRECTED_DATA column after the first round of selfcal using four output channels. This was followed by model interpolation using Smops, to 16 and 80 channels. Each set of the new high-frequency-resolution models were inserted into the MS and subtracted from the CORRECTED_DATA column resulting in residuals.

Using the `aimfast` tool, we performed some statistical tests on these residuals, comparing the 4-channel model residuals to the 16 and 80 channel model residuals.[17] These statistics were drawn from random pixel regions within the weighted residual maps. They include:

- The RMS, standard deviation, and median absolute deviation (MAD): all measures of the variability within the data. A reduction here means that spikes within the data are minimised.
- The minimum and maximum pixel values: used to obtain the DR, an indicator of artefact suppression in the image.
- The absolute sum of negative pixels: since artefacts present themselves as negative values due to sidelobe effects, a reduction in this sum means reduction in the artefacts.

The results are shown in Tab. 4.2.

Table 4.2: Comparison of residual statistics from 4, 16 and 80 channel models.

mJy/beam	4 channels	16 channels	80 channels
min	−8.85	−9.12	−8.97
max	45.58	45.65	45.72
RMS	0.63	0.56	0.54
MAD	0.29	0.26	0.24
Sum of negatives	−3502.52	−3059.47	−2904.57
Dynamic range			
DR1	72.46	81.08	84.82

This table illustrates that higher-frequency resolution models result in a decrease in both variability and negative pixel contributions, while the DR increases. This means an increasing model-frequency-resolution improves the existing models, thus resulting in better source subtraction.

It is possible for `WSClean` to natively generate any larger number of sub-band images. However this gets computationally expensive and time consuming depending on the dataset and image size, and an increasing number of sub-bands. Therefore, `Smops` acts as a shortcut to obtaining better model images without performing imaging and deconvolution with a large number of output channels. This tool has proven especially useful in the direction-dependent calibration of the WHS.

4.5 Towards Polarimetry

4.5.1 *Polarimetric Imaging*

In Sec. 3.2, we established that the initial stage of polarimetry involves generating images of Stokes I, Q, U, V. Furthermore, we emphasised that acquiring RMs necessitates measurements across multiple wavelengths (λ^2). This is achieved by running `WSClean` in a multi-frequency mode whereby multiple sub-band I, Q, U, and V images are generated after an imaging run.

`WSClean`'s documentation recommends specific settings when preparing images for polarimetric analysis to improve the resulting Stokes images. Amongst them is `-join-polarizations` whereby peaks (as highlighted for the CLEAN process) are located from a combination of the polarised images (i.e. $\sqrt{Q^2 + U^2}$) rather than from each individual Stokes image. Component strengths are then obtained from the individual Stokes images after peak finding.[18] Another option exists, `-squared-channel-joining`, which finds peaks in the image of $Q^2 + U^2$ instead, preventing the

17 https://github.com/Athanaseus/aimfast
18 https://wsclean.readthedocs.io/en/latest/polarimetric_deconvolution.html

Q, and U flux from averaging to zero. During our experimentation and at the time of this writing, this option was unstable due to technicalities in `WSClean` and was excluded.

Fitting a spectral polynomial may be desired to smooth the behaviour across frequencies. However, we note here that this setting, `-fit-spectral-pol`, does not work with the join-polarization option and, thus, was not used. Therefore, spectral fitting could be performed after the imaging step. Below, we show an example of the command used in the generation of our images using `WSClean`.

```
wsclean -name output/image -mem 50 -weight briggs 0.0 -size 4096 4096 \
    -scale 1.0asec -channels-out 80 -pol IQU -join-channels \
    -data-column CORRECTED_DATA -fits-mask mask.fits -niter 200000 \
    -auto-threshold 2 -gain 0.1 -mgain 0.9 -padding 1.5 -log-time \
    -multiscale-scales 0,19,39,78,134 -multiscale -j 20 -nwlayers-factor 3 \
    -join-polarizations -temp-dir temps -no-update-model-required pictora.ms
```

Listing 4.3: The `WSClean` command used in generating our polarimetric images.

The `-channels-out` option determines the number of sub-band images generated, which could then be used to produce image cubes. To do this, `WSClean` splits the MS into evenly spaced frequency chunks across the bandpass, equal to the desired channels. Because of this refined imaging, channels that are heavily affected by RFI even after the flagging steps or other artefacts are included in the weighted MFS image (see Sec. 4.5.2). Initial scales chosen for multi-scale cleaning were automatically determined by `WSClean`. These were later modified to the the ones shown in in Lst. 4.3 based on visual inspection and scale measurement of some structure on our image, such as the WHS, mainly because the focus of this work was specific to Pictor A and not its surrounding sources. As mentioned in the previous section, multi-scale is required to model the extended emission, which is inadequately modelled using delta functions.

A very large large memory footprint is required to generate the multiple images needed for image cubes as all images must be stored in RAM simultaneously during deconvolution. This results in high computational intensity. `WSClean` provides an option `-deconvolution-channels`, which reduces the number of deconvolution channels in memory. Setting this value to 8 in Lst. 4.3, for instance, would mean that averaging is done over every 10 images, and CLEANing is performed on the resulting 8 averaged images (i.e. averaging is done on every channels-out/deconvolution-channels). However, from experience, this option requires some form of frequency interpolation and consequently must be used with spectral polynomial fitting. In summary, the `WSClean` options required for polarimetric imaging are `-channels-out, -join-channels, -join-polarizations` and `-squared-channel-joining`.

The choice of the number of output frequency channels plays an important role, such that extremely small channel widths could result in a significant dip in the signal-to-noise. On the other hand, if selected channel widths are too large, bandwidth depolarisation could occur (see Sec. 3.2.3). A good balance of the two must be struck to maintain a good signal-to-noise ratio and improve sensitivity. Therefore, we determined the maximum allowable channel width, $\delta\nu$, using the following equation (a modification of Eqn.4 of Sebokolodi et al., 2020):

$$\delta\nu = \frac{\Delta\chi\nu}{2\lambda_\nu^2 RM},$$

where ν is the centre of the observational bandwidth, $\Delta\chi$ is the per-channel maximum allowable rotation of the plane of polarization in radians, and RM is the maximum rotation measure of the source. We used a maximum RM of Pictor A of $\sim$100 rad m^{-2} reported by Perley et al. (1997), a condition that maximum rotation limit is 5°, and a centre frequency of 1.28 GHz to derive a maximum channel width of $\sim$10.2 MHz. This was adjusted to $\sim$10.7 MHz resulting in 80 frequency

channels. We then instructed `WSClean` to generate 80 sub-band I, Q, and U images. Considering that our data originally had 4096 channels, this step effectively averaged every 51 channels together. No primary beam correction was applied as it seemed unnecessary for these data since our interest was the central source (Pictor A) whose angular size is $\sim 8'$ – well within the MeerKAT main beam of 1.2 degrees.

Inspection of the variation of the restoring beams' dimensions with frequency of our resulting images revealed that some sub-band images exhibited abnormal variations in the beam sizes, possibly arising from effects of RFI primarily from GSM satellites. Fortunately, `WSClean` assigns lower weights to problematic sub-band during imaging. With these weights, we used our tool `sc-beam-plot` (discussed in Sec. 6.2.1) to automatically select good sub-band images while excluding lower weighted sub-band images based on a set threshold. As a result, 41 usable sub-bands were selected. Fig. 4.19, auto-generated by `sc-beam-plot`, shows the excluded channels represented by crosses, and the included channels represented by dots. The good channels' images were then combined to form cubes of Stokes I, Q and U.

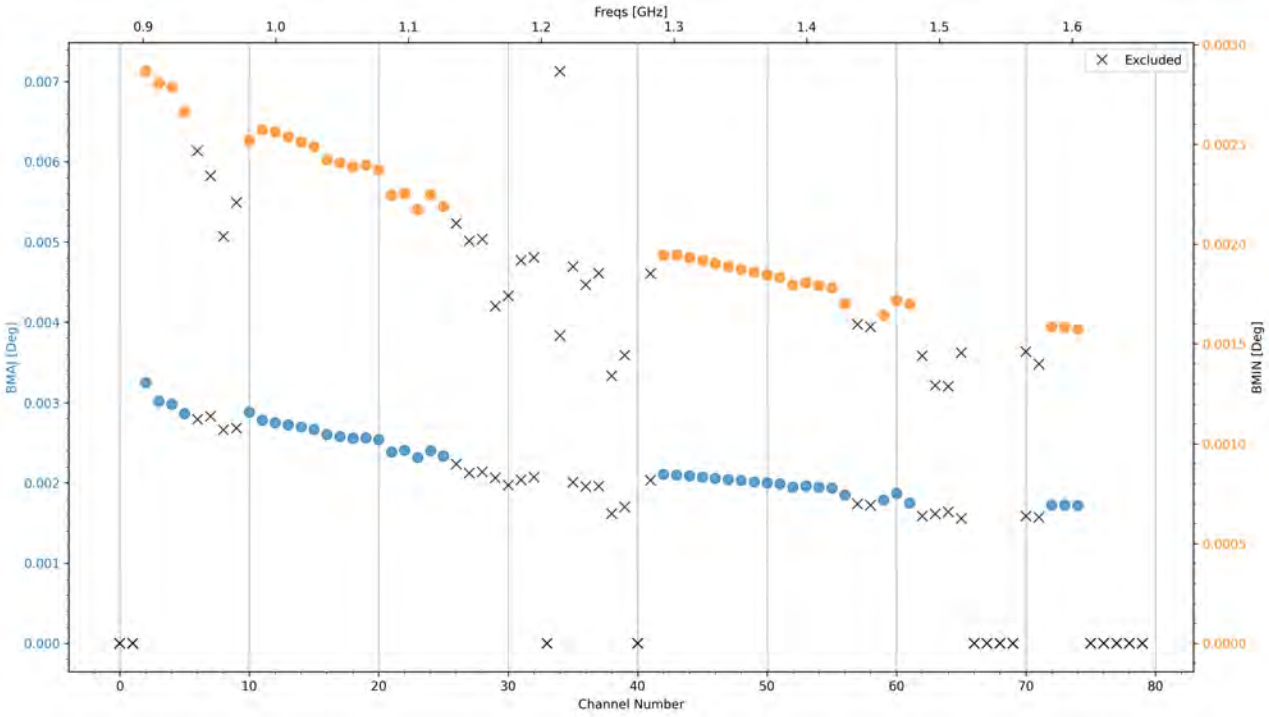

Figure 4.19: The channels auto-selected by `sc-beam-plot` based on channel weights. Excluded channels are represented by the crosses. The major and minor beam dimensions are shown on the left (blue axis) and right (orange axis) respectively. The plots colours match the beam axis color.

Variations of the CLEAN beam across frequency could induce resolution-dependent polarimetric effects. To avoid this, image cubes are commonly convolved to the same resolution across all frequency planes, thereby ensuring that all the involved images are of the same resolution (e.g. O'Sullivan et al., 2012; Schnitzeler et al., 2019). We convolved all images to the same resolution of $11'' \times 10''$ using the `Spimple Python` package.[19] The resulting cubes were then used for the spectropolarimetric analysis of Pictor A. The general steps taken are summarised as follows:

1. Generate I, Q, U, and (V) images.
2. Remove any bad quality sub-band images.
3. If required, convolve the remaining images to the same resolution to avoid resolution-induced effects during polarimetric analysis. Depending on the image stacking software used, it is

19 https://github.com/landmanbester/spimple

important to convolve the sub-band images individually at this stage to preserve beam information, which may not be appropriately stored/accessed if image stacking is done first.

4. Stack these Stokes images together to form $I, Q, U, (V)$ image cubes.
5. If there are significant variations along frequency within the Stokes I cube, perform a spectral polynomial fit to enforce smooth behaviour across frequency.
6. Perform RM-Synthesis.

We estimated an off-source noise of 21.85 μJy/beam for the Stokes I MFS image, while the per-channel off-source noise for our selected sub-band images ranged between 95 – 278 μJy in Q, and 41 – 233 μJy in U. The noise close to the WHS increases by almost an order of magnitude for each image.

4.5.2 *What Do Bad Channels Look Like?*

Upon visual inspection of the spectral behaviour of our Stokes I image cubes (consisting of 80 channels as previously stated) per pixel and our corrected visibilities, the dependence between flagged channels and discarded images became apparent. We realised that the heavily flagged frequency channels corresponded to the frequencies of the excluded sub-band images. An example of this is shown in Fig. 4.20. At the bottom panel, frequencies without data points are where data were completely flagged, and frequencies with data points at lower amplitudes than its neighbouring frequencies indicates heavy flagging. Missing data within these channels may cause a significant reduction in the signal-to-noise, resulting in low-quality images such as that in Fig 4.21 as `WSClean` divides the input data into sub-bands depending on the number of selected output channels. Because of heavy flagging in those bands, the PSF becomes poor with high sidelobes, which leads to negative emission that is difficult to deconvolve. The top panel of Fig. 4.20 shows above zero values even in frequencies where data was completely flagged most likely due to `WSClean`'s sub-division of frequency bands, where frequency portions with data and those without could be located in the same sub-band.

Since the final MFS image obtained from `WSClean` is a weighted sum of all the available images, images such as this (albeit with a lower weight) could introduce unexpected structure. We imaged the same data to test this idea, reducing the number of output channels to four from 80, and found that no images with such a structure were produced. We also tested this by creating our own MFS image using only our selected sub-band images (out of the initial 80) and the `Python` script shown in Lst. B.4. The negative structure around in the source in Pictor A's MFS image also reduced significantly.

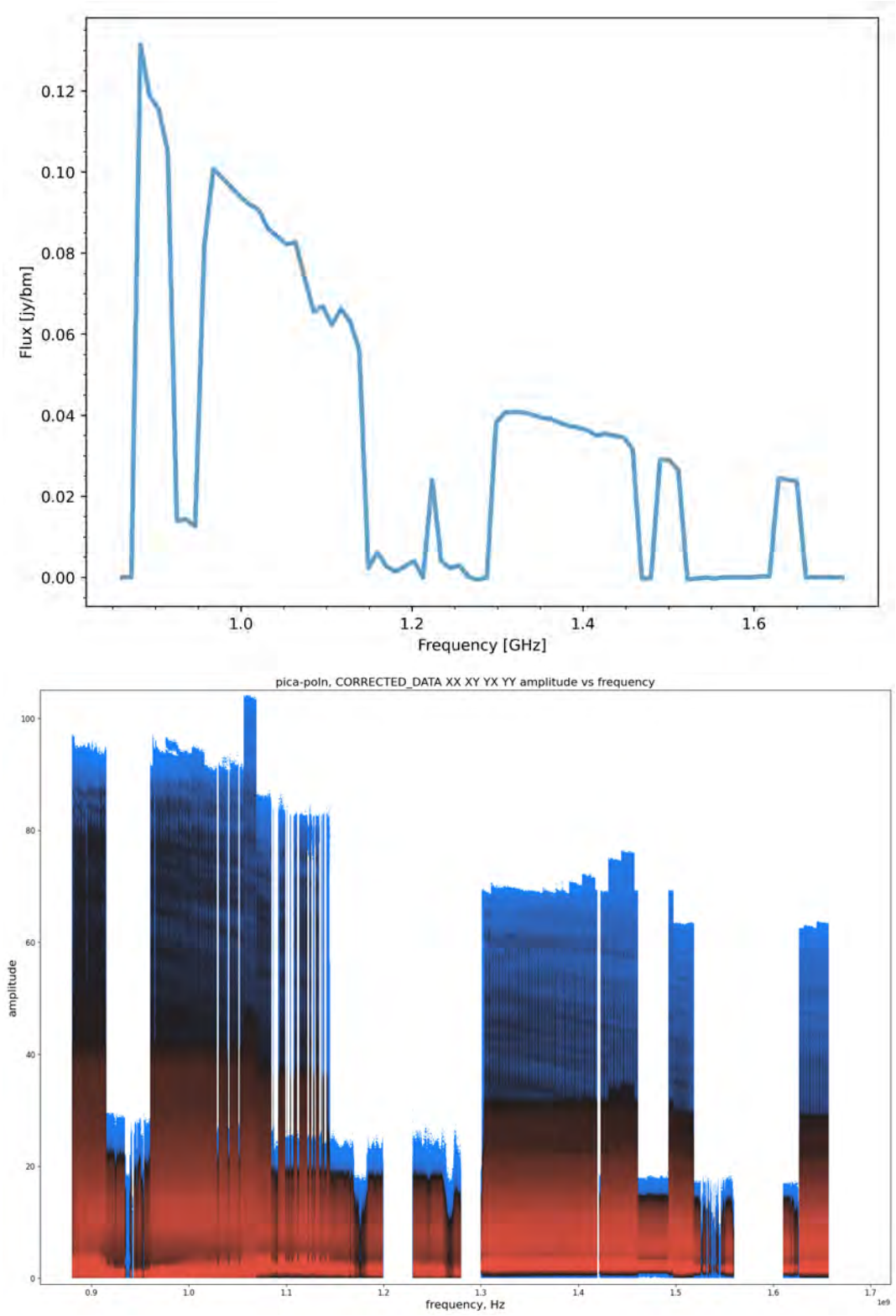

Figure 4.20: Illustrating the correspondence between the heavily flagged channels and bad images. *Top*: The Stokes *I* spectrum of a single pixel across frequency. *Bottom*: Visibility plot of amplitude against frequency, showing our CORRECTED_DATA column with flags applied. The colours indicate the density of visibility data points, and are not relevant to this illustration. The heavily/completely flagged channels align well with those whose sub-band images were excluded from polarimetric analysis as highlighted by Fig. 4.19.

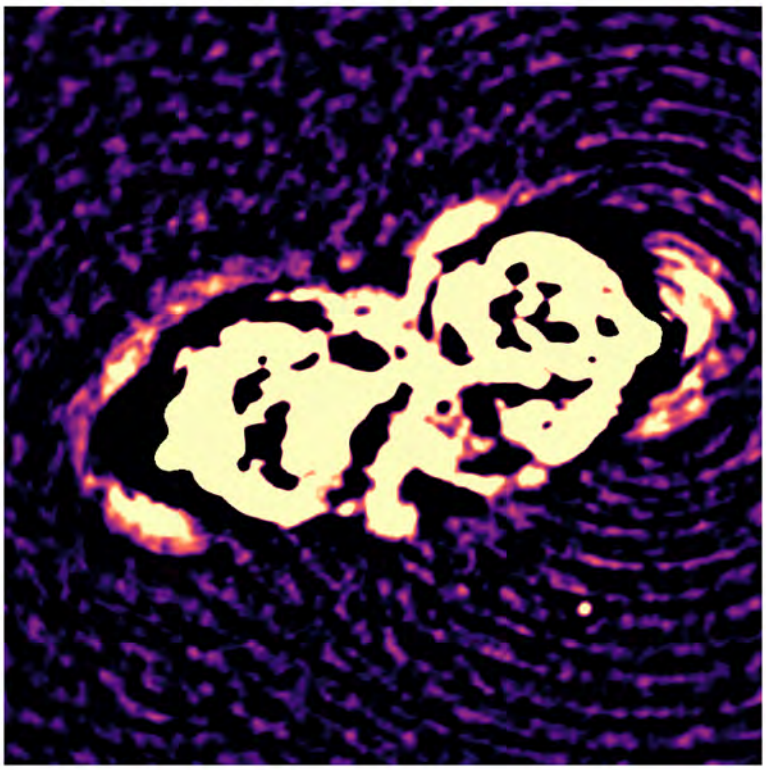

Figure 4.21: An example of how a bad image appears. We excluded such images from our spectropolarimetric analysis.

4.6 Summary

This chapter described our transition from observed visibilities to the final images used for spectropolarimetric analysis. We briefly introduced calibration concepts and highlighted the steps taken towards achieving our polarimetry-ready images, i.e. 1GC and 2GC. We noted that our 2GC involved two intermediate steps, in the first step, we used only the Stokes I models while excluding Stokes Q, U models as they caused errors that later manifested as unexpected repolarisation in our data. However, these models were included in the second step. Furthermore, we also availed imaging parameters used for polarimetric imaging, justifying our choices. The recipes and default configuration files used for 1GC and 2GC have been availed in Apps. B.1, B.2 and B.2.2. The effects of RFI flagging and their effect on resulting imaging were additionally demonstrated. The next chapter presents our findings based on the reduced, calibrated and imaged data.

We note that the 1GC data reduction was performed by this author in collaboration with Athanaseus J. T. Ramaila. The 2GC project was divided into two distinct paths: this author focused on the spectropolarimetric imaging route, while A. J. T. Ramaila explored improvements made by 3GC and developed a recipe for higher dynamic range imaging.

5

KEEPING UP WITH PICTOR A: A SPECTROPOLARIMETRIC STUDY

In this chapter, we present the results of a polarimetric study from our new high-sensitivity L-band (0.8–1.7 GHz) observation of Pictor A with the MeerKAT radio telescope. We confirm the presence of the radio jet extending from the nucleus to the western hotspot of this source. Additionally, we show the radio emission expected to be coincident with previously observed X-ray emission in the radio lobes, confirming that the emission mechanism is of inverse Compton (IC) origin, as suggested by a previous study. Our spectropolarimetric analysis using the RM-Synthesis technique reveals a relatively uniform mean rotation measure (RM) distribution across the lobes of Pictor A, with most lines-of-sight (LoSs) exhibiting single-peaked Faraday spectra. However, a number of the LoSs exhibit single peaked spectra with a wide base or multiple peaks, suggesting the presence of multiple Faraday components or a Faraday thick structure along Pictor A's LoSs. We also confirm the asymmetry in RM variability and depolarisation between the two lobes of this source which were reported in a previous study.

This chapter was published in the *Monthly Notices of the Royal Astronomical Society (MNRAS)* under the title *A spectropolarimetric study of the radio galaxy Pictor A using MeerKAT*, Volume 529, Issue 2, April 2024, Pages 1626–1641 (Andati et al., 2024). Most of the material is from the published manuscript and has been adapted to maintain the thesis flow.

5.1 Extracting Spectropolarimetric Information

To study the polarimetric composition of Pictor A, we applied the RM-Synthesis technique earlier introduced in Sec. 3.2.2.2. As previously mentioned, one of its advantages is mitigating the $n\pi$ ambiguity problem, which plagues the traditional linear fitting of the polarisation angle against λ^2. In this context, erroneous values of RM and zero-wavelength position angle may be obtained due to polarisation angle wrapping (or jumping) through multiple cycles, hence the ambiguity. Note that from here on, we will use capital letters such as Q and U to present intensities, and small q and u to represent fractional quantities (e.g. $q = Q/I$).

According to Brentjens and de Bruyn (2005), the maximum Faraday depth, $|\phi_{\rm max}|$, that we can probe is dependent on the channel width, $\delta\lambda$, of our observations as follows:

$$|\phi_{\rm max}| = \frac{\sqrt{3}}{\delta\lambda^2}, \tag{5.1}$$

For our data we find $\phi_{\rm max}$ of ∼1981 rad m^{-2} for our channel width of 10.7 MHz.[1] On the other hand, Schnitzeler et al. (2009) showed that the expected depth resolution, $\delta\phi$, which is determined by the FWHM of the RMTF (described using Eqn. 3.13), is dependent on the bandwidth in λ^2 space, $\Delta(\lambda^2) = \lambda^2_{\rm max} - \lambda^2_{\rm min}$, as follows:

$$\delta\phi = \frac{3.8}{\Delta(\lambda^2)}. \tag{5.2}$$

1 According to Brentjens and de Bruyn (2005), $\delta\lambda^2 \approx \frac{2c^2\delta\nu}{\nu^3}\left(1 + \frac{1}{2}\left(\frac{\delta\nu}{\nu_c}\right)^2\right)$, where $\delta\nu$ is the channel width, ν_c is the central frequency of that channel.

Our data's bandwidth is 856 MHz (see Tab. 4.1); therefore, the RMTF resolution for our data is ∼41 rad m^{-2}, and its structure is illustrated in Fig. 5.1. Due to a large gap in the data (resulting from flagging frequencies that were significantly affected by RFI), our RMTF exhibits large sidelobes, as discussed in Sec. 3.2.2.2.

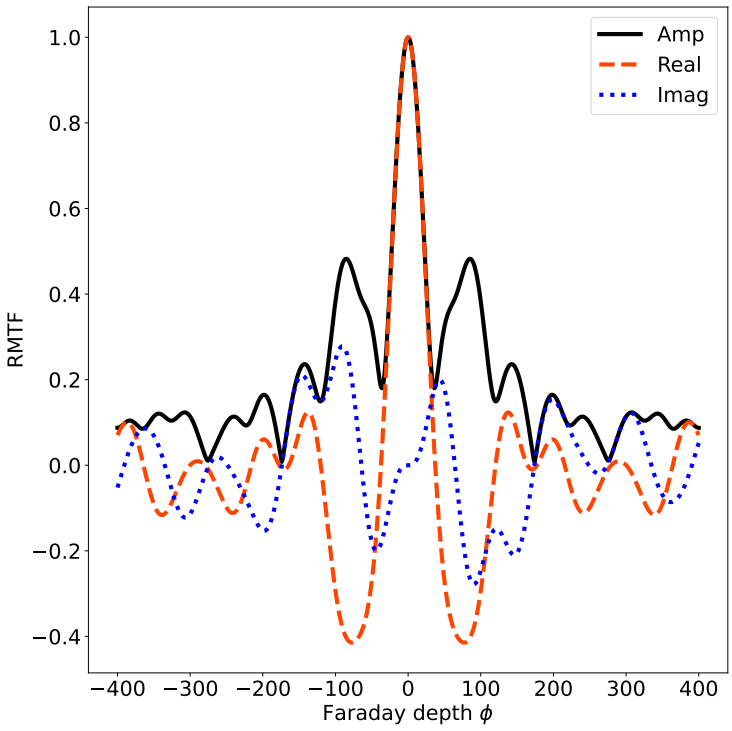

Figure 5.1: The RMTF of our data with a resolution of 41 rad m^{-2}. The solid, dashed and dotted lines represent the amplitude, real, and imaginary components, respectively. The high sidelobes result from missing frequencies that were flagged out due to RFI.

5.2 Total Intensity

5.2.1 *Hotspots*

In Fig. 5.2, we show the total intensity map of Pictor A obtained from our L-band data at 7.5″ resolution – the highest possible resolution for our observations. Our data show a single hotspot at the extremity of the western lobe, herein the western hotspot (WHS), and two hotspots at the extremity of the eastern lobe, herein the eastern hotspot (EHS). The presence of these hotspots is consistent with previous observations of Pictor A. The WHS is exceptionally bright, with a peak brightness of 7.2 Jy beam^{-1} (∼118 mJy arcsec^{-2}), while the inner WHS shows a peak brightness of 1.62 Jy beam^{-1} (∼26.5 mJy arcsec^{-2}), and the outer shows 1.01 Jy beam^{-1} (∼ 16.5 mJy arcsec^{-2}). At our resolution, these hotspots and radio core remain unresolved.

According to the dentist drill model (Scheuer, 1982), the inner hotspot is the primary hotspot (most recent), and the outer hotspot is the secondary hotspot (older). This model implies that the eastern jet was first directed towards the secondary hotspot and then later changed direction towards the primary hotspot. The change in the jet direction occurred on time-scales shorter than the time taken for the secondary hotspot to dissipate due to expansion losses. Perhaps this may explain the differences in peak brightness of the hotspots – with the primary hotspot being brighter than the secondary – but this inference remains inconclusive and subjective.

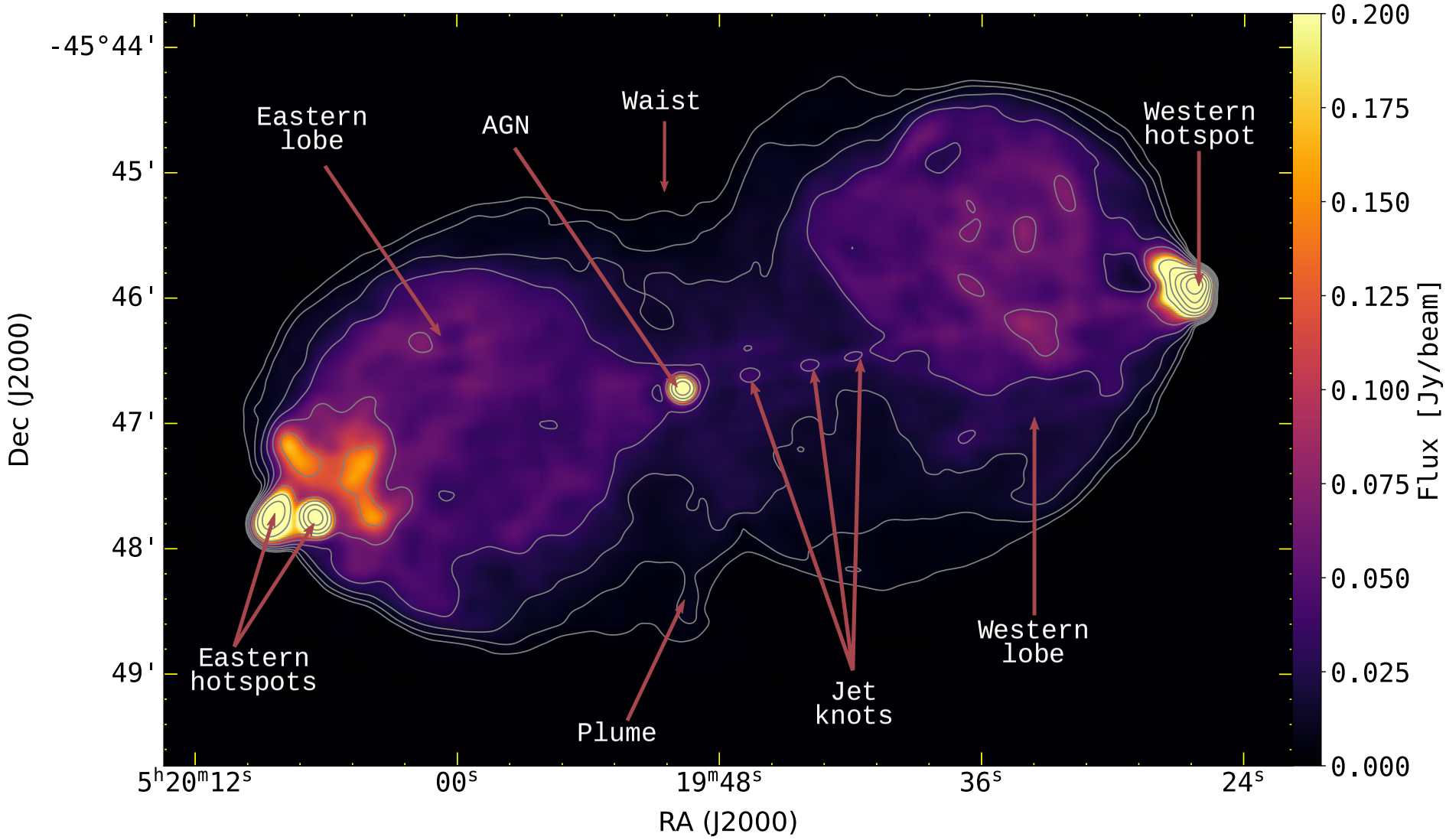

Figure 5.2: An MFS image of Pictor A from our new MeerKAT L-band observations centred at 1.28 GHz with a bandwidth of 856 MHz and 7.5″ resolution. The contour levels shown start from 4 mJy beam^{-1} and increase by a factor of 2. The off-source noise is 22 μJy beam^{-1}. The source emission shows a single hotspot at the extreme end of the western lobe and two hotspots at the extremity of the eastern lobe. The jet radio knots on the west side of the source are seen with a clear path from the AGN to the hotspot (see also Fig. 5.3).

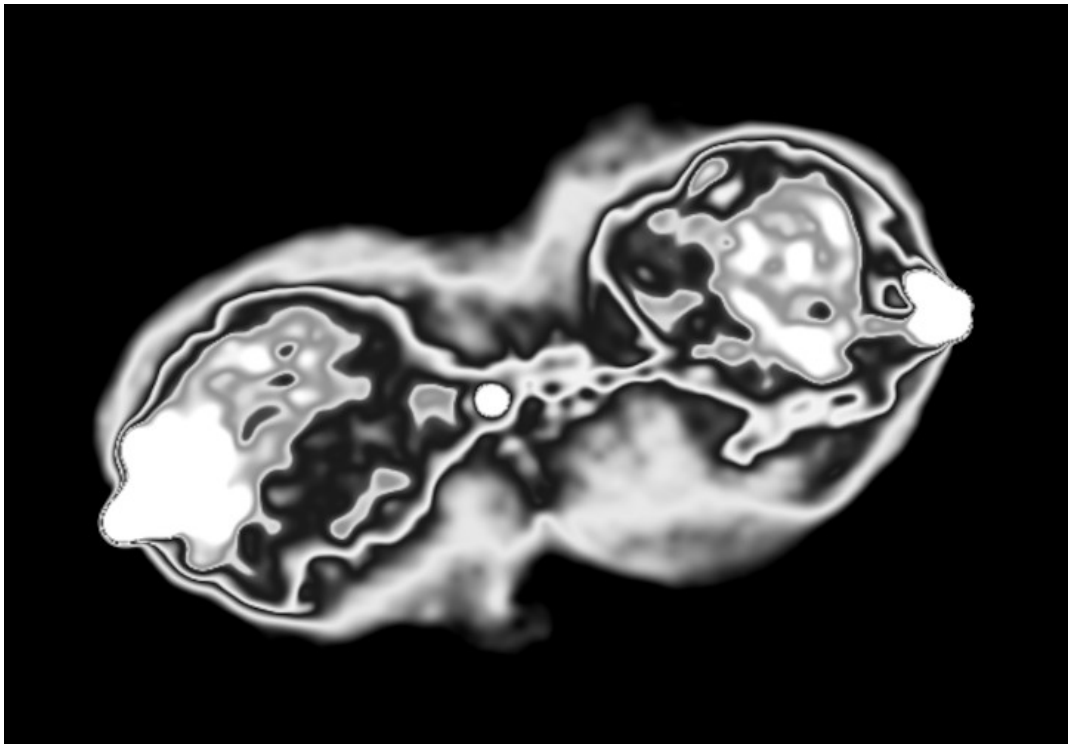

Figure 5.3: This visualisation (made using GIMP) emphases both low and high emission structures in Pictor A. The full extent of the jet is more amplified.

From the spectral index analysis presented in Sec. 5.2.2.2, the spectral index of the primary hotspot (inner) is -0.76 and of the secondary (outer) hotspot is -0.79 with standard deviations of 0.01 and 0.021 respectively (we define the relationship between spectral index, α, and integrated flux density, S, as $S_\nu \propto \nu^\alpha$). Assuming that the spectral index provides a good representation of the emission's age, the spectral index of the hotspots suggests that the primary hotspot is younger than the secondary – consistent with the prediction by the Dentist drill model. However, the difference in the spectral indices is minimal – comparable to the spread (standard deviation) in the spectral index distribution within the hotspots; thus, it cannot provide strong evidence for the age difference between them.

5.2.2 *Lobes*

The notably round radio lobes are also visible from Fig. 5.2 are consistent with those seen in previous studies, except that our data reveals more diffuse emission due to higher sensitivity. The eastern lobe has an integrated flux density of 20.9 Jy, and the western lobe of 20.5 Jy, leading to a flux density lobe ratio of the eastern to western lobe of ~ 1.02. Radio filaments within the lobes are also observed similar to those seen by Perley et al. (1997). These filamentary structures are known to form as a result of shearing and strengthening of weak magnetic fields due to the dynamo amplification effect in filamentary regions (see Clarke, 1996; Donnert et al., 2018, for MHD simulation and details of the dynamo effect).

The 'un-jetted' lobe has also been shown to be associated with a slightly steeper spectral index (see also our spectral indices in Sec. 5.2.2.2) and is thought to be spatially smaller owing to higher pressure from its denser environment (Perley et al., 1997). This high pressure was speculated to enhance its magnetic field, leading to a higher observed spectral age (Liu and Pooley, 1991a; Liu and Pooley, 1991b). Similar to Perley et al. (1997), we find the length ratio of the western to the eastern lobe to be 1.19 and a comparable ratio between the widths, indicating that the western lobe is larger. However, this could also be a projection effect.

In Figs. 5.2 and 5.4, we also note a region akin to what Carilli and Barthel (1996) call 'radio plumes'. In Pictor A's case, plumes appear midway between the lobes on both the far south and north of the lobe emission. These plumes appear as emission 'spilling' from the central lobe emission. Carilli and Barthel (1996) attribute plumes to the displacement of radio-emitting plasma away from the galactic core due to pressure gradients from the intracluster medium. Hardcastle et al. (2016) also pointed out that diffuse X-ray emission appeared to extend beyond the visible lowest VLA data radio contour at 0.6 mJy (see fig. 1 of Hardcastle et al., 2016) at the 'waist' of the source. This contradicts expectations since the X-ray lobe emission is suggested to be IC in origin; thus, we expect to see the spatial superposition of the X-ray and radio. The missing radio emission was attributed to either 1) the limited sensitivity of the VLA at the time, 2) the X-ray emission being thermal in origin within these regions, or 3) the radio emission being too faint or of steep-spectrum.

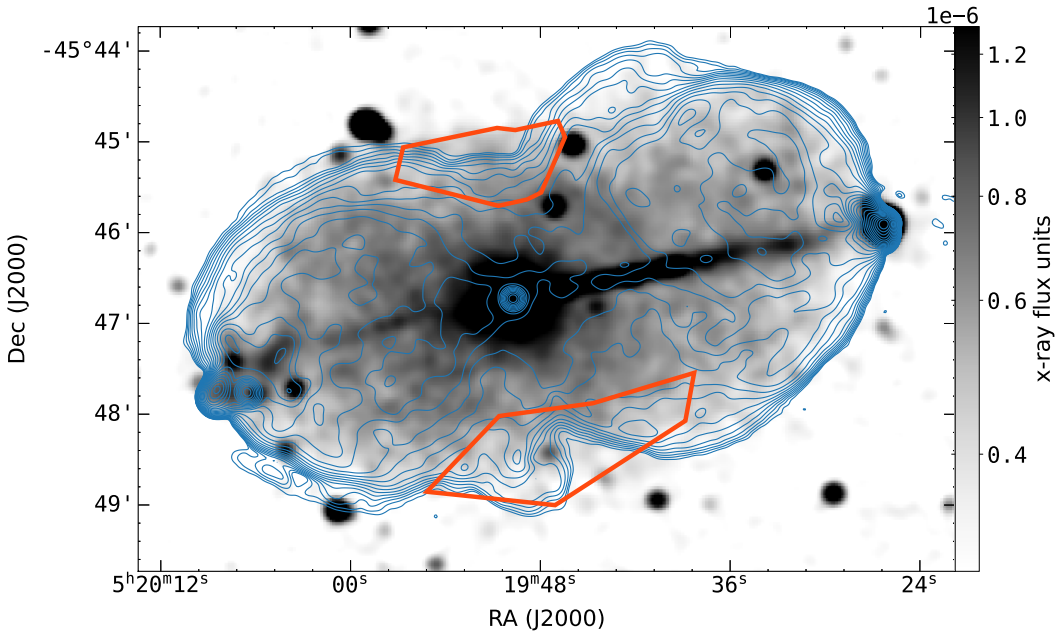

Figure 5.4: The Pictor A Chandra X-ray image from Hardcastle et al. (2016) made with 0.5–5.0 keV passband data (in greyscale) overlaid with radio emission contours from our data (in blue) at ∼7.5″ resolution. Contours start from 0.6 mJy beam^{-1} similar to Fig 1 of Hardcastle et al. (2016), and separated by a factor of $\sqrt{2}$. The X-ray image was convolved to a resolution similar to our radio data and is shown in a log scale to emphasize the low-level emission. The orange polygons show a region previously identified by Hardcastle et al. (2016) as a region with missing radio flux emission. This radio emission is visible in the image. The X-ray jet is also excellently aligned with the radio jet.

Fig. 5.4 shows an X-ray image of Pictor A in greyscale from Hardcastle et al. (2016) overlaid with contours from our radio data. The lowest radio contour here is 0.6 mJy beam^{-1}, with consecutive contours separated by a factor of $\sqrt{2}$. The previously unseen radio emission is visible (marked by the orange polygons whose exact region definitions are shown in App. A.5), consistent with the suggestion that X-ray lobe emission is predominantly of IC/CMB origin. However, Hardcastle et al., 2016 pointed out that the soft-thermal emission cannot be ruled out.

5.2.2.1 *Radio Jets*

Pictor A's jets are remarkably visible in the X-rays (e.g. see Fig. 5.4 and Wilson et al., 2001; Hardcastle et al., 2016), the western jet clearly shows to extend from the core and terminates at the hotspot (∼ 174 kpc). The jets emission was determined to be of synchrotron origin (Hardcastle et al., 2016). While the western radio jet was slightly noticeable in the study of Perley et al. (1997) using the VLA data, the authors remarked that it was very faint and was best visible on a TV monitor. We show for the first time in Fig. 5.2 a more pronounced western radio jet from the radio

nucleus to the WHS. Although this radio jet remains unresolved, it is collimated and consists of a series of elongated knots, similar to those observed by Carilli and Barthel (1996) on the jets of Cygnus A. These knots were also partially observed in optical frequencies using the Hubble Space Telescope (HST) by Gentry et al. (2015). This radio jet has a position angle (as per the IAU convention) of $\sim 281 \pm 1^{\circ}$ and runs from the centre of the radio core to about $1.93'$, after which its emission diffuses into the western lobe. Though the jet becomes indistinguishable at this point, tracing it along this position angle leads directly to the WHS.

By contrast, the counter-jet is still not detected in radio images. Although discernible in the X-ray, it seems to diffuse into the lobe emission near the nucleus and hotspots (Hardcastle et al., 2016). Our findings are consistent with those of the previous studies; there is no discernible counter-jet. This apparent jet single-sidedness in a radio galaxy like Pictor A's (in Fig. 5.2) could result from the Doppler boosting effect that makes the jet closer to the observer appear brighter and more visible.

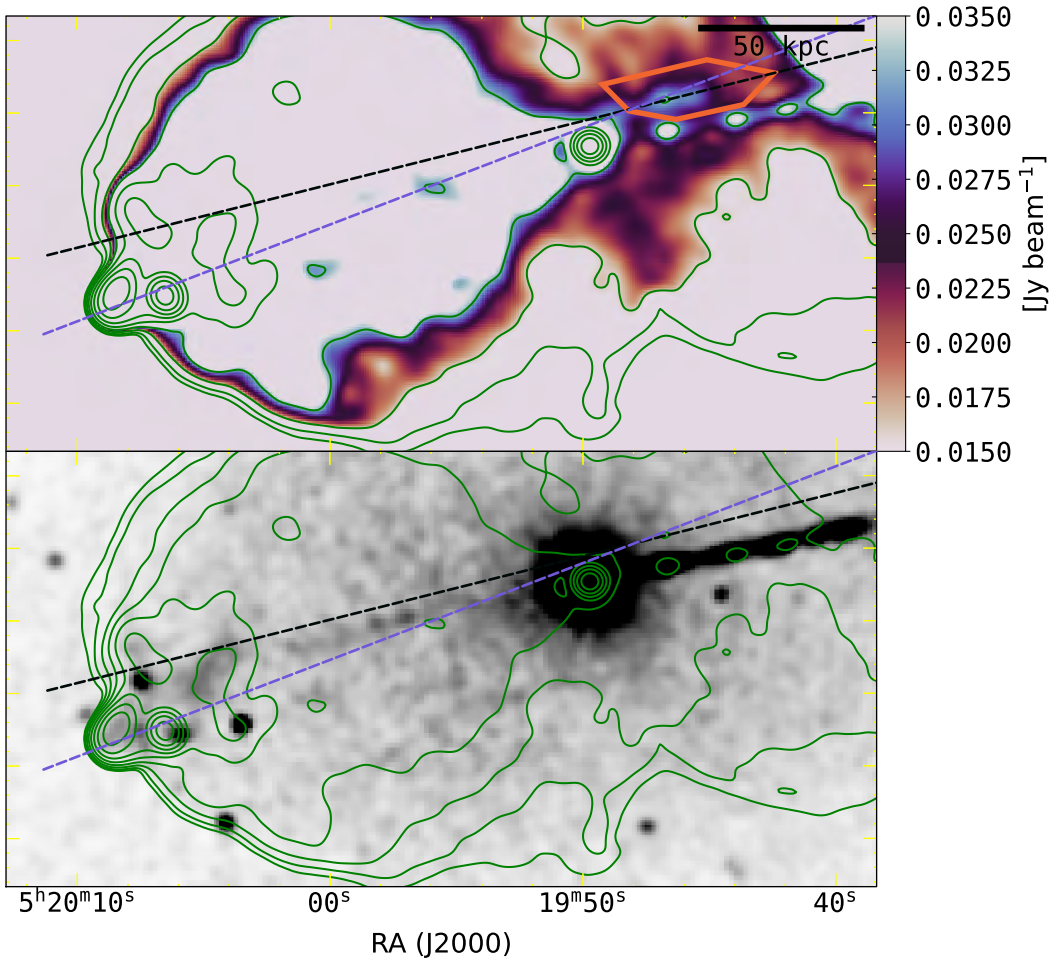

Figure 5.5: A novel collimated feature reminiscent of a radio jet observed from our data. The top panel highlights this feature marked by the orange polygon. The green contours show the radio emission, while the straight lines show the possible extension of the paths of this feature. The bottom panel shows the X-ray image superposed with the same radio contours as the top panel. The straight lines are also drawn at the same position.

Fig. 5.5 shows a feature near and North-West of the AGN reminiscent of a radio jet due to its semblance in total intensity and collimation to the jet's emission rather than the neighbouring lobe emission. To our knowledge, this feature was not seen in previous radio images and may be of interest in the future. Since this feature is not directly aligned with the WHS and the core, it is difficult to tell conclusively. Nevertheless, we drew two possible lines based on the knot extension

Table 5.1: Mean spectral indices for selected regions within Pictor A. The mean frequency is 1.21 GHz. The last column of this table shows the number of independent beams that fit in the specified regions within the source.

Region	Mean α	Std Deviation α	Beams
E-lobe	$-0.88 \pm 2.0 \times 10^{-4}$	0.09	291
W-lobe	$-0.85 \pm 3.7 \times 10^{-4}$	0.08	382
E-Hotspot (inner)	$-0.76 \pm 6.4 \times 10^{-6}$	0.010	2
E-Hotspot (outer)	$-0.79 \pm 3.0 \times 10^{-5}$	0.021	3
W-Hotspot	$-0.64 \pm 2.0 \times 10^{-4}$	0.085	11
Core	$-0.48 \pm 2.0 \times 10^{-5}$	0.27	5
Plume	$-1.02 \pm 7.0 \times 10^{-4}$	0.074	38
Waist	$-0.94 \pm 3.1 \times 10^{-4}$	0.12	223

to trace its extension towards the lobe's extremity. To our knowledge, this feature was not seen in previous radio images and may be of interest in the future.[2]

5.2.2.2 *Spectral Index*

As a result of the excision of data affected by RFI, we generated our spectral index map using a frequency range smaller than that of the MeerKAT telescope's L-band, 0.89–1.64 GHz, using the `spimple` tool. We consider $0 > \alpha \geq -0.7$ as flat and $\alpha < -0.7$ as steep.

The top panel in Fig. 5.6 reveals that both lobes have fairly similar spectral indices, with a mean of $\langle\alpha\rangle = -0.86$. Furthermore, the WHS pair displays a steeper spectral index of $\langle\alpha\rangle = -0.76$ and -0.79 for the inner and outer hotspots, respectively, compared to that of the WHS $\langle\alpha\rangle = -0.64$, while the radio core has $\langle\alpha\rangle = -0.48$. These values are summarised in Table 5.1.[3] In that table, we also indicate the number of independent beams that fit within the specified region of Pictor A rounded off to the nearest integer. They were obtained by dividing the region area by the beam's area.

In contrast, the source's waist region displays significant spectral steepening away from the core and towards its periphery along the north and south edges. These spectral indices align well with the observations of Perley et al. (1997), who stated a value of $\langle\alpha\rangle = -0.8$ for the lobes and noted that the eastern lobe has a steeper spectrum than the western lobe. However, we found a maximum of $\alpha \sim -1.3$ along the waist compared to Perley et al.'s -1.7. Errors associated with our spectral index fitting are shown in the bottom panel of Fig. 5.6. Higher error areas appear to be associated with the lobe's edges. We attribute this to low signal-to-noise along those regions coupled with edge effects. The 'stripy' structure on both maps results from residual calibration artefacts.

This type of spectral variation is typical of FR-II sources. Usually, the hotspots and core exhibit a flatter spectrum, while the lobe exhibits a generally steeper spectrum. For Pictor A, this is true except for the eastern hotspots, with spectral indices comparable to the lobes. Flat spectral indices indicate the presence of younger electrons, and conversely, a steeper spectral index indicates older electrons. Our map shows that the age of electrons increases away from the core in the N-S direction.

Spectral ageing is thought to occur due to more energetic electrons radiatively losing their energy faster in the absence of acceleration, resulting in spectral cooling and a steepened spectrum. Models such as the Kardashev–Pacholczyk (KP) and Jaffe–Perola (JP) have been proposed to predict the energy spectral shapes resulting from spectral ageing (see Harwood et al., 2013, for a summary and references therein for a complete treatment). These models assume a fixed magnetic field strength

2 Its exact region is defined in App. A.3.
3 The region definitions of the components are in App. A.6.

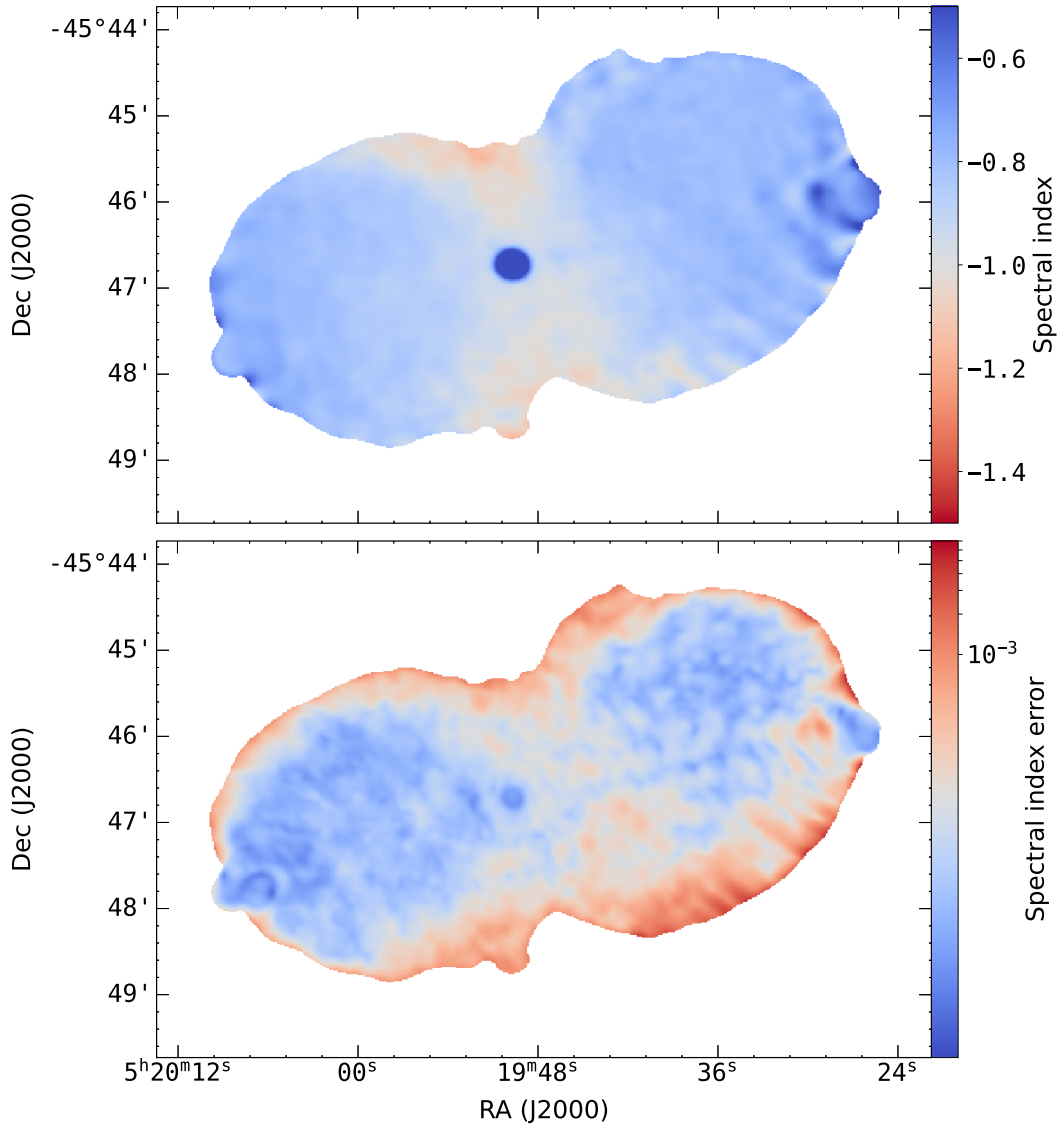

Figure 5.6: The spectral index map generated using channelised images between 0.88 and 1.65 GHz at a resolution of 11″ by 10″ (top panel). The spectral index colour bar ranges from −0.5 to −1.2. Spectral steepening is seen towards the waist of Pictor A, while the core shows a flat spectral index. The bottom panel shows errors associated with spectral index fitting, whereby higher errors are associated with the lobe edges.

across the source and a single injection electron distribution at the jet termination points. However, to factor in a more realistic magnetic field structure, Tribble (1993) introduced more advanced spectral ageing models that assume a Gaussian randomly varying magnetic field that allowed electrons to diffuse with the varying field strengths. Identifying the more accurate model without deeply understanding the underlying physical processes is difficult. Unfortunately, the relatively limited bandwidth of our current data confines the extent to which we can probe the spectral behaviour of this source. Thus, studies with a broader bandwidth coverage will be invaluable in better characterising the spectral indices of Pictor A.

5.3 Polarimetry

5.3.1 *Linear Polarised Intensity and Fractional Polarisation*

Fig. 5.7 shows the linear polarisation (top) and degree of polarisation across the lobes of Pictor A at 1.65 GHz and 11″ by 10″ resolution. We compute the polarised brightness using Eqn. 3.2. High linear polarisation in Pictor A is found at the hotspots, within the western lobe's filamentary structure and close to the WHS. This is similar to the findings of Perley et al. (1997). There seems to be no correlation between filaments in the total intensity image and those in the polarised brightness distribution.

The degree of polarisation (fractional polarisation), p, as earlier introduced in Sec. 3.2.1. We obtained images of p from the sub-band I maps as described in Sec. 5.1. No Ricean bias correction was made for any of the images.

High degrees of polarisation are seen around the edges of Pictor A, and a single filamentary structure located at around RA $5^{\mathrm{h}}19^{\mathrm{m}}41^{\mathrm{s}}$ and Dec $-45^{\circ}46'00''$. In this figure, the colour bar is representative of the degree of polarisation. Levels of the fractional polarisation over most of the lobes' regions are below 10 per cent, whereby the western lobe demonstrates more regions with higher fractional polarisation values than the eastern lobes. As noted by Perley et al., there seems to be no correlation between the regions of higher total intensity and fractional polarisation. Their observations at 7.5″ resolution showed that some regions displayed up to 70 per cent fractional linear polarisation. From our data in Fig. 5.7, a few regions within the western lobe also appear to show a degree of polarisation approaching 60 per cent. It should be noted that a range of frequencies was used in the study by Perley et al. (1997), including some significantly higher than those used in this study. Hence, the maximum degrees of polarisation may not be directly comparable.

5.3.2 *Line-of-Sight Fractional Polarisation*

Fig. 5.8 shows polarisation structures for the individual LoSs across the lobe of Pictor A. We have 2389 LoSs across Pictor A, spatially separated by approximately 6″. These LoSs were chosen using the criteria of having a signal-to-noise ratio (SNR) above 50 in total intensity image at 1 GHz. For illustration, we can only show eight of the LoSs. The left column is the degree of polarisation as a function of wavelength-squared, and the middle column consists of the unwrapped polarisation angle as a function of wavelength-squared in blue points and the fitted linear model in green dashed lines. The third column is the cleaned Faraday spectrum (cleaned FDF) in black. In this plot, the top three rows highlight examples of LoSs with a single peak in the FDF, the fourth and fifth rows show examples with double peaks, and the last three rows show examples with multiple peaks. The lobes of Pictor A are dominated by single-peaked FDF.

Quantitatively, ∼43.5 per cent of the LoS exhibited Faraday spectra with a single dominant peak such as those illustrated in row one of Fig. 5.8. Additionally, we found that for these single-peaked LoS, ∼78 per cent showed a maximum fractional polarisation greater than 10 per cent, while ∼33 per cent showed fractional polarisation of more than 20 per cent. On the other hand, ∼32.6 per cent of the single-peaked LoS spectra showed a wide base and/or smaller peaks on either side (such as those of rows two and three of Fig. 5.8). We also found that ∼23.5 per cent of the spectra showed double peaks (e.g. those in rows 4, 5 and 6 of Fig. 5.8), while spectra of some of the regions neighbouring each other that show a drastic RM changes are associated with more than two peaks (rows 7-8 in the same figure). The remaining ∼0.3 per cent of Los spectra were deemed to be noisy.

Shown in Fig. 5.9 are the locations of these various categories of spectra, whereby LoS spectra with single, single wide base, and multiple peaks are represented by green, blue and orange respectively. Noisy regions are represented by purple. Fig. 5.9 also highlights the positions of the LoSs exem-

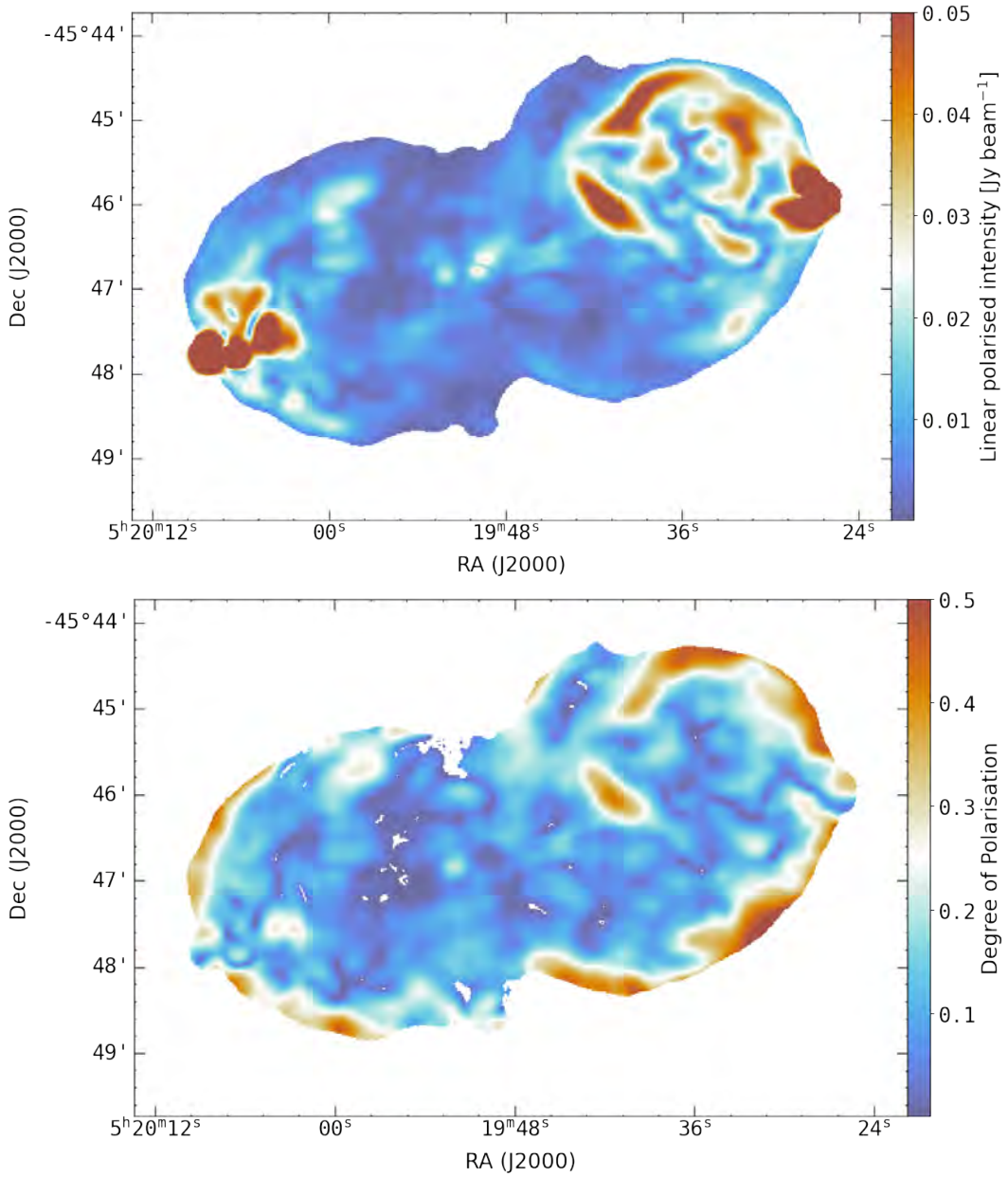

Figure 5.7: The linear polarised intensity across Pictor A (top panel) and the degree of polarisation (bottom panel) at 1.65 GHz, whereby the hotspots and radio filaments show the highest amounts of linear polarisation. Both images are at 11″ by 10″ in resolution, and the top panel's units are in Jy beam^{-1}.

plified in Fig. 5.8 using yellow outlines and labels. These LoS have also been labelled accordingly. Pictor A's LoSs are available at `https://pica.ratt.center/` displayed using the `PolarVis` tool (Andati et al., 2023a, introduced and discussed in Sec. 6.1), which allows the visualisation of various diagnostic plots associated with the specific LoSs.[4] The LoSs and their corresponding interactive plots were generated using `Scrappy`, another `Python`-based tool that semi-automates generation of the LoS depending on a user's specifications (this tool is also introduced and discussed in Sec. 6.2).[5] We probed further into regions showing RM gradients and double peaks to determine if these effects were real. This is discussed in Sec. 5.3.6. The behaviour of fractional polarisation vs λ^2 is quite complex, even for single-peaked spectra. In some cases, repolarisation appears to occur at longer wavelengths with highly oscillatory structure. The position angle vs λ^2 mostly exhibits linearity except for the double and multi-peaked spectra. On the other hand, the double

4 `https://github.com/Mulan-94/polarvis`
5 `https://github.com/Mulan-94/scrappy`

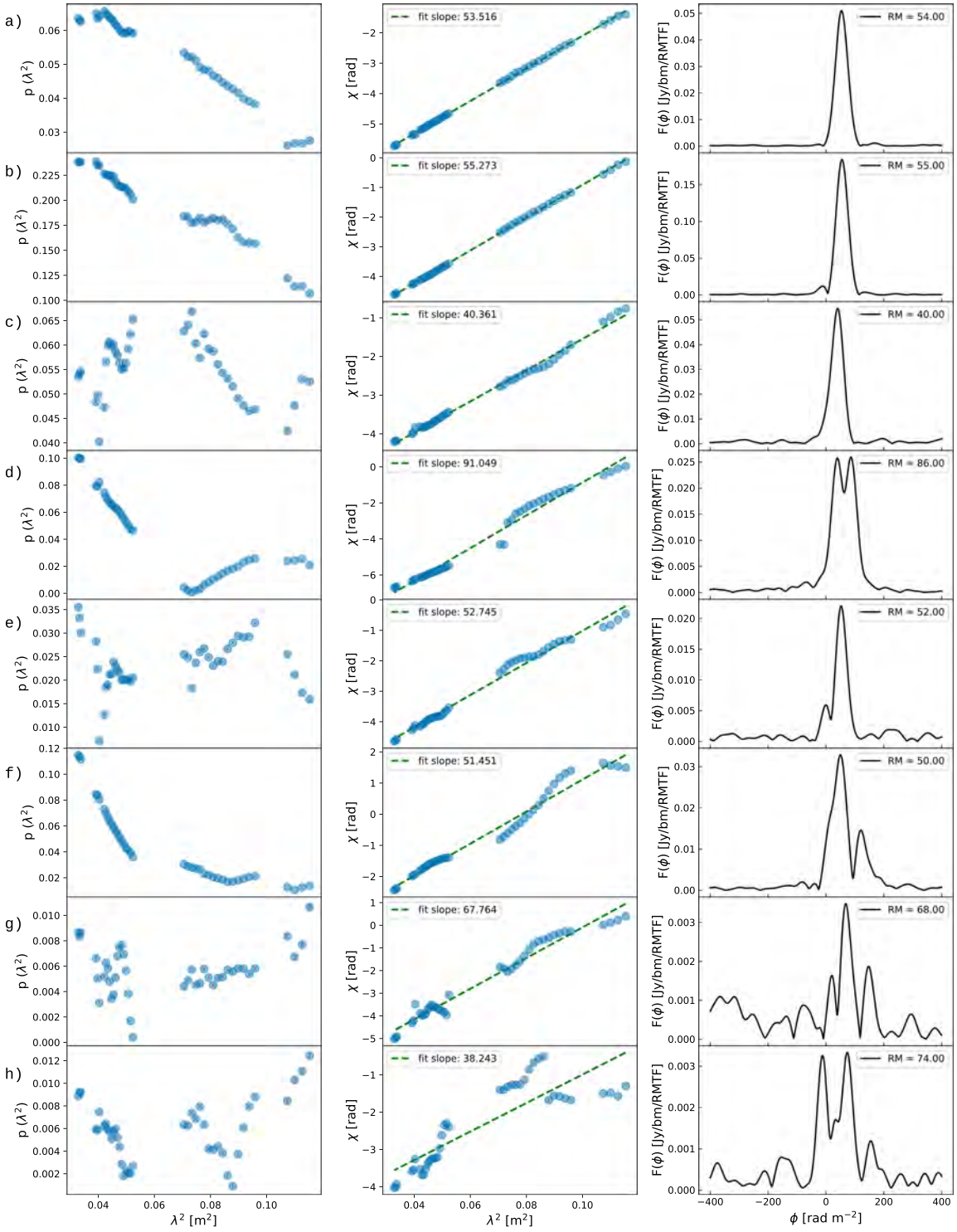

Figure 5.8: The polarisation behaviour of example LoSs across the lobes of Pictor A. Left column: fractional polarisation vs λ^2. Middle column: polarisation angle vs λ^2 superimposed by a linear fit (green dashed line). Right column: the RM-cleaned Faraday spectra are represented. RM values shown on the legend of this column indicate the position in Faraday depth of the Faraday spectrum's highest peak. The RMTF is shown in Fig. 5.1.

and multi-peaked Faraday spectra show a wide range of behaviour: in some LoSs the components are well resolved, and in some cases, the components are blended. The spectra of the last row resemble that of a Burn-slab (Burn, 1966) – a region in which polarised emission and Faraday ro-

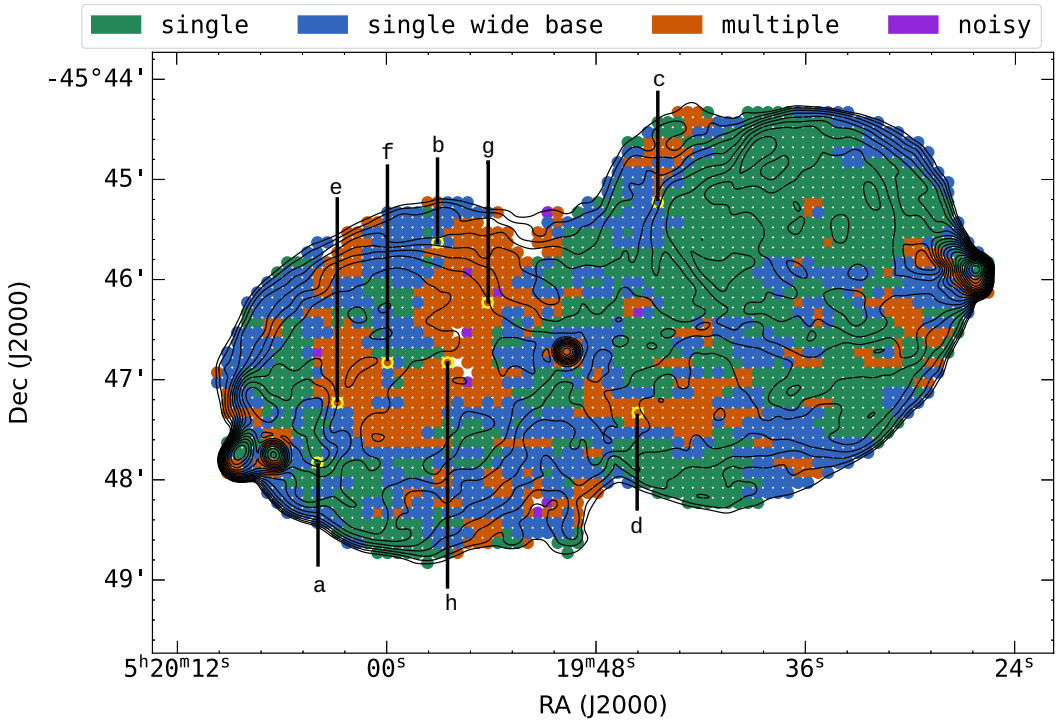

Figure 5.9: Locations of the various categories of LoS Faraday spectra exhibited by Pictor A. Most of the LoSs show Faraday spectra with a single dominant peak (shown in green). In other cases, this single peak has a wide base or an additional smaller peak on either side (in blue). This source also exhibits multiple peaks in some regions (represented by orange). Noisy LoSs are represented by purple. Lines-of-sight outlined in yellow are those exemplified by Fig. 5.8, and are labelled accordingly.

tation occur simultaneously. It is evident that the polarisation behaviour across the lobes of Pictor A is complex.

5.3.3 *Depolarisation*

Depolarisation, as introduced in Sec. 3.2.3, refers to decreased observed fractional polarisation as a function of resolution or frequency. It can result from effects internal to the source (due to mixed thermal and magneto-ionised gas) or external to the source (such as beam depolarisation) as highlighted by Burn (1966) and Sokoloff et al. (1998) and manifests more prominently at the longer wavelengths (lower frequencies). Depolarisation can be quantified using a ratio of fractional polarisation measurements at two different frequencies or resolutions – i.e. the depolarisation ratio.

In Fig. 5.10, we show the depolarisation ratio map obtained by dividing the fractional polarisation map at 0.88 GHz with a map at 1.65 GHz, both at 11″ by 10″ resolution. The depolarisation is expected to be stronger at longer wavelengths; thus, a depolarisation ratio of < 1 (the bluer) suggests a depolarised region, while >1 (redder) suggests a re-polarising region. Here, we show only regions where the fractional depolarisation error[6] was less than 0.6. We find that the eastern lobe shows more depolarisation than the western lobe, particularly in the extreme lobe region – consistent with the results of Perley et al. (1997), with some patches of re-polarisation. This map bears a striking boundary separating the two lobes. The depolarisation or re-polarisation may be caused by unresolved Faraday structures (beam depolarisation) or internal mixing of thermal and ionised gas within the lobes. Our data are insufficient to determine the actual cause for the depolarisation and re-polarisation within the lobes of Pictor A. However, these depolarisation ratios must be interpreted cautiously, particularly because of our narrow bandwidth and significant variations in

6 I.e. the standard propagated depolarisation error ratio divided by the depolarisation ratio.

fractional polarisation vs λ^2 (left column of Fig. 5.8). The re-polarisation may not necessarily be real or true but a result of limited bandwidth, because a lack of higher frequencies constrain the degree of polarisation in the absence of Faraday rotation.

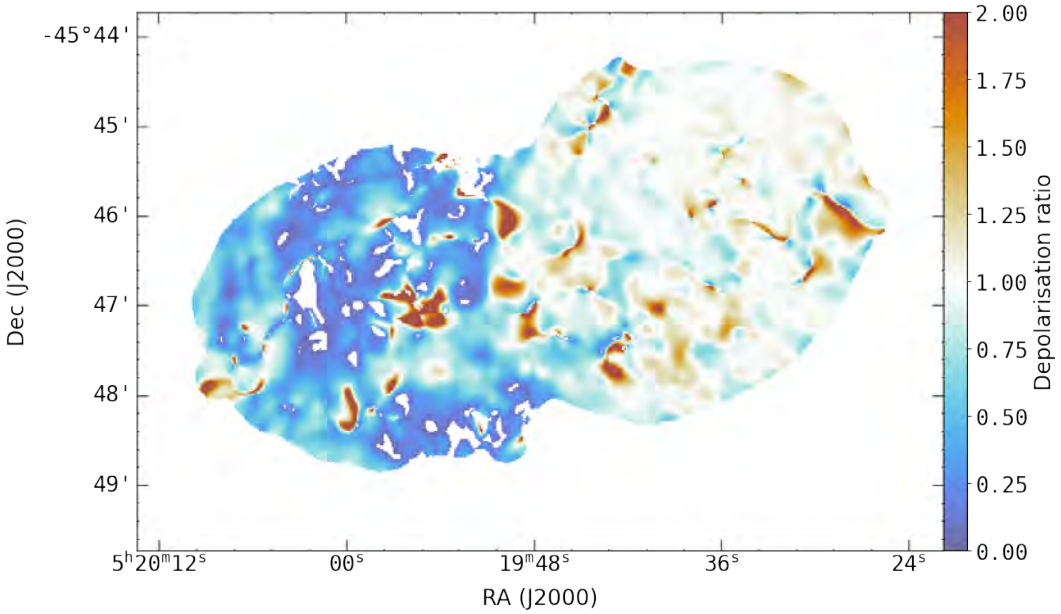

Figure 5.10: The depolarisation ratio obtained by taking a ratio of the fractional polarisation map at 0.88 GHz and 1.65 GHz, both at 11″ by 10″ resolution. The eastern lobe shows more depolarisation than the western lobe. Here, values > 1 (towards bright red) show re-polarisation, while those < 1 (towards deep blue) show depolarisation. Only data where the depolarisation error to depolarisation ratio was > 0.6 are shown. Higher errors are associated with the eastern lobe.

Supporting depolarisation profiles of both lobes are also shown in Fig. 5.12 as a function of distance from the radio core, obtained by sub-dividing the source into box regions of 30″ in width[7] along the jet axis as illustrated in Fig. 5.11, and calculating a simple mean, median, and standard deviation from our depolarisation map within the bins. The western lobe of this source shows consistent behaviour across the lobe, with values centred around a depolarisation ratio of 1, indicating little to no depolarisation. Contrastingly, the eastern lobe shows a more erratic spread with no particular trend with increasing core distance.

The asymmetric depolarisation observed, where the jet-sided lobe depolarises slower than its counterpart, has previously been defined as the Laing-Garrington effect (Laing, 1988; Garrington et al., 1988). This is an orientation effect that affects the lobe further from the observer because its emission undergoes more depolarisation effects resulting from passing through a longer path length along the magneto-ionic halo of its host galaxy. Asymmetric depolarisation is a common feature in FR-II sources e.g. Goodlet et al., 2004; Ishwara-Chandra et al., 1998. Assuming the eastern lobe is further, its higher observed depolarisation could result from external Faraday dispersion. This means that its emission may go through various turbulent magneto-ionised cells along a LoS towards the observer, which causes depolarisation and a resulting low polarised signal. Even so, higher frequency observations are required to properly characterise the depolarisation behaviour of Pictor A's lobes.

5.3.4 *Faraday Rotation Measures*

We performed pixel-by-pixel RM-synthesis across the entirety of Pictor A, resulting in the RM map shown in the top panel of Fig. 5.13. Its colour bar ranges between 0 and 60 rad m^{-2}. Each pixel

7 Except for the bin encompassing the radio core, whereby the width is $\sim 20''$. The radio core region was excluded from these bins. The exact region definitions are presented in App. A.7

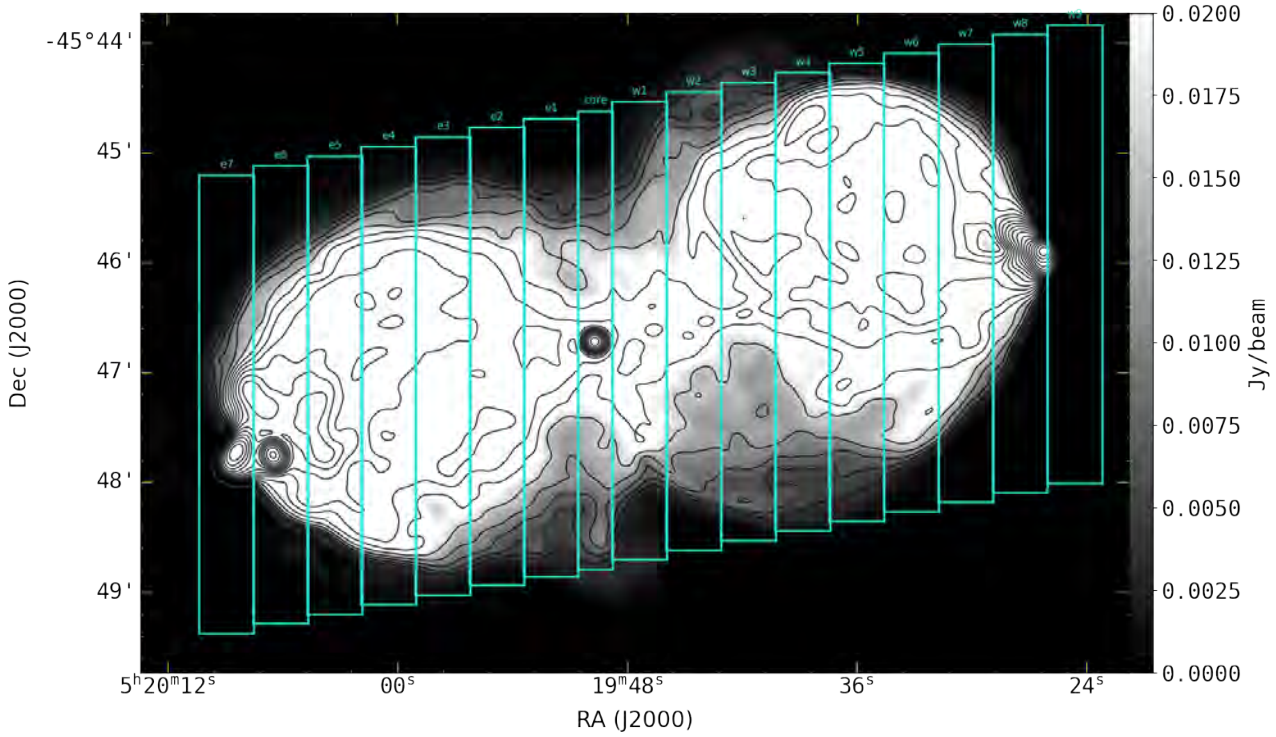

Figure 5.11: The regions used for determining RM and depolarisation profiles with increasing distance from the radio nucleus.

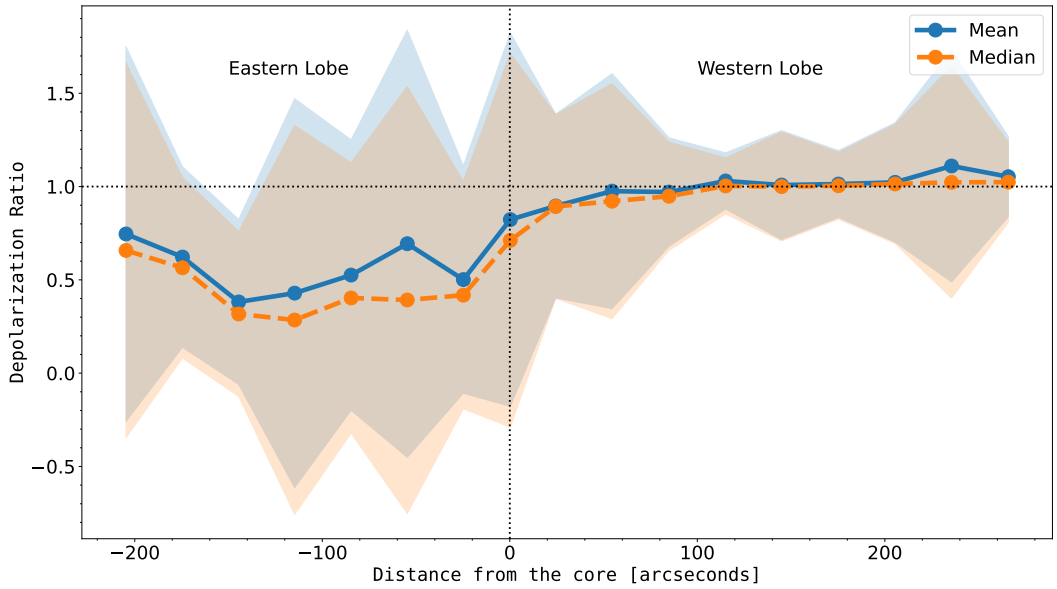

Figure 5.12: The binned depolarisation ratio with distance from the radio core. Data points were obtained by subdividing Pictor A into rectangular regions of 30″ in width along the jet axis and calculating the mean, median and standard deviation of data within those regions. The standard deviation is shown in the filled coloured patches, while the solid and dashed lines indicate the mean and median, respectively. For clarity, we also show a dotted line at a depolarisation ratio of 1. Negative distances indicate a leftward direction from the radio core, while positive ones indicate a rightward direction. The vertical dashed line indicates the core's position.

value in this map represents the Faraday depth corresponding to the highest peak of the cleaned Faraday spectrum. We only show rotation measures in regions of the source whereby $p_{\rm err}/p < 0.6$, in addition to masking out unphysical values (i.e. where $p \neq [0, 1]$). Our lobe edges are the regions where the total intensity falls below 4 mJy beam^{-1}.

Generally, the RM distribution seems relatively similar across the entire source, whereby our derived mean RM for the source was 48 rad m^{-2} with a standard deviation of 10.2 rad m^{-2}. The per lobe RM distribution showed mean RMs of 49.7 for the eastern lobe and 46.7 rad m^{-2} for the western lobe, with widths of 14.4 and 4.5 rad m^{-2} respectively. However, patches of significant and sudden RM gradients are observed, especially within the eastern lobe, forming boundary-like structures. A few regions also exhibit negative RMs, such as those near the waist region towards the eastern lobe.

Perley et al. found the average RM to be approximately 43.5±1.4 rad m^{-2}, with the RM for each lobe falling within the margin of error in the L-band. For a more direct comparison, we used our defined lobe boundaries and the VLA L-band RM maps made available to us to extract the per lobe RM distribution from the VLA data. This test yielded RMs for the VLA data centred around 55 and 52 rad m^{-2} and widths of 10.8 and 6.4 rad m^{-2} for the eastern and western lobes, respectively. Furthermore, the eastern lobe displays a broader variation than the western lobe in good agreement with the observations of Perley et al. The difference in our mean values may be attributed to either a small systematic error in the L-band position angles in Perley et al. (1997), coupled to a small λ^2 interval, or our high spatial sensitivity. The spread in the RM distribution is not significantly different for each distribution. Simple statistics were also performed based on this RM map to characterise the rotation measure behaviour with distance from the core as illustrated in Fig. 5.14. The variability of the eastern lobe's RMs is more erratic than the western lobe, with regions closer to the core showing more variation. Haverkorn (2015) showed that Galactic contributions within spatially co-located RM largely correlate, making the estimation of contribution on individual LoSs possible. Therefore, we estimated the Galactic contribution towards Pictor A (galactic longitude of 251.6° and latitude −34.63°) by taking the mean and standard deviation of Galactic RM measurements derived by Hutschenreuter et al. (2022) (these authors used Bayesian inferencing to cater for noisy data). We found a mean of 23.57 rad m^{-2} and mean standard deviation of 10.87 rad m^{-2} estimated over a 5° region. Our Galaxy may contribute to the mean RM, but it cannot explain the small-scale fluctuations, suggesting that some fraction of the observed RMs may result from the intergalactic medium, X-ray gas or other unknown intervening material.

5.3.5 *Magnetic Fields*

The bottom panel of Fig. 5.13 shows the orientation of the projected magnetic field (electric field rotated by 90°) overlaid on top of the cleaned and integrated Faraday spectra map (obtained by integrating Eqn. 11 of Burn (1966)). We set the length of the field vectors to 1 for demonstration purposes. The magnetic field vectors align along the edges of the lobes. Such alignment is common in radio galaxies (see Taylor et al., 1990; Eilek and Owen, 2002; Heald et al., 2009; Sebokolodi et al., 2020). Work by Laing (1980) ascribes this effect to the shearing and compression of originally random magnetic fields, making them tangential to the source's boundaries. They argue that the coexistence of aligned magnetic fields and regions of a high fractional polarisation only suggests the constriction of the magnetic field to planes along a LoS and not necessarily an originally uniform magnetic field. Moreover, the projected magnetic field vectors also align along the highly linearly polarised filamentary structures within the lobes, especially in the western lobe.

Magnetic fields along the jet also appear to be oriented perpendicular to the jet axis (see bottom panel of Fig. 5.13). This orientation is uncommon for FRII sources, which typically show magnetic fields parallel to the jet axis. However, such perpendicular alignment can result from perturbed jet flows (Bridle and Perley, 1984). According to Bridle and Perley (1984), magnetic fields with this configuration within knots of such jets could result from oblique shocks that accelerate relativistic

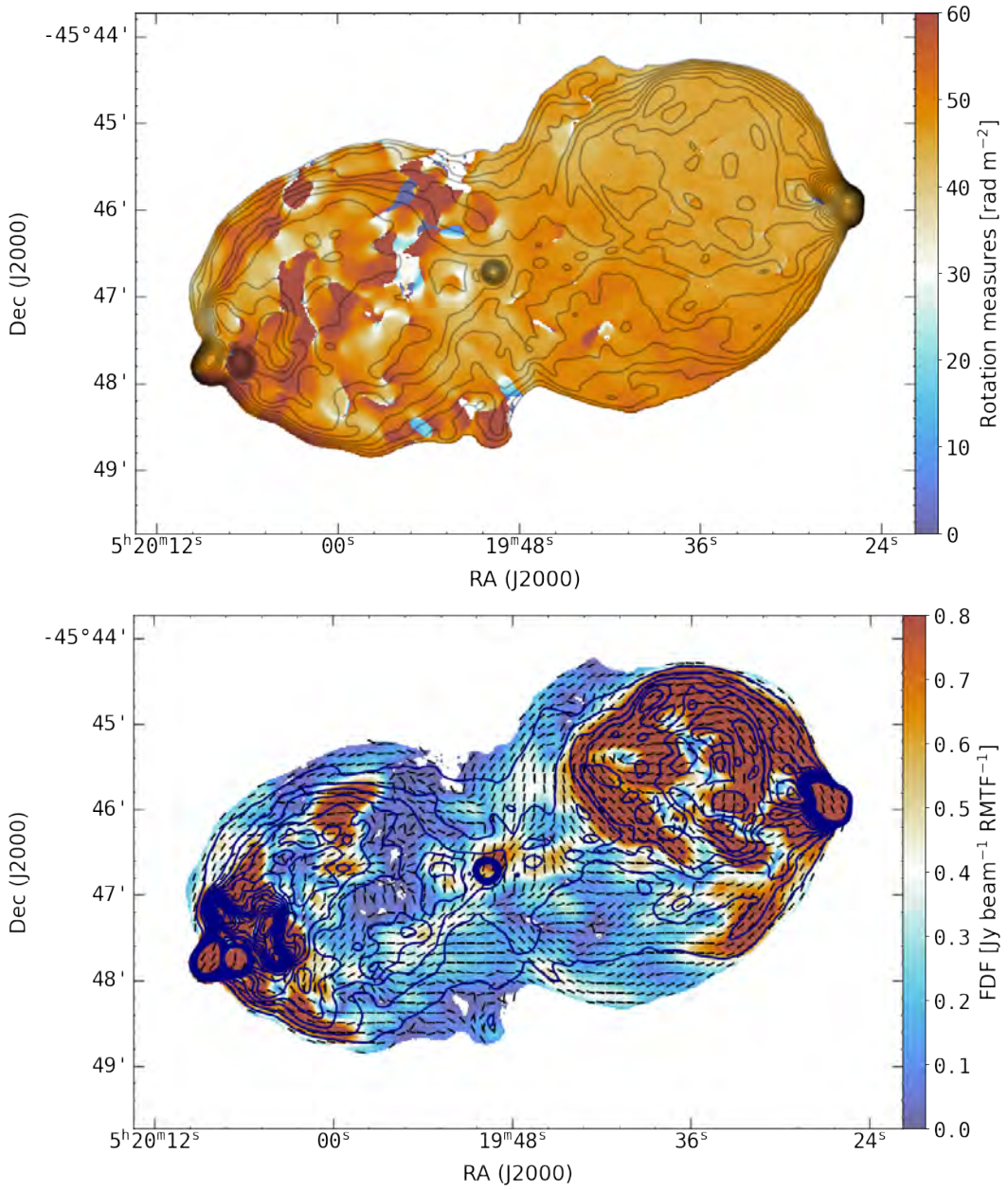

Figure 5.13: Top panel: The rotation measure map of Pictor A overlaid by Stokes I radio contours. The RMs across the western lobe are generally smooth, while those across the eastern lobe exhibit more variability. Bottom panel: The polarised intensity map obtained from integrating the cleaned FDF (Eqn. 11 of Burn, 1966), superimposed by the projected magnetic field vectors (polarisation vectors rotated by 90°) whose length is set to 1. We also overlay total intensity contours ranging from 0.01 to 0.2 Jy/beam with a step of 0.1 Jy/beam. The field orientation is well aligned along the lobe edges and the filamentary structures. Both maps are at 11″ by 10″ resolution.

particles and amplify the magnetic field component parallel to the shock, making the perpendicular field component more dominant.

5.3.6 *RM Gradients and Multiple-Peaked Faraday Spectra*

In this section, we investigate the cause of the observed RM gradients across Pictor A radio lobes and the presence of Faraday spectra with a single-peak and a wide base, or multiple-peaks. We find that many LoS with sudden RM changes show multiple high FDF peaks, making it difficult to differentiate from sidelobes. Furthermore, they had much lower polarised emission (the lowest

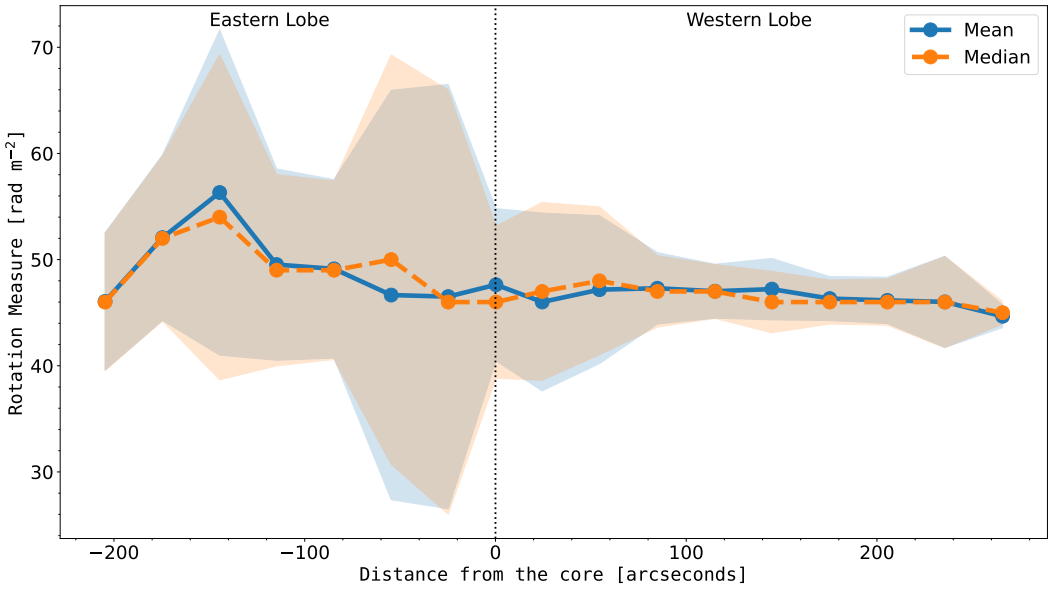

Figure 5.14: Binned rotation measure profiles with increasing distance from the radio core of Pictor A. The separation of these bins and the distances indicated are similar to those stated in Fig. 5.12. RMs in the western lobe show a decreasing variation with increasing distance from the radio core.

polarised SNR per LoS ranged between 0.4 and 2). The largely flagged out λ^2 data samples could also contribute to this issue because a reduction in the number of λ^2 samples has been shown to increase the RMTF sidelobes (see Fig.7 of Brentjens and de Bruyn, 2005). A combination of low SNR and large gaps in λ^2 resulted in higher and erratic side lobes on the deconvolved Faraday spectra (due to sidelobes on the RMTF as illustrated in Fig. 5.1), thus, unstable solutions.

However, there are regions of high polarised SNR (up to two or three orders of magnitude) showing double/multiple peaks and high RM gradients. These often consist of one dominant peak and a secondary one of lesser intensity, while others show more than two peaks. Spectra showing more than a single peak appear to show "more" complex behaviour in the fractional polarisation as a function of wavelength. In most cases, it is difficult to determine whether the LoS depolarises at longer wavelengths, particularly for those showing re-polarisation. We will need both high- and low-frequency data to properly determine if these LoSs depolarise indefinitely with increasing λ^2. The ideal type of data would be, for example, similar to that of the wideband polarimetric study of Cygnus A by Sebokolodi et al. (2020), which consisted of a very broad frequency coverage (2–18 GHz) finely sampled along λ^2 space. Thus, the authors could characterise the decaying behaviour of fractional polarisation for various LoSs (see Figs. 4 and 2 of that work for demonstrations of the various categories of $p(\lambda^2)$ and the RMTF from their data). Their well-sampled λ^2 space resulted in minimum sidelobes. Using our data, it is impossible to properly characterise the behaviour of $p(\lambda^2)$.

We further investigated whether the multiple peaks were real or whether our high RMTF sidelobe resulted in a false positive peak. To do this, we used the *QU*-fitting method (see for example Feain et al., 2009; Farnsworth et al., 2011; O'Sullivan et al., 2012; Sun et al., 2015; Miyashita, 2019), to fit specific models to the data in λ^2, and determine whether the modelling favoured a model with double peaks or not. Since most of the sight lines across Pictor A exhibited single peaked clean FDF, at least a single Faraday rotating screen was anticipated. Therefore, we explored a single polarised emitting component model coupled with a depolarising component. For our models, we assumed the external Faraday depolarising screen (FDS) as the main cause of the observed depolarisation. The above Faraday effect is modelled using the following:

$$p = p_0 e^{-2\sigma_{RM}^2 \lambda^4} e^{2i(\chi_0 + RM\lambda^2)}, \tag{5.3}$$

where the first exponential term represents depolarisation and σ_{RM} is the Faraday dispersion (O'Sullivan et al., 2012). Eqn. 5.3 has a physical basis for beam depolarisation models and is expected for a linear gradient of Faraday rotation across a Gaussian observing beam (Sokoloff et al., 1998). Thus, it is a reasonable approximation for any distribution of RM that is representable by a Taylor series in position provided that the depolarisation is small. We also explored two emitting components, each with an associated depolarisation effect. This is done by summing up the contributions of each component, i.e. summing up Eqn. 5.3 as $p_{\mathrm{t}} = p_1 + p_2$.

Farnsworth et al. (2011) suggested that besides inspecting the goodness of fit to solely $q(\lambda^2)$ and $u(\lambda^2)$, inspection of fits on fractional polarisation $p(\lambda^2)$ and polarisation angle $\psi(\lambda^2)$ models could avail comprehensive insight on the underlying Faraday structure. Hence, we inspected the suggested plots for our lines-of-sight.

Visual inspection of the single-component models generally showed bad fits, which was most apparent in the fractional polarisation plots. In contrast, the double-component model fit all the data reasonably well. As mentioned in Sec. 3.2.2.3, an increase in model complexity could result in overfitting the data. Thus, we use the Bayes Factor (BF) to determine the better model. This is a marginal likelihood ratio between the two competing models and is given by:

$$\mathrm{BF} = \frac{\mathcal{L}(\theta \mid \text{data; double component model})}{\mathcal{L}(\theta \mid \text{data; single component model})},$$

and could also be denoted in logarithmic values. Here, we take a double-component model (also noted as dual) to be model 1 and a single-component to be model 2. Bayes Factor is a relative quantity, such that a value $\gg 1$ means model 1 is favoured over model 2 (see Kass and Raftery, 1995, for more on Bayes factors). The BF for our competing models are highlighted by Fig. 5.15, which shows that the dual component model is preferred over the single component one.

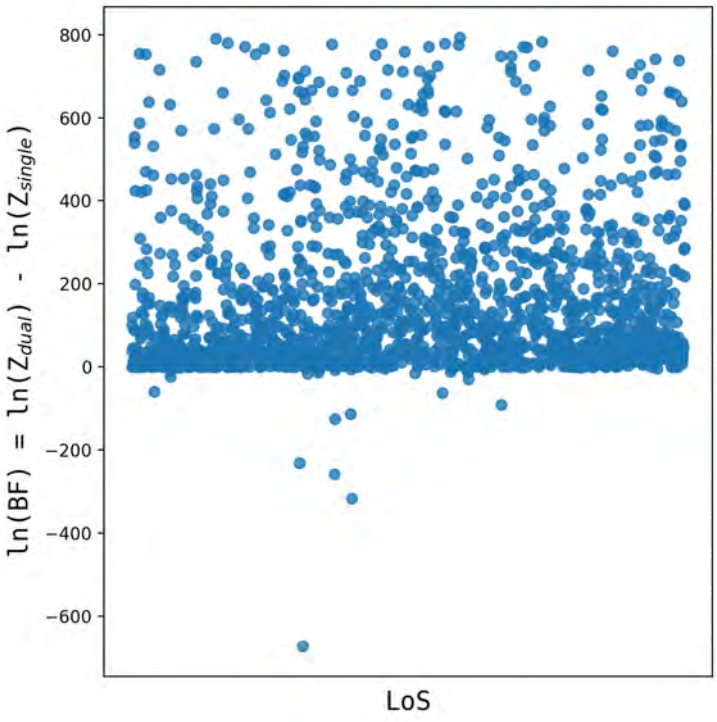

Figure 5.15: Model selection using the Bayes Factor selection criterion for modelling done on real data. The dual component model shows a larger Bayes Factor, making it the preferred model.

This is unsurprising, especially given the structure we see in fractional polarisation, which is unexpected for a simple uniform foreground screen. A physical interpretation of these results is that multiple Faraday depths or a Faraday thick structure exists along most sight lines across the

source. Variations across the observing beam could also lead to the observed behaviour. We note that models with more than two Faraday rotation components were not tested.

5.3.7 *Do the Missing Frequencies Affect RM Measurements?*

One lingering question was whether missing frequency samples affected our RM measurements. As an additional check, we simulated data at 80 evenly spaced channels and set known fiduciary values of fractional polarisation, RM, and Stokes I spectral variation. This formed our control dataset, to which Gaussian random noise was added to make it more realistic. We then set the test dataset up to match our actual observed data by excluding the same frequencies that were excised from our channelised images. Specific details about the setup of this experiment are highlighted in App. 5.5.1.

Inspection of the results of QU-fitting and RM-synthesis showed that in both the control and test data cases, it was still possible to recover the correct peak and its corresponding location despite missing λ data (some examples are shown in Fig. 5.16). However, QU-fitting within test cases where the maximum degree of polarisation was less than 20 per cent, and two Faraday components had difficulty locating the secondary (lesser) FDF peak position. On the other hand, the strongest FDF peak was correctly identified in almost all cases. Furthermore, the sidelobes were considerably higher, which caused confusion in the validity of a peak.

Two possible interpretations of the multiple peaks observed arise. The first is that there is a single complex continuous Faraday structure (i.e. with a wide Faraday depth) along the LoS of Pictor A. Rudnick and Cotton (2023) (in sec. 4 of their work) have shown that the resolution of the RMTF approximated by Brentjens and de Bruyn (2005) incorrectly identifies a continuous tophat Faraday distributions as two narrow-peaked components located at the opposite edges of the original distributions. The second possibility is that two or more Faraday components exist along this LoS. At this point, it is impossible to definitively determine the correct interpretation of the two; wideband data with higher Faraday depth resolution could illuminate this issue better.

5.4 Summary and Conclusions

Using MeerKAT L-band data, we have generated a high-sensitivity map of Pictor A shown in Fig. 5.2. We observe the bright but unresolved WHS, the double WHS and the radio core. Furthermore, we have confirmed the presence of the kpc scale radio jet from the radio core to the WHS. This radio jet is in good alignment with the X-ray jet from Hardcastle et al. (2016). However, the counter-jet remains undetected.

Hardcastle et al. (2016) speculated that if the X-ray emission within the lobes of Pictor A is inverse Compton in nature, it must be co-spatial with synchrotron emission. From the low sensitivity VLA radio observations by Perley et al. (1997), X-ray emission appeared to extend beyond the radio emission, which was strange. However, from our observations, the diffuse emission extending away from the core is now clearly visible (see Fig. 5.4), with some emission extending beyond the X-ray emission. Thus, we conclude that X-ray emission within the lobes of Pictor A could result from inverse Compton scattering.

Pictor A has also shown spectral variation typical of any FR-II source; it exhibits a flat spectral index in the radio core and hotspots, but spectral steepening occurs within the lobes and especially away from the radio core towards the source edges (see Fig. 5.6 and Table 5.1 for a summary of the spectral indices). More accurate model fitting and characterisation using wideband data is necessary to distinguish between different variants of spectral ageing models and to determine their parameters.

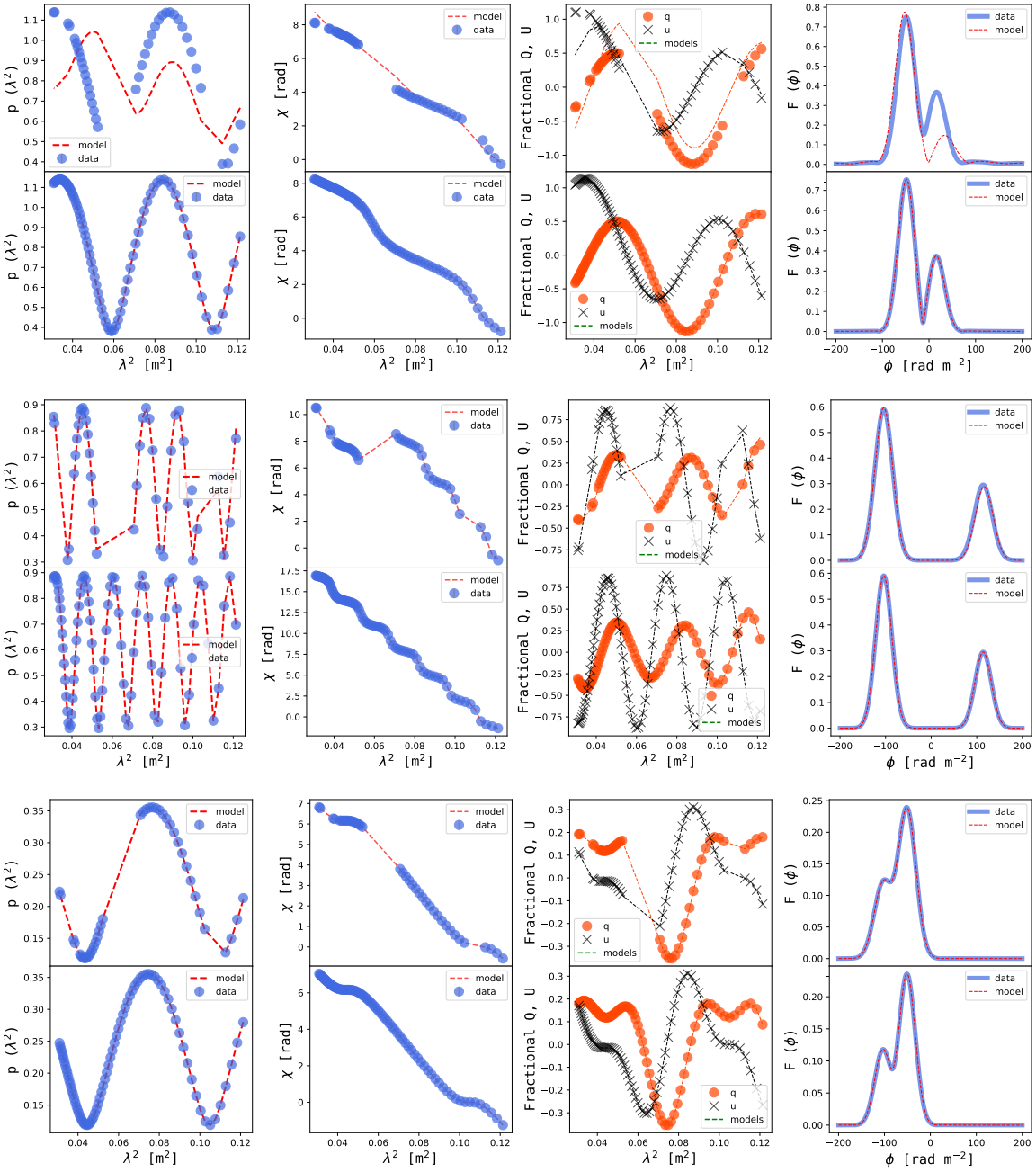

Figure 5.16: Example plots showing the result of experimental *QU*-fitting on simulated Q and U to ensure that missing frequencies within our data do not affect results. A pair of rows represents a single LoS, with test data on the top panel and the control data on the bottom. Both *QU*-fitting and RM-synthesis could correctly locate the peak amplitude of the emitting components, even with some missing frequency chunks.

We have additionally performed a spectropolarimetric study of the lobes of Pictor A (Sec. 5.3.4), where we show that this source exhibits mostly smooth and positive rotation measures within both its lobes, with an average RM of 48.06 rad m^{-2} and a standard deviation of 10.19 rad m^{-2}. However, the eastern lobe is associated with a wider RM variation, more sudden RM changes and higher depolarisation than the western lobe. We have estimated the average RM in the eastern lobe to be 50 rad m^{-2}, while the western lobe averages 47 rad m^{-2}. The Galactic contribution was estimated to be 23.57 ± 16.12 rad m^{-2} in the direction of Pictor A. Although Galactic contributions could dominate our observed rotation measures, narrowing down the various contributions with our current data is difficult. This characteristically smooth RM behaviour could indicate a large-scale

Faraday rotating screen in the foreground of Pictor A. However, this could also be caused by our data's low Faraday depth resolution directly linked to our limited bandwidth (see Fig. 5.1), which limits our view of smaller Faraday depth scales.

Furthermore, we have demonstrated that lines-of-sight across Pictor A show varied Faraday spectra, with some showing single, double or multiple peaks. Lines-of-sight with more than one peak indicate the presence of multiple polarised components at different Faraday depths. It is difficult, however, to establish their depolarisation characteristics, as the behaviour of fractional polarisation is highly variable with wavelength. This directly stems from the limited frequency coverage and missing frequency chunks of our data. Moreover, limited frequency coverage further lowers our depth resolution. Despite this, we have also demonstrated through *QU*-fitting that the missing frequency chunks do not affect our observed rotation measures (Sec. 5.3.7) and that the multiple peaks observed in our data are possibly real, caused by either the existence of multiple Faraday components or the inability of the RMTF to correctly distinguish a single continuous Faraday complex structure (Sec. 5.3.6).

Therefore, wideband observations will prove helpful in resolving the rotation measure variations and determining whether the observed smoothness across Pictor A is intrinsic to the source or its environs. For example, Sebokolodi et al. (2020) showed that at higher spatial and depth resolution, Cygnus A exhibited higher degrees of polarisation and, hence, more polarisation structure. Therefore, with better depth and spatial resolutions, the origin of the depolarisation and repolarisation patches and the RM gradients seen in Figs. 5.10 and 5.13 could be explained better.

Acknowledgements

We would like to thank M. J. Hardcastle for kindly making the Chandra X-ray images of Pictor A available to us. LALA also thanks U. A. Sob and C. Russeeawon for many helpful consultations and support.

The MeerKAT telescope is operated by the South African Radio Astronomy Observatory, which is a facility of the National Research Foundation, an agency of the Department of Science and Innovation. OS and LA's research is supported by the National Research Foundation of South Africa (grant number 81737). The financial assistance of the South African Radio Astronomy Observatory (SARAO) towards this research is hereby acknowledged (`http://www.sarao.ac.za`).

Data Availability

The data are available from the SARAO archive under proposal number SCI-20190418-LS-01. The sub-band Stokes *I*, *Q* and *U* spectral images, and their corresponding MFS images are available at `https://doi.org/10.48479/kg33-es24`.

5.5 Chapter Appendix

5.5.1 *Data Simulations and QU-fitting Specifics*

As highlighted in Sec. 5.3.7, data was simulated for 100 lines-of-sight to investigate the effect of missing frequency chunks on our data. We replicated the presence of two Faraday peaks through data simulated using some fiduciary RM and fractional polarisation values. The first step was using

the 80 frequency channels corresponding to our observation frequency to generate the channelised Stokes I data, with an arbitrary peak of 4 Jy using the following function:

$$I_{\text{obs}} = I_{\text{true}}(\frac{\nu}{\nu_0})^{\alpha}, \tag{5.4}$$

where α is the spectral index. A Gaussian random noise was added to make the data more realistic. Using set values of initial fractional polarisation, RM and polarisation angle, we generated our 'observed' fractional polarisation data using the model in Eqn. 5.3. We also ensured that there is a single dominating peak by setting $p_0 = 0.5p_1$ (see the bottom panel of Fig. 5.17). We used the fractional Stokes relationship: $p = q + iu$ to derive the values of Q and U from their fractional analogues (q, u) and our simulated Stokes I data. Furthermore, we included noise values to make the data more realistic. We then stored the fractional polarisation, RM and polarisation angle for both components and the Q and U data for each frequency channel.

The next step was determining if the peaks and their positions could be recovered accurately, even with missing samples, using QU-fitting and RM-synthesis. Therefore, our control experiment involved the data when all available samples were contained. Our test data were similar to the control one, except for the exclusion of channels flagged out in our original data. This was done to replicate our scenario better. This process was repeated 100 times, representing one hundred different LoSs.

We chose RM values ranging between -150 and 150 rad m^{-2}, as Perley et al. (1997) reported a maximum RM for Pictor A of $\sim$100 rad m^{-2}. These data are shown in Fig. 5.17. The polarisation angles are between $[-\frac{\pi}{2}, \frac{\pi}{2}]$. The bottom panel of Fig. 5.18 shows the distribution of the artificial noise added to make the I, Q, and U data more realistic. The exact values are shown at the top panel of the same figure.

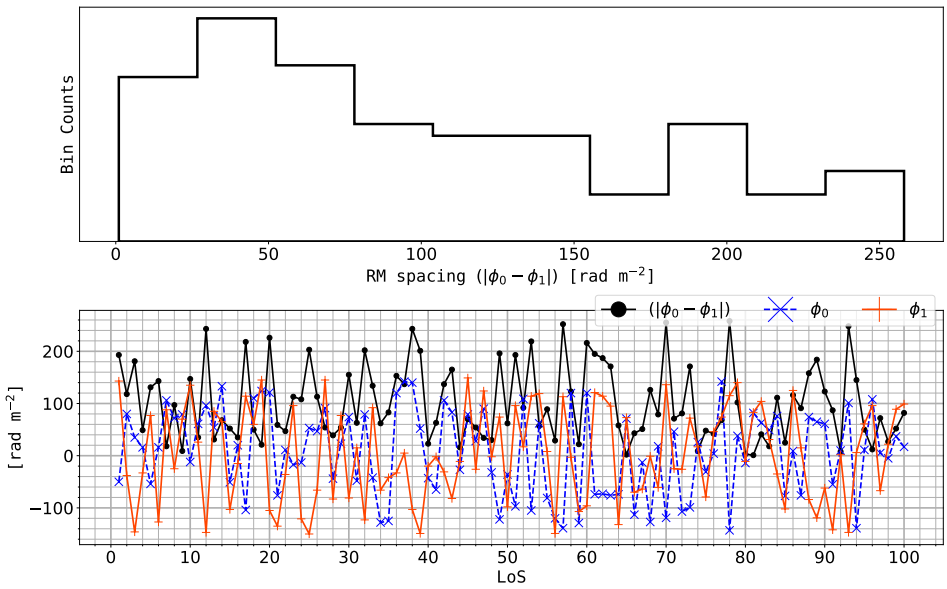

Figure 5.17: The top panel shows the distribution of RM difference between our two simulated emitting components. The selected range of our RMs was between -150 and 150 rad m^{-2} because Perley et al. (1997) reported a maximum RM value of 100 rad m^{-2} for Pictor A. The bottom panel shows the actual input Faraday depth values; ϕ_0 is illustrated by the blue dashed line with a cross marker, and ϕ_1 is illustrated by the red solid line with plus sign markers. The black solid with point markers shows their difference.

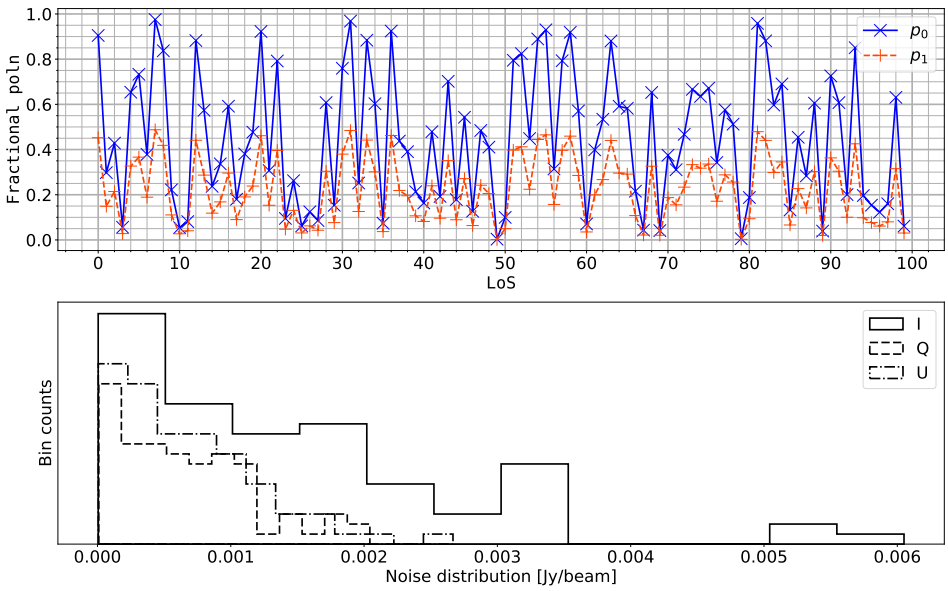

Figure 5.18: The input fractional polarisation values are shown in the top panel. The dominant fractional polarisation component is shown in the blue solid line with cross markers, while the secondary component is in the red dashed lines with plus sign markers. This component is always half of the dominant component. *Bottom panel*: Distribution of the input noise added to the simulated I, Q and U to make it more realistic. All LoSs had the same noise across the band.

5.5.2 *Estimating Magnetic Fields of the Radio Plumes*

According to Miley (1980), the minimum energy density (erg cm^{-3}) and its corresponding magnetic field (in Gauss) can be given by:

$$U_{\rm me} = \frac{7}{3 \cdot 8\pi} B_{\rm me}^2 \tag{5.5}$$

$$B_{\rm me} = 5.69 \times 10^{-5} \left[\frac{(1+k)}{\eta} (1+z)^{3-\alpha} \frac{1}{s \cdot \theta_x \theta_y \sin^{\frac{3}{2}} \varphi} \frac{F_R}{\nu_0^{\alpha}} \frac{(\nu_2^{\alpha+\frac{1}{2}} - \nu_1^{\alpha+\frac{1}{2}})}{\alpha + \frac{1}{2}} \right]^{2/7} \tag{5.6}$$

where k is the ratio of energy in the heavy particles to that in the electrons, η is the filling factor of the emitting regions, z is the redshift, θ_x and θ_y (arcsec) correspond either to the source/component sizes φ to the equivalent beam widths, s (kpc) is the path length through the source in the line sight, φ is the angle between the uniform magnetic field and the line of sight, F_0 (Jy or Jy per beam) is the flux density or brightness of the region at frequency ν_0 (GHz), ν_1 and ν_2 (GHz) are the upper and lower cut frequencies presumed for the radio spectrum, and α is the spectral index.

Using the assumptions that $k = 1$, $\eta = 1$, $\sin\varphi = 1$, $\nu_1 = 0.01$ GHz, $\nu_2 = 100$ GHz and $\alpha = -0.8$, Eqn. 5.6 approximately becomes:

$$B_{\rm me} \backsimeq 1.4 \times 10^{-4} (1+z)^{1.1} \nu_0^{0.22} \left(\frac{F_0}{s \cdot \theta_x \theta_y} \right)^{2/7} \tag{5.7}$$

On the other hand, the distribution of magnetic field strengths can be obtained based on the fact that electrons producing synchrotron emission are also the same that scatter the CMB photons to X-rays. The resultant magnetic field strength, $B_{\rm imp}$ in Gauss, can be approximated to about $\pm 10\%$ for $-0.6 > \alpha > -1.4$ (Harris and Grindlay, 1979) as:

$$B_{\rm imp} = [6.6 \times 10^{-40} 4800^{\alpha} (1+z)^{3-\alpha} F_R F_X^{-1} \nu_R^{-\alpha} E_X^{\alpha}]^{\frac{1}{1-\alpha}} \tag{5.8}$$

where F_R is the radio flux density in Jy at frequency ν_R in GHz, F_X is the X-ray flux in erg cm^{-2} Hz^{-1} at energy E_X in keV.

We estimated the implied magnetic fields in the radio plumes of Pictor A to be 1.039 μG using Eqn. 5.8. In comparison, we found a minimum energy condition magnetic field of 2.677 μG (setting $\alpha = -0.6$ as in the paper) and 3.21 μG (using our obtained radio plume α shown in Tab. 5.1) using Eqns. 5.7 and 5.6 respectively using a frequency of 1.283 GHz.[8] In either case, we find that the implied magnetic fields in these radio plumes are lower than the minimum condition magnetic fields, similar to the findings of Perley et al. (1997) and Hardcastle et al. (2016). This is similar to other FR-IIs in showing this slight departure from equipartition (Croston et al., 2005).

5.5.3 *Estimating the Jet-Counterjet Ratio*

Bridle and Perley (1984) define a jet feature as one that is four times as long as it is wide, and is separable from other extended structures either in brightness contrast or spatially. In the case where one of the jets is not clearly visible, we add an extra requirement that the jet must align with the compact radio core at the point where it is closest to that core. We follow the procedure outlined in Mullin et al. (2008) to estimate Pictor A's jet flux:

1. Draw a region containing and spanning the entire visible jet, excluding the radio core and hotspot and measure the flux within that region, $S_{\rm obs}$.
2. Draw two regions of equal size and parallel to the jet containing region (to the top and bottom) and measure those fluxes and average them to get a mean background flux, $S_{\rm back}$.
3. Estimate the jet flux as $S_{\rm j} = S_{\rm obs} - S_{\rm back}$

Since the counterjet is not visible, we estimate the upper limit of its flux by measuring the integrated flux of a region of width ~ 2 times the restoring beam width across the entire distance between the core and the EHS, and repeat the same procedure carried out with the jet. However, if the flux associated at the central region is not the highest, the upper limit becomes the norm of the difference between the the lowest flux measured. Therefore, the obtained ratio will be the lower limit. Using these specifications, we find a jet/counterjet ratio of ~ 0.9, which suggests that Pictor A as two-sided according to Bridle and Perley (1984). Perley et al. (1997) stated a ratio of greater than three. Calculations of the jet/counterjet ratio are complicated by problems both of counterjet recognition (such as, confusion by filaments in the lobes) and of correcting faint features for a spatially variable lobe background. Furthermore, the counterjet is not necessarily a faint replica of the main jet (e.g see Bridle et al., 1994, for a brief overview). Therefore, the ratio obtained here should be interpreted cautiously.

8 We set $\theta_x = 25''$, $\theta_y = 59''$ for the top plume and $\theta_x = 37''$, $\theta_y = 98''$ for the bottom plume, and $s = 334.355$ kpc. We used X-ray parameters of the plumes from Tab.4 of Hardcastle et al. (2016), labelled as *lobe outside contours* with a power-law model.

6

SEEING IS BELIEVING

Visualisation is integral to data quality assessment which facilitates quick error and trend identification. There are two facets of visualisation. The first is the non-imaging kind, where the uncalibrated and calibrated visibilities and calibration products are visually inspected (we introduced the concepts of visibilities and calibration in Sec. 3.3 and 4.1). Here, data corrupted by RFI, instrumental, and atmospheric effects can be identified and removed. Furthermore, the suitability of derived calibration solutions is gauged, and calibrated data is checked for any lingering effects. Multiple existing tools perform these functions, such as `RaGaVi`[1] (Andati et al., 2022), `shadeMS`[2] (Smirnov et al., 2022) and `CASA-PlotMS` (McMullin et al., 2007). Non-imaging visualisation is essential as it allows earlier problem detection before imaging, which can be a time-consuming and computationally expensive affair. Furthermore, some errors are more recognisable and better localised in the visibility plane (e.g. low or high amplitudes, spikes in the visibilities), while others are more apparent in the image plane (e.g. persistent low-level calibration errors, and artefacts). Successful data calibration is followed by imaging the calibrated data, which generates scientific FITS images, the essential consumable product of data reduction. Visualisation and inspection of these images form the pinnacle of astronomy.

With the drastic increase in radio astronomical data due to the technological advancements made with newer telescopes and data communication in general, remote data reduction and quality assessment have become inevitable. The large quantity of astronomical data requires that it be kept in remote data centres and servers, providing the necessary and suitable storage and processing capabilities. Such services are provided by powerful remote clusters such as those availed by The Inter-university Institute for Data Intensive Astronomy (IDIA).[3] This current setup means that a data consumer (i.e. the astronomer) can no longer easily download and process raw data (visibilities) or its products (e.g. images and image cubes) in their individual computer due to their size. Furthermore, data reduction and quality assessment tools must be fast, scalable, and, more importantly, remotely accessible within a reasonable time. Data visualisation is a quintessential example of the shift towards modern workflows.

Inspection of imaged visibility data mostly requires using FITS image viewers such as `DS9` (Joye and Mandel, 2003), `Tigger`[4], `Kvis` (Gooch, 1996), among others. In the traditional sense, this meant that FITS viewers were installed at the data's storage location. Users needed to launch the viewer's graphical user interface (GUI) on the remote machine for all the image's data to become visible on the user's screen. But for this to occur, the entire size of the image viewed had to be transferred from the remote machine through a network. The speed of this process is contingent on the internet connectivity speed between the remote and local computers and the size of the image being retrieved. In the case of very large images and standard connectivity time, loading up images could take up to minutes. Consider an image of size 200 megabytes (MB) and an internet connection speed of 1 Megabits per Second (1 Mbps). This means that it takes 1 second to transport 1 Mb (∼0.125 MB). Therefore, it will take approximately 27 minutes (1600 seconds = 200 MB/0.125 Mbps) to transfer the image data to a local computer for viewing. This is too long.

Hence, modern FITS image viewers have adopted the client-server architecture to reduce the time between opening an image and viewing it on one's screen. In this model, the remote computer

1 https://github.com/ratt-ru/ragavi
2 https://github.com/ratt-ru/shadeMS
3 https://idia.ac.za/
4 https://github.com/ratt-ru/tigger

becomes the server, handling the resource-intensive and complex image processing tasks. Here, large images are downsampled and/or subdivided into smaller sizes (e.g. through tiled rendering) for fast access and then transferred to the client. On the other hand, the client is the local computer whose task is only to render and display the associated data. This means that very large images are viewable with minimal wait time. Notable examples of software using this model are the Cube Analysis and Rendering Tool for Astronomy (CARTA)[5] (Wang et al., 2020; Comrie et al., 2020; Comrie et al., 2021) and JS9[6] (Mandel and Vikhlinin, 2022).

In the context of this thesis, visual inspection of polarimetric data on individual lines-of-sight of interest could offer insight into the kind of spectra associated with different regions and components (e.g. radio lobes and hotspots) across a radio source. The CARTA viewer is equipped with an advanced Stokes analysis tool that could be used to display useful polarimetric products per pixel on demand. The tool allows Stokes I, Q, U and V cubes loading to form a "hypercube" that allows it to generate interactive polarimetric products such as polarised intensity, fractional polarisation profiles, and magnetic field orientation vectors, among many other functionalities.

Although useful, CARTA does not yet offer options for displaying RM-synthesis products such as the Faraday spectra and the RMTF. This chapter presents a simple tool called PolarVis, which allows viewing and inspection of interesting LoSs and their corresponding RM-synthesis product plots over the web. This tool uses the JS9 remote FITS image viewer for its operation. For illustration, PolarVis was deployed for visualisation of Pictor A's lines-of-sight and is available at: https://pica.ratt.center. PolarVis was also used to visualise the LoSs of Cygnus A using data kindly provided by Dr Lerato Sebokolodi Baidoo and can be accessed using at https://cygnus.ratt.center/. We also present Scrappy (Sec. 6.2), whose primary use is automatically generating independent LoS across a source, besides providing other functionalities.

6.1 PolarVis

The Polarimetric Visualiser (PolarVis, Andati et al. 2023a) is a tool capable of displaying interactive plots associated with various chosen LoSs at the click of a button. Its development was led by the need to quickly examine these regions to get insight into trends of polarisation structure across a source. For example, Sebokolodi et al. (2020) highlighted LoSs exhibiting three distinct categories of depolarisation characteristics for the Cygnus-A radio galaxy: smooth decay, oscillatory with "sinc like" structure in the longer wavelengths, and complex decay, which exhibited a mixture of the smooth and oscillatory behaviour. These were revealed by inspecting plots of polarisation spectra in λ^2 and Faraday depth space for the LoSs. To determine the location of these LoSs on the source, one must manually take note of their pixel numbers on the FITS image and associate them with a region on the source. This task could quickly prove drudging and repetitive if there are many LoSs (for example, Sebokolodi et al. (2020) had approximately 2000 LoSs). PolarVis affords a bridge between the inspection plots and the FITS image by facilitating the quick transition between the two. Such an association could expedite the identification of trends across a source, e.g. if certain depolarisation characteristics correspond to a specific source component.

6.1.1 *Architecture*

This tool naturally adopts the client-server model since it is web-based. A client is the software used to access a website, e.g. a web browser. However, it is standard to refer to the device hosting the browser as the client; thus, it is a computer or an internet-capable phone. Because the browser is the interface through which a user directly interacts with a website, this is known as the front end. On the other hand, a server is software that handles requests from the client, processes them and returns a result. A machine that dedicatedly hosts server software is also commonly called "a

5 https://carta.readthedocs.io/en/latest
6 https://js9.si.edu/

server". Servers typically also perform any resource-intensive or complicated tasks of a website's operation, such as processing data (e.g. an image in the case of PolarVis). This is known as the back-end because the user usually has no direct interaction with the server's operations. Fig. 6.1 demonstrates a simplified example of this process in operation is searching for something on Google, which the following series of steps can highlight:

1. Open a browser (the client) and type in Google's web address. This constitutes the first request sent to Google's servers (via the internet), where it is interpreted as a request for Google's homepage.
2. Google's server then locates and returns the Google homepage to the client, allowing a query to be entered.
3. User enters their query in the search bar and sends it back to the server (by clicking the search button).
4. The server receives this request and processes it. If valid results for the query are found, they are returned. Otherwise, some error message is returned. Either way, a result is returned by the server.

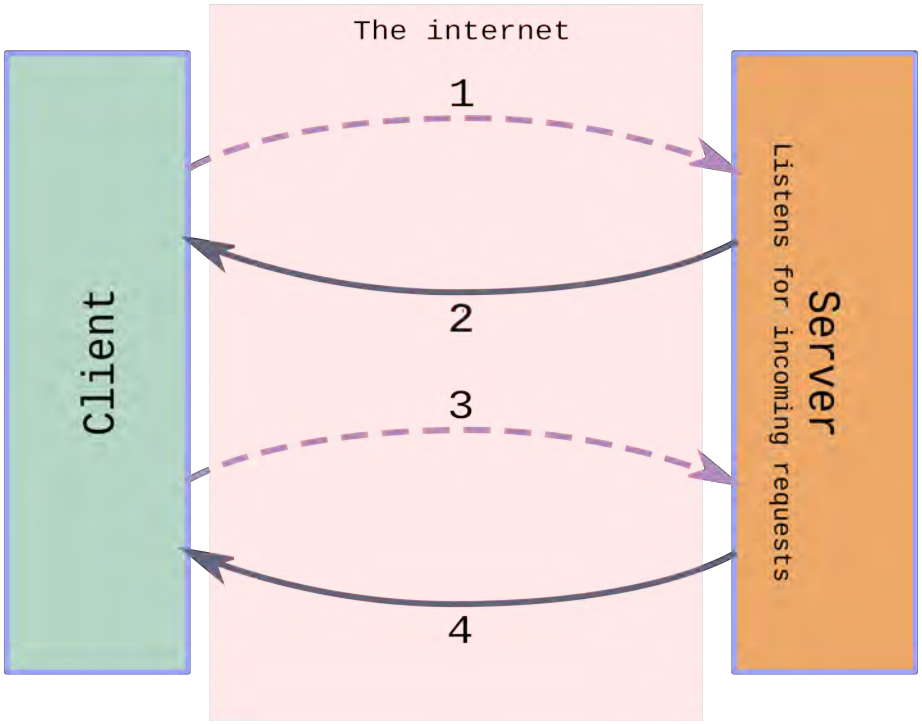

Figure 6.1: An illustration of the client-server model. The client sends requests (marked by the dashed arrows), and the server returns responses (marked by solid line arrows). All this is done over a network connecting the server and the client; this is typically The Internet.

Back-end

The main operational back-end service for PolarVis is provided by JS9. It is known as the JS9Helper, which provides its computational and data processing services and FITS image manipulation functionality, such as downsampling large images and performing mathematical operations. This is based on NodeJS, a JavaScript (JS) runtime environment that compiles JS, making its execution fast and efficient. NodeJS, therefore, allows for using JS as both a front- and back-end language. Because of this, JS9 can manipulate images from both the server and client sides using an Application Programmers Interface (API). For JS9 to remain functional and accessible through the web browser, the JS9Helper must remain active in the background *listening* for incoming re-

quests. The interactive LoS Faraday spectra plots are pre-generated using `Bokeh`, a `Python` plotting library that generates interactive plots given data. More on this will be elaborated in Sec. 6.2.

Front-End

The fundamental building block of a webpage is an HTML (Hyper Text Markup Language) document. This consists of constructs known as *elements*, which define how a webpage should be structured top-down; it tells the browser how to *render* a webpage. Left alone, a webpage made from only HTML appears plain and monotonous. CSS (Cascading Style Sheets) adds the pomp and colour required to make a webpage aesthetically pleasing. The `JS` programming language allows for its interactivity such that it can respond to events such as clicks and scrolling. These form the basis of websites as we know them today.

Accordingly, viewing FITS images on a web browser requires setting up the basic HTML structure and mechanisms that provide the user with the level of interactivity offered by traditional desktop applications such as `DS9`. Fortunately, the `JS9` web FITS viewer already provides these facilities. It comes bundled with a template of the basic HTML structure required to accommodate a FITS image and thus forming its base GUI, which is entirely malleable to one's needs. Furthermore, `JS9` provides an easy-to-use API which allows customisation of actions and behaviour of the image viewer from the front-end using `JS`. This is directly linked to the fact that `JS9` uses a `NodeJS` server to load and manipulate the FITS image. For example, it provides spatial geometric shapes known as *regions*, which act as filters that select the pixels contained only within itself. Therefore, a single region could act as an isolated entity within which mathematical operations involving the specifically selected pixels could be performed. Moreover, events such as clicking or dragging are attachable to regions through `JS` constructs known as *callback functions*.[7] For these reasons, `PolarVis` uses `JS9` as its image viewer – this is illustrated in Fig. 6.2.

The other aspect of `PolarVis`' front-end is the interactive LoS Faraday spectra plots, presented in Fig. 6.3. Since `JS9` allows for the event-based execution of custom actions on regions, the plots and regions are easily linked using `JS`, which is executed by the web browser. Therefore, plots corresponding to specific regions are loaded up when clicked. Fig. 6.4 presents the current front-end of `PolarVis`.

6.1.2 *Operation*

Upon loading, the initial webpage displays the Stokes I image of Pictor A and the available lines-of-sight coloured in green (Fig. 6.2). This viewer window has the standard FITS image viewer capabilities such as setting colour scales, zooming, and panning, among others. On clicking a particular region, the main FITS viewer moves to the left-hand side of the screen, while a plot corresponding to the LoS loads up towards the right-hand side. Here, plots of the three recently clicked LoS are shown simultaneously, with the most recent one appearing at the top (Fig. 6.3). Three of the most recently selected sight lines are highlighted in purple, orange and blue. In contrast, any older previously selected sight line is coloured black to keep track of selected regions. Additionally, the colour of a recently selected region is matched to a colour patch shown towards the left of the associated plot for easier identification, as shown in Fig. 6.4.

Plots could be enlarged by clicking the arrow icon next to the identification colour swatch, which will reopen the plot in a new tab – the controls are marked in Fig. 6.5. These plots are interactive, so one can zoom, pan and even download and save the actual data points forming the plot. Legends on the plot are clickable and could be used to select what is visible by toggling on and off. For example, in the case of complex-valued functions, the real, imaginary, phase, and amplitude plots could be made visible by clicking on the corresponding legend (see Fig. 6.6).

7 These are just functions called when an event such as a click occurs.

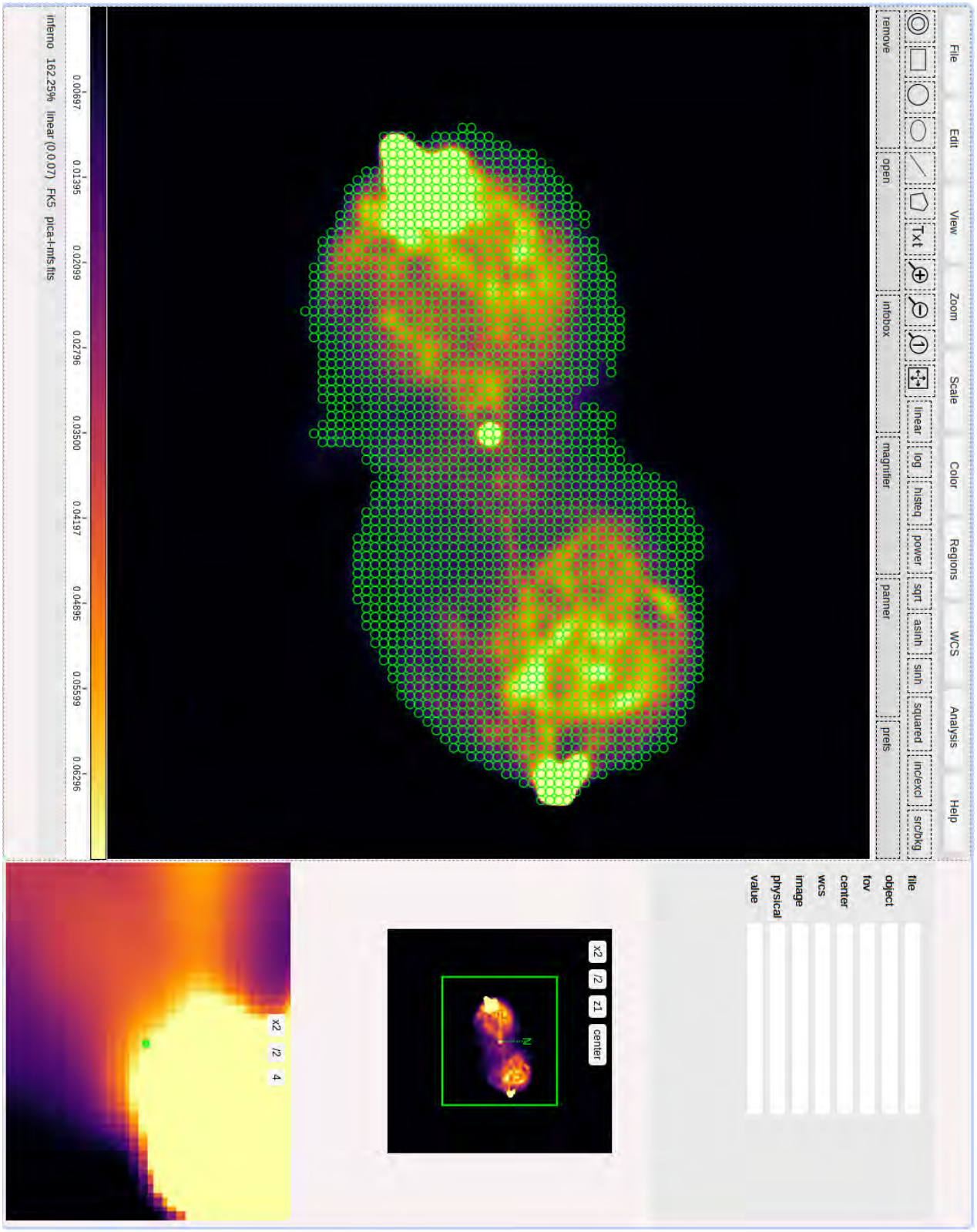

Figure 6.2: `PolarVis`' FITS image viewer using `JS9`. This is an MFS image of Pictor A. The green circles are the `JS9` *regions* representing the independent lines-of-sight, each of a radius of $3''$. The right side of this figure shows auxiliary windows: the image information box, image panner and panner. Above the main FITS image are the standard imager controls.

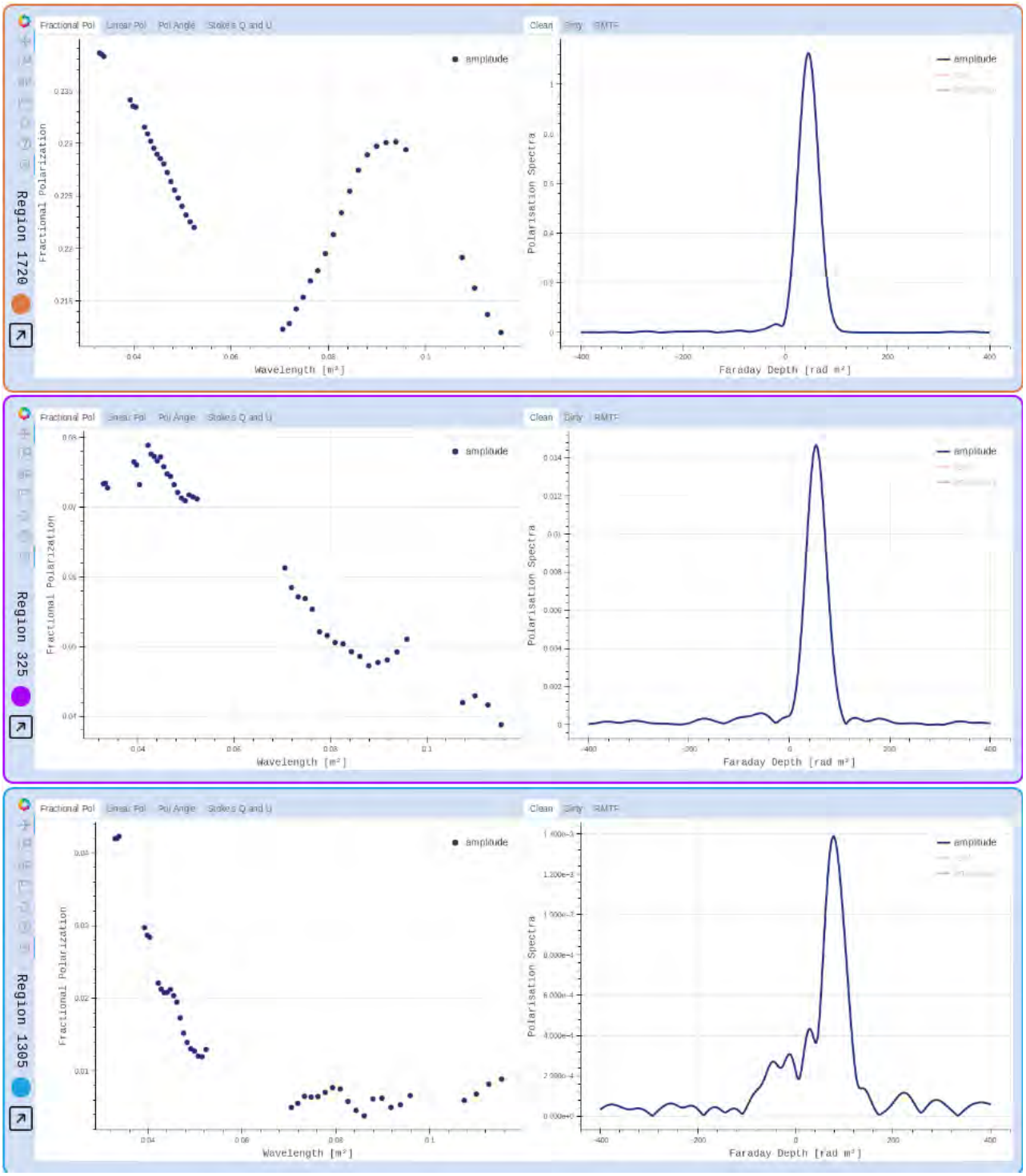

Figure 6.3: The plot layout in `PolarVis`' GUI. These plots correspond to specific LoS that were clicked. They are interactive, so different plots are viewable.

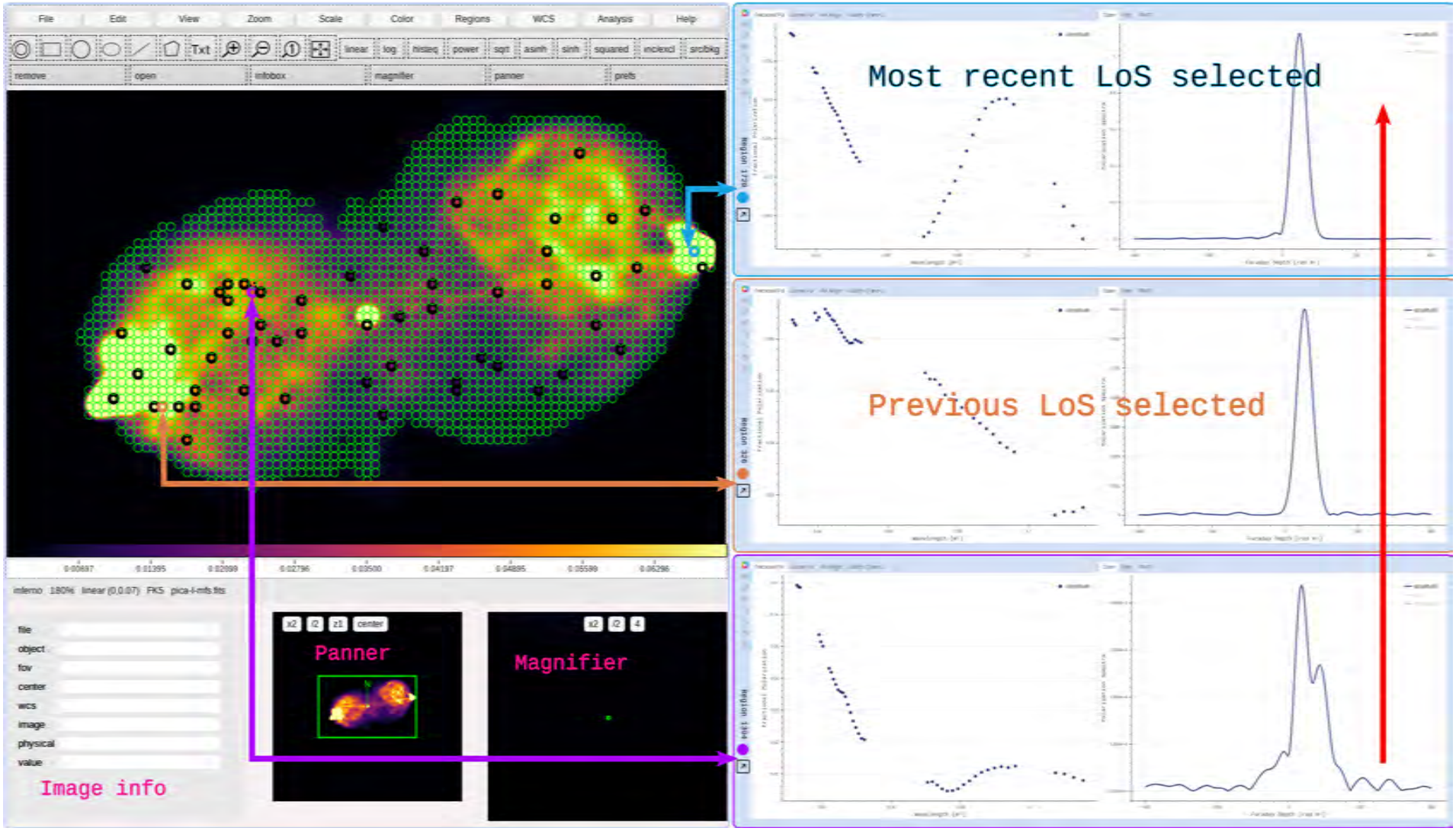

Figure 6.4: A demonstration of `PolarVis`' GUI. The left panel shows the FITS viewer, while the right side shows the three most recently selected plots. The black circles are the older previously selected LoS while the blue, orange and purple circles are the three most recent selections, and whose plots are displayed. Unselected LoSs remain green.

Furthermore, there are multiple tabs at the top of each plot, which allow one to select the category of plots that are made visible by clicking. There are two different groups of plots, those in λ^2-space and those in Faraday depth space. For λ^2-space, the tabs are fractional polarisation and Q and U vs wavelength [$p(\lambda^2), |P|(\lambda^2), \psi(\lambda^2), Q(\lambda^2)$ and $U(\lambda^2)$], while for ϕ-space, they are cleaned and dirty FDF as well as the RMTF of the data. This way, multiple aspects of a LoS's data are all explorable in a single place (see Fig. 6.7).

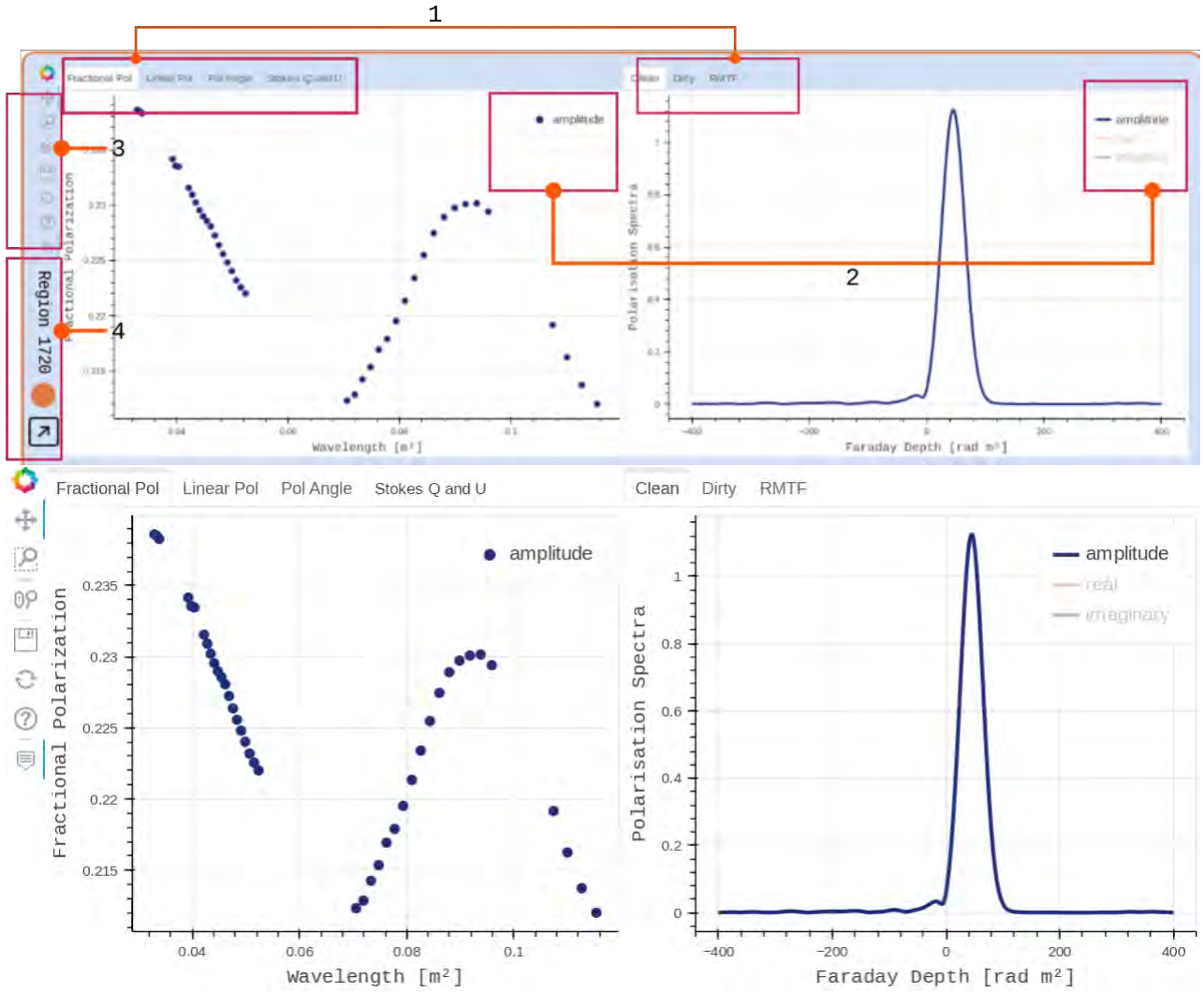

Figure 6.5: Parts of an interactive plot. 1: Clickable tabs which allow selection of the plots to be seen. 2: Legends that can be toggled to hide or show specific aspects of the same plots. For example, in this plot, only the amplitude is shown; the hidden plots are greyed out. 3: Interactive tools for panning, zooming and selection. 4: Shows the region identifier, a colour swatch, which identifies the selected region. This colour will correspond to a region of the same colour in the FITS viewer. Also shown in area 4 is a small arrow enclosed in a box that allows a larger version of the same plot to be opened in a new tab upon being clicked.

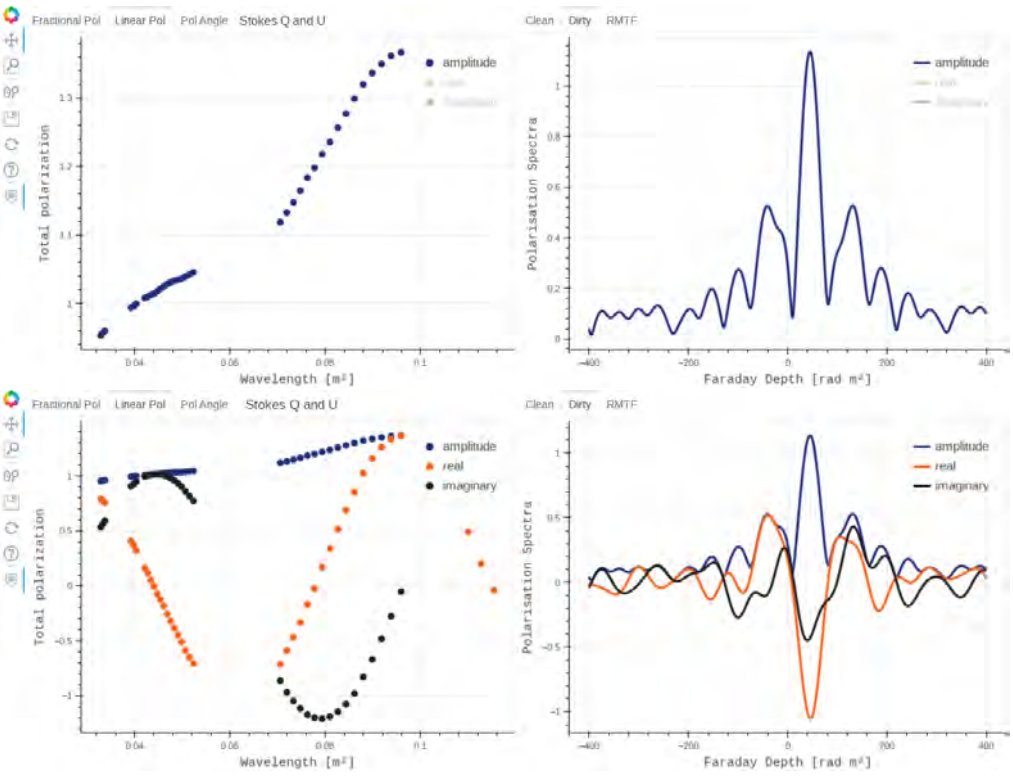

Figure 6.6: Plots can be toggled on and off by clicking on their respective legends.

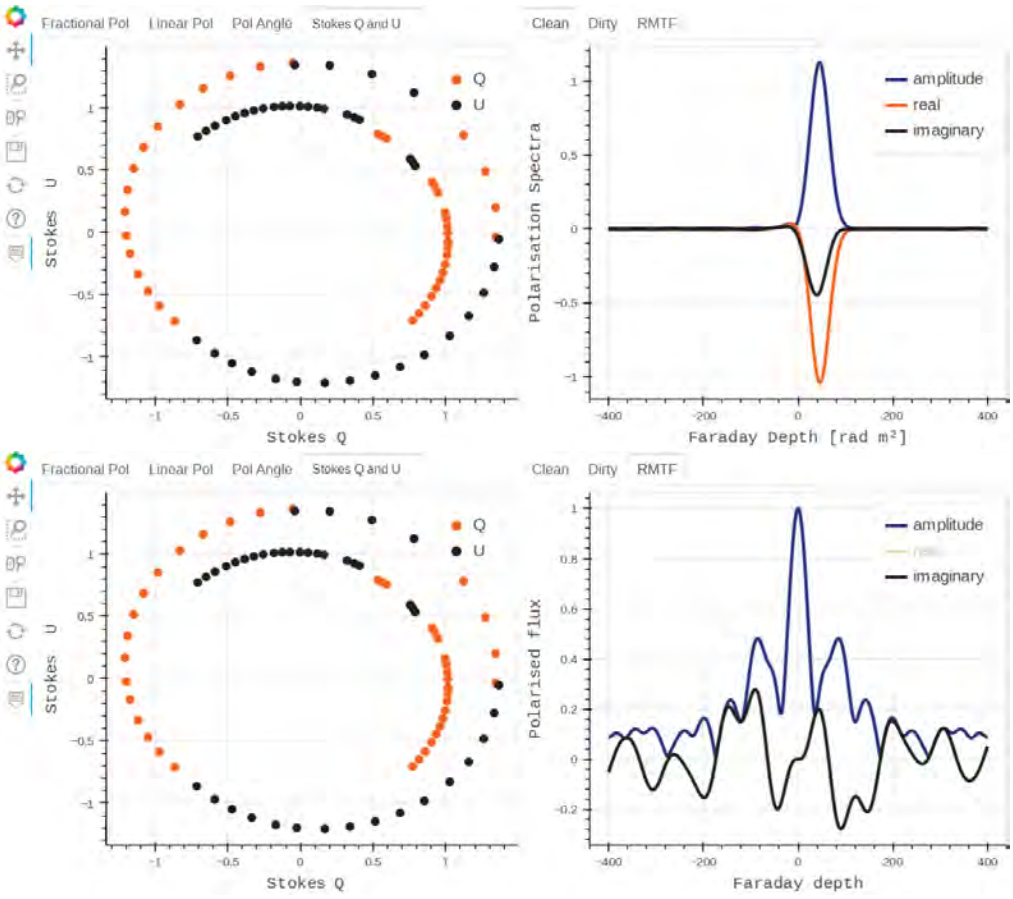

Figure 6.7: It is possible to switch between different types of plots as they all reside in the same place. This selection is done by clicking on the panels atop the plots.

6.1.3 *Application: Visualising Pictor A's Lines-of-Sight*

In the previous chapter, we showed that Pictor A exhibits varying categories of Faraday spectra: the majority with a single peak at a specific depth, some with a single dominant peak with a wide base/flanked by one or more smaller peaks. In contrast, others showed more than one significant peak. The locations of the different peak categories were illustrated in Fig. 5.9. In most cases, LoSs showing more than one distinct Faraday peak exhibited oscillatory behaviour of the fraction polarisation as a function of λ^2. As emphasised in Sec 3.2.2, plots in λ^2-space provide valuable diagnostics for the underlying Faraday structure, making their examination of paramount importance.

Hence, to aid this, we deployed our Pictor A LoS data to a server to practically demonstrate the usefulness of `PolarVis` onto a website at `https://pica.ratt.center`. Spectra for the LoS were created using pre-specified pixel locations representing the various LoS and the pre-generated corresponding data. This was done using `Scrappy`, a tool that we developed, which is discussed in Sec. 6.2.

Setting up

The Pictor A website is hosted on a virtual AWS cloud machine with 4 gigabytes (GB) of RAM, a connectivity of up to 5 Gbps and based on the Ubuntu Linux operating system.[8] This means the website's content is stored on a cloud computing facility accessible remotely through the Secure Shell (SSH) protocol. A cloud-hosted website's obvious benefit is its inherent redundancies, ensuring maximum uptime. Its software stack is as illustrated in Fig. 6.8, whose setup we summarise.

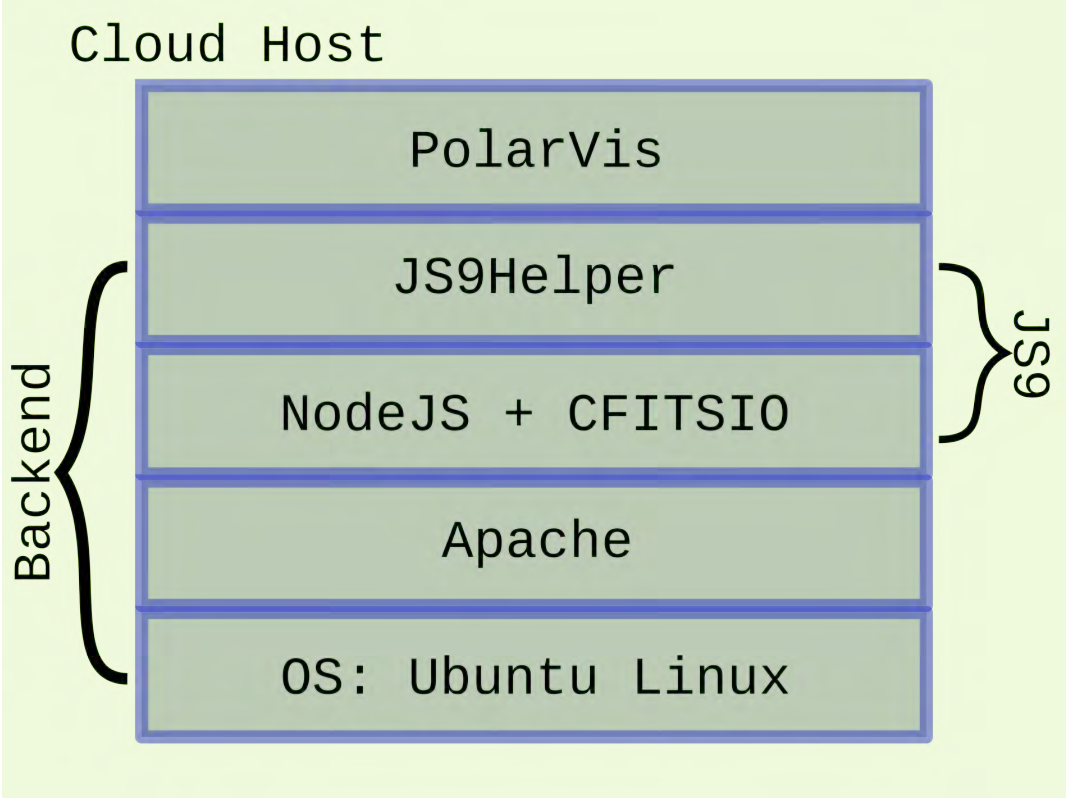

Figure 6.8: The current setup of `PolarVis`.

8 Specifically an EC2.t3 medium instance: `https://aws.amazon.com/ec2/instance-types/`

The first step was to allow content availability to the public via the general Internet; we installed and set up the Apache web-server software. Apache has the advantage of being configurable through text-based files and having a broad support community and extensive documentation.

The installation and setup of JS9 followed. One thing to note is that the size of a FITS image could be inhibitively large, as mentioned in the introduction of this chapter. This means that images must be downsampled, reducing their storage size so that they can be quickly and easily rendered on a web page and provide a good user experience. A side effect of this process is the reduction of the image dimensions as the image pixels are binned based on some specified binning factor. For instance, if the original image has pixel dimensions of 4096×4096 and a binning factor of 4 is selected, the displayed image will have a 1024×1024 dimension.

Thus, JS9 uses more miniature versions of the original images, *representation files*, to facilitate quick displays. However, representation files are still linked to the original FITS file in case a more detailed analysis is required. To do this, JS9 requires the installation of the CFITSIO software library based on the C programming language (Pence, 1999).[9] Also mentioned previously, the JS9Helper provides the necessary functionality for JS9 and an API interface to the server-side. As a result, the JS9Helper must remain active all through. We achieve this by running it as a *daemon service*, an automatically initiated background process in the Linux system environment (even after a machine restart). This is shown in Lst. 6.1. A step-by-step tutorial on the entire setup of this website is outlined in Appendix C.

```
# save this at : /etc/systemd/system/startjs9.service
[unit]
Description=Daemon to restart js9 helper automatically

[Service]
Type=simple
User=username
Group=username
WorkingDirectory=/home/username
ExecStart=/bin/bash -c '/home/username/daemons/start_js9.sh'
RestartSec=300
Restart=on-failure
StandardOutput=file:/home/username/website/logs/js9node.log
StandardError=file:/home/username/website/logs/js9node.log

[Install]
WantedBy=multi-user.target
```

```
# start_js9.sh
export PATH=$HOME/website/bin:$PATH
echo "Starting JS9"
# daemon service at /etc/systemd/system/startjs9.service
node /home/username/website/js9install/js9Helper.js
```

Listing 6.1: Setting up a daemon service for JS9Helper. The lower code snippet shows the contents of start_js9.sh.

9 https://www.gnu.org/software/gnuastro/manual/html_node/CFITSIO.html

6.1.3.1 *Showcase*

All the illustrations of `PolarVis` shown until this point have been done using our data. For example, from Fig. 6.3, we see the varying behaviours of Faraday spectra in terms of the number of peaks. From random inspection of plots across the source, we noticed that many fractional polarisation plots from the western lobe's lines-of-sight showed repolarisation on the longer wavelengths. This is consistent with our findings of Sec. 5.3.3, where the eastern lobe exhibited more depolarisation, while the western lobe showed little to no depolarisation.

6.1.4 *Application: Visualising Cygnus A's Lines-of-Sight*

Previous studies of Cygnus A showed high levels of linear polarisation within its lobes and hotspots and a typical fractional polarisation of $\sim$40% up to the theoretical limit of 70%. This galaxy also displays high RM values ranging between -4000 to $+3000$ rad m^{-2} and high RM gradients of up to 1000 rad m^{-2} arcsec^{-1}. The origin of these high observed RM values remains under speculation. However, the largest contributors have been argued to be the X-ray cluster gas surrounding Cygnus A and the cocoon shock resulting from the jet's progression into the surrounding medium. Using data with a frequency coverage spanning from 2 – 18 GHz from the VLA telescope, Sebokolodi et al. (2020) reported observing three distinct categories of depolarisation structure with increasing λ^2:

(i) Smooth decay: fractional polarisation decreases monotonically,

(ii) "sinc-like" decay: fractional polarisation behaves like a sinc function where the amplitude of an oscillating peak decreases with increasing λ^2,

(iii) complex decay: a combination of the previous two.

Similar to Pictor A, we deployed the Cygnus A LoS data to a server available at `https://cygnus.ratt.center/cygnus/`. We note here that the development of `PolarVis` was initially centred around Cygnus A data. As mentioned in the introduction of this chapter, this Cygnus A data had $\sim$ 2000 independent lines-of-sight, selected manually, at a resolution of $0.75''$. These are illustrated in Fig. 6.9.

We stated earlier that various lines-of-sight of Cygnus A exhibited sinc-like, smooth and complex oscillatory behaviour. Examples of these are demonstrated in Fig. 6.10 in the top, middle and bottom panels, respectively, and their corresponding locations are highlighted. As expected, Lines-of-sight exhibiting the complex and sinc-like depolarisation structure show multiple peaks in the Faraday spectra, which usually indicates multiple Faraday components along a LoS.

The smoothly decaying LoS exhibits a single dominant Faraday peak, usually indicating a single Faraday rotating screen along that line of sight. Focussing only on this LoS as in Fig. 6.11, the q, Q and u, U signals show smooth and similar oscillatory behaviour. As a result, more constructive interference is bound to occur, leading to a more highly polarised signal. The action of RM-CLEAN is also clearly illustrated on the right-hand panels of rows two and three Fig. 6.11, which show the CLEANed and dirty Faraday spectra, respectively. Sidelobes flanking the central peak are significantly reduced, thus alleviating confusion from interpreting the "mini-peaks" in the dirty spectra as valid. One thing to note is that all these plots are contained in a single file as presented by `PolarVis`, i.e. one does not need to open multiple different plots simultaneously.

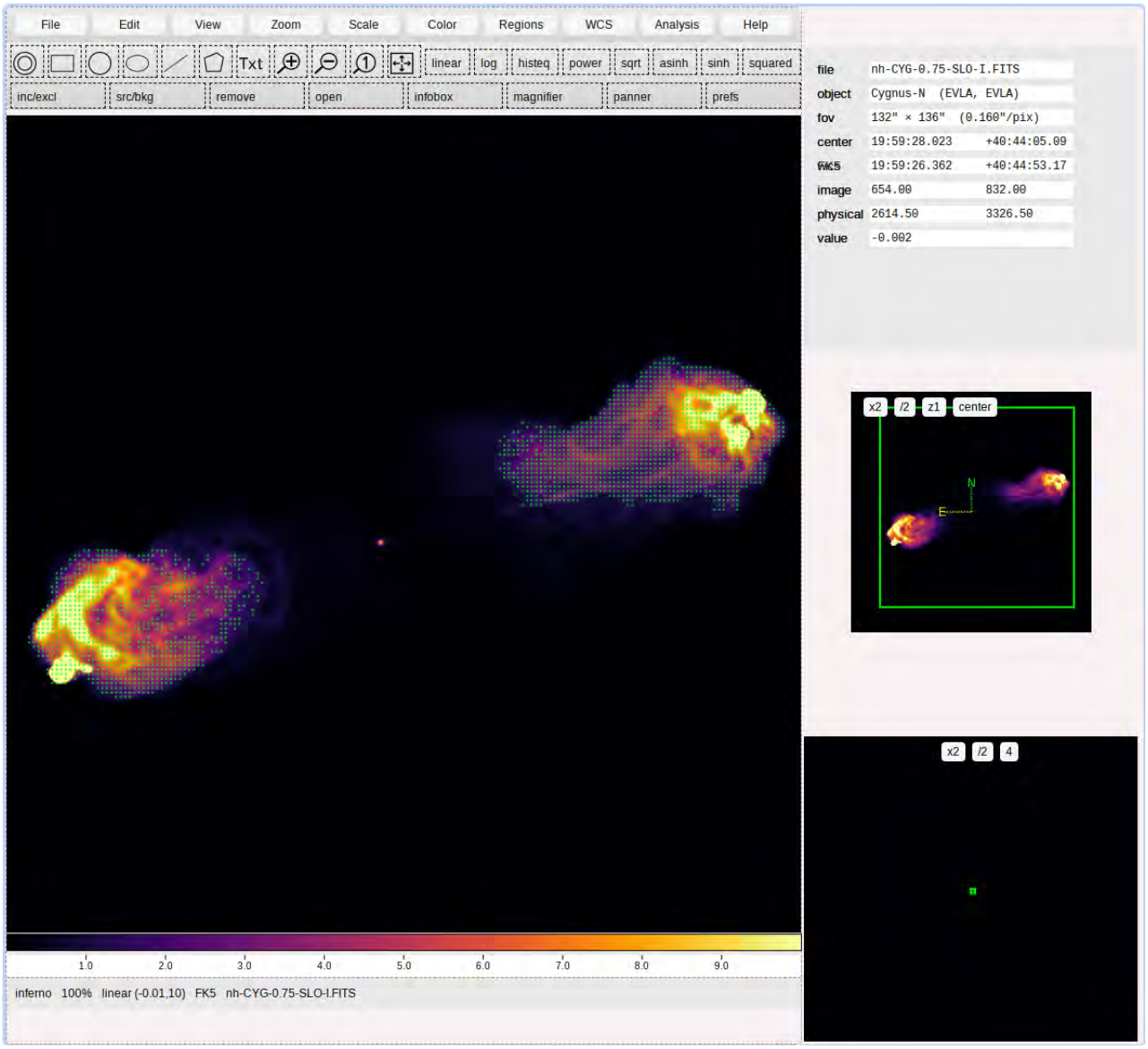

Figure 6.9: Cygnus A and its ∼ 2000 LoS represented by the green circles.

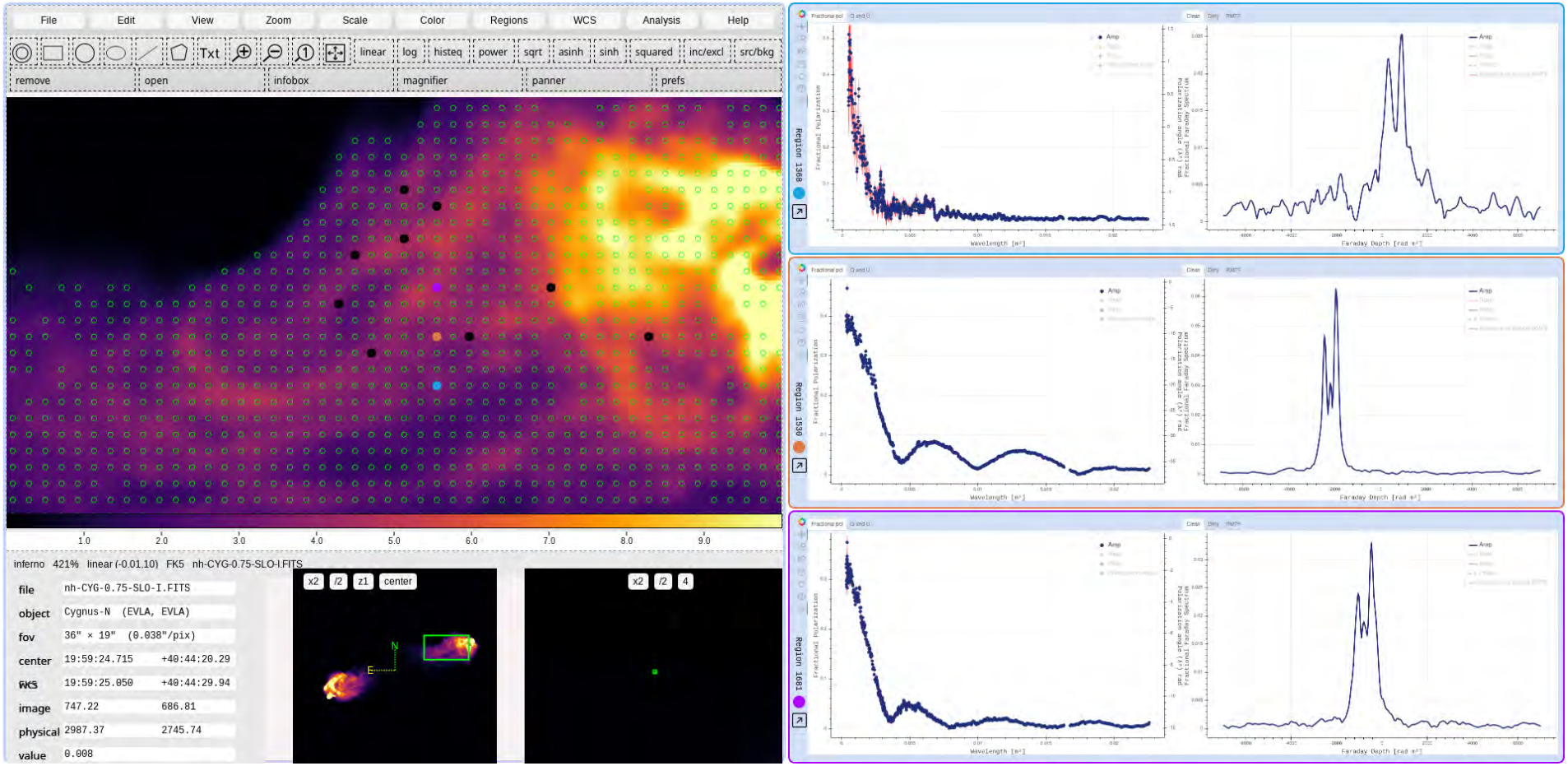

Figure 6.10: The three different categories of spectra exhibited by Cygnus A highlighted on its western lobe.

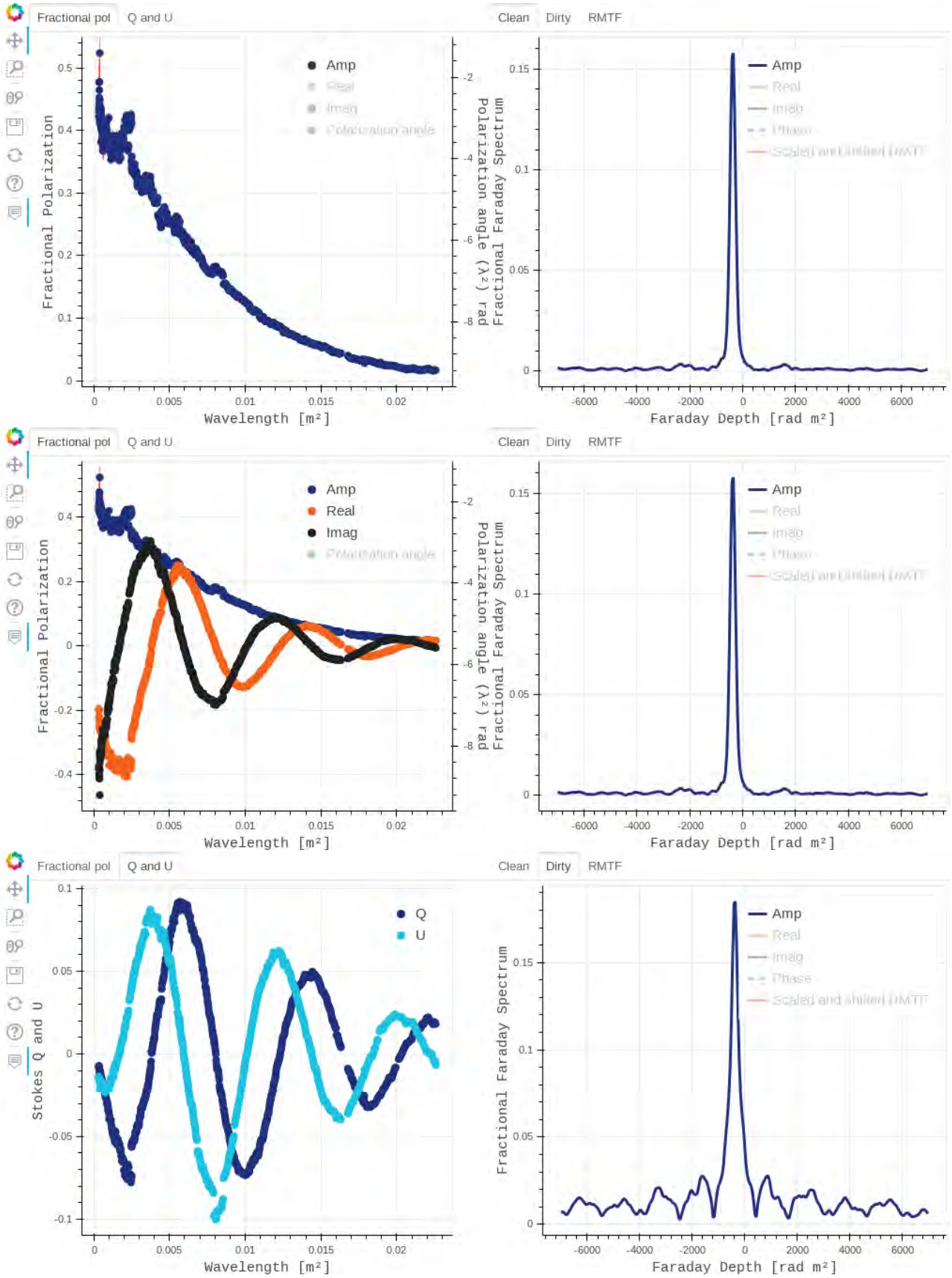

Figure 6.11: The two groups of plots are those in wavelength space on the left-hand side and those in depth space on the right-hand side. The legends could be used to toggle which plots should be visible in each plot. The left-hand side of rows two and three also demonstrate the pertinence of RM-CLEAN.

Fig. 6.12 shows the RMTF for the Cygnus A data. The FWHM of this RMTF was found to be 175 rad m^{-2} for a frequency from 2 to 18 GHz, a very high Faraday depth resolution in comparison to the typical rotation measures of this source. This RMTF was derotated to a reference λ_0^2 to reduce the number of rotations in its real and imaginary components, thus maximising the amplitude. Clicking on the legends on this plot could toggle each component on and off.

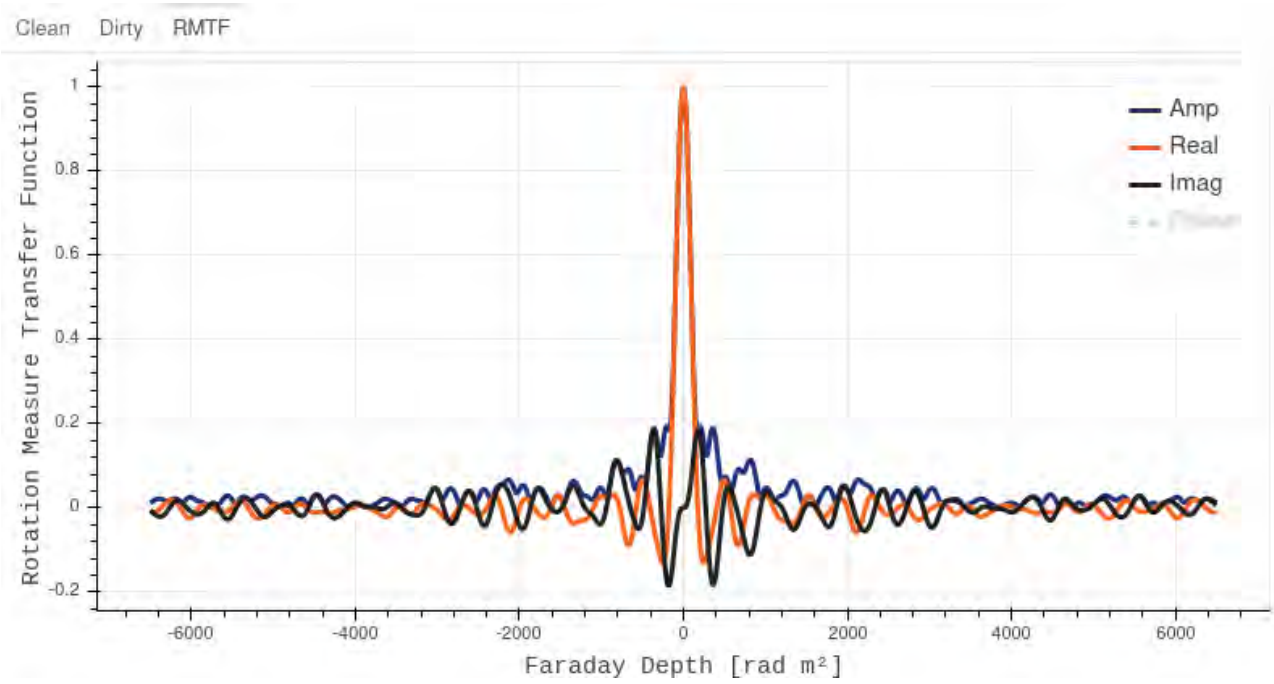

Figure 6.12: Illustrating interactive legends of `PolarVis`' plots. The RMTF is a complex function; its amplitude real and imaginary components are shown as an example. This was generated from the 2 – 18 GHz frequency coverage data.

While it is possible to generate a single plot containing subplots to convey similar information with tools like `matplotlib`, interactive plots facilitate data exploration.[10] Furthermore, the plotted data could be availed by a simple download for supplementary manipulation or visualisation. We obtain spectra from the central pixel of a region, because noise highly correlates in pixels separated by a distance smaller than a single beam's FWHM, thus averaging over an area smaller than the beam's FWHM slightly reduces resolution without significantly improving accuracy.

6.1.5 *Known Issues*

One conspicuous quirk that plagues `PolarVis` is the unsmooth rendering and resizing of the FITS viewer after a browser window resizing, which causes the shifting of some elements to undesirable positions. From simulations using the `Chromium` browser's device simulator, which allows mimicking varying screen sizes, this especially affects screens with a portrait configuration where the aspect ratio (i.e. the ratio between the x and y client screen dimensions) is less than 1. It occurs because `PolarVis` is set up such that all the elements in its GUI are automatically resized and re-organised. Therefore, a mismatch occurs because all the FITS viewing panels are set to maintain an immutable aspect ratio. This issue, however, does not affect typical laptop screen pixel dimension (e.g. the pixel configuration of the laptop on which this test was being done was 1920×1080 pixels) where the aspect ratio is more than 1.

`PolarVis` is also not yet optimised for touch screens and smaller screens. Though it will still work, it will not provide the best user experience.

10 `https://matplotlib.org/`

During normal web browser operations, each browser tab is allocated a specific hard limit on the amount of RAM it could use. This also limits the number of renderable regions since these are processed within the browser and not on the server-side. As a result, loading too many regions on `JS9` could cause a browser tab to crash. Another insidious issue is caused by the web browser used. Different browsers could render `PolarVis` differently. The tests here were done using Chromium-based browsers (Brave, Microsoft Edge, Google Chrome), `Safari` and the `Mozilla Firefox`. `Firefox` however, exhibited difficulty in rendering the main FITS image. Our efforts in investigating why bore no fruit; thus, `firefox` browser should be avoided for this particular application at the moment.

6.1.6 *Metrics*

One of the most important metrics on the responsiveness of a website is the *First contentful paint* (FCP) - the amount of time taken for the first item to be rendered on a webpage. It measures the user's first impression of the website's speed and must be kept low to improve a user's experience with the website. An FCP <1.8 is considered fast. Testing this website with Google Chrome's Lighthouse testing tool yielded an FCP of 0.8 s.[11] Other metrics tested were:

- The *largest contentful paint* (LCP) - time taken to render the largest component of a webpage (<2.5 seconds is fast).
- The *cumulative layout shift* (CLS) - how much the layout changes until the final render (a score of < 0.1 is good).

Our scores for these metrics were measured to be 1.4 seconds and 0.002, respectively as displayed in Fig. 6.13. However, other metrics such as the *speed index* - how fast content is displayed on

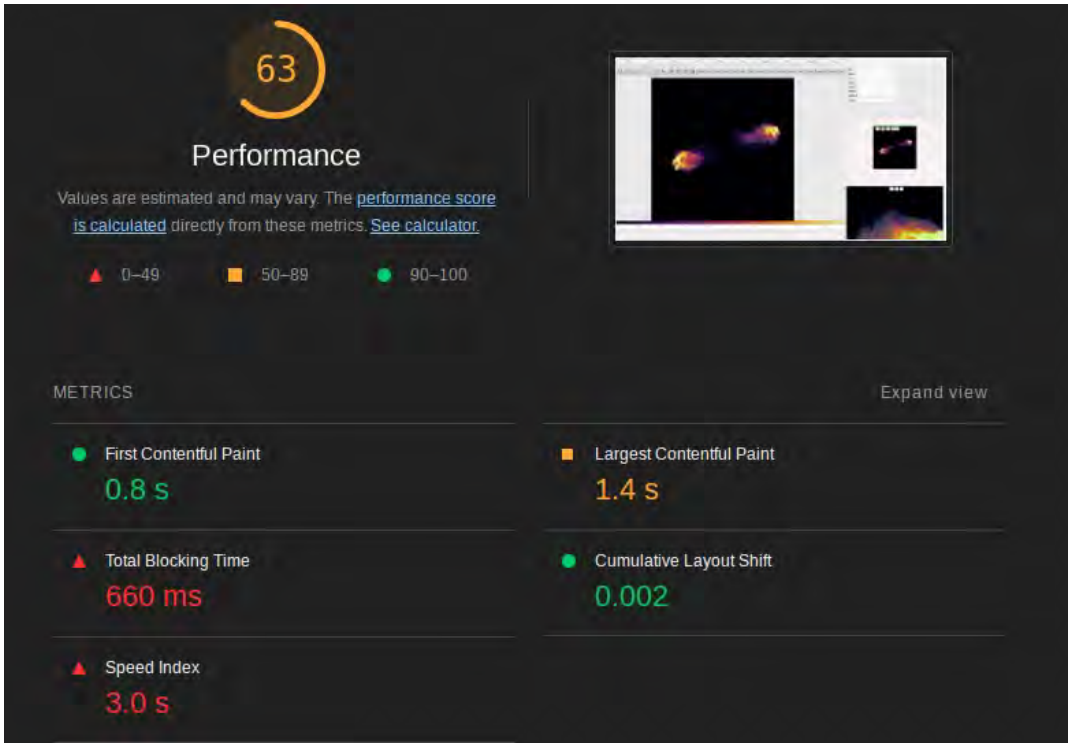

Figure 6.13: Metrics for the Cygnus A website measured by Lighthouse. The overall performance score was 63/100, which is reasonable but could be improved.

a webpage, and the *total blocking time* - the time until the website accepts user input gave low rankings at 3.0 seconds (<5.8 seconds is moderate) and 660 ms (>600 ms is slow). These low

11 https://developer.chrome.com/docs/lighthouse/overview/

scores result from the time taken to load the JS libraries required for the functionality of JS9, which must be loaded, parsed and compiled before any FITS image is rendered on the webpage (hence why they are said to block the page rendering). This is in addition to the time taken to download the representation FITS file used during testing, ∼3.5 MB in size, which Lighthouse also flags as a "large network payload."[12] A possible solution for this is using a higher binning factor to generate the representation file, which will significantly reduce the downloaded file size.

6.2 Scrappy

A suite of Python scripts was developed for the automated pre-generation of the line-of-sight data used and displayed in PolarVis. These scripts were bundled into a single package, Scrappy, which is installable via pip, the Python package installer.[13] The tools that it avails can be listed using the help function as demonstrated in Lst. 6.2.

```
# installing scrappy
pip install scrappy

# list all the tools it contains
scrappy -h
```

Listing 6.2: Setting up Scrappy.

The scripts perform the following major tasks:

1. Generate valid and independent regions (lines-of-sight) across Pictor A; a region's validity depended on whether a certain threshold was met.
2. For each region, the associated I, Q, and U data was recorded.
3. For each valid region, perform RM synthesis and linear fitting of $\psi(\lambda^2)$ and generate the data.
4. Use data generated by the previous two steps to create the interactive plots.

In the following subsections, we highlight some available tools and their usage.

6.2.1 *sc-beam-plot*

Selection of good-quality images is tedious, particularly when hundreds or thousands of images are involved, as it entails a step-by-step inspection of all the available sub-band images. To overcome this, we developed the sc-beam-plot script, which performs automatic image selection using the imaging weights set by WSClean (e.g. see Sec. 4.5). Low-quality images are mostly down-weighted. Hence, this script excludes all images whereby the ratio of its weight to the maximum image weight available is less than a certain threshold – which is adjustable as needed. The help menu is accessible using the following command:

```
sc-beam-plot --help
```

The outputs of sc-beam-plot are multiple text files containing:

12 See https://developer.chrome.com/docs/lighthouse/performance/ for the typical performance metrics used.
13 Available at: https://github.com/Mulan-94/scrappy

- Selected sub-band channel numbers.
- Names of the selected sub-band images.
- Their respective frequencies.
- Their respective weights.
- A file containing the largest beam size among the selected images.

Other files include all the beam dimensions (both selected and unselected), frequencies, and weights and a file containing the unselected image channels. A plot showing the beam dimensions while singling out the excluded channels is also generated for easier inspection, such as the one shown in Fig. 4.19 – the other tools within `Scrappy` use many of the generated files listed above.

6.2.2 *sc-los*

This script performs `Scrappy`'s tasks 1 and 2 above. It can automatically generate independent lines-of-sight as *regions* across a source such as those shown in Fig. 5.9. For basic functionality, `sc-los` requires a: (i) reference Stokes I image used to obtain the noise reference value (ii) radius of the size of the regions to be created (iii) mask or a `DS9` region file specifying the boundaries within which regions should be generated. (iv) region used to obtain the off-source noise – specified as a `DS9` region file (v) threshold below which values are ignored (vi) the location of the channelised images or names of the Stokes cubes. `sc-los` also accepts pre-existing region files, eliminating the auto-generation of new regions (i.e. eliminating the need for (iii)). Other settings are available using the help menu accessible as:

```
sc-los --help
```

`sc-los` allows for using sub-band images instead of Stokes cubes as the memory size required to hold all three cubes – I, Q, U – in the RAM simultaneously can be large. For example, consider a case where each sub-band image has 4096×4096 pixels, $\sim$70 MB in size, and there are 80 channels. This would mean that the amount of memory required to hold each Stokes cube in RAM simultaneously would be $3 \times 80 \times 65 = 15600$ MB or $\sim$15.3 GB. This size will grow dramatically if there is an increase in the number of frequency channels and image sizes – e.g. 4096 channels with the same image dimensions would require $\sim$780 GB of RAM! In a shared computing environment, it is important to minimize memory usage to ensure fair usage of resources.

Thus, two options present themselves; the first involves dividing the data into small chunks and processing it; this is possible with `Python` libraries such as `Dask`[14] which facilitates the efficient processing of larger-than-memory datasets by dividing large data into chunks, and processing the chunks in a parallel fashion. A second option entails only processing Stokes images on a single frequency channel. This means that only three FITS images will be held in RAM at any given time, in addition to the noise reference image. This option could be relatively time-consuming as the channels are processed sequentially. Nevertheless, in our case, only read operations are performed on the input images, after which computations are performed on the read data. Since images from each channel are independent, it was possible to embarrassingly parallelise their processing using the `concurrent` library. Hence, this option was availed. However, a `Dask` implementation should be considered in extremely large datasets such as those involving surveys. Nonetheless, we note that `sc-los` also takes image cubes as inputs and can process them accordingly.

On the other hand, specification of the region sizes allows varied spacing between two consecutive regions, thus allowing the existence of "independent lines-of-sight" that are sufficiently separated. Furthermore, this could be used to maintain their numbers low enough so that they are loaded into `PolarVis` without crashing the browser. The basic algorithm for `sc-los` is as follows:

14 https://www.dask.org/

1. Auto-generate circularly shaped regions across the source within boundaries specified by the input mask or boundary region file.
2. Excise the regions whose signal is below the specified threshold.
3. For the remaining created regions:
    a) Read noise data from the off-source region (this is the RMS of that region) for each available frequency channel.
    b) Read the I, Q and U pixels data enclosed in this region for each available frequency channel.
    c) If the S/N value ($I/I_{\rm RMS}$ or $|P|/P_{\rm noise}$) is more than the specified threshold in at least 50% of the channels, this is a valid region.
    d) Calculate the polarised intensity, fractional polarisation and their errors S/N and other meta-information for each channel.
    e) Mask all channels where the fractional polarisation is not within $[0, 1]$.
    f) Store all the data in `NumPy` pickle files.

One subtle thing to note is that some form of buffer is required for parallel channel processing. An easy choice of data structure would be an empty array of the same size as the number of frequency channels being processed to store incoming data. However, "normal" arrays cannot be used directly, e.g., those provided by the `NumPy` library.[15] Because we perform some computation on the data read from input images, multiple *processes* are used. A process can be considered a self-contained unit of execution within a computing environment; thus, each process has its unique memory, which cannot be shared with other processes. Therefore, it is not directly possible to share the same array amongst multiple processes, which is required in our case. Fortunately, the `multiprocessing` library provides a shared array construct, `import multiprocessing.Array`, which is modifiable by multiple processes.

For each LoS, this script outputs a single file containing the following data for each available frequency channel: the corresponding Stokes I, Q, and U data and their associated off-source RMS noise, frequencies and channel widths for each channel, polarised S/N, total intensity S/N, fractional and linear polarisation polarisation angles and their associated errors. A `DS9` region file containing the initial default created regions and the valid regions (those whose values met the set threshold) is also produced. This is done to ensure that the exact regions are reproducible for future analyses if the need arises. Plots showing the locations of those regions are also generated, e.g. the illustration in Fig. 6.14.

6.2.3 *sc-losrm*

The per LoS data files generated by `sc-los` are then passed to `sc-losrm`, where RM-synthesis is performed. In addition to RM data, this script also generates some static plots useful in examining the quality of the RM-synthesis. Parameters could then be tweaked as needed, and the script could be re-run. The `sc-bokehplot` script utilizes the combined data from `sc-los` and `sc-losrm` to generate interactive plots. Subsequently, the created `DS9` regions and interactive plots are directly ported for use with `PolarVis`. The help menus for both tools are accessible by:

15 https://numpy.org/

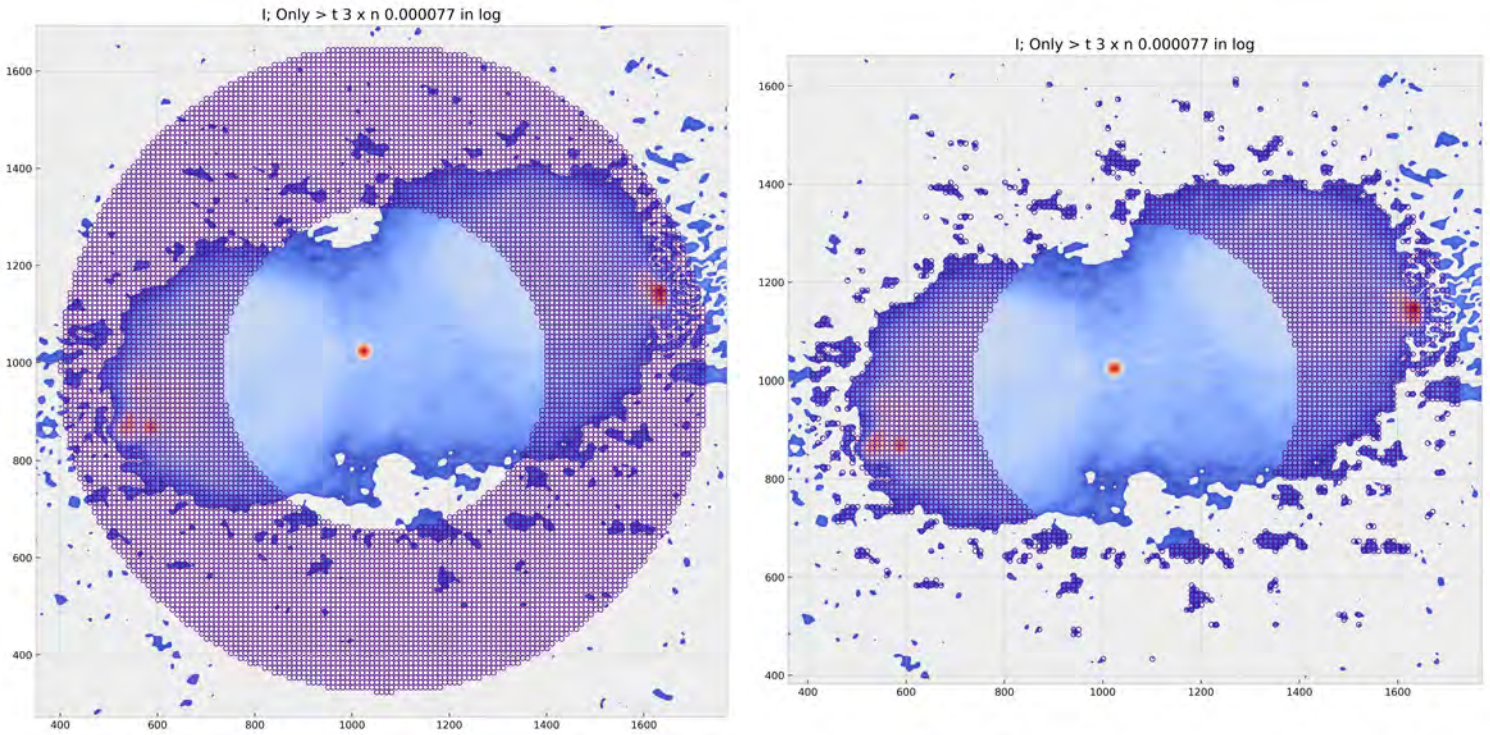

Figure 6.14: Example `sc-los` plots showing locations of the autogenerated regions. The left panel shows the initial default generated regions after `sc-los`' algorithm step 1, while the right panel shows regions remaining after `sc-los`' algorithm step 2.

```
# Help for the RM synthesis per LoS
sc-los-rm --help

# Help with generating interactive plots
sc-bokehplot --help
```

The procedure running from start to finish of the three `Scrappy` scripts occurs in minutes depending on the number of lines-of-sight, the speed of the machine in use and its workload. For our data, a typical run of approximately 2,500 lines-of-sight took about 10 minutes to finish on a machine using 21 processors.

6.2.4 *sc-rmmap*

Used to generate the per-pixel RM maps such as those displayed in Fig. 5.13. This tool also generates linear and fractional polarisation maps, the peak of the recovered FDF after RM-Clean, and polarisation angle maps, among others.

6.2.5 *Tying It All Together: showrunner.sh*

Traversing from the initial channelised Stokes images required for polarimetry (as described in Sec. 4.5) to the final step of generating visualisation-ready information demonstrated in this chapter involves a series of steps chained together to form a *processing pipeline*. The process could be repetitive and prone to mistakes; thus, automating the steps involved is a natural option towards mitigating errors introduced by multiple tweaks and alterations to the data processing. Moreover,

the consistency enforced by automation ensures that the resulting data products are reproducible, provided the pipeline is run with the same settings, which fosters transparency within the scientific process. For this reason, we created an automation script in the `Bash` scripting language (tested with version 5). `Bash` (Bourne Again Shell) facilitates daisy-chaining of various CLI based commands in the Linux, and generally the Unix environments, through the use of *shell scripts*. Here, the different steps are structured as programming functions only executed on demand. In brief, this script performs the following functions:

1. Auto-selects good channels.
2. Convolves all the images to the same resolution.
3. Creates Stokes I, Q, and U cubes.
4. Generates spectral index maps (if necessary).
5. Generates maps of the rotation measure and polarised intensity at peak depth, among others.
6. Create the independent LoS data.
7. Perform RM-synthesis on these LoS.
8. Generate their interactive plots.

`showrunner.sh` comes bundled within `Scrappy` with default configurations which **must be changed to suit one's data**. This script must first be initialised in a child subdirectory relative to where the polarimetric images are to enable its customisation and usage. Initialisation is done by:

```
# to generate showrunner.sh
scrappy -i

# to run it
./showrunner.sh
```

Listing 6.3: Initialising `showrunner.sh`.

which copies the requisite files to that directory. Once the setup is suited to one's needs and executed, `showrunner.sh` will automatically install software to be used in the script (a summary of these is given in Tab. 6.1). For now, `showrunner.sh` is presented as a shell script to: (i) Give a simple introduction on how to use the various tools within `Scrappy`. (ii) Demonstrate in verbatim our use of other external tools used within our pipeline. (iii) Enable the swift addition of other functionalities to this pipeline by incorporating commonly known and used CLI tools.

6.3 Future Work

While developing a `Bash` script was helpful in this case, it may not be easily accessible to those without a programming background. Fortunately, pipelining tools using the `Python` language, which has enjoyed more adoption within the astronomical field, are under active development, intending to streamline the pipeline creation process. One such tool is `Stimela`, whereby a command and its options are known as a *cab*. The steps taken to achieve a particular product form what is known as a *recipe*.[16] These are usually defined in plain-text files in the `YAML` format, which presents them in an easy-to-read manner. Thus, one only needs to know the syntax for cab and recipe creation and the tools required to achieve their goal without learning shell scripting. Furthermore, `Stimela` can automatically redirect outputs of one step to the input of another, provided

16 See the documentation on how `Stimela` works `https://stimela.readthedocs.io/en/latest/`

Table 6.1: Software required for the automation script.

Python based software		
Name	command	task
montagePy	fitsheader	Read FITS headers
owlcat	fitstool.py	Creating Stokes cubes
spimple	spimple-imconv	Image convolution to the same beam
	spimple-spifit	Spectral index fitting
Scrappy	sc-beam-plot	Channel auto-selection and beam dimension plotting
	sc-rmmap	Generate per-pixel RM maps among other things
	sc-los	Generate independent LoSs
	sc-losrm	Perform RM-synthesis on LoSs from Scrappy
	sc-bokehplot	Generate interactive plots for the LoS
	sc-houdini	Generate simple image masks given input images
Native Bash commands (most are default to Linux)		
	cp	Copy files and folders
	ls	Listing files and folders
	sed	For some text processing
	mv	Moving and renaming files
	rm	Deleting files and folders
	rename.ul	Batch file renaming

the correct configuration has been done. Therefore, a logical next step would be implementing this Bash script as a Stimela recipe. Since Stimela is already in use within the CARACal pipeline, such an implementation could benefit the larger astronomy community.

Moreover, the tools within Scrappy currently work, but could be significantly refined and improved to increase their robustness, speed and efficiency. As such, more testing with varying kinds of data is required to aid in its development.

On the other hand, PolarVis could benefit from real-time RM-synthesis and subsequent interactive plots of the processed data upon clicking on a region compared to pre-generated interactive plots.

6.4 Summary

In this chapter, we introduced a new polarimetric visualisation tool, PolarVis, which provides an interactive display of independent lines-of-sight across a source. This tool is built on the JS9 FITS viewer. It avails interactive regions on a source's image, which, when clicked, display its associated interactive plots in both wavelength and Faraday depth space.

Furthermore, we presented a Python-based package, Scrappy, that auto-generates these independent LoSs, performs RM-synthesis on them and generates their corresponding interactive plots for display with PolarVis. We have also introduced an automated script, showrunner.sh– a pipeline of sorts – that avails polarimetry-ready data products for analysis and visualisation given the input channelised Stokes images using a combination of tools provided by Scrappy and other publicly available tools. PolarVis and Scrappy have been made available at:

- https://github.com/Mulan-94/polarvis

- https://github.com/Mulan-94/scrappy

To demonstrate PolarVis' use, we deployed it with Pictor A and Cygnus A data on two different websites:

- https://pica.ratt.center
- https://cygnus.ratt.center/cygnus

The steps taken to set this website up have also been highlighted and availed in App. C.

7

SUMMARY, CONCLUSIONS, AND FUTURE WORK

This thesis hinges on three themes:

1. Data reduction involving calibration and imaging of Pictor A's L-band raw visibility data obtained from the MeerKAT telescope,
2. The scientific interpretation of spectropolarimetric results acquired from the data reduction and,
3. Development of software and a pipeline that facilitates, at least in part, the analysis and visualisation of spectropolarimetric data products.

We have presented the reduction procedures for our data in Chap. 4, detailing the steps, commands, and software used. Most of the steps and techniques presented in this chapter represent standard practice in radio data reduction. Furthermore, we have introduced a new tool, `Smops` (Sec. 4.4), that improves source modelling by interpolating low-frequency-resolution models to finer-frequency models, improving the models and allowing better subtraction and calibration. The benefits of selfcal in improving resulting images have also been illustrated. Moreover, in the interest of transparency, we have justified our imaging choices, emphasizing the specific imaging configurations required for polarimetric imaging in Sec. 4.5.

Based on our observational data, we have shown the first image showing the full extent of the radio jet in Pictor A, extending from the radio core to the WHS in Chap. 5. The spectropolarimetric study of Pictor A was also addressed in that chapter, confirming previous RM observations and depolarisation characteristics of this source at a higher sensitivity.

In Chap 6, we justified the importance of visualising spectropolarimetric data products to provide more insights into trends across extragalactic sources. As such, we presented `PolarVis` (in Sec. 6.1), a web-based visualisation tool that displays spectra of the various LoS across a source, and `Scrappy` (in Sec. 6.2) a `Python`-based CLI tool that automatically generates the various independent LoS across our source, in addition to the corresponding interactive plots to be used in conjunction with `PolarVis`. `Scrappy` also avails another tool, `showrunner.sh`, a pipeline that facilitates the automated generation of these data products, ensuring reproducibility.

On the other hand, Chap. 4 has especially demonstrated the adverse effects of RFI in the L-band to spectropolarimetric studies, which result in the exclusion of almost 50% of the λ^2 samples due to low signal-to-noise. These effects resulted in high sidelobes in our RMTF (shown in Fig. 5.1) and caused great difficulty in reconstruction in Faraday spectra. This necessitates better RFI mitigation techniques that will reduce signal loss and leave the data quality intact. Since not much can be done at this point, another option to increase our λ^2 coverage is observing this source at frequencies higher and lower than the L-band, where RFI from telecommunication equipment is reduced. However, at lower frequencies, atmospheric effects are more pronounced as the ionosphere introduces time and direction-dependent Faraday rotation to incoming data, altering the polarimetric characteristics. This places more stringent calibration demands.

Nevertheless, combining data from higher and lower frequency bands of Pictor A will result in a higher RMTF resolution, perhaps allowing better resolution of the Faraday structure intrinsic to the source. Based on this work, we submitted a proposal for MeerKAT observations of Pictor A at the

UHF and S-bands, which was accepted. Therefore, further investigations of this source's underlying structure are expected to continue. Additionally, a wider bandwidth will allow for a more detailed exploration and characterisation of Pictor A's spectral behavior, and hopefully, help us answer some puzzling questions such as why the spectral index of the eastern hotspots is unusually steep compared to other radio hotspots, and whether there is any associated curvature.

With the increasing number of wideband polarimetric surveys, the need for fast and memory-efficient tools for spectropolarimetric analysis beckons. This was briefly discussed in Sec. 6.2 due to the anticipated growth of image sizes and frequency samples, which will undoubtedly incur high computation costs. Current tools like `RM-Tools`[1] work around this by chunking large data cubes into multiple, smaller cubes as a preprocessing step and then recombining them afterwards, but this approach is also inefficient. A new generation of software tools is needed. To this extent, the development and refinement of `Scrappy` is expected to continue, using the already available "big data" `Python` libraries to make it more robust and adaptable. As mentioned in Sec. 6.2, we believe that implementation of `showrunner.sh` using the `Stimela` pipelining tool will benefit the greater astronomical community.

There has recently been a concerted effort in the radio polarimetry community to standardise the storage and representation of useful polarisation information, especially with large-scale radio polarisation catalogues. For example, Van Eck et al. (2023) have presented `RMTable2023` and `PolSpectra2023` tools for storage of ancillary polarisation data and metadata. The authors also detailed the prescribed methods for deriving the information. This was motivated by the following needs: (i) To act as a guide for future authors on data that may be superfluous to the author but important to the larger scientific community (ii) To establish standard procedures for RM derivation and the increase of disparate dataset compatibilities (iii) To facilitate easy combination of multiple catalogues for analysis. Although these prescriptions are geared towards large RM catalogues, they could be adapted for use within the exploration of single diffuse and resolved galaxies such as Pictor A with thousands of LoS. Van Eck et al. (2023) have placed a caveat on using these tools with resolved sources, stating that it is beyond the intended scope. However, I think this may be a worthy endeavour in a push for transparency and reproducibility on all fronts.

1 `https://github.com/CIRADA-Tools/RM-Tools/tree/master`

Part III

APPENDIX

Umbali tumetoka hadi hapa tumefika, tunatambua kwamba Wewe ni Ebenezer!

A

REGION DEFINITIONS USED FOR THIS THESIS

Here, we show the coordinates of the regions we chose to represent the various coordinates. These use the DS9 region file definitions.

a.1 Pictor A's noise estimate region

The region used to estimate Pictor A's off-source RMS noise.

```
# Region file format: DS9 CARTA 3.0.0
global color=green dashlist=8 3 width=1 font="helvetica 10 normal roman"
 ↪  select=1 highlite=1 dash=0 fixed=0 edit=1 move=1 delete=1 include=1
 ↪  source=1
fk5
box(80.065279091, -45.853757357, 53.6462", 53.6462", 0) # color=#2EE6D6
 ↪  width=2
```

a.2 Lobes

What we considered the Eastern and Western lobes.

```
# Region file format: DS9 CARTA 3.0.0-beta.3
global color=green dashlist=8 3 width=1 font="helvetica 10 normal roman"
 ↪  select=1 highlite=1 dash=0 fixed=0 edit=1 move=1 delete=1 include=1
 ↪  source=1
fk5
box(79.896236510, -45.771622694, 308.7539", 312.6540", 100) # color=#2EE6D6
 ↪  width=3 text={w-lobe}
line(80.152223465, -45.802694730, 79.763181475, -45.754853795) #
 ↪  color=#3752DB width=4 text={center-line}
box(80.007846963, -45.785598278, 308.5421", 256.7625", 100) # color=#DB3737
 ↪  width=3 text={e-lobe}
```

a.3 Novel Jet-like Feature

Coordinates for the novel jet-like feature shown in Fig. 5.5 reminiscent of a radio jet. The projected paths of this feature are also included.

```
# Region file format: DS9 CARTA 3.0.0
global color=green dashlist=8 3 width=1 font="helvetica 10 normal roman"
 ↪  select=1 highlite=1 dash=0 fixed=0 edit=1 move=1 delete=1 include=1
 ↪  source=1
fk5
polygon(79.955539073, -45.772027485, 79.951185219, -45.775064009,
 ↪  79.943423897, -45.776053552, 79.932256074, -45.774335292, 79.927241761,
 ↪  -45.770703298, 79.938315170, -45.769187336) # color=#F1652F width=4
```

a.4 Jet Position angle

The axis used to estimate the Pictor A's radio jet position angle.

```
# Region file format: DS9 CARTA 3.0.0-beta.3
global color=green dashlist=8 3 width=1 font="helvetica 10 normal roman"
 ↪  select=1 highlite=1 dash=0 fixed=0 edit=1 move=1 delete=1 include=1
 ↪  source=1
fk5
line(79.846175684, -45.763787494, 80.041648219, -45.790311379) #
 ↪  color=#2EE6D6 width=2 text={90-axis}
```

a.5 Missing IC/CMB radio emission

Shown in Fig. 5.4

```
# Region file format: DS9 CARTA 3.0.0
global color=green dashlist=8 3 width=1 font="helvetica 10 normal roman"
 ↪  select=1 highlite=1 dash=0 fixed=0 edit=1 move=1 delete=1 include=1
 ↪  source=1
fk5
polygon(79.986529421, -45.751374844, 79.988562257, -45.757296327,
 ↪  79.961438163, -45.762063902, 79.953872250, -45.760905283, 79.950181778,
 ↪  -45.759617717, 79.943910261, -45.749446738, 79.945755792, -45.746485934,
 ↪  79.957009349, -45.748160121, 79.961806041, -45.747773810, 79.986515890,
 ↪  -45.751335039) # color=#FF4A0F width=4
polygon(79.980284181, -45.814537113, 79.961263081, -45.800663229,
 ↪  79.936561765, -45.798307460, 79.909910605, -45.792724334, 79.912213469,
 ↪  -45.801521750, 79.946509740, -45.817016832, 79.979755715, -45.814590362)
 ↪  # color=#FF4A0F width=4
```

a.6 Spectral index regions

The region used to estimate the spectral indices of the various components of Pictor A in Tab. 5.1.

```
# Region file format: DS9 CARTA 3.0.0
global color=green dashlist=8 3 width=1 font="helvetica 10 normal roman"
 ↪  select=1 highlite=1 dash=0 fixed=0 edit=1 move=1 delete=1 include=1
 ↪  source=1
fk5
polygon(79.956395548, -45.774998312, 79.951467606, -45.777424253,
 ↪  79.954366130, -45.782276528, 79.947986597, -45.792587050, 79.941895551,
 ↪  -45.799864649, 79.926813584, -45.804107289, 79.911147917, -45.809965111,
 ↪  79.888528845, -45.806314676, 79.873751405, -45.797004897, 79.867098261,
 ↪  -45.786891181, 79.861896513, -45.776980463, 79.859004910, -45.772934543,
 ↪  79.869451053, -45.765664770, 79.865407619, -45.757170302, 79.864260308,
 ↪  -45.750093295, 79.874412406, -45.742418476, 79.883690885, -45.736157420,
 ↪  79.893832476, -45.733130875, 79.905708352, -45.732732485, 79.922797138,
 ↪  -45.733143229, 79.928010345, -45.733953373, 79.937278811, -45.734966219,
 ↪  79.950602047, -45.742852535, 79.949152295, -45.751748081, 79.954656968,
 ↪  -45.761654832, 79.954946456, -45.768933094, 79.957554994, -45.772774413,
 ↪  79.956685397, -45.774796135, 79.957555007, -45.774593973) # color=#2EE6D6
 ↪  width=2 text={wlobe}
polygon(79.962192893, -45.775806903, 79.964512290, -45.779243727,
 ↪  79.960743914, -45.781467816, 79.957265153, -45.783287431, 79.956105368,
 ↪  -45.791172194, 79.953785330, -45.798854746, 79.949433586, -45.812602341,
 ↪  79.957845383, -45.818263459, 79.966548324, -45.819880467, 79.974668886,
 ↪  -45.813005608, 79.992073593, -45.814619021, 80.009477410, -45.814208064,
 ↪  80.021364596, -45.809349857, 80.032089906, -45.804693361, 80.031506641,
 ↪  -45.802267651, 80.021932226, -45.798634337, 80.018445708, -45.792571043,
 ↪  80.032070880, -45.790541212, 80.042501145, -45.785479583, 80.045970188,
 ↪  -45.779209566, 80.044807461, -45.777188729, 80.037265486, -45.773555109,
 ↪  80.031172329, -45.768909223, 80.025948627, -45.763453779, 80.019858881,
 ↪  -45.760020330, 80.017828847, -45.758606203, 80.011160802, -45.755374760,
 ↪  79.998120485, -45.753964943, 79.988268599, -45.753563700, 79.981314375,
 ↪  -45.753161019, 79.973490936, -45.752555880, 79.966247159, -45.751950163,
 ↪  79.963929255, -45.752354682, 79.959872928, -45.754780929, 79.957844687,
 ↪  -45.761048338, 79.960742980, -45.766911321, 79.962772274, -45.772369919,
 ↪  79.961323305, -45.776009100, 79.963062645, -45.777222081) # color=#2EE6D6
 ↪  width=2 text={elobe}
circle(79.957167007, -45.778860992, 15.0000") # color=#2EE6D6 width=2
 ↪  text={core}
ellipse(80.027194821, -45.796090739, 9.5318", 9.2244", 90) # color=#2EE6D6
 ↪  width=2 text={ehs-inner}
ellipse(80.035524786, -45.795914552, 11.9917", 10.4543", 90) # color=#2EE6D6
 ↪  width=2 text={ehs-outer}
circle(79.863091782, -45.766428092, 22.3133") # color=#2EE6D6 width=2
 ↪  text={whs}
polygon(79.965686592, -45.812933130, 79.954525039, -45.816905924,
 ↪  79.945500808, -45.814588059, 79.944789237, -45.810698247, 79.948826673,
 ↪  -45.807222659, 79.948233594, -45.803663892, 79.944553710, -45.802008340,
 ↪  79.938380197, -45.802917868, 79.928881829, -45.805067680, 79.920929116,
 ↪  -45.802582634, 79.929007627, -45.790998394, 79.948235571, -45.791332518,
 ↪  79.961055139, -45.803415896, 79.961173894, -45.803746940) # color=#2EE6D6
 ↪  width=2 text={plume}
box(79.952815081, -45.778517774, 114.4919", 266.6250", 0) # color=#2EE6D6
 ↪  width=2 text={waist}
```

a.7 Profile bins

Definitions for the bins used to generate the depolarization profiles in Fig. 5.12, and the RM profiles in Fig. 5.14. These bins are displayed in Fig. 5.11.

```
# Region file format: DS9 CARTA 3.0.0
global color=green dashlist=8 3 width=1 font="helvetica 10 normal roman"
 ↪  select=1 highlite=1 dash=0 fixed=0 edit=1 move=1 delete=1 include=1
 ↪  source=1
fk5
box(80.037512885, -45.788493468, 30.0000", 250.0000", 0) # color=#2EE6D6
 ↪  width=2 text={e7}
box(80.025703811, -45.787019307, 30.0000", 250.0000", 0) # color=#2EE6D6
 ↪  width=2 text={e6}
box(80.013931908, -45.785618739, 30.0000", 250.0000", 0) # color=#2EE6D6
 ↪  width=2 text={e5}
box(80.002233498, -45.784157395, 30.0000", 250.0000", 0) # color=#2EE6D6
 ↪  width=2 text={e4}
box(79.990416903, -45.782710829, 30.0000", 250.0000", 0) # color=#2EE6D6
 ↪  width=2 text={e3}
box(79.978675179, -45.781232089, 30.0000", 250.0000", 0) # color=#2EE6D6
 ↪  width=2 text={e2}
box(79.966915315, -45.779915515, 30.0000", 250.0000", 0) # color=#2EE6D6
 ↪  width=2 text={e1}
box(79.957255761, -45.778817217, 19.0000", 250.0000", 0) # color=#2EE6D6
 ↪  width=2 text={core}
box(79.947651479, -45.777350978, 30.0000", 250.0000", 0) # color=#2EE6D6
 ↪  width=2 text={w1}
box(79.935862524, -45.775912964, 30.0000", 250.0000", 0) # color=#2EE6D6
 ↪  width=2 text={w2}
box(79.923955458, -45.774473416, 30.0000", 250.0000", 0) # color=#2EE6D6
 ↪  width=2 text={w3}
box(79.912126790, -45.772941109, 30.0000", 250.0000", 0) # color=#2EE6D6
 ↪  width=2 text={w4}
box(79.900413816, -45.771523317, 30.0000", 250.0000", 0) # color=#2EE6D6
 ↪  width=2 text={w5}
box(79.888528101, -45.770015231, 30.0000", 250.0000", 0) # color=#2EE6D6
 ↪  width=2 text={w6}
box(79.876678929, -45.768604561, 30.0000", 250.0000", 0) # color=#2EE6D6
 ↪  width=2 text={w7}
box(79.864869481, -45.767122049, 30.0000", 250.0000", 0) # color=#2EE6D6
 ↪  width=2 text={w8}
box(79.852986592, -45.765710377, 30.0000", 250.0000", 0) # color=#2EE6D6
 ↪  width=2 text={w9}
```

B

DATA REDUCTION RECIPES

Software

The software used for data reduction and preparation of some of the figures in this thesis:

Software

Name	Task
`Aplpy`	FITS Image figure visualisation
`CARACal`	Automated 1 GC data reduction
`CubiCal`	selfcal
`OwlCat`	Sub-band image stacking
`WSClean`	Imaging

b.1 Caracal: 1GC

Here, we show the `CARACal` pipeline recipe used for first-generation calibration. This is usually done in a text file with a `YAML`, making it easy to read. To launch this recipe, `CARACal` was ran as:

```
caracal -c config.yml -ct singularity
```

```yaml
schema_version: 1.0.3

general:
  prefix: with-polcal
  # msdir: '/vault-ike/andati/pica_redux/msdir'
  rawdatadir: '/net/sinatra/vault-ike/andati/pica_redux/msdir'
  # output: '/vault-ike/andati/pica_redux/output'

  msdir: '/home/andati/pica/reduction/experiments/final-cut/msdir'
  output: '/home/andati/pica/reduction/experiments/final-cut/output'
  # cabs:
  #   - name: shadems_direct
  #     tag: '1.7.1'
  #   - name: owlcat_plotelev
  #     tag: 1.2.6
  final_report: false

getdata:
  dataid: ['1576687564_sdp_l0']

obsconf:
  obsinfo:
```

```
    enable: false
  refant: 'm005'
  report: false
  target:
    - all
  fcal:
    - longest
  bpcal:
    - longest
  gcal:
    - all
  xcal:
    - 'J0521+1638'

transform:
  enable: false
  label_out: cal_with_pcal
  field: calibrators
  split_field:
    enable: true
    col: data
  report: true

prep:
  enable: false
  label_in: cal_with_pcal
  field: calibrators
  specweights:
    enable: true
    mode: uniform
  report: true

flag:
  enable: false
  field: calibrators
  label_in: cal_with_pcal
  flag_autopowerspec:
    enable: false
  flag_autocorr:
    enable: true
  flag_spw:
    enable: true
    chans: '*:856~880MHz , *:1658~1800MHz, *:1419.8~1421.3MHz'
    ensure_valid: false
  flag_mask:
    enable: true
    mask: meerkat.rfimask.npy
    uvrange: '0~1000'
  summary:
    enable: true
  report: true

flag__2:
  enable: false
  field: calibrators
  label_in: cal_with_pcal
  flag_rfi:
    enable: true
    col: DATA
```

```
    flagger: tricolour
  summary:
    enable: true
  report: true

flag__3:
  enable: false
  field: calibrators
  label_in: cal_with_pcal
  flag_antennas:
    enable: true
    antennas: 'm003'
  flag_scan:
    enable: true
    scans: '22'
  summary:
    enable: true
  report: true

crosscal:
  enable: false
  uvrange: '>150'
  label_in: cal_with_pcal
  set_model:
    enable: true
    meerkat_skymodel: false
  primary:
    reuse_existing_gains: true
    order: KGBAKGB
    combine: ["", "", "", null, "", "", ""]
    solint: [inf, inf, inf, null, 60s, 60s, inf]
    calmode: [a, ap, ap, null, a, ap, ap]
    b_fillgaps: 70
    plotgains: true
  secondary:
    reuse_existing_gains: true
    order: KGAKF
    apply: B
    combine: ["", "", null, "", ""]
    solint: [inf, inf, null, inf, inf]
    calmode: [a, ap, null, a, ap]
    plotgains: true
  apply_cal:
    applyto:
      - gcal
      - bpcal
      - xcal

polcal:
  enable: false
  label_in: cal_with_pcal
  label_cal: pcal
  otfcal:
    enable: true
    label_cal: 1gc1
  extendflags: True
  feed_angle_rotation: '-90'
  uvrange: '>150'
  reuse_existing_tables: false
```

```
  pol_calib: xcal
  leakage_calib: bpcal
  set_model_leakage:
    enable: false
  set_model_pol: true
  gain_solint: 'int'
  time_solint: 'inf'
  #freq_solint: 'inf'
  freqsel: '0:1.45~1.50GHz'
  plotgains: true
  apply_pcal: true
  applyto:
    - gcal
    - bpcal
    - xcal

inspect:
  enable: false
  label_in: 'cal'
  field: 'calibrators'
  label_plot: '1gc'
  dirname: crosscal
  standard_plotter: none # ragavi_vis
  real_imag:
    enable: true
    avgtime: '60'
  amp_phase:
    enable: false
    avgtime: '60'
  amp_uvwave:
    enable: true
    avgtime: '60'
  amp_ant:
    enable: false
    avgtime: '60'
  phase_uvwave:
    enable: true
    avgtime: '60'
  amp_scan:
    enable: false
    avgtime: '60'
  shadems:
    enable: true
    default_column: CORRECTED_DATA
    plots_by_field:
      - "-x BASELINE_M -y FREQ -c amp"
      - "-x real  -y imag   -c SCAN_NUMBER --cnum 100"
      - "-x real  -y imag   -c ANTENNA1 --cnum 100"
      - "-x ANTENNA1 -y ANTENNA2 -c SCAN_NUMBER --cnum 100 --aaxis phase
 ↪  --ared std"
      - "-x ANTENNA1 -y ANTENNA2 -c SCAN_NUMBER --cnum 100 --aaxis amp --ared
 ↪  mean"
      - "-x UV    -y amp    -c SCAN_NUMBER --cnum 100"
      - "-x UV    -y amp    -c ANTENNA1 --cnum 64"
      - "-x UV    -y phase  -c ANTENNA1 --cnum 64"
      - "-x FREQ  -y amp    -c SCAN_NUMBER --cnum 100"
      - "-x FREQ  -y amp    -c ANTENNA1 --cnum 64"
      - "-x U     -y V      -c amp"
      - "-x U     -y V      -c phase --cmin -5 --cmax 5"
```

```
    plots:
      - "-x real  -y imag   -c SCAN_NUMBER --cnum 100 --col
↪  CORRECTED_DATA/MODEL_DATA --iter-field"
      - "-x real  -y imag   -c ANTENNA1 --cnum 100 --col
↪  CORRECTED_DATA/MODEL_DATA --field {bpcal} --iter-field"
      - "-x real  -y imag   -c ANTENNA1 --cnum 100 --col
↪  CORRECTED_DATA/MODEL_DATA --field {gcal} --iter-field"
      - '-x FREQ -y amp:I -c SCAN_NUMBER --cnum 100 --cmin 0 --cmax 30 --field
↪  {bpcal} --dir {msbase}-bpcal-iamp-byant --iter-ant'
      - '-x FREQ -y amp:I -c SCAN_NUMBER --cnum 100 --cmin 0 --cmax 30 --field
↪  {gcal} --dir {msbase}-gcal-iamp-byant --iter-ant'
      - '-x ANTENNA1 -y ANTENNA2 -a CORRECTED_DATA:amp --ared std --cmap
↪  pride --amin 0 --amax 1 --field {bpcal} --dir
↪  {msbase}-bpcal-stdamp-byscan --iter-scan'
      - '-x ANTENNA1 -y ANTENNA2 -a CORRECTED_DATA:amp --ared std --cmap
↪  pride --amin 0 --amax 5 --field {gcal} --dir {msbase}-gcal-stdamp-byscan
↪  --iter-scan'
      - '-x ANTENNA1 -y ANTENNA2 -a CORRECTED_DATA:phase --ared std --cmap
↪  pride --amin 0 --amax 3 --field {bpcal} --dir
↪  {msbase}-bpcal-stdphase-byscan --iter-scan'
      - '-x ANTENNA1 -y ANTENNA2 -a CORRECTED_DATA:phase --ared std --cmap
↪  pride --amin 3 --amax 10 --field {gcal} --dir
↪  {msbase}-gcal-stdphase-byscan --iter-scan'
      - '-x FREQ -y SCAN_NUMBER -a CORRECTED_DATA:amp --ared std --cmap pride
↪  --amin 5 --amax 25--field {bpcal} --dir {msbase}-bpcal-stdamp-byant
↪  --iter-ant'
      - '-x FREQ -y SCAN_NUMBER -a CORRECTED_DATA:amp --ared std --cmap pride
↪  --amin 0 --amax 10 --field {gcal} --dir {msbase}-gcal-stdamp-byant
↪  --iter-ant'
      - '-x FREQ -y SCAN_NUMBER -a CORRECTED_DATA:phase --ared std --cmap
↪  pride --amin 0 --amax 10 --field {bpcal} --dir
↪  {msbase}-bpcal-stdphase-byant --iter-ant'
      - '-x FREQ -y SCAN_NUMBER -a CORRECTED_DATA:phase --ared std --cmap
↪  pride --amin 0 --amax 10 --field {gcal} --dir
↪  {msbase}-gcal-stdphase-byant --iter-ant'
      - '-x BASELINE_M -y FREQ --iter-scan -a CORRECTED_DATA:imag --ared std
↪  --amin 0 --amax 2 --cmap pride --field {bpcal} --dir
↪  {msbase}-bpcal-stdimag-byscan'
      - '-x BASELINE_M -y FREQ --iter-scan -a CORRECTED_DATA:imag --ared std
↪  --amin 0 --amax 2 --cmap pride --field {gcal} --dir
↪  {msbase}-gcal-stdimag-byscan'
    ignore_errors: true

inspect__polcal:
  enable: false
  label_in: cal_with_pcal
  field: 'calibrators'
  label_plot: '1gc'
  dirname: crosscal-polcal-v3
  standard_plotter: none # ragavi_vis
  correlation: all
  shadems:
    enable: true
    default_column: CORRECTED_DATA
    plots:
      - desc: "plots by field"
        field: "{all_fields}"
        cnum: 100  # up 100 colours
        iter_field: true
```

```
      plots:
        # phaseball plots
        - dir: "phaseballs-{msbase}"
          plots:
            - "-x real -y imag -c CORR --corr IQUV --hline 0: --vline 0:"
            - "-x real -y imag -c SCAN_NUMBER"
            - "-x real -y imag -c ANTENNA1"
        - dir: "phaseballs-bycorr-{msbase}"
          iter_corr:
          plots:
            - "-x real -y imag -c SCAN_NUMBER"
            - "-x real -y imag -c ANTENNA1"
        # normalized phaseballs
        - dir: "normballs-{msbase}"
          col: "CORRECTED_DATA/MODEL_DATA"
          corr: "XX,YY"
          iter_corr:
          plots:
            - "-x real -y imag -c SCAN_NUMBER"
            - "-x real -y imag -c ANTENNA1"
        # block and triangle plots
        - dir: "blockplots-{msbase}"
          plots:
            - "-x BASELINE_M -y FREQ -c amp"
            - "-x ANTENNA1 -y ANTENNA2 -c SCAN_NUMBER --aaxis phase --ared
↪ std"
            - "-x ANTENNA1 -y ANTENNA2 -c SCAN_NUMBER --aaxis amp --ared
↪ mean"
       # amp/phase versus uv-distance, and uv-coverage coloured by amp/phase
        - dir: "uvdist-{msbase}"
          plots:
            - "-x UV -y amp    -c SCAN_NUMBER"
            - "-x UV -y amp    -c ANTENNA1"
            - "-x UV -y phase  -c ANTENNA1 --corr XX,YY"
            - "-x U  -y V      -c amp"
            - "-x U  -y V      -c phase --cmin -5 --cmax 5"
        # spectral plots
        - dir: "spectra-{msbase}"
          plots:
            - "-x FREQ  -y amp  -c SCAN_NUMBER"
            - "-x FREQ  -y amp  -c ANTENNA1"
            - "-x FREQ  -y real -c CORR --corr IQUV --hline 0:"
    # per-antenna plots
    - iter_ant:
      desc: "plots by antenna"
      cmap: pride
      corr: XX,YY
      plots:
        - '-x FREQ -y amp:I -c SCAN_NUMBER --cnum 100 --cmin 0 --cmax 30
↪ --field {bpcal} --dir bpcal-iamp-byant-{msbase}'
        - '-x FREQ -y SCAN_NUMBER -a amp --ared std --dir
↪ stdamp-byant-{msbase}'
        - '-x FREQ -y SCAN_NUMBER -a phase --ared std --dir
↪ stdphase-byant-{msbase}'
    # per-scan plots
    - iter_scan:
      desc: "plots by scan"
      cmap: pride
      ared: std
```

```
        corr: XX,YY
        plots:
          - '-x ANTENNA1 -y ANTENNA2 -a amp --dir stdamp-byscan-{msbase}'
          - '-x ANTENNA1 -y ANTENNA2 -a phase --dir stdphase-byscan-{msbase}'
          - '-x BASELINE_M -y FREQ -a imag --amin 0 --amax 2 --dir
 ↪  stdimag-byscan-{msbase}'


# split the small MS not derotated
transform__pica:
  enable: true
  field: target
  split_field:
    enable: true
    otfcal:
      enable: true
      derotate_pa: false
      label_cal: '1gc1'
      label_pcal: 'pcal'
  label_out: polcal-full

prep__pica:
  enable: true
  label_in: polcal-full
  field: target
  specweights:
    enable: true
    mode: uniform


flag__pica:
  enable: true
  field: target
  label_in: polcal-full
  summary:
    enable: true
  flag_autocorr:
    enable: true
  flag_spw:
    enable: true
    # the first 3 are the default flagged ones. The last 3 are LExy's personal
 ↪  additions
    chans: '*:856~880MHz , *:1658~1800MHz, *:1419.8~1421.3MHz, *:1200~1230MHz
 ↪  , *:1280~1300MHz, *:1560~1610MHz'
    ensure_valid: false
  flag_mask:
    enable: true
    mask: meerkat.rfimask.npy
    uvrange: '0~1000'
  flag_rfi:
    enable: true
    # maintaining this column because after split, the corrected data from
 ↪  1GC becomes the new data
    # column in the newly created MS.
    col: DATA
    flagger: tricolour
    tricolour:
      backend: 'zarr-disk'
      strategy: gorbachev.yaml
```

```
    mode: manual
  report: true
```

Listing B.1: The CARACal pipeline configuration file used for 1 GC

b.2 SelfCal

The following bash script was used to run selfcal:

b.2.1 *Selfcal Steps*

```
set -e


# mkdir -p changes/{00,01,02,02-b,03} temps

logsave changes/00/log.txt wsclean -name changes/00/image \
    -mem 40 -weight briggs 0.0 -size 4096 4096 -scale 1.0asec -channels-out 4
     ↪  \
    -pol I -join-channels -data-column DATA -fits-mask true_mask.fits -niter
     ↪  200000 \
    -auto-threshold 2 -gain 0.1 -mgain 0.9 -padding 1.5 \
    -log-time -multiscale-scales 0,19,39,78 -multiscale -j 128
     ↪  -nwlayers-factor 3 \
    -no-update-model-required -temp-dir temps pica-poln.ms


logsave changes/00/predict-I-model.txt wsclean -log-time -channels-out 4 \
    -pol I -predict -name changes/00/image pica-poln.ms


gocubical parsets/kunislope.parset --data-ms pica-poln.ms --sol-jones k
 ↪  --k-time-int 1 --k-freq-int 0 \
    --data-freq-chunk 4096 --data-time-chunk 1 --out-mode sc --model-list
     ↪  MODEL_DATA --k-max-prior-error 0.3 \
    --k-max-post-error 0.3 --k-type f-slope --k-update-type unislope
     ↪  --k-ref-ant m005 --k-max-iter 50 \
    --dist-ncpu 13 --dist-min-chunks 13 --out-dir cubic --out-name after-00 \
    --out-column CORRECTED_DATA --model-pa-rotate 1 --model-feed-rotate auto
     ↪  --out-derotate 1 \
    --madmax-enable 0



logsave changes/01/after-kunislope1.txt wsclean -name changes/01/image \
    -mem 40 -weight briggs 0.0 -size 4096 4096 -scale 1.0asec -channels-out 4
     ↪  \
    -pol I -join-channels -data-column CORRECTED_DATA \
    -fits-mask true_mask.fits -niter 200000 \
    -auto-threshold 2 -gain 0.1 -mgain 0.9 -join-channels -padding 1.5 \
    -log-time -multiscale-scales 0,19,39,78 -multiscale -j 128
     ↪  -nwlayers-factor 3 \
    -no-update-model-required -temp-dir temps pica-poln.ms
```

```
logsave changes/01/predict-selfcal-I-model.txt wsclean -log-time
 ↪  -channels-out 4 \
    -pol I -predict -name changes/01/image pica-poln.ms



gocubical parsets/kunislope.parset --data-ms pica-poln.ms --sol-jones k
 ↪  --k-time-int 1 --k-freq-int 0 \
  --data-freq-chunk 4096 --data-time-chunk 1 --out-mode sc --model-list
   ↪  MODEL_DATA --k-max-prior-error 0.3 \
  --k-max-post-error 0.3 --k-type f-slope --k-update-type unislope
   ↪  --k-ref-ant m005 --k-max-iter 50 \
  --dist-ncpu 13 --dist-min-chunks 13 --out-dir cubic --out-name after-01 \
  --out-column CORRECTED_DATA --model-pa-rotate 1 --model-feed-rotate auto
   ↪  --out-derotate 1 \
  --madmax-enable 0



logsave changes/02-b/after-kunislope2.txt wsclean -name changes/02-b/image \
    -mem 50 -weight briggs 0.0 -size 1024 1024 -scale 1.0asec -channels-out
     ↪  80 \
    -pol IQU -join-channels -data-column CORRECTED_DATA \
    -fits-mask true_mask_1k.fits -niter 200000 -join-polarizations \
    -auto-threshold 2 -gain 0.1 -mgain 0.9 -padding 1.5 \
    -log-time -multiscale-scales 0,19,39,78 -multiscale -j 40
     ↪  -nwlayers-factor 3 \
    -no-update-model-required -temp-dir temps pica-poln.ms


logsave changes/02-b/predict-IQU-model.txt wsclean -log-time -channels-out 80
 ↪  -pol IQU -predict \
  -name changes/02-b/image pica-poln.ms



gocubical parsets/kunislope.parset --data-ms pica-poln.ms --sol-jones G \
  --data-freq-chunk 64 --data-time-chunk 8 --out-mode sc --model-list
   ↪  MODEL_DATA \
  --g-type complex-2x2 --g-update-type full \
  --k-ref-ant m005 --k-max-iter 50 --dist-ncpu 16 --dist-max-chunks 16
   ↪  --out-dir cubic \
  --out-name after-02 --out-column CORRECTED_DATA --model-pa-rotate 1
   ↪  --model-feed-rotate auto \
  --out-derotate 1 --madmax-enable 0


logsave changes/03/after-gfull.txt wsclean -name changes/03/image \
    -mem 50 -weight briggs 0.0 -size 1024 1024 -scale 1.0asec -channels-out
     ↪  80 \
    -pol IQU -join-channels -data-column CORRECTED_DATA \
    -fits-mask surround-1k.fits -niter 200000 \
    -auto-threshold 2 -gain 0.1 -mgain 0.9 -padding 1.5 \
    -log-time -multiscale-scales 0,19,39,78 -multiscale -j 40
     ↪  -nwlayers-factor 3 \
```

```
    -join-polarizations \
    -no-update-model-required -temp-dir temps pica-poln.ms
```

Listing B.2: Our specific selfcal steps

b.2.2 *CubiCal config file*

The CubiCal parset file used `kunislope.parset` is shown below

```
[data]
_Help = Visibility data options
ms = msdir/pica-poln.ms
column = DATA
time-chunk = 1
freq-chunk = 4096
rebin-time = 1
rebin-freq = 1
chunk-by = SCAN_NUMBER
chunk-by-jump = 1
single-chunk =
single-tile = -1
normalize = 0
renormalize = 0

[sel]
_Help = Data selection options
field = 0
ddid = None
taql =
chan =
diag = False

[out]
_Help = Options for output products
dir = cubical_out
name = cubical_out.cc-out/00-after-1gc
overwrite = False
backup = 1
mode = sc
apply-solver-flags = True
column = CORRECTED_DATA
derotate = 1
model-column =
weight-column =
reinit-column = False
subtract-model = 0
subtract-dirs = 0:
correct-dir = -1
plots = 1
casa-gaintables = False

[model]
_Help = Calibration model options
list = MODEL_DATA
ddes = auto
beam-pattern = None
```

```
beam-l-axis = None
beam-m-axis = None
feed-rotate = auto
pa-rotate = True
null-v = 0

[montblanc]
_Help = Montblanc simulation options
device-type = CPU
dtype = float
mem-budget = 1024
verbosity = WARNING
threads = 0
pa-rotate = None

[weight]
_Help = Weighting options
column = WEIGHT
fill-offdiag = False
legacy-v1-2 = False

[flags]
_Help = General flagging options
apply = -cubical
auto-init = legacy
save = cubical
save-legacy = auto
reinit-bitflags = False
warn-thr = 0.3
see-no-evil = 0

[degridding]
_Help = Options for the degridder. Only in use when predicting from
 ↪  DicoModels using DDFacet
OverS = 11
Support = 7
Nw = 100
wmax = 0.0
Padding = 1.7
NDegridBand = 16
MaxFacetSize = 0.25
MinNFacetPerAxis = 1
NProcess = 8
BeamModel = None
NBand = 0
FITSFile = beam_$(corr)_$(reim).fits
FITSFeed = None
FITSFeedSwap = False
DtBeamMin = 5.0
FITSParAngleIncDeg = 5.0
FITSLAxis = -X
FITSMAxis = Y
FITSVerbosity = 0
FeedAngle = 0.0
FlipVisibilityHands = 0

[postmortem]
_Help = Options for "postmortem" flagging based on solution statistics
enable = False
```

```
tf-chisq-median = 1.2
tf-np-median = 0.5
time-density = 0.5
chan-density = 0.5
ddid-density = 0.5

[madmax]
_Help = Options for the "Mad Max" flagger
enable = 0
residuals = 1
estimate = corr
diag = True
offdiag = True
threshold = 10
global-threshold = 12
plot = 1
plot-frac-above = 0.01
plot-bl =
flag-ant = 0
flag-ant-thr = 5

[sol]
_Help = Solution options which apply at the solver level
jones = k
precision = 32
delta-g = 1e-06
delta-chi = 1e-06
chi-int = 5
last-rites = True
stall-quorum = 0.99
term-iters = 50
flag-divergence = 0
min-bl = 0.0
max-bl = 0
subset =
$term-iters = [50]

[bbc]
_Help = Options for baseline-based corrections (a.k.a. BBCs, a.k.a.
 ↪  interferometer gains).
load-from =
compute-2x2 = False
apply-2x2 = False
save-to = {out[name]}-BBC-field_{sel[field]}-ddid_{sel[ddid]}.parmdb
per-chan = True
plot = True

[dist]
_Help = Parallelization and distribution options
ncpu = 10
nworker = 0
nthread = 0
max-chunks = 0
min-chunks = 10
pin = 0
pin-io = False
pin-main = io
safe = 1.0
```

```
[log]
_Help = Options related to logging
memory = True
stats = chi2:.3f
stats-warn = chi2:10
boring = False
append = False
verbose = solver=2
file-verbose = None

[debug]
_Help = Debugging options for the discerning masochist
pdb = True
panic-amplitude = 0.0
stop-before-solver = False
escalate-warnings = False

[misc]
_Help = Miscellaneous options
random-seed = None
parset-version = 0.1

[JONES-TEMPLATE]
_Help = Options for {LABEL}-Jones term
_NameTemplate = {LABEL}
_ExpandedFrom = --sol-jones
_OtherTemplates = _Help:label
label = {LABEL}
solvable = 1
type = complex-2x2
delay-estimate-pad-factor = 8
load-from =
xfer-from =
save-to = {out[name]}-{JONES}-field_{sel[field]}-ddid_{sel[ddid]}.parmdb
dd-term = False
fix-dirs =
update-type = full
estimate-pzd = False
time-int = 1
freq-int = 1
max-prior-error = 0.1
max-post-error = 0.1
low-snr-warn = 75
high-gain-var-warn = 30
clip-low = 0.1
clip-high = 10.0
clip-after = 5
max-iter = 20
pin-slope-iters = 0
epsilon = 1e-06
delta-chi = 1e-06
conv-quorum = 0.99
ref-ant = None
prop-flags = default
diag-only = 0
offdiag-only = False
robust-cov = compute
robust-scale = 0
robust-npol = 2
```

```
robust-int = 1
robust-flag-weights = 0
robust-cov-thresh = 1
robust-sigma-thresh = 3
robust-save-weights = 0
estimate-delays = False

[g]
_Templated = True
dd-term = 0
time-int = 1
freq-int = 0
clip-low = 0.1
clip-high = 10
clip-after = 5
conv-quorum = 0.99
ref-ant = m005
_Help = Options for G-Jones term
label = G
solvable = 1
type = f-slope
delay-estimate-pad-factor = 8
load-from =
xfer-from =
save-to = {out[name]}-{JONES}-field_{sel[field]}-ddid_{sel[ddid]}.parmdb
fix-dirs =
update-type = phase-diag
estimate-pzd = False
max-prior-error = 0.3
max-post-error = 0.3
low-snr-warn = 75
high-gain-var-warn = 30
max-iter = 50
pin-slope-iters = 0
epsilon = 1e-06
delta-chi = 1e-06
prop-flags = default
diag-only = 0
offdiag-only = 0
robust-cov = compute
robust-scale = 0
robust-npol = 2
robust-int = 1
robust-flag-weights = 0
robust-cov-thresh = 1
robust-sigma-thresh = 3
robust-save-weights = 0
estimate-delays = False

[de]
_Templated = 1
dd-term = 1
clip-low = 0.0
clip-high = 0
delta-chi = 1e-05
max-prior-error = 0.44
max-post-error = 0.44

[k]
```

```
_Help = Options for k-Jones term
label = k
solvable = 1
type = f-slope
delay-estimate-pad-factor = 8
load-from =
xfer-from =
save-to = {out[name]}-{JONES}-field_{sel[field]}-ddid_{sel[ddid]}.parmdb
dd-term = False
fix-dirs =
update-type = unislope
estimate-pzd = False
time-int = 1
freq-int = 0
max-prior-error = 0.3
max-post-error = 0.3
low-snr-warn = 75
high-gain-var-warn = 30
clip-low = 0.1
clip-high = 10.0
clip-after = 5
max-iter = 50
pin-slope-iters = 0
epsilon = 1e-06
delta-chi = 1e-06
conv-quorum = 0.99
ref-ant = m005
prop-flags = default
diag-only = 0
offdiag-only = False
robust-cov = compute
robust-scale = 0
robust-npol = 2
robust-int = 1
robust-flag-weights = 0
robust-cov-thresh = 1
robust-sigma-thresh = 3
robust-save-weights = 0
estimate-delays = False
_Templated = True
```

Listing B.3: `CubiCal` parset file used for 2GC

b.2.3 *Generating a custom MFS image*

```
from natsort import natsorted
from glob import glob
from astropy.io import fits
import numpy as np

def get_infos(fname, header=False):
    """
    Parameters
    ----------
```

```
    fname: str
        Name of input FITS file
    header: bool
        Whether or not to return the FITS header

    Returns
    -------
    header | weighted data and its respective weight
    """
    print(f"{fname}")
    data = fits.getdata(fname).squeeze()
    hdr = fits.getheader(fname)
    weight = hdr["WSCVWSUM"]
    # WSCIMGWG
    # https://sourceforge.net/p/wsclean/wiki/FitsKeywords/
    # weight = hdr["WSCIMGWG"]

    if header:
        return hdr
    return weight * data, weight

def make_mfs(gstring, fname):
    """
    Parameters
    ----------
    gstring: str
        Pattern of wsclean image names to search for
    fname: str
        Name of output file

    """
    imgs = natsorted(glob(gstring))
    stack = np.zeros((4096, 4096))
    weights = 0
    for i, img in enumerate(imgs):
        data, weight = get_infos(img)
        stack += data
        weights += weight

    stack /= weights

    hdr = get_infos(img, header=True)
    print("Finishing")

    fits.writeto(fname, data=stack, header=hdr, overwrite=True)
```

Listing B.4: A simple script to generate a new MFS image by excluding the problematic ones.

C

SETTING UP POLARVIS ON A WEB SERVER

We practically demonstrate how to set up `PolarVis` using the `Apache` web server and `JS9` over a HTTPS connection. This is done using a docker container.

c.1 Setting up Apache

Websites are made known to `Apache` using configuration text files known as virtual host files, which define the basic information about the website. An example is shown in listing. C.1. This must first be set up before a website is accessible over the web browser. This forms a larger part of the setup, described fully in the `Dockerfile` shown in Sec. C.2.

```
<VirtualHost *:80>
    # Handle traffic to in HTTP

    ServerName example.com

    DocumentRoot /var/www/example.com

    ErrorLog ${APACHE_LOG_DIR}/error.log
    CustomLog ${APACHE_LOG_DIR}/access.log combined

    # ADD THE LINE BELOW
    # Redirect permanent "/" "https://example.com/"
</VirtualHost>


<VirtualHost *:443>
    #setting up secure HTTP

    ServerName example.com

    DocumentRoot /var/www/example.com

    ErrorLog ${APACHE_LOG_DIR}/error.log
    CustomLog ${APACHE_LOG_DIR}/access.log combined

    SSLEngine                on
    #note lexy line below added
    SSLProxyEngine on
    SSLProxyVerify none
    SSLProxyCheckPeerCN off
    SSLProxyCheckPeerName off
    SSLProxyCheckPeerExpire off


    #set up proxy for js9helper
    RewriteEngine       On
```

```
    # new style:
    # https://socket.io/docs/v4/reverse-proxy/
    RewriteCond    %{HTTP:Upgrade} websocket [NC]
    RewriteCond  %{HTTP:Connection} upgrade [NC]
    #RewriteRule      ^/?(.*)            ws://localhost:2718/$1    [P]
    RewriteRule ^/?(.*) "wss://localhost:2718/$1" [P,L]

    ProxyPass      /socket.io    https://localhost:2718/socket.io
    ProxyPassReverse      /socket.io https://localhost:2718/socket.io

    # required to handle js9msg requests to the helper's httpd support:
    RewriteCond      %{REQUEST_URI}             ^/msg [NC]
    RewriteRule        ^/?(.*)         http://localhost:2718/$1 [P]


    # <Directory /var/www/example.com>
        # Options Indexes FollowSymLinks
        # AllowOverride All
        # Require all granted
    # </Directory>

    SSLCertificateFile /etc/ssl/example.com-certs/certificate.crt
    SSLCertificateKeyFile /etc/ssl/example.com-certs/private.key
</VirtualHost>
```

Listing C.1: Virtual host file to setup an example website for `PolarVis`.

c.2 Website Setup

Most of the content in this section is extracted from the `JS9` help manual at `https://js9.si.edu/js9/help/helper.html`. The following listing contains a `Dockerfile` highlighting and performing all the steps required to bring up `PolarVis`.

```
FROM ubuntu:22.04
SHELL ["/bin/bash", "-c"]
RUN apt-get update && apt-get upgrade -y

# Install apache2
RUN apt-get install -y apache2 \
    curl \
    wget \
    git \
    openssl

# Install dependencies of cfitsio
RUN apt-get install -y build-essential \
    gfortran \
    libbz2-dev \
    zlib1g-dev \
    libcfitsio-dev \
    libcurl3-dev

RUN apt-get clean; apt-get autoclean
```

```
# Install nodejs 16
RUN curl -fsSL https://deb.nodesource.com/setup_16.x | bash -
RUN apt-get install -y nodejs

RUN mkdir -p downloads
WORKDIR /downloads

# Download and build cfitsio from source
RUN wget
 ↪  http://heasarc.gsfc.nasa.gov/FTP/software/fitsio/c/cfitsio_latest.tar.gz
RUN tar -zxvf cfitsio_latest.tar.gz
RUN mv cfitsio*/ cfitsio
WORKDIR /downloads/cfitsio

# Run executables otherwise you will get an error
RUN ./configure --prefix=/usr/local --enable-sse2 --enable-reentrant
RUN make
RUN make utils
RUN make testprog
RUN make install


# Testing weather this install is ok the output of this should be nothing
RUN testprog > testprog.lis
RUN diff testprog.lis testprog.out
RUN cmp testprog.fit testprog.std
RUN rm cookbook fitscopy imcopy smem speed testprog


# Download and build funtools from source
WORKDIR /downloads
RUN git clone https://github.com/ericmandel/funtools.git funtools
WORKDIR /downloads/funtools
RUN ./mkconfigure
RUN ./configure --prefix=/usr/local
RUN make
RUN make install
RUN make clean

# Download and build regions from source
WORKDIR /downloads
RUN git clone https://github.com/ericmandel/regions.git regions
WORKDIR /downloads/regions
RUN ./configure --prefix=/usr/local --with-cfitsio=/downloads/cfitsio
RUN make
RUN make install

# Download and unzip JS9
WORKDIR /downloads
RUN wget https://js9.si.edu/downloads/js9-3.6.1.tgz
RUN tar -zxvf js9-3.6.1.tgz
RUN mv js9*/ js9

RUN rm -r /var/www/html

# create a directory that will host the website's files
RUN mkdir -p /var/www/example.com
```

```
#make a link to it for easy access from home
RUN ln -s /var/www/example.com /home/example.com

# copy polarvis my host machine into this dictionary in the container
COPY to-be-copied/polarvis /home/example.com/polarvis

# make a js9 isntallation directory
RUN mkdir -p /home/example.com/polarvis/js9install

WORKDIR /downloads/js9
# install JS9 into polarvis
RUN ./configure --with-webdir=/home/example.com/polarvis/js9install \
    --with-helper=nodejs \
    --with-cfitsio=/downloads/cfitsio \
    # --prefix=/home/example.com
    --prefix=/usr/local

RUN make
RUN make install

# copy the pref files into the js9install directory
WORKDIR /home/example.com/polarvis
RUN mv js9/js9Prefs.json js9install/
RUN mv js9/js9prefs.js js9install/

# Create a dictionary where to store logs from js9, incase of debugging stuff
RUN mkdir -p /home/logs
RUN echo "echo"
# copy virtual host files to /etc/apache2/sites-available
COPY to-be-copied/vhost-file /etc/apache2/sites-available/example.com.conf

RUN mkdir -p /home/daemons
COPY to-be-copied/start_js9.sh /home/daemons/
# make it executable
RUN chmod +x /home/daemons/start_js9.sh

# copy the daemon service
COPY to-be-copied/daemon.service /etc/systemd/system/startjs9.service

# copy the ssl certs
COPY to-be-copied/example.com-certs /etc/ssl/example.com-certs

WORKDIR /home


# start proxy tunnel modules for apache
RUN a2enmod proxy proxy_http proxy_wstunnel

# enabling https
RUN a2enmod ssl
RUN a2enmod rewrite

# enabling the website
COPY to-be-copied/vhost-file /etc/apache2/sites-available/example.com.conf

RUN a2dissite example.com.conf
RUN a2ensite example.com.conf

RUN apt install -y w3m
```

```
RUN apt clean

# # Start apache
# RUN service apache2 start

# In the actual server, run js9helper as a service. This will not work
# in a docker container
# RUN sysctl start startjs9.service


# start the js9 helper as a bg
RUN a2dissite 000-default.conf

# Expose ports for HTTP (80) and HTTPS (443)
EXPOSE 80
EXPOSE 443

CMD ["/bin/bash", "-c", "/home/daemons/start_js9.sh && apache2ctl -D
 ↪  FOREGROUND"]
```

Listing C.2: Dockerfile to build container with `PolarVis`.

A docker image must first be built to activate it. This is done by running the following in the directory containing the dockerfile:

```
docker -t build polarvis .
```

For an image to become useful, it must first be activated into a *container*, which provides an isolated environment containing all the resources and dependencies required for a specific task. This is started in the terminal using `docker` as:

```
# Run it in detached mode as
# -p host-port:container-port
docker run -d -p 8080:80 -p 80801:443 --add-host www.example.com:127.0.0.1
 ↪  polarvis:latest

# For simplicity, switch off the SSL

# to stop the container
# docker stop polarvis:latest
```

Listing C.3: Running a Docker container for `PolarVis`

Now, the container should be active and running in the background. To view the web page, navigate to the browser at the address: `127.0.0.1:80/polarvis`. Commands similar to those in this `Dockerfile` could be used in a typical Ubuntu Linux environment.

D

CALIBRATION AND IMAGING GOTCHAS/TIPS/TRICKS

d.1 In General

During the reduction process of this data, various issues came up while calibrating and imaging which became frustrating but offered invaluable insights on the importance of specificity.

- General rule of thumb in data reduction: Try it on a smaller MS, if it works, repeat for the larger MS.
- While using `CARACal`, ensure that `label-in` under the polcal section is set. Without this setting, polcal solutions will not be applied hence no polarisation calibration
- Pay attention to your diagnostic plots! If the data point is straying away from the mob, it's probably flawed.
- The first self-calibration (selfcal) rounds assist improving Stokes I models. **Do not** image or predict Stokes Q, U, V at this point, these will only be required when preforming the complex gain calibration which updates all the 4x4 matrices, XX, XY, YX, YY. Premature polarisation models created strange problems with the derived fractional polarization, among other unpleasant things.
- Phase calibration always comes before amplitude calibration! Signals out of phase will decorrelate. Therefore, it is important to maximise for the constructive interference of signals in each baseline, otherwise, the cause is lost.
- Keep `WSClean` logs!! Don't delete them. Since there's no option in `WSClean` directly to save them, use the `logsave` or `tee` CLI tools. A quick search should get you acquainted with this.
- Ensure that the timestamps are enabled with `-log-time` option in `WSClean`. This will be important for when the imaging hangs (which happens sometimes to even the most experienced ancestors).
- The imaging process sometimes goes wrong in this event, a `WSClean` log file becomes of utmost importance and must be maintained so that issues that crop up are easily traced. There are certain things to look out for while imaging which can visually inform whether the imaging was successful.
    1. Check the residual image: did deconvolution happen to noise level? e.g. if CLEAN-ing with a mask, does the region being CLEAN-ed resemble the surrounding noise like region without sources? If not CLEAN deeper
    2. Does the resulting deconvolved image resemble the residual? Something is very wrong and needs to be investigated. As a first step, check the log file and identify while CLEAN stopped/finished. Was it because the maximum threshold / number of iterations was reached? If yes, check the model image, does it contain anything? if not the CLEAN did not happen. Unless a custom threshold was set, check and ensure that the threshold automatically set by `WSClean` was not 0 Jy.
- "Reverse halos" (shadows surrounding your sources) are unholy. They are caused by missing short spacings. Rinse and repeat.

d.2 Some CubiCal

Cubical has two solver parameters:

- sol-type: This is the solver type,
- sol-update-type: How to update the gains.

In order to do chained solutions, all the solver types **Must be complex 2x2**.

Solver-types: We have tslope and fslope, which fit slopes (straight lines) across time and frequency, respectively. There can also be:

- amplitude only: solve only amplitudes and fix phases,
- phase only: solve phases only and fix amplitude (set to 1),
- phase-diags: solve diagonal phases only,
- amplitude-diag: solve diagonal amplitudes only fix the rest and phase to 0.

Solver update types: When we say update:

- full: it means to update the full gains,
- diag: the diagonals,
- off-diag: off diagonals.

Usually, if the model has no polarisation information, then it is pointless to do a full update or off-diag update. Usually, these are needed for leakages etc.

d.3 Image Presentation

The images presented in this thesis have made with the help of some combination of the following `Python` packages and free software:

1. Matplotlib (Hunter, 2007) `https://matplotlib.org`
2. APLpy (Robitaille, 2019) `https://aplpy.readthedocs.io`
3. Astropy (Astropy Collaboration et al., 2022) `https://www.astropy.org`
4. cmasher (Velden, 2020) `https://cmasher.readthedocs.io`
5. InkScape
6. GNU Image Manipulation Program (GIMP)

BIBLIOGRAPHY

Alfvén, Hannes and Nicolai Herlofson (1950). '115. Cosmic Radiation and Radio Stars'. In: *115. Cosmic Radiation and Radio Stars*. Harvard University Press, pp. 779–781. isbn: 978-0-674-36668-8. doi: 10.4159/harvard.9780674366688.c123.

Andati, L. A. L., O. M. Smirnov and S. Makhathini (July 2022). 'RAGaVI: A Radio Astronomy Gains and Visibilities Inspector'. In: *Astronomical Data Analysis Software and Systems XXX*. Vol. 532, p. 529.

Andati, L. A. L. et al. (Dec. 2023a). *PolarVis: Towards Web-based Polarimetric Analysis*. doi: 10.48550/arXiv.2312.07645. arXiv: 2312.07645 [astro-ph]. url: https://github.com/Mulan-94/polarvis.

Andati, Lexy A. L., Oleg M. Smirnov and Landman H. Bester (Dec. 2023b). *Smops: A Sub-Band Model FITS Image Interpolator*. url: https://github.com/mulan-94/smops.

Andati, Lexy A L et al. (Feb. 2024). 'A Spectropolarimetric Study of Pictor A Radio Galaxy with MeerKAT'. In: *Monthly Notices of the Royal Astronomical Society*, pp. 1626–1641. issn: 0035-8711. doi: 10.1093/mnras/stae598.

Anderson, C. S. et al. (Mar. 2018). 'Broadband Radio Polarimetry of Fornax A. I. Depolarized Patches Generated by Advected Thermal Material from NGC 1316'. In: *Astrophysical Journal* 855.1, p. 41. issn: 15384357. doi: 10.3847/1538-4357/aaaec0. arXiv: 1802.04812.

Astropy Collaboration et al. (Aug. 2022). 'The Astropy Project: Sustaining and Growing a Community-oriented Open-source Project and the Latest Major Release (v5.0) of the Core Package'. In: *The Astrophysical Journal* 935, p. 167. issn: 0004-637X. doi: 10.3847/1538-4357/ac7c74.

Baidoo, Lerato et al. (Sept. 2023). 'A Wideband Polarization Observation of Hydra A with the Jansky Very Large Array'. In: *The Astrophysical Journal* 955.1, p. 16. issn: 0004-637X. doi: 10.3847/1538-4357/acebc5.

Barth, Aaron J., Luis C. Ho and Wallace L. W. Sargent (Jan. 2003). 'The Black Hole Masses and Host Galaxies of BL Lacertae Objects'. In: *The Astrophysical Journal* 583.1, p. 134. issn: 0004-637X. doi: 10.1086/345083.

Beck, Rainer (Dec. 2015). 'Magnetic Fields in Spiral Galaxies'. In: *Astronomy and Astrophysics Review* 24.1, p. 4. issn: 1432-0754. doi: 10.1007/s00159-015-0084-4.

Beckmann, Volker and Chris R. Shrader (Feb. 2013). *The AGN Phenomenon: Open Issues*. doi: 10.48550/arXiv.1302.1397. arXiv: 1302.1397 [astro-ph].

Begelman, Mitchell C., Roger D. Blandford and Martin J. Rees (Apr. 1984). 'Theory of Extragalactic Radio Sources'. In: *Reviews of Modern Physics* 56.2, p. 255. issn: 00346861. doi: 10.1103/RevModPhys.56.255.

Begelman, Mitchell C. and Denis F. Cioffi (Oct. 1989). 'Overpressured Cocoons in Extragalactic Radio Sources'. In: *Astrophysical Journal* 345, p. L21. issn: 0004-637X. doi: 10.1086/185542.

Bell, A. R. (Feb. 1978). 'The Acceleration of Cosmic Rays in Shock Fronts – I'. In: *Monthly Notices of the Royal Astronomical Society* 182.2, pp. 147–156. issn: 0035-8711. doi: 10.1093/mnras/182.2.147.

Bennett, A. S. and F. G. Smith (July 1962). 'The Preparation of the Revised 3C Catalogue of Radio Sources'. In: *Monthly Notices of the Royal Astronomical Society* 125.1, pp. 75–86. issn: 0035-8711. doi: 10.1093/mnras/125.1.75.

Blandford, R. D. and J. P. Ostriker (Apr. 1978). 'Particle Acceleration by Astrophysical Shocks.' In: *The Astrophysical Journal* 221, pp. L29–L32. issn: 0004-637X. doi: 10.1086/182658.

Blandford, R. D. and M. J. Rees (Dec. 1974). 'A 'Twin-Exhaust' Model for Double Radio Sources'. In: *Monthly Notices of the Royal Astronomical Society* 169.3, pp. 395–415. issn: 0035-8711. doi: 10.1093/mnras/169.3.395.

Bolton, J. G. (July 1948). 'Discrete Sources of Galactic Radio Frequency Noise'. In: *Nature* 162.4108, pp. 141–142. issn: 1476-4687. doi: 10.1038/162141a0.

Bolton, J. G. and G. J. Stanley (Feb. 1948). 'Variable Source of Radio Frequency Radiation in the Constellation of Cygnus'. In: *Nature* 161.4087, pp. 312–313. issn: 1476-4687. doi: 10.1038/161312b0.

Booth, R. S. and J. L. Jonas (Mar. 2012). 'An Overview of the MeerKAT Project'. In: *African Skies* 16, p. 101.

Brentjens, M. A. and A. G. de Bruyn (Oct. 2005). 'Faraday Rotation Measure Synthesis'. In: *Astronomy and Astrophysics* 441.3, pp. 1217–1228. issn: 0004-6361. doi: 10.1051/0004-6361:20052990.

Bridle, Alan H. and Richard A. Perley (Jan. 1984). 'Extragalactic Radio Jets'. In: *Annual Review of Astronomy and Astrophysics* 22, pp. 319–358. issn: 0066-4146. doi: 10.1146/annurev.aa.22.090184.001535.

Bridle, Alan H. et al. (Sept. 1994). 'Deep VLA Imaging of Twelve Extended 3CR Quasars'. In: *The Astronomical Journal* 108, p. 766. issn: 0004-6256. doi: 10.1086/117112.

Brown, Anthony M. and Jenni Adams (Apr. 2012). 'Discovery of γ-Ray Emission from the Broad-Line Radio Galaxy Pictor A'. In: *Monthly Notices of The Royal Astronomical Society* 421, pp. 2303–2309. issn: 0035-8711. doi: 10.1111/j.1365-2966.2012.20451.x.

Buchner, J. et al. (Apr. 2014). 'X-Ray Spectral Modelling of the AGN Obscuring Region in the CDFS: Bayesian Model Selection and Catalogue'. In: *Astronomy & Astrophysics* 564, A125. issn: 0004-6361, 1432-0746. doi: 10.1051/0004-6361/201322971.

Burn, B. J. (July 1966). 'On the Depolarization of Discrete Radio Sources by Faraday Dispersion'. In: *Monthly Notices of The Royal Astronomical Society* 133.1, pp. 67–83. issn: 0035-8711. doi: 10.1093/mnras/133.1.67.

Campbell, Donald B. (Dec. 2002). 'Measurement in Radio Astronomy'. In: *Single-Dish Radio Astronomy: Techniques and Applications*. Vol. 278, pp. 81–90.

Carilli, C. L. and P. D. Barthel (1996). 'Cygnus A'. In: *Astronomy and Astrophysics Review* 7.1, pp. 1–54. issn: 09354956. doi: 10.1007/s001590050001.

Carretti, E et al. (Oct. 2019). 'S-Band Polarization All-Sky Survey (S-PASS): Survey Description and Maps'. In: *Monthly Notices of the Royal Astronomical Society* 489.2, pp. 2330–2354. issn: 0035-8711. doi: 10.1093/mnras/stz806.

Chen, Kaiyou and Jules P. Halpern (Sept. 1989). 'Structure of Line-emitting Accretion Disks in Active Galactic Nuclei: ARP 102B'. In: *The Astrophysical Journal* 344, p. 115. issn: 0004-637X. doi: 10.1086/167782.

Chen, Kaiyou, Jules P. Halpern and Alexei V. Filippenko (Apr. 1989). 'Kinematic Evidence for a Relativistic Keplerian Disk: ARP 102B'. In: *The Astrophysical Journal* 339, p. 742. issn: 0004-637X. doi: 10.1086/167332.

Christiansen, W. N. et al. (Nov. 1977). 'Observations of 15 Southern Extragalactic Sources with the Fleurs Synthesis Telescope'. In: *Monthly Notices of the Royal Astronomical Society* 181.2, pp. 183–202. issn: 0035-8711. doi: 10.1093/mnras/181.2.183.

Clark, B. G. (Sept. 1980). 'An Efficient Implementation of the Algorithm 'CLEAN''. In: *Astronomy and Astrophysics* 89, p. 377. issn: 0004-6361.

– (Jan. 1999). 'Coherence in Radio Astronomy'. In: *Synthesis Imaging in Radio Astronomy II*. Vol. 180, p. 1.

Clarke, David A (1996). 'The Standard Model Revisited: Propagation of a 3D Jet'. In: *Energy Transp. Radio Galaxies Quasars*. Vol. 100, p. 311.

Comrie, A. et al. (July 2020). 'Development and Application of an HDF5 Schema for SKA-scale Image Cube Visualization'. In: *Astronomy and Computing* 32, p. 100389. issn: 2213-1337. doi: 10.1016/j.ascom.2020.100389.

Comrie, Angus et al. (2021). 'CARTA: The Cube Analysis and Rendering Tool for Astronomy'. In: *zndo*. doi: 10.5281/ZENODO.3377984.

Condon, J. J. et al. (May 1998). 'The NRAO VLA Sky Survey'. In: *The Astronomical Journal* 115.5, p. 1693. issn: 1538-3881. doi: 10.1086/300337.

Condon, James J and Scott M Ransom (2016). *Essential Radio Astronomy*. Vol. 2. Princeton University Press.

Cooper, B. F. C., R. M. Price and D. J. Cole (Dec. 1965). 'A Study of the Decimetric Emission and Polarization of Centaurus A'. In: *Australian Journal of Physics* 18, p. 589. issn: 0004-9506. doi: 10.1071/PH650589.

Cornwell, T. J. and P. N. Wilkinson (Oct. 1981). 'A New Method for Making Maps with Unstable Radio Interferometers'. In: *Monthly Notices of the Royal Astronomical Society* 196.4, pp. 1067–1086. issn: 0035-8711. doi: 10.1093/mnras/196.4.1067.

Cornwell, Tim J. (Oct. 2008). 'Multiscale CLEAN Deconvolution of Radio Synthesis Images'. In: *IEEE Journal of Selected Topics in Signal Processing* 2.5, pp. 793–801. issn: 1941-0484. doi: 10.1109/JSTSP.2008.2006388.

Cornwell, Tim and Robert Braun (Jan. 1989). 'Deconvolution'. In: 6, p. 167.

Cornwell, Tim and Ed B. Fomalont (Jan. 1999). 'Self-Calibration'. In: *Synthesis Imaging in Radio Astronomy II*. Vol. 180, p. 187.

Croston, J. H. et al. (June 2005). 'An X-Ray Study of Magnetic Field Strengths and Particle Content in the Lobes of FR II Radio Sources'. In: *Astrophysical Journal* 626.2, pp. 733–747. issn: 0004-637X. doi: 10.1086/430170.

Crutcher, Richard M. and Athol J. Kemball (Oct. 2019). 'Review of Zeeman Effect Observations of Regions of Star Formation'. In: *Frontiers in Astronomy and Space Sciences* 6. issn: 2296-987X. doi: 10.3389/fspas.2019.00066.

Danziger, I. J., R. A. E. Fosbury and M. V. Penston (May 1977). 'Optical Observations of Pictor A'. In: *Monthly Notices of the Royal Astronomical Society* 179.1, 41P–45P. issn: 0035-8711. doi: 10.1093/mnras/179.1.41P.

De Gouveia Dal Pino, Elisabete (2012). '3D MHD Simulations of the Central Region of the Perseus Galaxy Cluster: The Role of Starburst and AGN Activity and Particle Acceleration by Magnetic Reconnection'. In: *Proceedings of AGN Physics in the CTA Era — PoS(AGN 2011)*. Vol. 141, p. 031. doi: 10.22323/1.141.0031.

Dewdney, Peter E. et al. (Aug. 2009). 'The Square Kilometre Array'. In: *Proceedings of the IEEE* 97.8, pp. 1482–1496. issn: 1558-2256. doi: 10.1109/JPROC.2009.2021005.

Dolag, K., C. Vogt and T. A. Enßlin (Apr. 2005). 'Pacerman — I. A New Algorithm to Calculate Faraday Rotation Maps'. In: *Monthly Notices of the Royal Astronomical Society* 358.3, pp. 726–731. issn: 0035-8711. doi: 10.1111/j.1365-2966.2005.08851.x.

Donnert, J. et al. (Nov. 2018). 'Magnetic Field Amplification in Galaxy Clusters and Its Simulation'. In: *Space science reviews* 214.8, p. 122. issn: 1572-9672. doi: 10.1007/s11214-018-0556-8.

Edge, D. O. et al. (Jan. 1959). 'A Survey of Radio Sources at a Frequency of 159 Mc/s.' In: *Memoirs of the Royal Astronomical Society* 68, pp. 37–60.

Eilek, Jean A. and Frazer N. Owen (Mar. 2002). 'Magnetic Fields in Cluster Cores: Faraday Rotation in A400 and A2634'. In: *Astrophysical Journal* 567.1, pp. 202–220. issn: 0004-637X. doi: 10.1086/338376.

Ekers, R. D. (Jan. 1969). 'Interferometric Observations of the Brightness Distribution of Southern Radio Sources'. In: *Australian Journal of Physics, Astrophysical Supplement* 6, p. 3.

Eracleous, Michael and Jules P. Halpern (Dec. 2003). 'Completion of a Survey and Detailed Study of Double-peaked Emission Lines in Radio-loud Active Galactic Nuclei'. In: *The Astrophysical Journal* 599.2, p. 886. issn: 0004-637X. doi: 10.1086/379540.

Fan, J. H., G. Z. Xie and R. Bacon (Apr. 1999). 'The Central Black Hole Masses and Doppler Factors of the γ-Ray Loud Blazars'. In: *Astronomy and Astrophysics Supplement Series* 136.1, pp. 13–18. issn: 0365-0138, 1286-4846. doi: 10.1051/aas:1999194.

Fan, Zhong-Hui et al. (Jan. 2008). 'Stochastic Acceleration in the Western Hot Spot of Pictor A'. In: *The Astrophysical Journal Letters* 673.2, p. L139. issn: 0004-637X. doi: 10.1086/528372.

Fanaroff, B. L. and J. M. Riley (Apr. 1974). 'The Morphology of Extragalactic Radio Sources of High and Low Luminosity'. In: *Monthly Notices of The Royal Astronomical Society* 167.1, 31P–36P. issn: 0035-8711. doi: 10.1093/mnras/167.1.31p.

Farnsworth, Damon, Lawrence Rudnick and Shea Brown (May 2011). 'Integrated Polarization of Sources at $\sim$ 1 m And New Rotation Measure Ambiguities'. In: *Astronomy Journal* 141.6, p. 191. issn: 1538-3881. doi: 10.1088/0004-6256/141/6/191.

Feain, Ilana et al. (Oct. 2009). 'Faraday Rotation Structure on Kiloparsec Scales in the Giant Radio Lobes of Centaurus A'. In: *The Astrophysical Journal Letters* 707.1, pp. 114–125. doi: 10.1088/0004-637X/707/1/114.

Feroz, F. and M. P. Hobson (Feb. 2008). 'Multimodal Nested Sampling: An Efficient and Robust Alternative to Markov Chain Monte Carlo Methods for Astronomical Data Analyses'. In: *Monthly Notices of the Royal Astronomical Society* 384.2, pp. 449–463. issn: 0035-8711. doi: 10.1111/j.1365-2966.2007.12353.x.

Feroz, F., M. P. Hobson and M. Bridges (Oct. 2009). 'MultiNest: An Efficient and Robust Bayesian Inference Tool for Cosmology and Particle Physics'. In: *Monthly Notices of the Royal Astronomical Society* 398.4, pp. 1601–1614. issn: 0035-8711. doi: 10.1111/j.1365-2966.2009.14548.x.

Ferrière, K, J L West and T R Jaffe (Sept. 2021). 'The Correct Sense of Faraday Rotation'. In: *Monthly Notices of The Royal Astronomical Society* 507.4, pp. 4968–4982. issn: 0035-8711. doi: 10.1093/mnras/stab1641.

Fine, Maxwell A, Cameron L Van Eck and Luke Pratley (Apr. 2023). 'Correcting Bandwidth Depolarization by Extreme Faraday Rotation'. In: *Monthly Notices of the Royal Astronomical Society* 520.4, pp. 4822–4835. issn: 0035-8711. doi: 10.1093/mnras/stad423.

Fomalont, Ed B. and Richard A. Perley (Jan. 1999). 'Calibration and Editing'. In: *Synthesis Imaging in Radio Astronomy II*. Vol. 180, p. 79.

Fomalont, Edward B. et al. (Nov. 1989). 'Depolarization Silhouettes and the Filamentary Structure in the Radio Source Fornax A'. In: *Astrophysical Journal* 346, p. L17. doi: 10.1086/185568.

Forsyth, David (2018). 'Inferring Probability Models from Data'. In: *Probability and Statistics for Computer Science*. Ed. by David Forsyth. Cham: Springer International Publishing, pp. 197–222. isbn: 978-3-319-64410-3. doi: 10.1007/978-3-319-64410-3_9.

Frick, P. et al. (Jan. 2010). 'Wavelet-Based Faraday Rotation Measure Synthesis'. In: *Monthly Notices of the Royal Astronomical Society: Letters* 401.1, pp. L24–L28. issn: 1745-3925. doi: 10.1111/j.1745-3933.2009.00778.x.

Gardner, F. F. and R. D. Davies (1966). 'THE POLARIZATION OF RADIO SOURCES I. Observations Of Small Diameter Sources'. In: *Australian Journal of Physics* 19.3, pp. 441–460. issn: 1446-5582. doi: 10.1071/ph660441.

Gardner, F. F., D. Morris and J. B. Whiteoak (Jan. 1969). 'The Linear Polarization of Radio Sources between 11 and 20 Cm Wavelength. I. Observations.' In: *Australian Journal of Physics* 22, pp. 79–106. issn: 0004-9506. doi: 10.1071/PH690079.

Gardner, F. F. and J. B. Whiteoak (Sept. 1966a). 'The Polarization of Cosmic Radio Waves'. In: *Annual Review of Astronomy and Astrophysics* 4.Volume 4, 1966, pp. 245–292. issn: 0066-4146, 1545-4282. doi: 10.1146/annurev.aa.04.090166.001333.

– (1966b). 'The Polarization of Cosmic Radio Waves'. In: *Annual Review of Astronomy and Astrophysics* 4.1, pp. 245–292. doi: 10.1146/annurev.aa.04.090166.001333.

– (Jan. 1971). 'The Polarization of Extended Radio Sources at 6 Cm Wavelength. I. Extragalactic Sources.' In: *Australian Journal of Physics* 24, pp. 899–911. issn: 0004-9506. doi: 10.1071/PH710899.

Gardner, F. F., J. B. Whiteoak and D. Morris (Jan. 1975). 'The Linear Polarization of Radio Sources I: Observations at Wavelengths of 6, 11, 18 and 21 Cm'. In: 35, p. 1.

Garrington, S. T. et al. (Jan. 1988). 'A Systematic Asymmetry in the Polarization Properties of Double Radio Sources with One Jet'. In: *Nature* 331.6152, pp. 147–149. issn: 00280836. doi: 10.1038/331147a0.

Gaskell, C. M. (June 1983). 'Quasars as Supermassive Binaries'. In: 24, pp. 473–477.

Gentry, Eric S. et al. (July 2015). 'Optical Detection Of The Pictor A Jet and Tidal Tail: Evidence Against an IC/CMB Jet'. In: *Astrophysical Journal* 808.1, p. 92. issn: 0004-637X. doi: 10.1088/0004-637X/808/1/92.

Gooch, Richard (Jan. 1996). 'Karma: A Visualization Test-Bed'. In: *Astronomical Data Analysis Software and Systems V*. Vol. 101, p. 80.

Goodlet, J. A. et al. (Jan. 2004). 'The Depolarization Properties of Powerful Radio Sources: Breaking the Radio Power versus Redshift Degeneracy'. In: *Monthly Notices of the Royal Astronomical Society* 347.2, pp. 508–540. issn: 0035-8711. doi: 10.1111/j.1365-2966.2004.07225.x.

Goss, W. M., Claire Hooker and Ronald D. Ekers (2023). *Joe Pawsey and the Founding of Australian Radio Astronomy: Early Discoveries, from the Sun to the Cosmos*. Springer Nature. isbn: 978-3-031-07916-0. doi: 10.1007/978-3-031-07916-0.

Govoni, F. and L. Feretti (2004). *Magnetic Fields In Clusters of Galaxies*.

Grandi, Paola et al. (Mar. 2003). 'Detection of X-Ray Emission from the Eastern Radio Lobe of Pictor A'. In: *The Astrophysical Journal Letters* 586.1, p. 123. issn: 0004-637X. doi: 10.1086/367604.

Halpern, Jules P. and Michael Eracleous (Sept. 1994). 'Emergence of Double-Peaked Emission Lines in the Broad-Line Radio Galaxy Pictor A'. In: *Astrophysical Journal* 433, p. L17. doi: 10.1086/187537.

Hamaker, J. P. (May 2000). 'Understanding Radio Polarimetry - IV. The Full-Coherency Analogue of Scalar Self-Calibration: Self-alignment, Dynamic Range and Polarimetric Fidelity'. In: 143.3, pp. 515–534. issn: 0365-0138, 1286-4846. doi: 10.1051/aas:2000337.

Hamaker, J. P., J. D. Bregman and R. J. Sault (May 1996). 'Understanding Radio Polarimetry. I. Mathematical Foundations'. In: 117.1, pp. 137–147. issn: 0365-0138, 1286-4846. doi: 10.1051/aas:1996146.

Handley, W. (Sept. 2023). *REACH: Nested Sampling Tools*.

Hardcastle, M. J. and J. H. Croston (Oct. 2005). 'The Chandra View of Extended X-ray Emission from Pictor A'. In: *Monthly Notices of the Royal Astronomical Society* 363.2, pp. 649–660. issn: 0035-8711. doi: 10.1111/j.1365-2966.2005.09469.x.

– (June 2020). 'Radio Galaxies and Feedback from AGN Jets'. In: *New Astronomy Reviews* 88, p. 101539. issn: 1387-6473. doi: 10.1016/j.newar.2020.101539.

Hardcastle, M. J. et al. (Feb. 2016). 'Deep Chandra Observations of Pictor A'. In: *Monthly Notices of The Royal Astronomical Society* 455.4, pp. 3526–3545. issn: 0035-8711. doi: 10.1093/mnras/stv2553.

Hargrave, P. J. and M. Ryle (Feb. 1974). 'Observations of Cygnus a with the 5-Km Radio Telescope'. In: *Monthly Notices of The Royal Astronomical Society* 166.2, pp. 305–327. issn: 0035-8711. doi: 10.1093/MNRAS/166.2.305.

Harris, D. E. and J. E. Grindlay (Sept. 1979). 'The Prospects for X-ray Detection of Inverse-Compton Emission from Radio Source Electrons and Photons of the Microwave Background'. In: *Monthly Notices of the Royal Astronomical Society* 188.1, pp. 25–37. issn: 0035-8711. doi: 10.1093/mnras/188.1.25.

Harwood, Jeremy J. et al. (Nov. 2013). 'Spectral Ageing in the Lobes of FR-II Radio Galaxies: New Methods of Analysis for Broad-Band Radio Data'. In: *Monthly Notices of the Royal Astronomical Society* 435.4, pp. 3353–3375. issn: 0035-8711. doi: 10.1093/mnras/stt1526.

Haslam, C. G. T. et al. (Jan. 1982). 'A 408-MHZ All-Sky Continuum Survey. II. The Atlas of Contour Maps'. In: *Astronomy and Astrophysics Supplement Series* 47, p. 1. issn: 0365-01380004-6361.

Haverkorn, Marijke (2015). 'Magnetic Fields in the Milky Way'. In: *Magnetic Fields in Diffuse Media*. Ed. by Alexander Lazarian, Elisabete M. de Gouveia Dal Pino and Claudio Melioli. Berlin, Heidelberg: Springer Berlin Heidelberg, pp. 483–506. isbn: 978-3-662-44625-6. doi: 10.1007/978-3-662-44625-6_17.

Haves, P. (Dec. 1975). 'Polarization Parameters of 183 Extragalactic Radio Sources.' In: *Monthly Notices of The Royal Astronomical Society* 173, pp. 553–568. issn: 0035-8711. doi: 10.1093/mnras/173.3.553.

Heald, G., R. Braun and R. Edmonds (Aug. 2009). 'The Westerbork SINGS Survey: II Polarization, Faraday Rotation, and Magnetic Fields'. In: *Astronomy and Astrophysics* 503.2, pp. 409–435. issn: 00046361. doi: 10.1051/0004-6361/200912240.

Heald, George (Apr. 2009). 'The Faraday Rotation Measure Synthesis Technique'. In: 259, pp. 591–602. doi: 10.1017/S1743921309031421.

Heckman, Timothy M. and Philip N. Best (2014). 'The Coevolution of Galaxies and Supermassive Black Holes: Insights from Surveys of the Contemporary Universe'. In: *Annual Review of Astronomy and Astrophysics* 52.1, pp. 589–660. doi: 10.1146/annurev-astro-081913-035722.

Hey, James Stanley et al. (1948). 'An Investigation of Galactic Radiation in the Radio Spectrum'. In: *Proceedings of the Royal Society of London. Series A. Mathematical and Physical Sciences* 192.1030, pp. 425–445. doi: 10.1098/rspa.1948.0017.

Högbom, JA (1974). 'Aperture Synthesis with a Non-Regular Distribution of Interferometer Baselines'. In: *Astronomy and Astrophysics Supplement Series* 15, p. 417.

Hunter, John D. (May 2007). 'Matplotlib: A 2D Graphics Environment'. In: *Computing in Science & Engineering* 9.03, pp. 90–95. issn: 1521-9615. doi: 10.1109/MCSE.2007.55.

Hutschenreuter, S. et al. (Jan. 2022). 'The Galactic Faraday Rotation Sky 2020'. In: *Astronomy & Astrophysics* 657, A43. issn: 0004-6361, 1432-0746. doi: 10.1051/0004-6361/202140486.

Intema, H. T. et al. (July 2009). 'Ionospheric Calibration of Low Frequency Radio Interferometric Observations Using the Peeling Scheme: I. Method Description and First Results'. In: *Astronomy and Astrophysics* 501.3, pp. 1185–1205. issn: 00046361. doi: 10.1051/0004-6361/200811094.

Ishwara-Chandra, C. H. et al. (Oct. 1998). 'A Polarization Study of Radio Galaxies and Quasars Selected from the Molonglo Complete Sample'. In: *Monthly Notices of the Royal Astronomical Society* 300.1, pp. 269–286. issn: 0035-8711. doi: 10.1046/j.1365-8711.1998.01906.x.

Isobe, Naoki et al. (Dec. 2017). 'Mid-Infrared Excess from the West Hot Spot of the Radio Galaxy Pictor A Unveiled by *WISE*'. In: *The Astrophysical Journal Letters* 850.2, p. 193. issn: 1538-4357. doi: 10.3847/1538-4357/aa94c9.

Isobe, Naoki et al. (Aug. 2020). 'Herschel SPIRE Discovery of Far-infrared Excess Synchrotron Emission from the West Hot Spot of the Radio Galaxy Pictor A'. In: *The Astrophysical Journal Letters* 899.1, p. 17. issn: 1538-4357. doi: 10.3847/1538-4357/ab9d1c.

Jacobs, Daniel C. et al. (Oct. 2013). 'A Flux Scale For Southern Hemisphere 21 Cm Epoch Of Reionization Experiments'. In: *The Astrophysical Journal Letters* 776.2, p. 108. issn: 0004-637X. doi: 10.1088/0004-637X/776/2/108.

Jansky, Karl G (1933a). 'Electrical Disturbances Apparently of Extraterrestrial Origin'. In: *Proceedings of the Institute of Radio Engineers* 21.10, pp. 1387–1398.

Jansky, Karl G. (July 1933b). 'Radio Waves from Outside the Solar System'. In: *Nature* 132.3323, pp. 66–66. issn: 1476-4687. doi: 10.1038/132066a0.

Jonas, J. and MeerKAT Team (Jan. 2016). *The MeerKAT Radio Telescope*, p. 1. doi: 10.22323/1.277.0001.

Jones, R. Clark (July 1941). 'A New Calculus for the Treatment of Optical SystemsI. Description and Discussion of the Calculus'. In: *J. Opt. Soc. Am., JOSA* 31.7, pp. 488–493. doi: 10.1364/JOSA.31.000488.

Joye, W. A. and E. Mandel (Jan. 2003). 'New Features of SAOImage DS9'. In: 295, p. 489.

Józsa, Gyula I. G. et al. (June 2020). 'CARACal: Containerized Automated Radio Astronomy Calibration Pipeline'. In: *Astrophys. Source Code Libr.*, ascl:2006.014.

Kass, Robert E. and Adrian E. Raftery (June 1995). 'Bayes Factors'. In: *Journal of The American Statistical Association* 90.430, pp. 773–795. issn: 0162-1459. doi: 10.1080/01621459.1995.10476572.

Katz-Stone, Debora M., Lawrence Rudnick and Martha C. Anderson (Apr. 1993). 'Determining the Shape of Spectra in Extended Radio Sources'. In: *Astrophysical Journal* 407, p. 549. issn: 0004-637X. doi: 10.1086/172536.

Kenyon, JS et al. (2018). 'CUBICAL–Fast Radio Interferometric Calibration Suite Exploiting Complex Optimization'. In: *Monthly Notices of the Royal Astronomical Society* 478.2, pp. 2399–2415. doi: 10.1093/mnras/sty1221.

Kiepenheuer, K. O. (Aug. 1950). 'Cosmic Rays as the Source of General Galactic Radio Emission'. In: *Physical Review* 79.4, pp. 738–739. doi: 10.1103/PhysRev.79.738.

Klein, Ulrich and Andrew Fletcher (Nov. 2014). *Galactic and Intergalactic Magnetic Fields*. Springer. isbn: 978-3-319-08942-3.

Kriss, G. A. (Jan. 1985). 'X-Ray Luminosity and the Hydrogen-Line Ratios of Quasars and Seyfert Galaxies.' In: *Astronomy Journal* 90, pp. 1–5. issn: 0004-6256. doi: 10.1086/113702.

Kruschke, John (2014). *Doing Bayesian Data Analysis: A Tutorial with R, JAGS, and Stan.* Academic Press.

Kumazaki, Kohei et al. (June 2014). 'Properties of Intrinsic Polarization Angle Ambiguities in Faraday Tomography'. In: *Publications of the Astronomical Society of Japan* 66.3, p. 61. issn: 0004-6264. doi: 10.1093/pasj/psu030.

Lacy, M. et al. (Jan. 2020). 'The Karl G. Jansky Very Large Array Sky Survey (VLASS). Science Case and Survey Design'. In: *Publications of the Astronomical Society of the Pacific* 132.1009, p. 035001. issn: 1538-3873. doi: 10.1088/1538-3873/ab63eb.

Laing, R. A. (Dec. 1980). 'A Model for the Magnetic-Field Structure in Extended Radio Sources'. In: *Monthly Notices of The Royal Astronomical Society* 193.3, pp. 439–449. issn: 0035-8711. doi: 10.1093/mnras/193.3.439.

– (Jan. 1988). 'The Sidedness of Jets and Depolarization in Powerful Extragalactic Radio Sources'. In: *Nature* 331.6152, pp. 149–151. issn: 00280836. doi: 10.1038/331149a0.

Lang, Kenneth R. (2013). 'The Material Between the Stars'. In: *Essential Astrophysics.* Ed. by Kenneth R. Lang. Undergraduate Lecture Notes in Physics. Berlin, Heidelberg: Springer, pp. 357–380. isbn: 978-3-642-35963-7. doi: 10.1007/978-3-642-35963-7_11.

Larmor, Joseph (1919). 'How the Sun Might Have Become a Magnet'. In: *Elec. Rev* 85.2183, p. 412.

Lazarian, A. (Oct. 2005). 'Production of the Large Scale Superluminal Ejections of the Microquasar GRS 1915+105 by Violent Magnetic Reconnection'. In: *Astronomy & Astrophysics* 441.3, pp. 845–853. issn: 0004-6361, 1432-0746. doi: 10.1051/0004-6361:20042590.

Ledden, J. E. and S. L. O'Dell (Nov. 1985). 'The Radio-Optical-X-ray Spectral Flux Distributions of Blazars.' In: *The Astrophysical Journal* 298, pp. 630–643. issn: 0004-637X. doi: 10.1086/163647.

Ledlow, M.J. and F.N. Owen (1996). '20 Cm VLA Survey of Abell Clusters of Galaxies. VI. Radio/Optical Luminosity Functions'. In: *Astronomical Journal* 112.1, pp. 9–22. issn: 0004-6256. doi: 10.1086/117985.

Liu, R. and G. Pooley (Mar. 1991a). 'Spectral Index and Depolarization Asymmetry in Powerful Radio Sources'. In: *Monthly Notices of The Royal Astronomical Society* 249.2, pp. 343–351. issn: 0035-8711. doi: 10.1093/mnras/249.2.343.

Liu, Ronghui and Guy Pooley (Dec. 1991b). 'The Correlated Radio and Optical Asymmetries of Powerful Radio Galaxies'. In: *Monthly Notices of the Royal Astronomical Society* 253.4, pp. 669–674. issn: 0035-8711. doi: 10.1093/mnras/253.4.669.

Loi, F. et al. (Apr. 2022). 'A Depolarizing H I Tidal Tail in the Western Lobe of Fornax A'. In: *Astronomy and Astrophysics* 660, A48. issn: 0004-6361. doi: 10.1051/0004-6361/202142879.

Longair, M. S., M. Ryle and P. A. G. Scheuer (Oct. 1973). 'Models of Extended Radio Sources'. In: *Monthly Notices of The Royal Astronomical Society* 164.3, pp. 243–270. issn: 0035-8711. doi: 10.1093/mnras/164.3.243.

Longair, Malcolm S (2010). *High Energy Astrophysics.* Cambridge university press.

Mackay, Craig D. (Oct. 1971). 'Observations of the Structure of Radio Sources in the 3C Catalogue — V: The Properties of Sources in a Complete Sample'. In: *Monthly Notices of the Royal Astronomical Society* 154.2, pp. 209–227. issn: 0035-8711. doi: 10.1093/mnras/154.2.209.

Mandel, Eric and Alexey Vikhlinin (June 2022). 'Emandel/Js9: V3.8'. In: *Zenodo*. doi: 10.5281/zenodo.6675771.

Marshall, F. E. et al. (July 1979). 'New Hard X-ray Sources Observed with HEAO A-2.' In: *Astrophysical Journal, Supplement Series* 40, pp. 657–666. issn: 0067-0049. doi: 10.1086/190600.

Marshall, H. L. et al. (May 2010). 'A Flare in the Jet of Pictor A'. In: *Astrophysical Journal* 714.2, pp. L213–L216. doi: 10.1088/2041-8205/714/2/L213.

McKinnon, Mark et al. (2019). 'Ngvla: The next Generation Very Large Array'. In: *Bulletin of the American Astronomical Society* 51.7, p. 81.

McMullin, J. P. et al. (Oct. 2007). 'CASA Architecture and Applications'. In: *Astronomical Data Analysis Software and Systems XVI*. Vol. 376, p. 127.

McNamara, B. R. and P. E. J. Nulsen (May 2012). 'Mechanical Feedback from Active Galactic Nuclei in Galaxies, Groups and Clusters'. In: *New Journal of Physics* 14.5, p. 055023. issn: 1367-2630. doi: 10.1088/1367-2630/14/5/055023.

Meisenheimer, K. et al. (July 1989). 'The Synchrotron Spectra of Radio Hot Spots.' In: *Astronomy and Astrophysics* 219, pp. 63–86. issn: 0004-6361.

Migliori, Giulia et al. (Oct. 2007). 'Radio Lobes of Pictor A: An X-Ray Spatially Resolved Study'. In: *Astrophysical Journal* 668, pp. 203–208. issn: 0004-637X. doi: 10.1086/520870.

Miley, G. (Jan. 1980). 'The Structure of Extended Extragalactic Radio Sources'. In: *Annual Review of Astronomy and Astrophysics* 18, pp. 165–218. issn: 0066-4146. doi: 10.1146/annurev.aa.18.090180.001121.

Mingo, B et al. (Sept. 2019). 'Revisiting the Fanaroff–Riley Dichotomy and Radio-Galaxy Morphology with the LOFAR Two-Metre Sky Survey (LoTSS)'. In: *Monthly Notices of the Royal Astronomical Society* 488.2, pp. 2701–2721. issn: 0035-8711. doi: 10.1093/mnras/stz1901.

Miyashita, Yoshimitsu (Sept. 2019). 'Performance Test of QU-Fitting'. In: *Galaxies* 7.3, p. 69. issn: 2075-4434. doi: 10.3390/galaxies7030069.

Miyashita, Yoshimitsu et al. (Jan. 2019). 'Performance Test of QU-fitting in Cosmic Magnetism Study'. In: *Monthly Notices of the Royal Astronomical Society* 482.2, pp. 2739–2749. issn: 0035-8711. doi: 10.1093/mnras/sty2862.

Morganti, Raffaella (2017). 'The Many Routes to AGN Feedback'. In: *Frontiers in Astronomy and Space Sciences* 4, p. 42. issn: 2296-987X.

Morimoto, M. and I. A. Lockhart (Feb. 1968). 'High Resolution Mapping of Four Strong Radio Sources at 80 MHz'. In: *Publications of The Astronomical Society of Australia* 1, p. 99. issn: 0066-99971323-3580. doi: 10.1017/S1323358000010857.

Mukherjee, Pia, David Parkinson and Andrew R. Liddle (Jan. 2006). 'A Nested Sampling Algorithm for Cosmological Model Selection'. In: *The Astrophysical Journal Letters* 638.2, p. L51. issn: 0004-637X. doi: 10.1086/501068.

Mullin, L. M., J. M. Riley and M. J. Hardcastle (Oct. 2008). 'Observed Properties of FRII Quasars and Radio Galaxies at $z < 1.0$'. In: *Monthly Notices of the Royal Astronomical Society* 390.2, pp. 595–621. issn: 0035-8711. doi: 10.1111/j.1365-2966.2008.13534.x.

Nan, Rendong et al. (June 2011). 'The Five-Hundred-Meter Aperture Spherical Radio Telescope (Fast) Project'. In: *International Journal of Modern Physics D* 20.06, pp. 989–1024. issn: 0218-2718. doi: 10.1142/S0218271811019335.

Noordam, J. E. and O. M. Smirnov (Nov. 2010). 'The MeqTrees Software System and Its Use for Third-Generation Calibration of Radio Interferometers'. In: *Astronomy and Astrophysics* 524.2, A61. issn: 00046361. doi: 10.1051/0004-6361/201015013.

Noordam, Jan E. (Sept. 2004). 'LOFAR Calibration Challenges'. In: *Ground-Based Telesc.* Ed. by Jacobus M. Oschmann Jr. Vol. 5489. SPIE, p. 817. doi: 10.1117/12.544262.

O'Sullivan, S. P. et al. (Apr. 2012). 'Complex Faraday Depth Structure of Active Galactic Nuclei as Revealed by Broad-Band Radio Polarimetry'. In: *Monthly Notices of the Royal Astronomical Society* 421.4, pp. 3300–3315. issn: 0035-8711. doi: 10.1111/j.1365-2966.2012.20554.x.

Offringa, A. R. and O. Smirnov (Oct. 2017). 'An Optimized Algorithm for Multiscale Wideband Deconvolution of Radio Astronomical Images'. In: *Monthly Notices of the Royal Astronomical Society* 471.1, pp. 301–316. issn: 0035-8711. doi: 10.1093/mnras/stx1547.

Offringa, A. R. et al. (Oct. 2014). 'Wsclean: An Implementation of a Fast, Generic Wide-Field Imager for Radio Astronomy'. In: *Monthly Notices of the Royal Astronomical Society* 444.1, pp. 606–619. issn: 0035-8711. doi: 10.1093/mnras/stu1368.

Pence, William (Jan. 1999). 'CFITSIO, v2.0: A New Full-Featured Data Interface'. In: *Astronomical Data Analysis Software and Systems VIII*. Vol. 172, p. 487.

Perley, R. A., J. W. Dreher and J. J. Cowan (Oct. 1984). 'The Jet and Filaments in Cygnus A.' In: *Astrophysical Journal* 285, pp. L35–L38. doi: 10.1086/184360.

Perley, Richard A., Hermann-Josef Roser and Klaus Meisenheimer (Dec. 1997). 'The Radio Galaxy PictorA – a Study with the VLA'. In: *Astronomy and Astrophysics* 328, pp. 12–32.

Petrosian, V. and A. M. Bykov (2008). 'Particle Acceleration Mechanisms'. In: *Clusters of Galaxies: Beyond the Thermal View*. Ed. by Jelle Kaastra. New York, NY: Springer, pp. 207–227. isbn: 978-0-387-78875-3. doi: 10.1007/978-0-387-78875-3_11.

Prestage, R. M. (Jan. 1985). 'The Environments of Radio Galaxies'. PhD thesis. University of Edinburgh, UK. doi: 1842/27209.

Rau, U. and T. J. Cornwell (Aug. 2011). 'A Multi-Scale Multi-Frequency Deconvolution Algorithm for Synthesis Imaging in Radio Interferometry'. In: *Astronomy and Astrophysics* 532, A71. issn: 0004-6361. doi: 10.1051/0004-6361/201117104.

Rawlings, Steve and Matt J. Jarvis (Dec. 2004). 'Evidence That Powerful Radio Jets Have a Profound Influence on the Evolution of Galaxies'. In: *Monthly Notices of the Royal Astronomical Society* 355.3, pp. L9–L12. issn: 0035-8711. doi: 10.1111/j.1365-2966.2004.08234.x.

Reber, Grote (Feb. 1940). 'Cosmic Static'. In: *Proceedings of the IRE* 28.2, pp. 68–70. issn: 2162-6634. doi: 10.1109/JRPROC.1940.228921.

– (Apr. 1949). 'Galactic Radio Waves'. In: *Sky and Telescope* 8, p. 139. issn: 0037-6604.

Rees, M. J. (Jan. 1971). 'New Interpretation of Extragalactic Radio Sources'. In: *Nature* 229.5283, pp. 312–317. issn: 1476-4687. doi: 10.1038/229312a0.

Remazeilles, M. et al. (Aug. 2015). 'An Improved Source-Subtracted and Destriped 408-MHz All-Sky Map'. In: *Monthly Notices of the Royal Astronomical Society* 451.4, pp. 4311–4327. issn: 0035-8711. doi: 10.1093/mnras/stv1274.

Robitaille, Thomas (Feb. 2019). *APLpy v2.0: The Astronomical Plotting Library in Python*. doi: 10.5281/zenodo.2567476.

Roeser, Hermann-Josef and Klaus Meisenheimer (Mar. 1987). 'A Bright Optical Synchrotron Counterpart of the Western Hot SPOT in Pictor A'. In: *Astrophysical Journal* 314, p. 70. issn: 0004-637X. doi: 10.1086/165039.

Rudnick, Lawrence and William D. Cotton (Apr. 2023). 'Full Resolution Deconvolution of Complex Faraday Spectra'. In: *Monthly Notices of The Royal Astronomical Society* 522.1, pp. 1464–1479. issn: 0035-8711, 1365-2966. doi: 10.1093/mnras/stad1090.

Rybicki, George B. and Alan P. Lightman (Jan. 1991). *Radiative Processes in Astrophysics*. John Wiley & Sons. isbn: 978-0-471-82759-7.

Ryle, M. (May 1962). 'The New Cambridge Radio Telescope'. In: *Nature* 194.4828, pp. 517–518. issn: 1476-4687. doi: 10.1038/194517a0.

Ryle, M. and D. D. Vonberg (Sept. 1946). 'Solar Radiation on 175 Mc./s'. In: *Nature* 158.4010, pp. 339–340. issn: 1476-4687. doi: 10.1038/158339b0.

Sault, R. J. and M. H. Wieringa (1994). 'Multi-Frequency Synthesis Techniques in Radio Interferometric Imaging.' In: *Astronomy and Astrophysics* 108, pp. 585–594. issn: 0365-0138.

Sault, Robert J, Peter J Teuben and Mel C H Wright (1995). 'A Retrospective View of MIRIAD'. In: *Astronomical Data Analysis Software and Systems IV*. Vol. 77, p. 433.

Scheuer, P. A. G. (Mar. 1974). 'Models of Extragalactic Radio Sources with a Continuous Energy Supply from a Central Object'. In: *Monthly Notices of the Royal Astronomical Society* 166.3, pp. 513–528. issn: 0035-8711. doi: 10.1093/mnras/166.3.513.

– (1982). 'Morphology and Power of Radio Sources'. In: *Extragalactic Radio Sources*. Ed. by David S. Heeschen and Campbell M. Wade. Dordrecht: Springer Netherlands, pp. 163–165. isbn: 978-94-009-7781-5. doi: 10.1007/978-94-009-7781-5_46.

Schnitzeler, D. H. F. M., J. K. Banfield and K. J. Lee (July 2015). 'Polarization Signatures of Unresolved Radio Sources'. In: *Monthly Notices of the Royal Astronomical Society* 450.4, pp. 3579–3596. issn: 0035-8711. doi: 10.1093/mnras/stv708.

Schnitzeler, D. H. F. M., P. Katgert and A. G. de Bruyn (Feb. 2009). 'WSRT Faraday Tomography of the Galactic ISM at $\lambda \sim 0.86$ m'. In: *Astronomy and Astrophysics* 494.2, pp. 611–622. issn: 0004-6361. doi: 10.1051/0004-6361:20078912.

Schnitzeler, D H F M et al. (May 2019). 'S-PASS/ATCA: A Window on the Magnetic Universe in the Southern Hemisphere'. In: *Monthly Notices of The Royal Astronomical Society* 485.1, pp. 1293–1309. issn: 0035-8711. doi: 10.1093/mnras/stz092.

Schott, George Adolphus (1912). *Electromagnetic Radiation and the Mechanical Reactions Arising from It: Being an Adams Prize Essay in the University of Cambridge*. University Press. isbn: 978-0-598-95884-6.

Schwab, F. R. (July 1984). 'Relaxing the Isoplanatism Assumption in Self-Calibration; Applications to Low-Frequency Radio Interferometry'. In: *The Astronomical Journal* 89, pp. 1076–1081. issn: 0004-6256. doi: 10.1086/113605.

Schwarz, U. J., J. B. Whiteoak and D. J. Cole (1974). 'Synthesis Observations of Southern Radio Sources at 1410 MHz with the Parkes Interferometer. II. Polarization and Brightness Distributions Across Seven Sources'. In: *Australian Journal of Physics* 27.4, pp. 563–574. issn: 1446-5582. doi: 10.1071/ph740563.

Schwinger, Julian (June 1949). 'On the Classical Radiation of Accelerated Electrons'. In: *Physical Review* 75.12, pp. 1912–1925. doi: 10.1103/PhysRev.75.1912.

Sebokolodi, M. Lerato L et al. (Oct. 2020). 'A Wideband Polarization Study of Cygnus A with the Jansky Very Large Array. I. The Observations and Data'. In: *Astrophysical Journal* 903.1, p. 36. issn: 15384357. doi: 10.3847/1538-4357/abb80e.

Shaw, J. R., M. Bridges and M. P. Hobson (July 2007). 'Efficient Bayesian Inference for Multimodal Problems in Cosmology'. In: *Monthly Notices of The Royal Astronomical Society* 378.4, pp. 1365–1370. issn: 0035-8711, 1365-2966. doi: 10.1111/j.1365-2966.2007.11871.x.

Shepherd, M. C. (Jan. 1997). 'Difmap: An Interactive Program for Synthesis Imaging'. In: *Astronomical Data Analysis Software and Systems VI*. Vol. 125, p. 77.

Simkin, S. M. et al. (Aug. 1999). 'Pictor A (PKS 0518-45): From Nucleus to Lobes'. In: *Astrophysical Journal, Supplement Series* 123.2, pp. 447–465. issn: 0067-0049. doi: 10.1086/313243.

Singh, K. P., A. R. Rao and M. N. Vahia (Oct. 1990). 'X-Ray Observations of the Radio Galaxy Pictor A.' In: *Monthly Notices of The Royal Astronomical Society* 246, p. 706. issn: 0035-8711.

Skilling, John (Nov. 2004). 'Nested Sampling'. In: *AIP Conference Proceedings* 735.1, pp. 395–405. issn: 0094-243X. doi: 10.1063/1.1835238.

Slee, O. B. and K. V. Sheridan (Oct. 1975). 'High-Resolution Observations of Centaurus-A and Pictor-A at 160 MHz'. In: *Publications of The Astronomical Society of Australia* 2.6, pp. 336–338. issn: 1323-3580, 1448-6083. doi: 10.1017/S1323358000014181.

Smirnov, O. M. (Mar. 2011a). 'Revisiting the Radio Interferometer Measurement Equation - II. Calibration and Direction-Dependent Effects'. In: *Astronomy & Astrophysics* 527, A107. issn: 0004-6361, 1432-0746. doi: 10.1051/0004-6361/201116434.

– (Mar. 2011b). 'Revisiting the Radio Interferometer Measurement Equation - III. Addressing Direction-Dependent Effects in 21 Cm WSRT Observations of 3C 147'. In: *Astronomy & Astrophysics* 527, A108. issn: 0004-6361, 1432-0746. doi: 10.1051/0004-6361/201116435.

– (Mar. 2011c). 'Revisiting the Radio Interferometer Measurement Equation: I. A Full-Sky Jones Formalism'. In: *Astronomy & Astrophysics* 527.14, A106. issn: 00046361. doi: 10.1051/0004-6361/201016082.

Smirnov, Oleg M. et al. (July 2022). 'ShadeMS: Rapid Plotting of Big Radio Interferometry Data'. In: *Astronomical Data Analysis Software and Systems XXX*. Vol. 532, p. 385.

Sob, U M et al. (June 2021). 'Solution Intervals Considered Harmful: On the Optimality of Radio Interferometric Gain Solutions'. In: *Monthly Notices of the Royal Astronomical Society* 504.2, pp. 1714–1732. issn: 0035-8711. doi: 10.1093/mnras/stab928.

Sokoloff, D. D. et al. (Aug. 1998). 'Depolarization and Faraday Effects in Galaxies'. In: *Monthly Notices of The Royal Astronomical Society* 299.1, pp. 189–206. issn: 0035-8711. doi: 10.1046/j.1365-8711.1998.01782.x.

Stanley, G. J. and O. B. Slee (1950). 'Galactic Radiation at Radio Frequencies II. The Discrete Sources'. In: *Australian Journal of Chemistry* 3.2, pp. 234–250. issn: 14450038. doi: 10.1071/CH9500234.

Subramanian, Kandaswamy (May 2016). 'The Origin, Evolution and Signatures of Primordial Magnetic Fields'. In: *Reports On Progress in Physics* 79.7, p. 076901. issn: 0034-4885. doi: 10.1088/0034-4885/79/7/076901.

Sun, X. H. et al. (Jan. 2015). 'Comparison of Algorithms for Determination of Rotation Measure and Faraday Structure. I. 1100-1400 MHz'. In: *Astronomy Journal* 149.2, p. 60. issn: 1538-3881. doi: 10.1088/0004-6256/149/2/60.

Sunada, Yuji et al. (June 2022). 'NuSTAR Discovery of the Hard X-ray Emission and a Wide-Band X-ray Spectrum from the Pictor A Western Hotspot'. In: *Publications of the Astronomical Society of Japan* 74.3, pp. 602–611. issn: 0004-6264. doi: 10.1093/pasj/psac022.

Taylor, A. R., J. M. Stil and C. Sunstrum (Aug. 2009). 'A Rotation Measure Image of the Sky'. In: *Astrophysical Journal* 702.2, p. 1230. issn: 0004-637X. doi: 10.1088/0004-637X/702/2/1230.

Taylor, GB et al. (1990). 'VLA Observations of the Radio Galaxy Hydra A (3C 218)'. In: *Astrophysical Journal* 360, pp. 41–54. doi: 10.1086/169094.

Thimmappa, R. et al. (Nov. 2020). 'Chandra Imaging of the Western Hotspot in the Radio Galaxy Pictor A: Image Deconvolution and Variability Analysis'. In: *Astrophysical Journal* 903, p. 109. issn: 0004-637X. doi: 10.3847/1538-4357/abb605.

Thimmappa, R. et al. (Nov. 2021). 'Complex Structure of the Eastern Lobe of the Pictor A Radio Galaxy: Spectral Analysis and X-Ray/Radio Correlations'. In: *Astrophysical Journal* 921.1, p. 44. issn: 0004-637X. doi: 10.3847/1538-4357/ac1ce3.

Thompson, A. Richard (Jan. 1999). 'Fundamentals of Radio Interferometry'. In: *Synthesis Imaging in Radio Astronomy II*. Vol. 180, p. 11.

Tingay, S. J. et al. (Apr. 2000). 'The Parsec-Scale Structure and Evolution of the Nearby Fanaroff-Riley Type II Radio Galaxy Pictor A'. In: *The Astronomical Journal* 119.4, p. 1695. issn: 1538-3881. doi: 10.1086/301283.

Tingay, S. J. et al. (Nov. 2008). 'A High Resolution View of the Jet Termination Shock in a Hotspot of the Nearby Radio Galaxy Pictor A: Implications for X-Ray Models of Radio Galaxy Hotspots'. In: *The Astronomical Journal* 136.6, pp. 2473–2482. issn: 00046256. doi: 10.1088/0004-6256/136/6/2473.

Tingay, S. J. et al. (Jan. 2013). 'The Murchison Widefield Array: The Square Kilometre Array Precursor at Low Radio Frequencies'. In: *Publications of The Astronomical Society of Australia* 30, e007. issn: 1323-3580, 1448-6083. doi: 10.1017/pasa.2012.007.

Tribble, Peter C. (Mar. 1993). 'Radio Spectral Ageing in a Random Magnetic Field'. In: *Monthly Notices of the Royal Astronomical Society* 261.1, pp. 57–62. issn: 0035-8711. doi: 10.1093/mnras/261.1.57.

Van Eck, C. L. et al. (July 2023). 'RMTable2023 and PolSpectra2023: Standards for Reporting Polarization and Faraday Rotation Measurements of Radio Sources'. In: *The Astrophysical Journal Supplement Series* 267.2, p. 28. issn: 0067-0049. doi: 10.3847/1538-4365/acda24.

Van Eck, Cameron (Oct. 2018). 'The Power of Low Frequencies: Faraday Tomography in the Sub-GHz Regime'. In: *Galaxies* 6, p. 112. doi: 10.3390/galaxies6040112.

Velden, Ellert van der (Feb. 2020). 'CMasher: Scientific Colormaps for Making Accessible, Informative and 'cmashing' Plots'. In: *Journal of Open Source Software* 5.46, p. 2004. issn: 2475-9066. doi: 10.21105/joss.02004.

Voronkov, M. A. and M. H. Wieringa (Dec. 2004). 'The Cotton-Schwab Clean At Ultra-High Dynamic Range'. In: *Experimental Astronomy* 18.1, pp. 13–29. issn: 1572-9508. doi: 10.1007/s10686-005-9000-7.

Wang, K. –S. et al. (Jan. 2020). 'CARTA: Cube Analysis and Rendering Tool for Astronomy'. In: *Astronomical Data Analysis Software and Systems XXIX*. Vol. 527, p. 213.

Wells, D. C. and E. W. Greisen (Jan. 1979). 'FITS - a Flexible Image Transport System'. In: *Image Processing in Astronomy*, p. 445.

Wilson, A. S., A. J. Young and P. L. Shopbell (Feb. 2001). 'Chandra X-Ray Observations of Pictor A: High-Energy Cosmic Rays in a Radio Galaxy'. In: *The Astrophysical Journal Letters* 547.2, p. 740. issn: 0004-637X. doi: 10.1086/318412.

Wilson, Warwick E. et al. (Sept. 2011). 'The Australia Telescope Compact Array Broad-band Backend: Description and First Results'. In: *Monthly Notices of The Royal Astronomical Society* 416.2, pp. 832–856. issn: 00358711. doi: 10.1111/j.1365-2966.2011.19054.x.

Wrobel, J. M. and R. C. Walker (Jan. 1999). 'Sensitivity'. In: *Synthesis Imaging in Radio Astronomy II*. Vol. 180, p. 171.

Xie, G. Z. et al. (June 1998). 'The Massive Black Hole in the Center of the Active Galaxy MRK 421'. In: *Astronomy and Astrophysics* 334, pp. L29–L31. issn: 0004-6361.

Zhang, Jin et al. (July 2009). 'Origin of The X-rays And Possible GeV-TeV Emission From The Western Hotspot of Pictor A'. In: *The Astrophysical Journal Letters* 701.1, p. 423. issn: 0004-637X. doi: 10.1088/0004-637X/701/1/423.

Zheng, Wei, Luc Binette and Jack W. Sulentic (Dec. 1990). 'A Double-Stream Model for Line Profiles'. In: *The Astrophysical Journal* 365, p. 115. issn: 0004-637X. doi: 10.1086/169462.

van Diepen, G. N. J. (Sept. 2015). 'Casacore Table Data System and Its Use in the MeasurementSet'. In: *Astronomy and Computing* 12, pp. 174–180. issn: 2213-1337. doi: 10.1016/j.ascom.2015.06.002.

van Diepen, Ger and Allen Farris (Jan. 1994). 'AIPS++ Table Data System'. In: *Astronomical Data Analysis Software and Systems III*. Vol. 61, p. 417.

Colophon

I have a very pedantic and exotic taste for things. There's never a gray area regarding this, I either like something or not. Unfortunately for me, my financial circumstances as per now do not afford me the luxury of choice (LOL!). Rather, I'm forced to create my own realities (read recreate my exotic tastes) with what I have, and all the freebies I can get (within good reason of course). More often than not, my recreations and adaptations must be outstanding to me before being presented publicly because they are, in essence, a representation of my palate. The aesthetic of this thesis encompasses this here opinion.

This thesis was an attempt at recreating the most aesthetically pleasing thesis I've ever seen from Aaron Turon[1]. However, since I could not find the original template, I was lucky enough to stumble upon the wonderful work developed by André Miede and Ivo Pletikosi who typeset this document using the typographical look-and-feel `classicthesis`. The style was inspired by Robert Bringhurst's seminal book on typography "*The Elements of Typographic Style*". I customised the template to my liking, and changed the main fonts to a mixture of BaskerValdADFstd (a freebie because the original font, Baskerville, is super expensive!) and LinuxBiolinum.

`classicthesis` is available for both LaTeX and LyX:

`https://bitbucket.org/amiede/classicthesis/`

Happy users of `classicthesis` usually send a real postcard to the author, who features the received postcards at:

`http://postcards.miede.de/`

A big thanks to them for making work easier :D!

Final Version as of 31st July 2024 (v2.0).

1 `https://www.khoury.northeastern.edu/home/turon/thesis.pdf`